TESIS DE LA UNIVERSIDAD DE ZARAGOZA

2014

78

Mario Morales Hernández

Efficient explicit finite volume schemes for the shallow water equations with solute transport

Departamento
Ciencia y Tecnología de Materiales y Fluidos

Director/es
García Navarro, Pilar

ISSN 2254-7606

Prensas de la Universidad Universidad Zaragoza

Universidad Zaragoza
1542

Tesis Doctoral

EFFICIENT EXPLICIT FINITE VOLUME SCHEMES FOR THE SHALLOW WATER EQUATIONS WITH SOLUTE TRANSPORT

Autor

Mario Morales Hernández

Director/es

García Navarro, Pilar

UNIVERSIDAD DE ZARAGOZA

Ciencia y Tecnología de Materiales y Fluidos

2014

Efficient explicit finite volume schemes for the shallow water equations with solute transport

Mario Morales Hernández

A thesis for the title of Doctor of Philosophy
Fluid Mechanics Doctoral Programme

March 2014

Supervisor
Prof. Dr. Pilar García Navarro

Escuela de Ingeniería y Arquitectura Universidad de Zaragoza

Efficient explicit finite volume schemes for the shallow water equations with solute transport

Abstract

This work is concerned with the design and the implementation of efficient and novel numerical techniques in the context of the shallow water equations with solute transport, capable to improve the numerical results achieved by existing explicit approaches. When dealing with realistic applications in Hydraulic Engineering, a compromise between accuracy and computational time is usually required to simulate large temporal and spatial scales in a reasonable time. With the aim to improve the existent numerical methods in such a way to increase accuracy and reduce computational time. Three main contributions are envisaged in this work: a pressure-based source term discretization for the 1D shallow water equations, the analysis and development of a Large Time Step explicit scheme for the 1D and 2D shallow water equations with source terms and the numerical coupling between the 1D and the 2D shallow water equations in a 1D-2D coupled model. The first improvement roughly consists of exploring the pressure and bed slope source terms that appear in the 1D and 2D shallow water equations to discretize them in an intelligent way to avoid extremely reductions in the time step size. On the other hand, the implementation of a Large Time Step scheme is carried out. In order to relax the stability condition associated to explicit schemes and to allow large time step sizes, reducing consequently the numerical diffusion associated to the original explicit scheme. Finally, two 1D-2D coupled models are developed. They are demonstrated to be fully conservative and are able to approximate well the results obtained by a fully 2D model in terms of accuracy, while the computational effort is clearly reduced. All the advances are analysed by means of different test cases, including not only academic configurations but also realistic applications, in which the numerical results achieved by the new numerical techniques proposed in this work are compared with the conventional approaches.

Esquemas explícitos eficientes en volúmenes finitos para las ecuaciones de aguas poco profundas con transporte de soluto

Resumen

El objetivo de este trabajo consiste en el diseño y la implementación de nuevas técnicas numéricas eficientes para las ecuaciones de las aguas poco profundas con transporte de soluto, capaces de mejorar los resultados numéricos que proporcionan los métodos explícitos existentes. En aplicaciones realistas relacionadas con la Ingeniería Hidráulica, normalmente se requiere un compromiso entre precisión y tiempo de cálculo para simular problemas a grandes escalas temporales y espaciales en un tiempo asumible. Sin embargo, es posible mejorar los métodos numéricos existentes de tal manera que sean capaces de aumentar la precisión y reducir el tiempo de cálculo. En este trabajo destacan tres contribuciones principales: una discretización de los términos fuente, basada en el cálculo de las fuerzas de presión para las ecuaciones 1D de aguas poco profundas, el análisis y el desarrollo de un esquema *Large Time Step* explícito para las ecuaciones 1D como 2D de aguas poco profundas con términos fuente y el acoplamiento numérico entre las ecuaciones 1D y 2D de aguas poco profundas mediante un modelo acoplado 1D-2D. La primera mejora consiste en explorar los términos fuente de fondo y presión que aparecen en las ecuaciones 1D y 2D de aguas poco profundas y discretizarlos de una manera inteligente para evitar reducciones extremas en el tamaño del paso de tiempo. Por otra parte, se propone la implementación de un esquema de tipo *Large Time Step*. Este método consigue relajar la condición de estabilidad asociada a los esquemas explícitos y permite pasos de tiempo más grandes, reduciendo por tanto la difusión numérica asociada al esquema explícito convencional. Por último, se desarrollan dos modelos acoplados 1D-2D. Se demuestra que son totalmente conservativos y que son capaces de aproximar bien los resultados obtenidos por un modelo completo 2D en términos de precisión, al mismo tiempo que se reduce la carga computacional. Todos los avances se analizan usando distintos casos test, incluyendo no solo configuraciones académicas sino aplicaciones realistas, en las que los resultados numéricos obtenidos con las nuevas técnicas propuestas en este trabajo se comparan con los esquemas convencionales.

A mis padres Pedro y Amelia, mi hermana Rosa por darme todo su cariño y apoyo.
A Natalia, por hacerme feliz

Agradecimientos

Me gustaría empezar este apartado agradeciendo a mi directora de tesis Dra. Pilar García Navarro la confianza depositada en mí desde el día en que llegué al departamento hasta el día en que escribo estas palabras. Esta confianza ha sido la base que me ha permitido desarrollarme como investigador y mejorar cada día. Su labor de guía durante estos cuatro años ha sido perfecta, manejando los tiempos acertadamente, haciéndome ver los errores y los aciertos que cometía y sacando lo mejor de mí en cada momento.

De la misma manera, me gustaría agradecer al Dr. Javier Burguete que se acordara de mí cuando yo no ni siquiera había terminado la carrera, confiara en mí y me guiara durante los primeros años de mi tesis. Igualmente me gustaría agradecer personalmente al Dr. Javier Murillo, con quien he podido trabajar codo con codo durante estos años, su desinteresada aportación al igual que su total disponibilidad. Parte de este trabajo es sin duda gracias a él. Me gustaría reconocer también el trabajo de la Dra. Pilar Brufau y su generosidad y apoyo en la última parte de mi tesis, y al Dr. Matthew Hubbard, por darme la oportunidad de trabajar con él durante mi estancia en Leeds.

También quiero agredecer a la Diputación General de Aragón la concesión de una ayuda de Formación de Personal Investigador, que financió la mayoría del tiempo de realización de la tesis.

Por otro lado, me gustaría agradecer a todos los compañeros de despacho y del Área de Mecánica de Fluidos el haberme hecho sentir tan a gusto desde el primer día. Aparte de la amistad que nos une, quiero agradecer a Asier Lacasta su comprensión, su apoyo en buenos y malos momentos y sus buenos consejos, a Daniel Caviedes, todo lo que he aprendido con él no solo en el ámbito laboral sino sobre la vida en general y a Carmelo Juez su afecto y espíritu crítico. Igualmente me gustaría nombrar a Javier Fernández, Samuel Ambroj y Borja Latorre. Todos ellos han contribuido de alguna manera a este trabajo.

Por último, mis amigos y mi familia también merecen un agradecimiento. En particular, me encanta compartir los éxitos con mis padres y éste es uno de ellos. Quiero darles las gracias por su interés, su preocupación, su afecto y su cariño. Pero sobre todo quiero agradecerles la educación que me han dado, basada en la cultura del esfuerzo, del sacrificio y del trabajo, que es garantía de éxito en cualquier ámbito de la vida. Y a mi hermana, por enseñarme que la vida se tiene que ver con optimismo y alegría y por hacerme ver que necesitamos mucho menos de lo que creemos para ser felices. Finalmente, pero no por ello menos importante, me gustaría reconocer a Natalia todo el cariño y el amor que me ha demostrado durante tantos años, apoyándome en los malos momentos y celebrando juntos los buenos. Ella ha sido el equilibrio perfecto para que todo esto saliese adelante. Muchas gracias por compartir conmigo esta aventura.

Contents

List of Figures

List of Tables

Introduction

Computational Hydraulics is concerned with the study of free surface flow dynamics using numerical solutions of non-linear equations that are assumed to govern the involved physical processes. The fluid movement is modelled by fundamental conservation laws that can be expressed in mathematical terms in the form of partial differential equations.

Hydraulic models can be classified according to the number of dimensions in which they represent the spatial domain as 1D, 2D or 3D. In general, 3D approaches may not be adequate to practical cases using the available information: topography, experimental measurements and real observed flooded areas and also due to the unacceptable computational cost required for simulating large scale and time problems. Moreover, certain questions concerning boundary conditions, the validity of turbulence models or pressure hypothesis are open nowadays [49]. For that reason, 1D and 2D models are preferred. Numerical models (1D and 2D) based on the Shallow Water Equations (SWE) have been widely used independently to simulate geophysical free surface flows [16, 19, 13, 14, 90, 10, 11].

One dimensional (1D) models are usually applied in long rivers and open channels with additional equations for hydraulic structures [16, 55, 1, 108, 105] due to their computational efficiency, particularly for river network systems. Their limitation arise in modelling floodplains. This restriction can be nevertheless avoided with the use of 2D shallow water models [31, 13, 12]. Depth-integrated 2D hydrodynamic models have been used for many years for predicting free surface flows. The increasing availability of digital topographic data in recent years provides this type of model with scope for wider application. Although 1D approximations require less information and are computationally time saving, 2D models give more precise results when dealing with a multidimensional flow pattern. However, in real world applications, 2D models can require refined grids resulting in costly and slow simulations.

The non-linear hyperbolic system of equations representing the hydrodynamic phenomena can be extended in order to include the solute transport. The controllability

of contaminant releases in a river has become an important issue in environmental impact analysis. The impact of human activity on surface stream habitats has been extensively studied throughout the world [66, 104], forming the basis for many stream restoration efforts [128]. In this context, the implementation of a predictive tool able to simulate the transport of substances in a shallow water model is clearly justified.

Being a hyperbolic system, the 1D and 2D SWE including the solute transport are a good candidate to apply upwind methods. In particular, a finite volume explicit Godunov's type method [54, 119] is the basis of the advances presented in this thesis. This kind of methods compute the numerical flux that updates the value of each cell by averaging the values of the different approximate solutions that appear when defining a local Riemann Problem between the involved cell and its neighbouring cells. The explicit choice of the numerical fluxes is related to its conceptual simplicity instead of implicit schemes, which require the resolution of an algebraic system of equations. However, in the explicit approach, the time step is restricted by stability criteria. Although the formulation of the numerical schemes is usually written in terms of a numerical flux, another point of view will be considered in this thesis. Following the upwind philosophy, which discriminates the sense of propagation of the information, the updating of a single cell can be seen as computing the in-going contributions that arrive to the cell. Therefore, the corresponding scheme can be described by means of different waves travelling to the left or the right side of each Riemann Problem defined at each edge or interface.

Most of the efforts of the last decade in solving the SWE have been devoted to an adequate source term discretization. The application to realistic scenarios where extreme slopes, important roughness and strong changes in the irregular topography play an important role is not a straightforward procedure. In fact, one of the most important issues in the 2D shallow water model is the correct formulation of wet/dry fronts, which is closely related to, but goes beyond the source term discrezation. The technique of projecting the average source term onto the eigenvector basis is widely accepted as leading to well balanced numerical solutions [122, 65]. The reason behind the treatment of the source terms as a sum of waves defined at the cell edge is related to the necessity of ensuring a perfect balance between flux derivatives and source terms in steady state. This has been previously discussed in [92]. For this purpose, a Roe's Augmented Riemann Solver is adopted in this work to include the presence of

source terms in the numerical resolution of the system of equations. While the Roe's approach [109] is used to decouple the original system and to define approximate Jacobian matrix at each edge to solve the approximate Riemann Problems, the Augmented technique [52, 92, 47] adds a stationary jump discontinuity acting as a source term, reinterpreting the effect associated to the source term in a discrete level. In fact, the Roe's scheme for the augmented system written in a wave propagation form results a special version of the path-conservative scheme proposed in [24, 103] and further developed in [41, 21, 43].

However, a simple source term discretization in complicated test cases involving wetting and drying and extreme slope and/or friction terms could lead to a time step reduction below the classical Courant-Friedrichs-Lewy (CFL) condition [32, 117, 72] required to ensure numerical stability and positivity of the scheme [17, 97, 92]. In order to avoid this, the integral formulation of the source term vector proposed in [92] is extended in this work. This good integration, not only applied on the bed slope source term but also on the friction term, combined with a limitation in the amount of numerical source is able to avoid reducing the time step size. More details relating to this procedure can be found in [92, 93].

The main goal of this work is the development of efficient numerical methods based on existing explicit upwind schemes, able to improve their results in terms of accuracy and computational time. For this purpose, three main contributions, corresponding to three clearly differentiated parts, are envisaged: the extension of the source term integral formulation to the 1D SWE with irregular geometries (part I), the development of Large Time Step (LTS) explicit schemes for the 1D and the 2D frameworks in square and triangular grids (part II) and the numerical coupling of both 1D and 2D models in a 1D-2D model, able to make the best of them (part III).

The aim of Part I will be the integral formulation of the pressure source terms present in the 1D SWE with irregular cross sections. However, this part is also conceived to describe and detail the whole process involving the numerical resolution of a scalar or a system of hyperbolic conservation laws with source terms. The focus is put on upwind explicit finite volume schemes and the Roe's Augmented Approximate Riemann Solver, which are applied to the 1D and 2D SWE with solute transport. Source terms discretization plays an important role in the shallow water context. Apart from maintaining the C-property and the discrete balance between flux and source terms giving rise to well-balanced schemes [122, 72, 117, 118], an adequate

numerical integration of the pressure force terms associated to the change in the river/channel geometry will be explored. In particular, the philosophy developed in [92] for rectangular cross sections will be extended for variable widths and irregular geometries in the 1D SWE.

In Part II, a Large Time Step (LTS) scheme is developed for scalar conservation laws as well as for systems of conservation laws with source terms. It is mainly based on relaxing the CFL condition, associated to the explicit resolution of hyperbolic conservation laws, to allow larger time step sizes. The implementation of the LTS scheme initially developed by Leveque [70, 71, 72] for the linear and non-linear scalar equations will be first performed. When applied to non-linear scalar cases, the proposed LTS scheme requires the discrete representation of the rarefaction wave in the form of several discontinuities travelling at different speeds if an accurate solution is sought at large CFL values. A simple rule to estimate these speeds will be proposed. The inclusion of source terms in the equations will be widely analysed, and a straightforward procedure similar to the homogeneous case will be provided. The extension to systems of conservation laws will be proposed in a general way and then particularly applied to the 1D shallow water equations [87]. The source term treatment and boundary conditions will be extended to this method.

The extension of the LTS scheme to the 2D configuration will be achieved in a first step by means of quadrilateral structured meshes. One general method to accomplish the 2D extension is the dimensional splitting where the equations are simplified to solve them many times in a 1D configuration. While the simplicity of solving 1D equations and the advances related to boundary conditions and source terms are preserved, the disadvantage of the computational time associated with the splitting formulation [115] is significantly reduced because of using large time step sizes in the numerical resolution of the equations [88].

In a second step, the LTS scheme is developed for triangular grids for the 2D configuration. The idea developed in the 1D case or in the dimensional splitting must be modified due to the flow orientation and the geometry/area of each triangle. In particular, the amount of information from each edge must be packed in a certain way, rescaling it conservatively according to the neighbouring edges. Moreover, not only the information is compacted in a particular way but also it is sent following the flow direction across the wall edges, defining branches and preferential paths to be able to reproduce correctly the velocity field. The heterogeneity in the area of each

element is also considered when dealing with unstructured triangular meshes hence cumbersome retriangularizations as in [94] are avoided. Both approaches (square and triangular grids) are validated using linear and non-linear equations and then extended to the 2D SWE. The wet/dry treatment an the source term discretization becomes crucial in the 2D framework thus an adequate formulation is presented, based on the previous advances.

Part III deals with the numerical coupling between the 1D and the 2D SWE. The implementation of a complete 1D-2D model seems to be a good solution to eliminate not only the limitations of the 1D model related with the underlying mathematical hypothesis which introduce some errors when modelling flooding waves over 2D domains, but also the uncertainty in the 2D model associated to the discrete representation of the topography. Moreover, the computational time should be reduced with the 1D-2D coupled model, not only because a large number of cells from the 2D model are eliminated from the computation but also because these cells are usually the responsible for the time step size.

Two different 1D-2D models will be presented in this work. Although both approaches require a careful meshing procedure in the sense that each 1D cell should be connected with and exact number of 2D cells (coupling zone), they are based on different techniques.

As a first approach, the requirement of common quantities in the junction zone between both models will be performed [86]. It will be called FC (Forced Conservative) 1D-2D coupled model. The OMC (Only Mass Conservation) technique evaluates the total water volume existing at the coupling zone and imposes a common water level surface. The MMC (Mass and Momentum Conservation) strategy, considered as an extension of the OMC, enforces not only a new common level at the coupling zone, but also the water velocity components. The use of each strategy will not be transparent to the boundary conditions of the 1D and the 2D models. They have to be revisited and, according to the flow regime, the OMC and/or MMC strategy must be used to avoid non-physical results. Both strategies will be based on the fully conservation property which considers the information that crosses the limits of the 1D or 2D domains [20]. The same philosophy will be applied to the solute transport equation, computing the total solute mass at each coupling zone and then imposing an average concentration.

Another 1D-2D numerical coupled model, called *RCE* (Riemann Coupled Edges) will be developed. When transforming the 1D conserved variables into 2D quantities in a conservative way, it is possible to apply the Roe's linearization [109] and to solve the corresponding Riemann Problem across each 1D-2D edge separating both models. Apart from resulting always conservative in the sense of Roe, the *RCE* 1D-2D coupled model allows to formulate the numerical method for both 1D and 2D cells in a simpler way, considering the contributions arriving from 1D-1D edges, 1D-2D edges and 2D-2D edges. The solute transport equation will be also formulated in terms of the *RCE* coupled model, defining an adequate numerical flux at each 1D-2D edge.

All the proposed numerical methods and strategies to increase accuracy and efficiency are validated not only with analytical solutions [63, 78, 79] but also with experimental and field data [85, 125]. They have been used to reproduce all kind of flow conditions and their performance has been illustrated using test cases with exact solution of steady and unsteady open channel flow problems. Academic configurations and real world applications in which the source terms play an important role are computed, and the efficiency in terms of computational time consumed by these new numerical methods is evaluated in contrast to the conventional schemes.

Part I

Finite volume schemes for conservations laws with source terms

Chapter 1

Conservation laws

1.1 Differential and integral formulation

Conservation laws are used to formulate the dynamics of different physical quantities such as mass, momentum or energy within a physical system. They are directly related to principles of symmetry and wave propagation serving consequently as a strong constraint on any theory in any branch of science [114]. They can be mathematically expressed in the form of a partial differential equation or a system of n partial differential equations:

$$\mathbf{U}_t + \nabla \cdot \mathbf{F}(\mathbf{U}) = \mathbf{S}(\mathbf{U}) \tag{1.1}$$

Here $\mathbf{U}$ is the conserved or vector of conserved variables, $\mathbf{F}(\mathbf{U})$ the flux or vector of fluxes of these conserved variables and $\mathbf{S}(\mathbf{U})$ represents the source terms. As a flux is used and partial derivatives appear in (1.1), the conservation law is named the conservative differential form, which assumes smooth solutions. However, equation (1.1) can also be written in a non-conservative formulation:

$$\mathbf{U}_t + \mathbf{J}(\mathbf{U})\ \nabla \cdot \mathbf{U} = \mathbf{S}(\mathbf{U}) \tag{1.2}$$

where $\mathbf{J}(\mathbf{U}) = \dfrac{\partial \mathbf{F}(\mathbf{U})}{\partial \mathbf{U}}$ is the transport speed or $n \times n$ Jacobian Matrix. The Jacobian eigenvalues and eigenvectors characterize the speed of propagation and the structure of the disturbances respectively. We will focus on the Shallow Water Equations (SWE), which is a non-linear hyperbolic system of equations. While the hyperbolicity of the system is associated to the real nature of the eigenvalues of the Jacobian matrix, the non-linearity represents the manner that the information is

propagated.

Equation (1.1) can be integrated over a fixed volume Ω so that the change in the amount of $\mathbf{U}$ will be only due to the flux contributions through the boundary Γ and the source term contribution inside the considered volume:

$$\frac{\partial}{\partial t}\int_{\Omega}\mathbf{U}d\Omega + \oint_{\Gamma}\mathbf{F}\mathbf{n}d\Gamma = \int_{\Omega}\mathbf{S}d\Omega \tag{1.3}$$

where $\mathbf{n}$ is the unit outward normal vector on the boundary Γ and the Gauss Divergence Theorem has been applied. Equation (1.3) is the so-called integral formulation of the conservation law. It is usually considered in problems admitting discontinuous solutions in which the smoothness hypothesis underlying the differential formulation is no longer true. Moreover, this formulation is deeply related to the numerical resolution of the equations from a finite volume point of view. In this approach the domain is discretized in a finite number of control volumes or computational cells over which the variables are locally conserved.

Both differential and integral formulations are equivalent if the solution is smooth, i.e, continuously differentiable. In non-linear hyperbolic problems the notion of classical solution is not sufficient because of the occurrence of discontinuities in the solution. In fact, when solving the corresponding discretized system of equations, discontinuities are always present hence the interest is put on the solution of the more general system (1.3) which is completely equivalent to seek a weak solution to (1.1) [53, 72, 123]. Therefore, the main effort will reside in the correct resolution in time of the original system of partial differential equations (1.1) with a discontinuous initial value problem, that is, the Riemann Problem.

1.2 The Riemann Problem for scalar conservation laws

In order to introduce the Riemann Problem concept, the one dimensional homogeneous scalar equation is first examined:

$$\frac{\partial u}{\partial t} + \frac{\partial f(u)}{\partial x} = 0 \tag{1.4}$$

where $f(u)$ is a linear or non-linear function of u. The resolution of (1.4) leads to the evolution in time and space of the conserved variable u given an initial condition defined as follows:

$$u(x,0) = u_0(x) = \begin{cases} u_L & if \quad x < 0 \\ u_R & if \quad x > 0 \end{cases} \tag{1.5}$$

where u_L and u_R are two constant values. This piecewise constant initial value problem for equation (1.4) is called the Riemann Problem, from now on RP (see Fig 1.1).

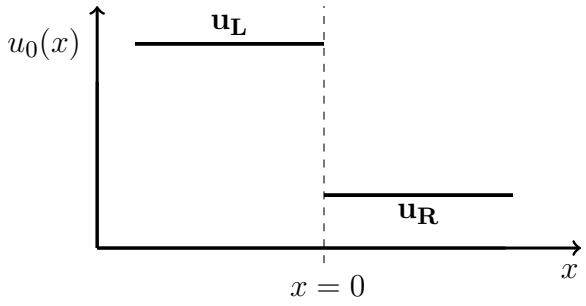

Figure 1.1: Riemann Problem (RP) for the scalar case

1.2.1 Linear scalar equation

The homogeneous linear scalar equation can be expressed as follows:

$$\frac{\partial u}{\partial t} + \frac{\partial f(u)}{\partial x} = 0 \;\rightarrow\; \frac{\partial u}{\partial t} + \lambda \frac{\partial u}{\partial x} = 0 \tag{1.6}$$

where $f(u) = \lambda u$ and λ is a constant wave propagation speed. Let consider $\lambda > 0$ (the reasoning is analogous for $\lambda < 0$). When solving this equations, *characteristic curves* or simply *characteristics* arise naturally. They are curves in the $x - t$ plane satisfying an interesting property: the change of the variable u along them is zero, that is, u is constant along the characteristics. In other words, the partial differential equation reduces to an ordinary differential equation along the characteristic line:

$$\frac{du}{dt} = 0 \quad \text{along} \quad \frac{dx}{dt} = \lambda \tag{1.7}$$

In the linear case, the family of characteristics is a set of parallel straight lines as shown in Figure 1.2 for $\lambda > 0$. This can be understood as any point of the x-domain is propagated a distance $d = \lambda t$ in a time t.

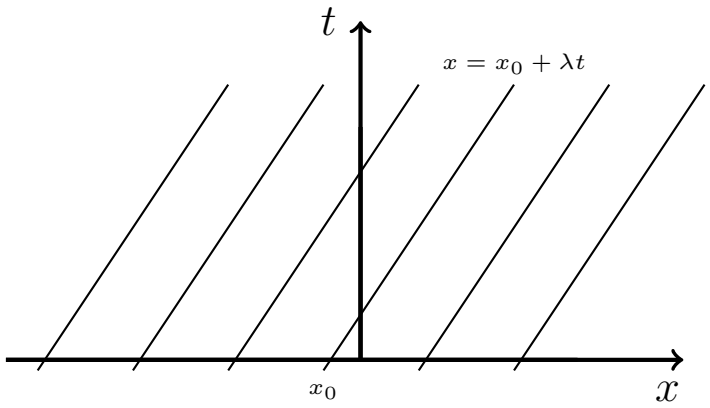

Figure 1.2: Family of characteristics for the linear scalar equation with $\lambda > 0$ in the $x - t$ plane

Given a RP as defined in (1.5), the exact solution can be consequently formulated as:

$$u(x,t) = u_0(x - \lambda t) = \begin{cases} u_L & if \quad x - \lambda t < 0 \\ u_R & if \quad x - \lambda t > 0 \end{cases} \tag{1.8}$$

Figure 1.3 illustrates the solution in the $x - t$ plane.

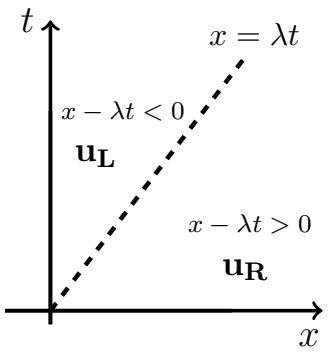

Figure 1.3: Solution in the $x - t$ plane of the RP (1.5) for the linear scalar equation with $\lambda > 0$

1.2.2 Non-linear scalar equation

The non-linear scalar equation emerges when assuming that $f(u)$ is a non-linear convex function in (1.4). It is possible to define an advection velocity

$$\lambda = \frac{df}{du} \qquad \lambda = \lambda(u) \tag{1.9}$$

where $\lambda(u)$ is no longer constant. The solution of the RP (1.5) will consist of a set of waves emerging from the initial jump [118, 72]. From a classical point of view, there are only two different types of genuinely non-linear waves: compressive or shock waves and rarefaction or fan waves [123]. As an example to illustrate how shocks and rarefactions arise, let consider the inviscid Burgers' equation.

The inviscid Burgers' equation is a particular case of scalar conservation law of the type (1.4) with $f(u) = \frac{1}{2}u^2$. This equation can be written as

$$\frac{\partial u}{\partial t} + \frac{\partial}{\partial x}\left(\frac{u^2}{2}\right) = 0 \qquad \text{or} \qquad \frac{\partial u}{\partial t} + u\frac{\partial u}{\partial x} = 0 \tag{1.10}$$

Two different situations appear depending on the relative value of u_L and u_R. When $u_L > u_R$ a right moving shock develops (see Figure 1.4).

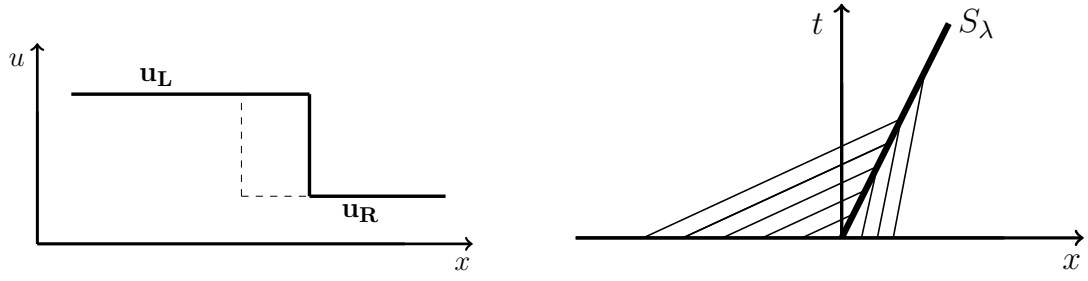

Figure 1.4: Initial data (dashed) and solution (solid) of a shock (left) and map of characteristic lines of a shock (right)

The discontinuous solution of the RP in this case is

$$u(x,t) = \begin{cases} u_L & if \quad x - S_\lambda t < 0 \\ u_R & if \quad x - S_\lambda t > 0 \end{cases} \tag{1.11}$$

where S_λ is the speed of the discontinuity that can be derived from the so-called

Rankine-Hugoniot conditions, defined by

$$[f] = S_\lambda \, [u] \tag{1.12}$$

where the brackets $[\cdot]$ denote the jump in the quantity across the discontinuity. They describe the relationship between the states on both sides of a Riemann Problem consisting of a shock. In the Burgers case, the speed of the discontinuity has the following expression:

$$S_\lambda = \frac{1}{2}(u_L + u_R) \tag{1.13}$$

Related to the speed of the discontinuity in this kind of waves is another relevant concept: the entropy condition. The main difficulty when seeking weak solutions of a non-linear hyperbolic equation or system of equations is the lack of uniqueness. In fact, for any given RP, many weak solutions may exist and additional conditions are required to select the physically relevant solution. These conditions are called *entropy conditions*, making reference to the gas dynamics. For instance in the scalar case, the Lax entropy conditions [72, 123] state that a shock wave satisfying the Rankine-Hugoniot conditions is admissible only if

$$f'(u_L) > S_\lambda > f'(u_R) \tag{1.14}$$

Regarding the RP in the Burgers' equation, when $u_L < u_R$ (Figure 1.5) the solution consists of a smooth rarefaction wave connecting the two constant states u_L an u_R:

$$u(x,t) = \begin{cases} u_L & if \quad x/t \leq u_L \\ x/t & if \quad u_L < x/t < u_R \\ u_R & if \quad x/t \geq u_R \end{cases} \tag{1.15}$$

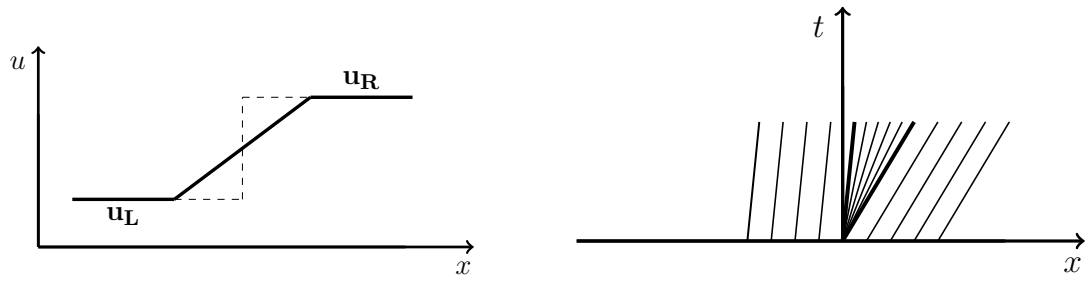

Figure 1.5: Initial data (dashed) and solution (solid) of a rarefaction (left) and map of characteristic lines of a rarefaction (right)

1.3 The Riemann Problem for systems of conservation laws

1.3.1 Linear systems

The linear hyperbolic system of equations is expressed:

$$\frac{\partial \mathbf{U}}{\partial t} + \frac{\partial \mathbf{F}(\mathbf{U})}{\partial x} = 0 \qquad \mathbf{F} = \mathbf{J}\mathbf{U} \tag{1.16}$$

The extension of the analysis developed for the scalar case to solve the Riemann Problem

$$\frac{\partial \mathbf{U}}{\partial t} + \frac{\partial \mathbf{F}(\mathbf{U})}{\partial x} = 0 \qquad \mathbf{U}(x,0) = \mathbf{U}_0(x) = \begin{cases} \mathbf{U}_L & if \quad x < 0 \\ \mathbf{U}_R & if \quad x > 0 \end{cases} \tag{1.17}$$

can be achieved using the Jacobian matrix. In fact, we have to solve a set of n hyperbolic PDE's of the form:

$$\frac{\partial \mathbf{U}}{\partial t} + \mathbf{J}\frac{\partial \mathbf{U}}{\partial x} = 0 \tag{1.18}$$

where all the coefficients in the Jacobian matrix $\mathbf{J}$ are constant. Furthermore, $\mathbf{J}$ has n real eigenvalues λ_i and n linearly independent eigenvectors $\mathbf{e}_i$. The eigenvalues can be ordered:

$$\lambda_1(\mathbf{U}) \leq \lambda_2(\mathbf{U}) \leq \cdots \leq \lambda_n(\mathbf{U}) \tag{1.19}$$

Let consider the matrix $\mathbf{E}$, whose columns are the right eigenvectors of $\mathbf{J}$ corresponding to the eigenvalues λ_i. It is possible to diagonalise matrix $\mathbf{J}$ using $\mathbf{E}$:

$$\mathbf{\Lambda} = \mathbf{E}^{-1}\mathbf{J}\mathbf{E} \tag{1.20}$$

where $\mathbf{\Lambda}$ is a diagonal matrix containing the eigenvalues. Now, a new set of independent variables $\mathbf{W}$ called characteristic variables is defined via

$$\mathbf{W} = \mathbf{E}^{-1}\mathbf{U} \tag{1.21}$$

Since $\mathbf{E}$ is constant, (1.18) can be directly re-written after the left multiplication by $\mathbf{E}^{-1}$ as:

$$\frac{\partial \mathbf{W}}{\partial t} + \mathbf{\Lambda}\frac{\partial \mathbf{W}}{\partial x} = 0 \tag{1.22}$$

and the system is totally decoupled into n linear scalar equations with an initial condition defined by

$$\mathbf{W}_0(x) = \mathbf{E}^{-1}\mathbf{U}_0(x) \tag{1.23}$$

Consequently, as an extension of the scalar case, the general solution in the $x-t$ plane will consist of n waves arising from the origin, each one associated with the eigenvalue λ_i as illustrated in Figure 1.6 [118, 53, 123].

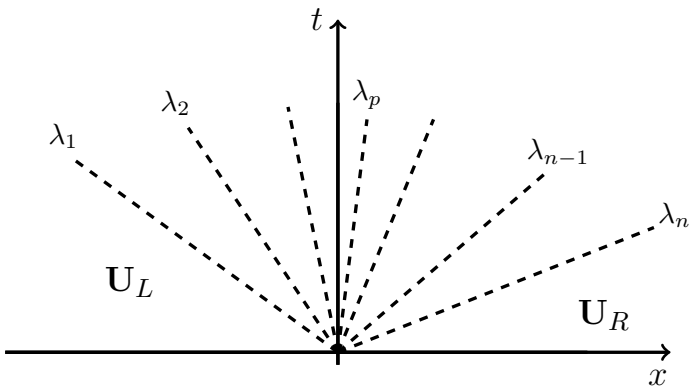

Figure 1.6: Solution in the $x-t$ plane of the Riemann Problem (1.17) for the $n \times n$ linear system of equations

The analytical expression can be deduced by expanding the initial states $\mathbf{U}_L$ and $\mathbf{U}_R$ into the eigenvectors basis as:

$$\mathbf{U}_L = \sum_{k=1}^{n} a_k \mathbf{e}_k \qquad\qquad \mathbf{U}_R = \sum_{k=1}^{n} b_k \mathbf{e}_k \tag{1.24}$$

The difference $\mathbf{U}_R - \mathbf{U}_L$ is evaluated

$$\delta\mathbf{U} = \mathbf{U}_R - \mathbf{U}_L = \sum_{k=1}^{n} (b_k - a_k)\mathbf{e}_k = \sum_{k=1}^{n} \alpha_k \mathbf{e}_k = \mathbf{E}\ \delta\mathbf{W} \tag{1.25}$$

and following the previous analysis for the scalar case and by simple algebraic manipulation, it is possible to arrive to the expression defining the analytic solution [118]:

$$\mathbf{U}(x,t) = \begin{cases} \mathbf{U}_L & if \quad x/t < \lambda_1 \\ \mathbf{U}_L + \alpha_1 \mathbf{e}_1 & if \quad \lambda_1 < x/t < \lambda_2 \\ \mathbf{U}_L + \alpha_1 \mathbf{e}_1 + \alpha_2 \mathbf{e}_2 & if \quad \lambda_2 < x/t < \lambda_3 \\ \vdots & \vdots \\ \mathbf{U}_L + \sum_{k=1}^{p} \alpha_k \mathbf{e}_k & if \quad \lambda_p < x/t < \lambda_{p+1} \\ \vdots & \vdots \\ \mathbf{U}_L + \sum_{k=1}^{n} \alpha_k \mathbf{e}_k = \mathbf{U}_R & if \quad \lambda_n < x/t \end{cases} \tag{1.26}$$

The initial jump in the Riemann Problem is projected onto the characteristic field and each wave strength $\alpha_k \mathbf{e}_k$ is propagated according to its own characteristic speed λ_k. As an example, the solution of the 2×2 linear system is illustrated in Figure 1.7. It consists of three states ($\mathbf{U}_L$, $\mathbf{U}^*$ and $\mathbf{U}_R$) delimited by two eigenvalues λ_1 and λ_2 where

$$\mathbf{U}^* = \mathbf{U}_L + \alpha_1 \mathbf{e}_1 \overset{(1.25)}{=} \mathbf{U}_R - \alpha_2 \mathbf{e}_2 \tag{1.27}$$

Therefore the solution is expressed as follows:

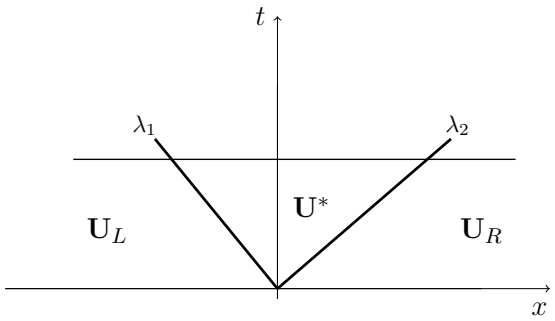

Figure 1.7: Sketch of the solution in the $x-t$ plane of the Riemann Problem for the 2×2 linear system of equations

$$\mathbf{U}(x,t) = \begin{cases} \mathbf{U}_L & if \quad x/t < \lambda_1 \\ \mathbf{U}^* = \mathbf{U}_L + \alpha_1 \mathbf{e}_1 = \mathbf{U}_R - \alpha_2 \mathbf{e}_2 & if \quad \lambda_1 < x/t < \lambda_2 \\ \mathbf{U}_R & if \quad \lambda_2 < x/t \end{cases} \tag{1.28}$$

1.3.2 Non-linear systems

The solution of the Riemann Problem (1.17) where $\mathbf{F}(\mathbf{U})$ is a non-linear vector of fluxes will consist of $n+1$ piecewise constant states separated by n elementary waves, each one related to each eigenvalue λ_i, similar to the linear system. However, in contrast to the linear system, the waves may contain discontinuities or smooth transitions and the general solution of the Riemann Problem should be carefully analysed by discriminating each particular type of wave. Shocks and rarefactions may arise when dealing with non-linearities. While rarefactions emerge when looking for piecewise constant continuous solutions or expansions, shocks accompany compressions or piecewise constant discontinuous solutions. The names for this waves and its meaning are borrowed from gas dynamics, where the gas propagates in a contracting or expanding way. However, they are not the unique waves that can appear in a non-linear system of conservation laws. For example, in the Euler equations, there exist waves across which both pressure and velocity are constant but there is a discontinuous jump in density and other density-dependent variables. More information can be found in [117, 118, 123].

As an example, Figure 1.8 illustrates a sketch of the solution of a non-linear Riemann Problem in the $x-t$ plane for a 2×2 system.

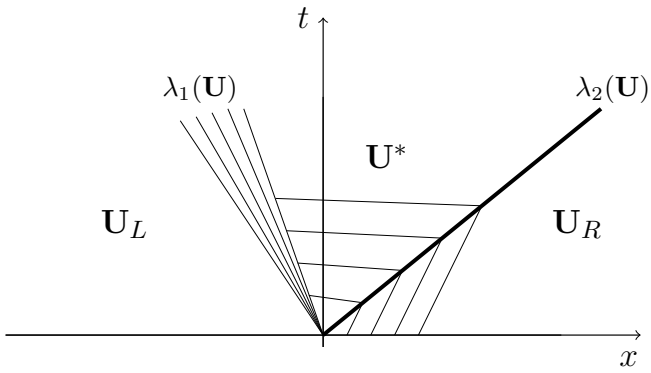

Figure 1.8: Example of solution in the $x-t$ plane of the Riemann Problem for a 2×2 non-linear system of equations

It shows a rarefaction associated to the first eigenvalue λ_1 and a right moving shock associated to λ_2. The solution will consist of three constant states separated by the moving waves. In this case, apart from the initial data $\mathbf{U}_L$ and $\mathbf{U}_R$, an intermediate state denoted by $\mathbf{U}^*$ is generated. The elucidation for the explicit expression of the middle star state, the effect of including source terms as well as the numerical resolution of the system of conservation laws by means of a certain solver will be deeply analysed in the following chapter.

Chapter 2

Finite volume schemes and the Augmented Roe's solver

2.1 Finite volume schemes

Three classical choices stand out for the resolution of problems in the context of fluid dynamics: finite difference (FD), finite element (FE) and finite volume (FV) methods [82]. The main advantage of FD codes is the easy way to work with high order of approximation at the extra cost of increasing the computational time. Moreover, the formulation becomes an arduous task when dealing with complex geometries in multiple dimensions. On the other hand, FE and FV methods are characterized by a relative simplicity when dealing with complex geometries. In particular, in the FE method, the problem domain is divided into elements with finite area. The solution is based on a function of space and varies between the nodes of elements. In a FV method the domain is composed of computational cells or control volumes Ω_i over which the conserved variables are integrated, achieving an approximation to the average value of the true solution. Accordingly, they offer an intuitive approach for solving system of conservation laws.

The application to the shallow water equations has been traditionally carried out by means of FV schemes [4, 6, 12, 5, 7, 112, 14] although several works have been developed in the context of FE [58, 59, 2, 36, 130] and even in FD, emphasizing the idea of locally and globally conservation [129, 101, 100]. In this work, the focus will be put on Godunov-type explicit upwind first order schemes [54, 119]. This means that the solution from time t^n to time $t^{n+1} = t^n + \Delta t$ is achieved by solving a sequence of local Riemann Problems and by assuming a piecewise constant data at each cell i. Moreover, the numerical integration of the temporal derivative is based

on the Euler forward rule. In fact, when evaluating the unknown values at the following time t^{n+1} using only the known values in time t^n, the family of methods are called explicit and are extensively used in Computational Fluids Dynamics. On the other hand, the discretization of the spatial derivative is performed by means of an upwind method, which discriminates the sense of propagation of the information.

2.1.1 1D finite volume schemes

Considering the one dimensional homogeneous scalar conservation law written in differential form:

$$\frac{\partial u}{\partial t} + \frac{\partial f(u)}{\partial x} = 0 \tag{2.1}$$

In order to obtain a numerical solution, the spatial domain of length L is discretized into a set of N grid cells $\Omega_i = [x_{i-1/2}, x_{i+1/2}]$ of size Δx. For simplicity, we assume a regular mesh (see Figure 2.1).

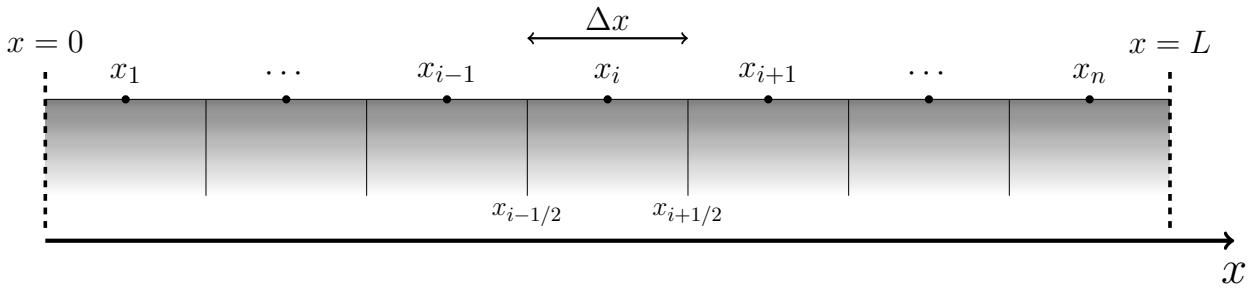

Figure 2.1: Mesh: discretization of the domain in N computational cells of size Δx

Integrating (2.1) over a control volume $[x_{i-1/2}, x_{i+1/2}] \times [t^n, t^{n+1}]$ where $t^{n+1} = t^n + \Delta t$:

$$\begin{aligned} &\int_{x_{i-1/2}}^{x_{i+1/2}} u(x, t^{n+1})\, dx - \int_{x_{i-1/2}}^{x_{i+1/2}} u(x, t^n)\, dx + \\ &\int_{t^n}^{t^{n+1}} f(u(x_{i+1/2}, t)\, dt - \int_{t^n}^{t^{n+1}} f(u(x_{i-1/2}, t)\, dt = 0 \end{aligned} \tag{2.2}$$

The finite volume method considers the spatially averaged value of the conserved variable $u(x,t)$ in cell i at a fixed time $t = t^n$, defined as

$$u_i^n = \frac{1}{\Delta x} \int_{x_{i-1/2}}^{x_{i+1/2}} u(x, t^n)\ dx \tag{2.3}$$

and the time-averaged fluxes at the cell interfaces:

$$f^*_{i\pm 1/2} = \frac{1}{\Delta t} \int_{t^n}^{t^{n+1}} f(u(x_{i\pm 1/2}, t)\ dt \tag{2.4}$$

Therefore, the numerical resolution of (2.1) for the updating of a single cell i from time t^n to time t^{n+1} can be expressed generally by means of:

$$u_i^{n+1} = u_i^n - \frac{\Delta t}{\Delta x}(f^*_{i+1/2} - f^*_{i-1/2}) \tag{2.5}$$

where $f^*_{i\pm 1/2}$ are the so-called numerical fluxes, that is, the numerical approximation of the exact flux integral through the cell interfaces. The choice of the numerical fluxes in (2.5) will determine the diverse numerical schemes described in the literature.

There exists an equivalent way of formulating a conservative scheme by using the flux difference splitting procedure. From the non-conservative form of (2.1)

$$\frac{\partial u}{\partial t} + \lambda(u)\frac{\partial u}{\partial x} = 0 \qquad \lambda = \lambda(u) = \frac{df}{du} \tag{2.6}$$

and the upwind approach, which discriminates the sense of propagation according to sign of the speeds, it is feasible to define the following quantities:

$$\lambda^{\pm} = \frac{\lambda \pm |\lambda|}{2} \qquad \delta f^{\pm} = \lambda^{\pm}(u)\delta u \tag{2.7}$$

and to express the numerical fluxes in (2.5) in terms of them:

$$f^*_{i+1/2} = f_i + \lambda^- \delta u_{i+1/2} \qquad f^*_{i-1/2} = f_i - \lambda^+ \delta u_{i-1/2} \tag{2.8}$$

Accordingly, the cell updating for (2.1) can be written:

$$u_i^{n+1} = u_i^n - \frac{\Delta t}{\Delta x}(\delta f^+_{i-1/2} + \delta f^-_{i+1/2}) \tag{2.9}$$

The meaning of this expression is very simple: cell i will be updated from time t^n to time t^{n+1} according to the arriving contributions from the left and from the right computational edges. In the explicit scheme the time step is restricted by stability reasons [32]:

$$\Delta t = \text{CFL} \ \min_i \left(\frac{\Delta x}{|\lambda|_i^n} \right), \qquad \text{CFL} \leq 1 \tag{2.10}$$

where CFL is the Courant-Friedrich-Lewy number. The extension to 1D homogeneous systems of conservations laws is a straightforward procedure. As an example, the 2×2 non-linear hyperbolic system of conservation is again examined:

$$\frac{\partial \mathbf{U}}{\partial t} + \frac{\partial \mathbf{F}(\mathbf{U})}{\partial x} = 0 \qquad \frac{\partial \mathbf{U}}{\partial t} + \mathbf{J}(\mathbf{U}) \frac{\partial \mathbf{U}}{\partial x} = 0 \tag{2.11}$$

where $\mathbf{J}(\mathbf{U})$ is the Jacobian Matrix. According to the integral formulation and the finite volume approach explained for the scalar case in (2.2), (2.3) and (2.4), the numerical scheme is formulated analogous to (2.5):

$$\mathbf{U}_i^{n+1} = \mathbf{U}_i^n - \frac{\Delta t}{\Delta x} (\mathbf{F}^*_{i+1/2} - \mathbf{F}^*_{i-1/2})^n \tag{2.12}$$

With a similar reasoning, it is possible to formulate the analogous flux difference splitting procedure:

$$\mathbf{U}_i^{n+1} = \mathbf{U}_i^n - \frac{\Delta t}{\Delta x} (\delta \mathbf{F}^+_{i-1/2} + \delta \mathbf{F}^-_{i+1/2})^n \tag{2.13}$$

where $\delta \mathbf{F}^{\pm} = \mathbf{J}^{\pm}(\mathbf{U}) \ \delta \mathbf{U}$.

2.1.2 2D finite volume schemes

In order to explain the finite volume scheme applied over a 2D configuration, the two dimensional scalar equation is first considered, written in differential form:

$$\frac{\partial u}{\partial t} + \nabla \cdot \mathbf{f}(u) = 0 \,, \qquad \mathbf{f}(u) = (f_x, f_y) \,, \tag{2.14}$$

The domain is divided into computational cells Ω_i with area A_i. Integrating (2.14) over a control volume Ω_i,

$$\frac{\partial}{\partial t}\int_{\Omega_i} u \; d\Omega + \int_{\Omega_i} \nabla \cdot \mathbf{f}(u) \; d\Omega = 0 \tag{2.15}$$

it is possible to apply the Gauss theorem to arrive to the following expression:

$$\frac{\partial}{\partial t}\int_{\Omega_i} u \; d\Omega + \oint_{\Gamma} \mathbf{fn} d\Gamma = 0 \tag{2.16}$$

where $\mathbf{n} = (n_x, n_y)$ is the outward unit normal vector to the volume Ω_i and Γ denotes the surface surrounding the volume Ω_i, i.e., the boundaries of Ω_i. In order to obtain a numerical solution from time t^n to time $t^{n+1} = t^n + \Delta t$, equation (2.16) is integrated over $[t^n, t^{n+1}]$:

$$\int_{\Omega_i} u(x, y, t^{n+1}) \; d\Omega - \int_{\Omega_i} u(x, y, t^n) \; d\Omega + \int_{t^n}^{t^{n+1}} \sum_{k=1}^{N_E} \mathbf{f}_k \mathbf{n}_k l_k \; dt = 0 \tag{2.17}$$

where the last contour integral in (2.16) has been replaced by the sum of the fluxes through the edges k of length l_k, separating cell i and the N_E neighbouring cells j_k ($N_E = 4$ for quadrilaterals and $N_E = 3$ for triangular cells). Figure 2.2 includes the mentioned variables in the case of a triangular grid.

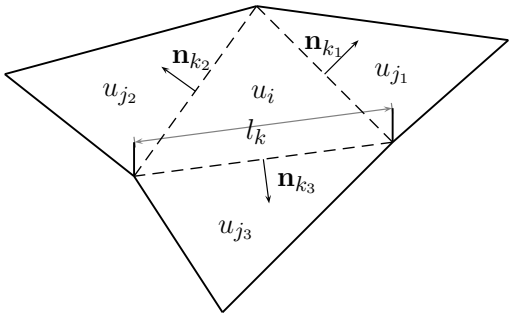

Figure 2.2: Sketch of the 2D finite volume approach

The finite volume considers the spatially averaged value of the variable $u(x, y, t)$ in the i-th cell at time t^n

$$u_i^n = \frac{1}{A_i}\int_{\Omega_i} u(x, y, t^n) \; d\Omega \tag{2.18}$$

and the time-averaged fluxes at each edge k:

$$\mathbf{f}_k^* \mathbf{n}_k = \frac{1}{\Delta t} \int_{t^n}^{t^{n+1}} \mathbf{f}_k(u(x,y,t)) \mathbf{n}_k \, dt \tag{2.19}$$

Thus, the numerical scheme can be written in terms of the numerical fluxes $\mathbf{f}_k^*$ as follows:

$$u_i^{n+1} = u_i^n - \frac{\Delta t}{A_i} \sum_{k=1}^{N_E} \mathbf{f}_k^* \mathbf{n}_k l_k \tag{2.20}$$

As described for the 1D framework, there exists another formulation called flux difference splitting formulation which is presented here for the 2D scalar case. The non-conservative formulation of (2.14)

$$\frac{\partial u}{\partial t} + \boldsymbol{\lambda} \nabla \cdot u = 0 \,, \qquad \boldsymbol{\lambda} = \frac{d\mathbf{f}}{du} \tag{2.21}$$

allows to define the following quantities:

$$\boldsymbol{\lambda}^{\pm} = \frac{\boldsymbol{\lambda} \pm \boldsymbol{\lambda}}{2} \tag{2.22}$$

Analogous to the 1D case, the numerical fluxes in (2.20) can be expressed in terms of (2.22):

$$\mathbf{f}_k^* \mathbf{n}_k = \mathbf{f}_k \mathbf{n}_k + \underbrace{\boldsymbol{\lambda}^- \mathbf{n}_k \delta u_k}_{(\delta \mathbf{fn})_k^-} \tag{2.23}$$

where $\delta u_k = u_j - u_i$. According to [53], the following property is satisfied:

$$\sum_{k=1}^{N_E} \mathbf{n}_k l_k = 0 \tag{2.24}$$

hence (2.20) is rewritten using (2.24) to achieve the flux difference formulation

$$u_i^{n+1} = u_i^n - \frac{\Delta t}{A_i} \sum_{k=1}^{N_E} (\delta \mathbf{fn})_k^- l_k \tag{2.25}$$

whose meaning is clear: cell i is updated from time t^n to time t^{n+1} according to the in-going contributions arriving from the neighbouring edges. The time step size is restricted again by the CFL condition [32] that can be expressed [92]:

$$\Delta t = \text{CFL} \ \min_k \frac{(\chi_i, \chi_j)}{|\boldsymbol{\lambda}\mathbf{n}|_k^n} \qquad \text{CFL} \leq 0.5 \tag{2.26}$$

where

$$\chi_i = \frac{A_i}{\max_{k=1,N_E} \ l_k} \tag{2.27}$$

The formulation of these ideas for 2D homogeneous systems or conservations laws is briefly commented. Considering the 3×3 system:

$$\frac{\partial \mathbf{U}}{\partial t} + \frac{\partial \mathbf{F}(\mathbf{U})}{\partial x} + \frac{\partial \mathbf{G}(\mathbf{U})}{\partial y} = 0 \qquad \frac{\partial \mathbf{U}}{\partial t} + \overrightarrow{\nabla}\mathbf{E} = 0 \tag{2.28}$$

where $\mathbf{E}$=($\mathbf{F}, \mathbf{G}$), the numerical scheme can be formulated by means of the numerical flux approach:

$$\mathbf{U}_i^{n+1} = \mathbf{U}_i^n - \frac{\Delta t}{A_i} \sum_{k=1}^{N_E} \mathbf{E}_k^* \mathbf{n}_k l_k \tag{2.29}$$

or with the flux difference splitting formulation:

$$\mathbf{U}_i^{n+1} = \mathbf{U}_i^n - \frac{\Delta t}{A_i} \sum_{k=1}^{N_E} (\delta \mathbf{E} \ \mathbf{n})_k^- l_k \tag{2.30}$$

2.2 Approximate Riemann Solvers

Exact Riemann Solvers such as the original Godunov's method require the resolution in time of each Riemann Problem at every cell edge or interface, i.e., they have to be fully aware of the states $\mathbf{U}(x_{i\pm 1/2}, t)$ to evaluate the corresponding flux. For many applications, specially under non-linear problems, costly iterative methods are necessary to converge to the solution, strategies that have fallen into disuse [118, 53, 72].

On the contrary, *approximate Riemann solvers* have been extensively developed during the last three decades, resulting an attractive strategy to face up this kind of problems. One of the most widespread approximate Riemann solver is due to Roe, and was presented in 1981 [109]. It briefly consists of computing the approximate linear solution from a local linearized formulation. This Roe's solver and, in particular, its weak formulation due to Toumi [120] will be the basis of the present work.

2.2.1 Roe's approximate Riemann solver

In order to explain Roe's solver, let consider (2.11), expressed in the non-conservative form and the Riemann Problem:

$$\mathbf{U}(x,0) = \mathbf{U}_0(x) = \begin{cases} \mathbf{U}_L & if \quad x < 0 \\ \mathbf{U}_R & if \quad x > 0 \end{cases} \tag{2.31}$$

When examining the numerical method in (2.12) or (2.13), the problem arises for the estimation of the numerical fluxes or the Jacobian matrix (respectively) at the interface defining the Riemann Problem, above all in the presence of non-linear fluxes.

The idea of Roe resides on replacing the Jacobian matrix $\mathbf{J}(\mathbf{U})$ by a locally linearized matrix $\widetilde{\mathbf{J}}$, function of the left and right states of each Riemann Problem:

$$\widetilde{\mathbf{J}} = \widetilde{\mathbf{J}}(\mathbf{U}_L, \mathbf{U}_R) \tag{2.32}$$

Consequently, the problem reduces to solving the Riemann Problem for a linear system of equations, which can be determined exactly (see Chapter 1). This linearized Jacobian matrix $\widetilde{\mathbf{J}}$ must satisfy the following properties:

- hyperbolicity, that is, it should be diagonalisable with real eigenvalues.
- consistency

$$\widetilde{\mathbf{J}}(\mathbf{U}, \mathbf{U}) = \mathbf{J}(\mathbf{U}) \tag{2.33}$$

- Conservation across discontinuities

$$\mathbf{F}(\mathbf{U}_R) - \mathbf{F}(\mathbf{U}_L) = \widetilde{\mathbf{J}}(\mathbf{U}_R - \mathbf{U}_L) \tag{2.34}$$

The construction of these matrices $\widetilde{\mathbf{J}}$ for the particular case of the shallow water equations as well as the entropy fix needed when linearizing the system will be discussed in Chapter 3.

2.2.2 The source terms: Augmented Roe's Riemann Solver

Most of the numerical methods have been firstly developed in the context of the homogeneous equation or system of equations. However, the incorporation of the source terms in the corresponding Riemann solvers does not represent a trivial task and should be carefully investigated.

The SWE with irregular geometries have been widely studied and great efforts have been put on developing source term treatments able to preserve the *C-property* or *well-balanced* property, that is, the exact conservation of quiescent flow. For this purpose, an upwind treatment of the source term was first proposed by Vázquez-Cendón [122] and later explored in [50, 65, 14, 13].

Another point of view was introduced by George [52], where a class of augmented Riemann solvers was presented. This approach consists of defining a proper steady state wave, i.e., a stationary jump discontinuity that acts as a source term. A simpler Riemann solver for a $n \times n$ system of conservation laws contains n discontinuities separating $n+1$ states or regions. In this procedure, the augmented Riemann solver uses $n+2$ states where the extra state corresponds to the steady wave associated to the source term. Furthermore, it is proved to maintain the well-balanced property.

It is possible to adapt the ideas of a steady jump discontinuity acting as a source term inside a Roe's approximate Riemann solver combined with an upwind treatment of the source terms. It was initially examined by Murillo et al. [92], where it was used to provide a rule to estimate the intermediate states that are generated inside a Riemann Problem (see Figure 1.8).

In order to illustrate the procedure and formulate the numerical scheme including the presence of source terms, let consider the 1D hyperbolic of conservation laws defined as in (2.11). The idea of an upwind treatment of the source terms will

allow to define a suitable vector $\mathbf{S}_{i+1/2}$ at each interface $i+1/2$ and to apply the difference splitting procedure leading to two vectors $\mathbf{S}^{+}_{i+1/2}$ and $\mathbf{S}^{-}_{i+1/2}$. Thus, the numerical scheme can be formulated for the updating of a cell i for time t^n to time t^{n+1} according to the in-going contributions of fluxes and source terms:

$$\mathbf{U}_i^{n+1} = \mathbf{U}_i^n - \frac{\Delta t}{\Delta x}\left((\delta\mathbf{F}-\mathbf{S})^{+}_{i-1/2} + (\delta\mathbf{F}-\mathbf{S})^{-}_{i+1/2}\right)^n \tag{2.35}$$

This expression can be seen as the equivalent of (2.13) but including the presence of source terms. For the 2D framework, the strategy will be completely analogous: the upwind approach is applied to the vector of source terms, which allows to define a suitable matrix $\mathbf{T}$ and to project it to each wall k according to the splitting procedure $(\mathbf{Tn})^{-}_{k}$. This last term, accounting for the in-going contributions coming from the vector of source terms projected over each wall k, is incorporated to the numerical scheme in (2.30) as follows:

$$\mathbf{U}_i^{n+1} = \mathbf{U}_i^n - \frac{\Delta t}{A_i}\sum_{k=1}^{N_E}(\delta\mathbf{E}\,\mathbf{n}-\mathbf{Tn})^{-}_{k} l_k \tag{2.36}$$

The same analysis of that carried out in [92] is performed here and approximate Riemann solutions are developed in the following sections for 2×2 and the 3×3 non-linear hyperbolic system of conservation laws, that will be the basis for the 1D and the 2D shallow water equations. As a matter of fact, the wet/dry treatment applied in this work is closely linked to the intermediate states or regions that appear in these mentioned approximate solutions.

2.3 1D system of conservation laws

2.3.1 Numerical scheme

The differential formulation of the 2×2 non-linear homogeneous hyperbolic system of conservation laws is first considered

$$\frac{\partial\mathbf{U}}{\partial t}+\frac{\partial\mathbf{F}}{\partial x}=0 \;\rightarrow\; \frac{\partial\mathbf{U}}{\partial t}+\mathbf{J}(\mathbf{U})\frac{\partial\mathbf{U}}{\partial x}=0 \tag{2.37}$$

In order to obtain the numerical solution, the domain is divided into N computational cells $\Omega_i = [x_{i-1/2}, x_{i+1/2}]$ of constant size Δx. We are therefore interested in weak solutions of the local Riemann Problem

$$\begin{gathered}\frac{\partial \mathbf{U}}{\partial t} + \frac{\partial \mathbf{F}}{\partial x}(\mathbf{U}_i, \mathbf{U}_{i+1}) = 0 \\ \mathbf{U}(x,0) = \begin{cases} \mathbf{U}_i & if \quad x < 0 \\ \mathbf{U}_{i+1} & if \quad x > 0 \end{cases}\end{gathered} \tag{2.38}$$

from a generic time $t^n = 0$ to time $t^{n+1} = \Delta t$. The solution of each Riemann Problem is obtained from exactly integrating over a control volume $[x_i, x_{i+1}] \times [0, \Delta t]$:

$$\int_{x_i}^{x_{i+1}} \mathbf{U}(x, \Delta t)\, dx = \Delta x \left(\mathbf{U}_{i+1} + \mathbf{U}_i\right) - \left(\mathbf{F}(\mathbf{U}_{i+1}) - \mathbf{F}(\mathbf{U}_i)\right) \tag{2.39}$$

On the other hand, in the Roe's approach (2.37) is linearized

$$\begin{gathered}\frac{\partial \hat{\mathbf{U}}}{\partial t} + \widetilde{\mathbf{J}} \frac{\partial \hat{\mathbf{U}}}{\partial x} = 0 \\ \hat{\mathbf{U}}(x,0) = \begin{cases} \mathbf{U}_i & if \quad x < 0 \\ \mathbf{U}_{i+1} & if \quad x > 0 \end{cases}\end{gathered} \tag{2.40}$$

hence the solution $\hat{\mathbf{U}}$ of the linearized Riemann Problem (2.40) must satisfy:

$$\int_{x_i}^{x_{i+1}} \hat{\mathbf{U}}(x, \Delta t)\, dx = \Delta x \left(\mathbf{U}_{i+1} + \mathbf{U}_i\right) - \widetilde{\mathbf{J}} \left(\mathbf{U}_{i+1} - \mathbf{U}_i\right) \tag{2.41}$$

where $\widetilde{\mathbf{J}}$ is the locally linearized matrix approximating the Jacobian Matrix $\mathbf{J}(\mathbf{U})$ in (2.37). The consistency condition of the Roe's approximate Riemann solver allows to link (2.39) and (2.41) as follows:

$$\int_{x_i}^{x_{i+1}} \hat{\mathbf{U}}(x, \Delta t)\, dx = \Delta x \left(\mathbf{U}_{i+1} + \mathbf{U}_i\right) - \left(\mathbf{F}(\mathbf{U}_{i+1}) - \mathbf{F}(\mathbf{U}_i)\right) \tag{2.42}$$

revealing an agreement with (2.34): $\delta \mathbf{F} = \widetilde{\mathbf{J}} \delta \mathbf{U}$. From the original Roe's solver, the approximate eigenvalues $\widetilde{\lambda}^1, \widetilde{\lambda}^2$ and eigenvectors $\widetilde{\mathbf{e}}^1, \widetilde{\mathbf{e}}^2$ of the locally linearized matrix $\widetilde{\mathbf{J}}$ satisfy the following property:

$$\widetilde{\mathbf{J}}_{i+1/2} = \widetilde{\mathbf{P}}_{i+1/2}\widetilde{\mathbf{\Lambda}}_{i+1/2}\widetilde{\mathbf{P}}^{-1}_{i+1/2} \tag{2.43}$$

where $\widetilde{\mathbf{P}} = (\widetilde{\mathbf{e}}^1, \widetilde{\mathbf{e}}^2)$ and $\widetilde{\mathbf{\Lambda}}_{i+1/2}$ is a diagonal matrix with eigenvalues $\widetilde{\lambda}^1, \widetilde{\lambda}^2$ in the main diagonal. The difference in the vector of conserved variables can be linearized using the eigenvectors basis:

$$\delta\mathbf{U}_{i+1/2} = \widetilde{\mathbf{P}}_{i+1/2}\widetilde{\mathbf{A}}_{i+1/2} \rightarrow \widetilde{\mathbf{A}}_{i+1/2} = \widetilde{\mathbf{P}}^{-1}_{i+1/2}\,\delta\mathbf{U}_{i+1/2} \tag{2.44}$$

with $\widetilde{\mathbf{A}}_{i+1/2} = \left(\widetilde{\alpha}^1, \widetilde{\alpha}^2\right)^T_{i+1/2}$. Therefore, the difference in fluxes can be expressed:

$$\delta\mathbf{F}_{i+1/2} = (\widetilde{\mathbf{P}}\widetilde{\mathbf{\Lambda}}\underbrace{\widetilde{\mathbf{P}}^{-1}\delta\mathbf{U}}_{\widetilde{\mathbf{A}}})_{i+1/2} = \sum_{m=1}^{2}\left(\widetilde{\lambda}\ \widetilde{\alpha}\ \widetilde{\mathbf{e}}\right)^m_{i+1/2} \tag{2.45}$$

With this definition, the scheme can be formulated according to the flux difference splitting formulation in (2.13) just defining

$$\delta\mathbf{F}^{\pm}_{i+1/2} = \sum_{m=1}^{2}\left(\widetilde{\lambda}^{\pm}\ \widetilde{\alpha}\ \widetilde{\mathbf{e}}\right)^m_{i+1/2} \tag{2.46}$$

A similar procedure can be done when incorporating the presence of source terms. Considering a 2×2 non-linear hyperbolic system of equations with source terms:

$$\frac{\partial\mathbf{U}}{\partial t} + \frac{\partial\mathbf{F}}{\partial x} = \mathbf{S} \tag{2.47}$$

The domain is again divided into N computational cells $\Omega_i = [x_{i-1/2}, x_{i+1/2}]$ of constant size Δx. The local Riemann Problem

$$\begin{gathered}\frac{\partial\mathbf{U}}{\partial t} + \frac{\partial\mathbf{F}}{\partial x}(\mathbf{U}_i, \mathbf{U}_{i+1}) = \mathbf{S}(\mathbf{U}_i, \mathbf{U}_{i+1}) \\ \mathbf{U}(x,0) = \begin{cases} \mathbf{U}_i & if \quad x < 0 \\ \mathbf{U}_{i+1} & if \quad x > 0 \end{cases}\end{gathered} \tag{2.48}$$

is considered from time $t^n = 0$ to time $t^{n+1} = \Delta t$. The solution of each Riemann Problem is achieved by integrating over a control volume $[x_i, x_{i+1}] \times [0, \Delta t]$:

$$\int_{x_i}^{x_{i+1}} \mathbf{U}(x,\Delta t)\,dx = \Delta x\,(\mathbf{U}_{i+1}+\mathbf{U}_i) - (\mathbf{F}(\mathbf{U}_{i+1}) - \mathbf{F}(\mathbf{U}_i)) + \int_0^{\Delta t}\int_{x_i}^{x_{i+1}} \mathbf{S}\,dx\,dt \tag{2.49}$$

For the last integral involving the source term $\mathbf{S}$, the following linearization in time is assumed

$$\int_0^{\Delta t}\int_{x_i}^{x_{i+1}} \mathbf{S}\,dx\,dt = \int_{x_i}^{x_{i+1}} \mathbf{S}(x,0)\,dx = \mathbf{S}^n_{i+1/2} \tag{2.50}$$

where $\mathbf{S}^n_{i+1/2}$ is a suitable numerical source vector. In the Roe's approach, (2.48) is approximated by the homogeneous linearized Riemann Problem

$$\begin{gathered}\frac{\partial \hat{\mathbf{U}}}{\partial t} + \widetilde{\mathbf{J}}^* \frac{\partial \hat{\mathbf{U}}}{\partial x} = 0 \\ \hat{\mathbf{U}}(x,0) = \begin{cases} \mathbf{U}_i & if \quad x<0 \\ \mathbf{U}_{i+1} & if \quad x>0 \end{cases}\end{gathered} \tag{2.51}$$

where $\widetilde{\mathbf{J}}^* = \widetilde{\mathbf{J}}^*(\mathbf{U}_i,\mathbf{U}_{i+1})$ is a suitable constant matrix. Integrating over the same control volume,

$$\int_{x_i}^{x_{i+1}} \hat{\mathbf{U}}(x,\Delta t)\,dx = \Delta x\,(\mathbf{U}_{i+1}+\mathbf{U}_i) - \widetilde{\mathbf{J}}^*\,(\mathbf{U}_{i+1}-\mathbf{U}_i) \tag{2.52}$$

the consistency condition connects again (2.49) and (2.52) leading to the following expression:

$$\int_{x_i}^{x_{i+1}} \hat{\mathbf{U}}(x,\Delta t)\,dx = \Delta x\,(\mathbf{U}_{i+1}+\mathbf{U}_i) - \left(\mathbf{F}(\mathbf{U}^n_{i+1}) - \mathbf{F}(\mathbf{U}^n_i) - \mathbf{S}^n_{i+1/2}\right) \tag{2.53}$$

with the constraint

$$\widetilde{\mathbf{J}}^*\delta\mathbf{U}_{i+1/2} = \delta\mathbf{F}^n_{i+1/2} - \mathbf{S}^n_{i+1/2} = (\widetilde{\mathbf{J}}\delta\mathbf{U})_{i+1/2} - \mathbf{S}^n_{i+1/2} \tag{2.54}$$

Apart from the difference in the vector of conserved variables as in (2.44), the vector of source terms can be linearized using the eigenvectors basis:

$$\mathbf{S}_{i+1/2} = \widetilde{\mathbf{P}}_{i+1/2}\widetilde{\mathbf{B}}_{i+1/2} \tag{2.55}$$

with $\widetilde{\mathbf{B}}_{i+1/2} = \left(\widetilde{\beta}^1, \widetilde{\beta}^2\right)^T_{i+1/2}$. Therefore, the difference in fluxes and the contributions due to the source terms are expressed compactly:

$$\begin{gathered}\delta\mathbf{F}_{i+1/2} - \mathbf{S}_{i+1/2} = (\widetilde{\mathbf{P}}\widetilde{\mathbf{\Lambda}}\underbrace{\widetilde{\mathbf{P}}^{-1}\delta\mathbf{U}}_{\widetilde{\boldsymbol{\alpha}}})_{i+1/2} - (\widetilde{\mathbf{P}}\widetilde{\mathbf{B}})_{i+1/2} = \\ \widetilde{\mathbf{P}}\widetilde{\mathbf{\Lambda}}\left(\widetilde{\boldsymbol{\alpha}} - \widetilde{\mathbf{\Lambda}}^{-1}\widetilde{\mathbf{B}}\right)_{i+1/2} = \sum_{m=1}^{2}\left(\widetilde{\lambda}\ \widetilde{\gamma}\ \widetilde{\mathbf{e}}\right)^m_{i+1/2}\end{gathered} \tag{2.56}$$

where $\widetilde{\gamma}^m_{i+1/2} = \left(\widetilde{\alpha} - \dfrac{\widetilde{\beta}}{\widetilde{\lambda}}\right)^m_{i+1/2}$. According to (2.35), the numerical scheme can be formulated by means of the difference splitting formulation:

$$\mathbf{U}_i^{n+1} = \mathbf{U}_i^n - \frac{\Delta t}{\Delta x}\left((\delta\mathbf{F} - \mathbf{S})^+_{i-1/2} + (\delta\mathbf{F} - \mathbf{S})^-_{i+1/2}\right)^n \tag{2.57}$$

where

$$(\delta\mathbf{F} - \mathbf{S})^\pm_{i+1/2} = \sum_{m=1}^{2}\left(\widetilde{\lambda}^\pm\ \widetilde{\gamma}\ \widetilde{\mathbf{e}}\right)^m_{i+1/2} \tag{2.58}$$

2.3.2 1D Augmented Approximate Riemann Solutions

According to the previous analysis, three approximate solutions satisfying (2.53) appear depending on the sign of the eigenvalues $\widetilde{\lambda}^1, \widetilde{\lambda}^2$. As a consequence of the philosophy of Augmented Roe's solver, each solution $\hat{\mathbf{U}}(x,t)$ will consist of four states or regions: apart from the two initial states and the corresponding star intermediate state, the fourth state comes from the assumption that there exists a stationary wave will null velocity acting as a source term. In order to examine all the cases, the eigenvalues can be ordered

$$\widetilde{\lambda}^1 \leq \widetilde{\lambda}^2 \tag{2.59}$$

and three possibilities arise [92]:

1. $\widetilde{\lambda}^1 < 0$, $\widetilde{\lambda}^2 > 0$. The solution is given by (see Figure 2.3) :

$$\hat{\mathbf{U}}(x,t) = \begin{cases} \mathbf{U}_i^n & \text{if} \quad x - \widetilde{\lambda}^1 t < 0 \\ \mathbf{U}_i^* & \text{if} \quad x - \widetilde{\lambda}^1 t > 0 \text{ and } x < 0 \\ \mathbf{U}_{i+1}^{**} & \text{if} \quad x > 0 \text{ and } x - \widetilde{\lambda}^2 t < 0 \\ \mathbf{U}_{i+1}^n & \text{if} \quad x - \widetilde{\lambda}^2 t > 0 \end{cases} \tag{2.60}$$

with

$$\begin{aligned} \mathbf{U}_i^*(\mathbf{U}_{i+1}, \mathbf{U}_i, \mathbf{S}_{i+1/2}) &= \mathbf{U}_i^n + (\widetilde{\gamma}\widetilde{\mathbf{e}})_{i+1/2}^1 \\ \mathbf{U}_{i+1}^{**}(\mathbf{U}_{i+1}, \mathbf{U}_i, \mathbf{S}_{i+1/2}) &= \mathbf{U}_{i+1}^n - (\widetilde{\gamma}\widetilde{\mathbf{e}})_{i+1/2}^2 \end{aligned} \tag{2.61}$$

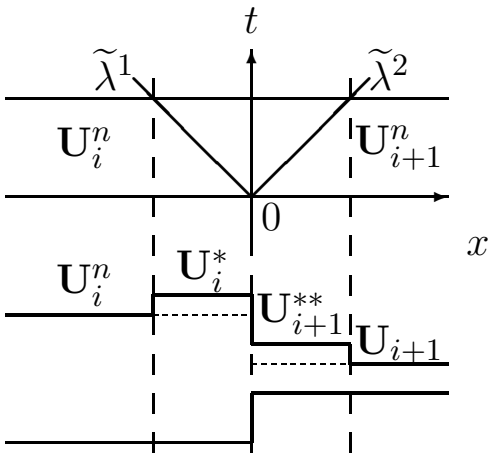

Figure 2.3: Values of the solution $\hat{\mathbf{U}}(x,t)$ in each wedge of the (x,t) plane for $\widetilde{\lambda}^1 < 0$, $\widetilde{\lambda}^2 > 0$

2. $\widetilde{\lambda}^1 > 0$, $\widetilde{\lambda}^2 > 0$. The solution is given by (see Figure 2.4):

$$\hat{\mathbf{U}}(x,t) = \begin{cases} \mathbf{U}_i^n & \text{if} \quad x < 0 \\ \mathbf{U}_{i+1}^* & \text{if} \quad x > 0 \text{ and } x - \widetilde{\lambda}^1 t < 0 \\ \mathbf{U}_{i+1}^{**} & \text{if} \quad x - \widetilde{\lambda}^1 t > 0 \text{ and } x - \widetilde{\lambda}^2 t < 0 \\ \mathbf{U}_{i+1}^n & \text{if} \quad x - \widetilde{\lambda}^2 t > 0 \end{cases} \tag{2.62}$$

with $\mathbf{U}_{i+1}^{**}$ defined as in (2.61) and

$$\mathbf{U}_{i+1}^*(\mathbf{U}_{i+1}, \mathbf{U}_i, \mathbf{S}_{i+1/2}) = \mathbf{U}_{i+1}^{**} - (\widetilde{\gamma}\widetilde{\mathbf{e}})_{i+1/2}^1 \tag{2.63}$$

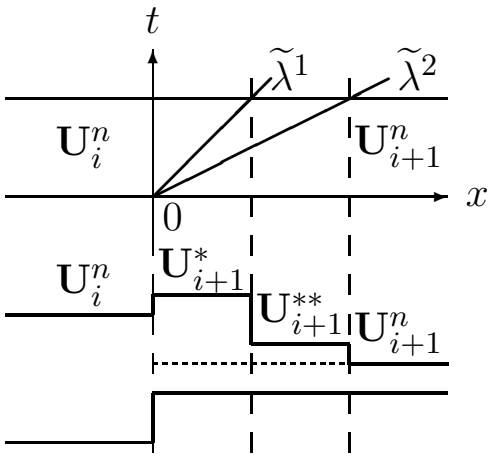

Figure 2.4: Values of the solution $\hat{\mathbf{U}}(x,t)$ in each wedge of the (x,t) plane for $\widetilde{\lambda}^1 > 0$, $\widetilde{\lambda}^2 > 0$

3. $\widetilde{\lambda}^1 < 0$, $\widetilde{\lambda}^2 < 0$. The solution is characterized by (see Figure 2.5):

$$\hat{\mathbf{U}}(x,t) = \begin{cases} \mathbf{U}_i^n & \text{if} \quad x - \widetilde{\lambda}^1 t < 0 \\ \mathbf{U}_i^* & \text{if} \quad x - \widetilde{\lambda}^1 t > 0 \text{ and } x - \widetilde{\lambda}^2 t < 0 \\ \mathbf{U}_i^{**} & \text{if} \quad x - \widetilde{\lambda}^2 t > 0 \text{ and } x < 0 \\ \mathbf{U}_{i+1}^n & \text{if} \quad x > 0 \end{cases} \tag{2.64}$$

with $\mathbf{U}_i^*$ defined as in (2.60) and

$$\mathbf{U}_i^{**}(\mathbf{U}_{i+1}, \mathbf{U}_i, \mathbf{S}_{i+1/2}) = \mathbf{U}_i^* + (\widetilde{\gamma}\widetilde{\mathbf{e}})_{i+1/2}^2 \tag{2.65}$$

2.4 2D system of conservation laws

2.4.1 Numerical scheme

The ideas presented for the 1D case can be extended to obtain approximate solutions in 3×3 non-linear hyperbolic system of conservation laws with source terms of the form:

$$\frac{\partial \mathbf{U}}{\partial t} + \frac{\partial \mathbf{F}(\mathbf{U})}{\partial x} + \frac{\partial \mathbf{G}(\mathbf{U})}{\partial y} = \mathbf{S}(\mathbf{U}) \tag{2.66}$$

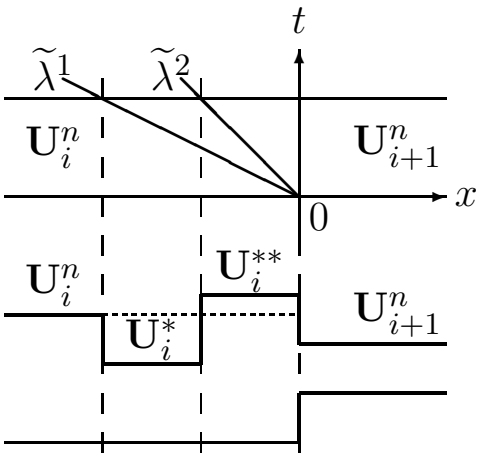

Figure 2.5: Values of the solution $\hat{\mathbf{U}}(x,t)$ in each wedge of the (x,t) plane for $\widetilde{\lambda}^1 < 0$, $\widetilde{\lambda}^2 < 0$

The domain is divided again into computational cells Ω_i with area A_i. In particular, the projection in (2.29) or (2.30) suggests that Roe's linearization is applied in the direction x' given by the normal vector $\mathbf{n}_k$ at each wall or edge k [92] hence the ideas presented for the 1D system of conservation laws can be extended (see Figure 2.6).

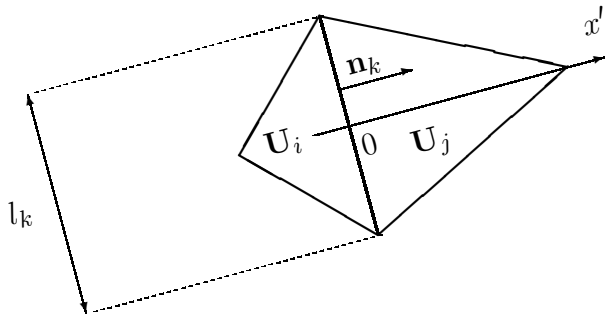

Figure 2.6: Riemann Problem in 2D projected through the normal direction to a cell edge.

Therefore, we are interested in achieving an approximate linearized solution $\hat{\mathbf{U}}(x',t)$ of the Riemann Problem defined at each edge k

$$\hat{\mathbf{U}}(x',0)_k = \begin{cases} \mathbf{U}_i & if \quad x' < 0 \\ \mathbf{U}_j & if \quad x' > 0 \end{cases} \tag{2.67}$$

that fulfils the Roe's consistency condition integrated over a suitable control volume $[x'_1, x'_2] \times [0, \Delta t]$:

$$\int_{x'_1}^{x'_2} \hat{\mathbf{U}}(x', \Delta t)\, dx' = \Delta x' \left(\mathbf{U}_j + \mathbf{U}_i\right) - \delta \mathbf{En} + \int_0^{\Delta t} \int_{x'_1}^{x'_2} \mathbf{S}\, dx'\, dt \tag{2.68}$$

Considering the following linearization in time of the vector of source terms

$$\int_0^{\Delta t} \int_{x'_1}^{x'_2} \mathbf{S}\, dx'\, dt = \int_{x'_1}^{x'_2} \mathbf{S}(x', 0)\, dx' = (\mathbf{Tn})_k^n \tag{2.69}$$

for a suitable matrix $\mathbf{T}$, the consistency condition is re-written:

$$\int_{x'_1}^{x'_2} \hat{\mathbf{U}}(x', \Delta t)\, dx' = \Delta x' \left(\mathbf{U}_j + \mathbf{U}_i\right) - (\delta \mathbf{E} - \mathbf{T})_k \mathbf{n}_k \tag{2.70}$$

Following Roe's linearization, the original Jacobian matrix $\mathbf{J}_{\mathbf{n}_k}$ of the flux normal to a direction given by the unit vector $\mathbf{n}_k = (n_x, n_y)$, $\mathbf{En}$, with $\mathbf{E} = \mathbf{F}n_x + \mathbf{G}n_y$

$$\mathbf{J}_{\mathbf{n}k} = \frac{\partial \mathbf{En}}{\partial \mathbf{U}} = \frac{\partial \mathbf{F}}{\partial \mathbf{U}} n_x + \frac{\partial \mathbf{G}}{\partial \mathbf{U}} n_y \tag{2.71}$$

can be locally linearized by constructing approximate matrices $\widetilde{\mathbf{J}}_{\mathbf{n}_k}$ for each local Riemann Problem, whose eigenvalues $\widetilde{\lambda}_k^m$ and eigenvectors $\widetilde{\mathbf{e}}_k^m$ satisfy:

$$\widetilde{\mathbf{J}}_{\mathbf{n}_k} = \widetilde{\mathbf{P}}_k \widetilde{\mathbf{\Lambda}}_k \widetilde{\mathbf{P}}_k^{-1} \tag{2.72}$$

with $m = 1...3$, $\widetilde{\mathbf{P}} = (\widetilde{\mathbf{e}}^1, \widetilde{\mathbf{e}}^2, \widetilde{\mathbf{e}}^3)$ and $\widetilde{\mathbf{\Lambda}}_k$ is a diagonal matrix with eigenvalues $\widetilde{\lambda}_k^m$ in the main diagonal. The difference in the vector of conserved variables as well as the vector of source terms at each edge k can be projected again onto the eigenvectors basis:

$$\delta \mathbf{U}_k = \widetilde{\mathbf{P}}_k \widetilde{\mathbf{A}}_k \qquad (\mathbf{Tn})_k = \widetilde{\mathbf{P}}_k \widetilde{\mathbf{B}}_k \tag{2.73}$$

with $\widetilde{\mathbf{A}}_k = \left(\widetilde{\alpha}^1, \widetilde{\alpha}^2, \widetilde{\alpha}^3\right)_k^T$ and $\widetilde{\mathbf{B}}_k = \left(\widetilde{\beta}^1, \widetilde{\beta}^2, \widetilde{\beta}^3\right)_k^T$. Consequently, the difference in fluxes and the contributions of source terms can be expressed in a compact way as in the 1D case:

$$\begin{gathered}\delta(\mathbf{En})_k - (\mathbf{Tn})_k = (\widetilde{\mathbf{P}}\widetilde{\mathbf{\Lambda}}\underbrace{\widetilde{\mathbf{P}}^{-1}\delta\mathbf{U}}_{\widetilde{\mathbf{A}}})_k - (\widetilde{\mathbf{P}}\widetilde{\mathbf{B}})_k = \\ \widetilde{\mathbf{P}}\widetilde{\mathbf{\Lambda}}\left(\widetilde{\mathbf{A}} - \widetilde{\mathbf{\Lambda}}^{-1}\widetilde{\mathbf{B}}\right)_k = \sum_{m=1}^{3}\left(\widetilde{\lambda}\ \widetilde{\gamma}\ \widetilde{\mathbf{e}}\right)_k^m\end{gathered} \tag{2.74}$$

with $\widetilde{\gamma}_k^m = \left(\widetilde{\alpha} - \dfrac{\widetilde{\beta}}{\widetilde{\lambda}}\right)_k^m$. According to (2.36), the numerical scheme is formulated using the difference splitting approach:

$$\mathbf{U}_i^{n+1} = \mathbf{U}_i^n - \frac{\Delta t}{A_i}\sum_{k=1}^{N_E}(\delta\mathbf{E}\ \mathbf{n} - \mathbf{Tn})_k^- l_k \tag{2.75}$$

where

$$(\delta\mathbf{E}\ \mathbf{n} - \mathbf{Tn})_k^- = \sum_{m=1}^{3}\left(\widetilde{\lambda}^-\ \widetilde{\gamma}\ \widetilde{\mathbf{e}}\right)_k^m \tag{2.76}$$

2.4.2 2D Augmented Approximate Riemann Solutions

Depending on the sign of the eigenvalues, $\widetilde{\lambda}^m$, a set of solutions is analysed. Each solution $\hat{\mathbf{U}}(x,t)$ will consist of five states or regions intrinsically related to the eigenvalues: the two initial states and the three intermediate states generated by the three eigenvalues plus the steady wave associated to the source term in the augmented philosophy. Let reorder the eigenvalues:

$$\widetilde{\lambda}^1 \leq \widetilde{\lambda}^2 \leq \widetilde{\lambda}^3 \tag{2.77}$$

Four possibilities are derived from a simple reasoning [92]:

1. $\widetilde{\lambda}^1 < 0,\ \widetilde{\lambda}^2, \widetilde{\lambda}^3 > 0$. The suggested solution is shown in Figure 2.7 (left) and is written as follows:

$$\hat{\mathbf{U}}(x',t) = \begin{cases} \mathbf{U}_i^n & \text{if} \quad x' - \widetilde{\lambda}^1 t < 0 \\ \mathbf{U}_i^* & \text{if} \quad x' - \widetilde{\lambda}^1 t > 0 \text{ and } x' < 0 \\ \mathbf{U}_j^{**} & \text{if} \quad x' > 0 \text{ and } x' - \widetilde{\lambda}^2 t < 0 \\ \mathbf{U}_j^{***} & \text{if} \quad x' - \widetilde{\lambda}^2 t > 0 \text{ and } x' - \widetilde{\lambda}^3 t < 0 \\ \mathbf{U}_j^n & \text{if} \quad x' - \widetilde{\lambda}^3 t > 0 \end{cases} \tag{2.78}$$

where

$$\begin{aligned} \mathbf{U}_i^*(\mathbf{U}_j, \mathbf{U}_i, (\mathbf{Tn})_k) &= \mathbf{U}_i^n + (\widetilde{\gamma}\widetilde{\mathbf{e}})_k^1 \\ \mathbf{U}_j^{***}(\mathbf{U}_j, \mathbf{U}_i, (\mathbf{Tn})_k) &= \mathbf{U}_j^n - (\widetilde{\gamma}\widetilde{\mathbf{e}})_k^3 \\ \mathbf{U}_j^{**}(\mathbf{U}_j, \mathbf{U}_i, (\mathbf{Tn})_k) &= \mathbf{U}_j^{***} - (\widetilde{\gamma}\widetilde{\mathbf{e}})_k^2 \end{aligned} \tag{2.79}$$

2. $\widetilde{\lambda}^1, \widetilde{\lambda}^2 < 0,\ \widetilde{\lambda}^3 > 0$. The solution is given by (see Figure 2.7 (right)):

$$\hat{\mathbf{U}}(x',t) = \begin{cases} \mathbf{U}_i^n & \text{if} \quad x' - \widetilde{\lambda}^1 t < 0 \\ \mathbf{U}_i^* & \text{if} \quad x' - \widetilde{\lambda}^1 t > 0 \text{ and } x' - \widetilde{\lambda}^2 t < 0 \\ \mathbf{U}_i^{**} & \text{if} \quad x' - \widetilde{\lambda}^2 t < 0 \text{ and } x' < 0 \\ \mathbf{U}_j^{***} & \text{if} \quad x' > 0 \text{ and } x' - \widetilde{\lambda}^3 t < 0 \\ \mathbf{U}_j^n & \text{if} \quad x' - \widetilde{\lambda}^3 t > 0 \end{cases} \tag{2.80}$$

with

$$\begin{aligned} \mathbf{U}_i^*(\mathbf{U}_j, \mathbf{U}_i, (\mathbf{Tn})_k) &= \mathbf{U}_i^n + (\widetilde{\gamma}\widetilde{\mathbf{e}})_k^1 \\ \mathbf{U}_i^{**}(\mathbf{U}_j, \mathbf{U}_i, (\mathbf{Tn})_k) &= \mathbf{U}_i^* + (\widetilde{\gamma}\widetilde{\mathbf{e}})_k^2 \\ \mathbf{U}_j^{***}(\mathbf{U}_j, \mathbf{U}_i, (\mathbf{Tn})_k) &= \mathbf{U}_j^n - (\widetilde{\gamma}\widetilde{\mathbf{e}})_k^3 \end{aligned} \tag{2.81}$$

3. $\widetilde{\lambda}^1, \widetilde{\lambda}^2, \widetilde{\lambda}^3 > 0$. The proposed solution is formulated:

$$\hat{\mathbf{U}}(x',t) = \begin{cases} \mathbf{U}_i^n & \text{if} \quad x' < 0 \\ \mathbf{U}_j^* & \text{if} \quad x' > 0 \text{ and } x' - \widetilde{\lambda}^1 t < 0 \\ \mathbf{U}_j^{**} & \text{if} \quad x' - \widetilde{\lambda}^1 t > 0 \text{ and } x' - \widetilde{\lambda}^2 t < 0 \\ \mathbf{U}_j^{***} & \text{if} \quad x' - \widetilde{\lambda}^2 t > 0 \text{ and } x' - \widetilde{\lambda}^3 t < 0 \\ \mathbf{U}_j^n & \text{if} \quad x' - \widetilde{\lambda}^3 t > 0 \end{cases} \tag{2.82}$$

with

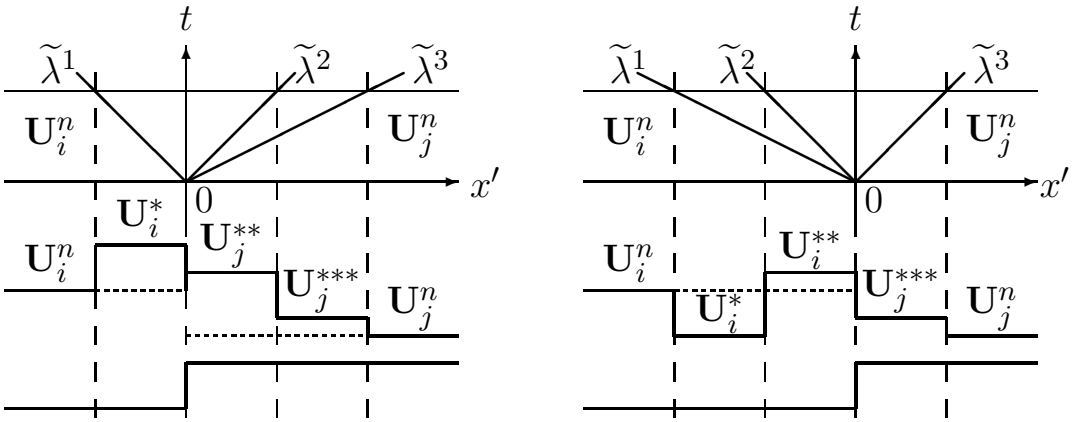

Figure 2.7: Values of the solution $\hat{\mathbf{U}}(x,t)$ in each wedge of the (x,t) plane for $\widetilde{\lambda}^1 < 0$, $\widetilde{\lambda}^2, \widetilde{\lambda}^3 > 0$ (left) and $\widetilde{\lambda}^1, \widetilde{\lambda}^2 < 0$, $\widetilde{\lambda}^3 > 0$ (right)

$$\mathbf{U}_j^*(\mathbf{U}_j, \mathbf{U}_i, (\mathbf{Tn})_k) = \mathbf{U}_j^{**} - (\widetilde{\gamma}\widetilde{\mathbf{e}})_k^1 \tag{2.83}$$

It is depicted in Figure 2.8 (left).

4. $\widetilde{\lambda}^1, \widetilde{\lambda}^2, \widetilde{\lambda}^3 > 0$. A sketch of the solution is plotted in Figure 2.8 (right) and the explicit expression can be easily found:

$$\hat{\mathbf{U}}(x',t) = \begin{cases} \mathbf{U}_i^n & \text{if} \quad x' - \widetilde{\lambda}^1 t < 0 \\ \mathbf{U}_i^* & \text{if} \quad x' - \widetilde{\lambda}^1 t > 0 \text{ and } x' - \widetilde{\lambda}^2 t < 0 \\ \mathbf{U}_i^{**} & \text{if} \quad x' - \widetilde{\lambda}^2 t > 0 \text{ and } x' - \widetilde{\lambda}^3 t < 0 \\ \mathbf{U}_i^{***} & \text{if} \quad x' - \widetilde{\lambda}^3 t > 0 \text{ and } x' < 0 \\ \mathbf{U}_j^n & \text{if} \quad x' > 0 \end{cases} \tag{2.84}$$

where

$$\mathbf{U}_i^{***}(\mathbf{U}_j, \mathbf{U}_i, (\mathbf{Tn})_k) = \mathbf{U}_i^{**} + (\widetilde{\gamma}\widetilde{\mathbf{e}})_k^3 \tag{2.85}$$

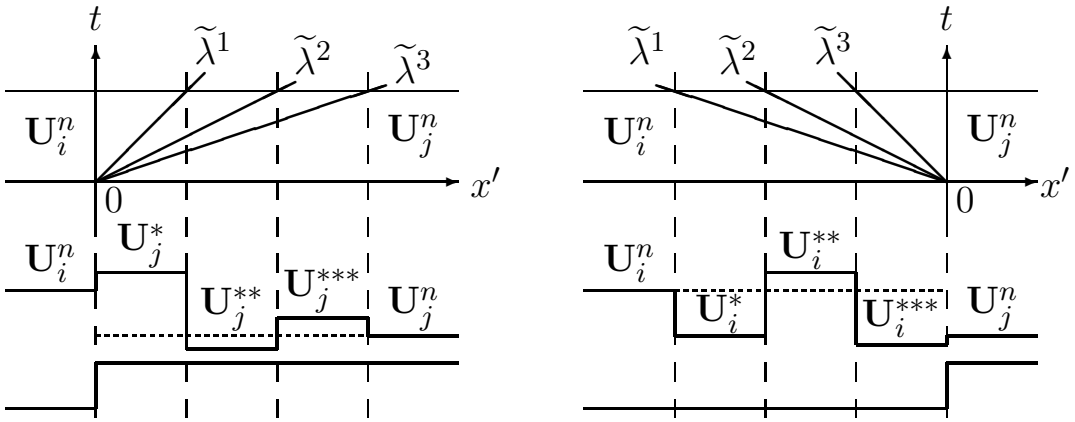

Figure 2.8: Values of the solution $\hat{\mathbf{U}}(x,t)$ in each wedge of the (x,t) plane for $\widetilde{\lambda}^1, \widetilde{\lambda}^2, \widetilde{\lambda}^3 > 0$ (left) and $\widetilde{\lambda}^1, \widetilde{\lambda}^2, \widetilde{\lambda}^3 < 0$ (right)

Chapter 3

The Shallow Water Equations

3.1 Introduction

The shallow water equations are able to model different phenomena such as tsunami waves, dam break problems, open channel hydraulics, overland run-off or simply the flooding wave in a river with floodplain areas. In summary, they model the propagation of disturbances in water and other incompressible fluids. The underlying assumption is that the water depth is small in comparison with the wave length of the disturbance.

The equations describing the three dimensional free surface flow can be derived from the Navier-Stokes equations, being sufficient to use the physical principles of mass and momentum conservation in the three space dimensions. Furthermore, closure hypothesis and boundary conditions referred to the fluid-solid (bottom) and fluid-fluid (free surface) interfaces have to be considered to totally deduce these equations.

Once the three dimensional free surface flow equations are determined, it is possible to derive the three dimensional shallow water equations by studying the characteristic scales of the problem. The three main hypothesis of the shallow water principles are summarized in:

- The pressure distribution in the vertical direction is hydrostatic, i.e., the waves produced in the free surface interface vary smoothly.
- Friction losses in unsteady flow do not differ from the same losses in steady flow.
- The average slope of the topography is small and the tangent of the angle can be approximated by the angle.

From the three dimensional shallow water equations it is possible to obtain both the 1D and 2D shallow water equations, just integrating them in the cross section or in the vertical direction respectively. The full derivation of the 1D and 2D shallow water equations can be found in [126, 35] and the direct expression of both models is addressed in the subsequent section.

3.2 Hydrodynamic equations

3.2.1 1D shallow water equations

Equations can be derived from mass and momentum control volume analysis:

$$\frac{\partial \mathbf{U}(x,t)}{\partial t} + \frac{d\mathbf{F}(x,\mathbf{U})}{dx} = \mathbf{H}(x,\mathbf{U}) \tag{3.1}$$

$$\mathbf{U} = \begin{pmatrix} A \\ Q \end{pmatrix}, \quad \mathbf{F} = \begin{pmatrix} Q \\ \frac{Q^2}{A} + gI_1 \end{pmatrix}, \quad \mathbf{H} = \begin{pmatrix} 0 \\ g\left[I_2 + A\left(S_0 - S_f\right)\right] \end{pmatrix} \tag{3.2}$$

where Q is the discharge, A is the wetted cross section area, $g = 9.8\ m/s^2$ is the acceleration due to the gravity, S_0 is the bed slope

$$S_0 = -\frac{\partial z_b}{\partial x} \tag{3.3}$$

where z_b is the bed level. S_f is the friction slope here represented by the empirical Manning law

$$S_f = \frac{Q^2 n^2}{A^2 R^{4/3}} \tag{3.4}$$

being R the hydraulic radius and n the Manning roughness coefficient. I_1 represents a hydrostatic pressure force term

$$I_1(x,t) = \int_0^{h(x,t)} (h-\eta)\sigma(x,\eta)\ d\eta \tag{3.5}$$

in a section of water depth $h = z_s - z_b$, water surface level z_s and width $\sigma(x,\eta)$ at a position η from the bottom (see Figure 3.1).

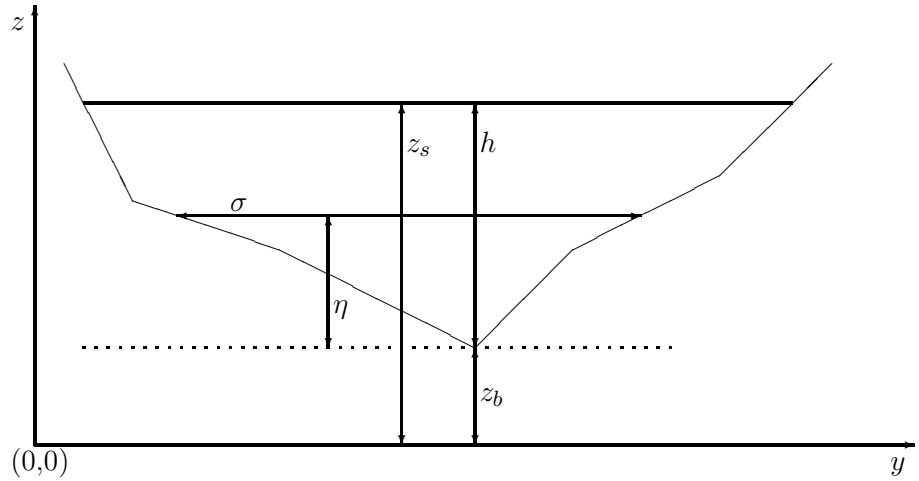

Figure 3.1: Coordinate system in a cross section as used in the 1D model

Therefore, the cross sectional wetted area can be expressed as follows:

$$A(x,t) = \int_0^{h(x,t)} \sigma(x,\eta)\ d\eta \tag{3.6}$$

On the other hand, I_2 accounts for the pressure force due to the longitudinal width variations:

$$I_2(x,t) = \int_0^{h(x,t)} (h-\eta)\frac{\partial \sigma(x,\eta)}{\partial x}\ d\eta \tag{3.7}$$

3.2.2 2D shallow water equations

The volume and momentum conservation are expressed as follows:

$$\frac{\partial \mathbf{U}}{\partial t} + \frac{\partial \mathbf{F}(\mathbf{U})}{\partial x} + \frac{\partial \mathbf{G}(\mathbf{U})}{\partial y} = \mathbf{H}(\mathbf{U}) \tag{3.8}$$

where the conserved variables:

$$\mathbf{U} = (h,\ q_x,\ q_y)^T \tag{3.9}$$

$q_x = uh$, $q_y = vh$ and (u, v) are the averaged components of the velocity vector $\mathbf{u}$ along the x and y coordinates respectively. The fluxes of these variables are:

$$\mathbf{F} = \left(q_x,\ \frac{q_x^2}{h} + \frac{1}{2}gh^2,\ \frac{q_x q_y}{h} \right)^T, \quad \mathbf{G} = \left(q_y,\ \frac{q_x q_y}{h},\ \frac{q_y^2}{h} + \frac{1}{2}gh^2 \right)^T \tag{3.10}$$

The source terms of the momentum are due to the bed slope and friction

$$\mathbf{H} = \left(0,\ gh(S_{0x} - S_{fx}),\ gh(S_{0y} - S_{fy})\right)^T \tag{3.11}$$

where the bed slopes of the bottom level z_b are

$$S_{0x} = -\frac{\partial z_b}{\partial x}, \qquad S_{0y} = -\frac{\partial z_b}{\partial y} \tag{3.12}$$

and the friction losses are written in terms of the Manning's roughness coefficient n:

$$S_{fx} = \frac{n^2 u\sqrt{u^2+v^2}}{h^{4/3}}, \qquad S_{fy} = \frac{n^2 v\sqrt{u^2+v^2}}{h^{4/3}} \tag{3.13}$$

3.3 Numerical scheme

The ideas developed for the numerical resolution of non-linear hyperbolic system of conservation laws with source terms by means of approximate Riemann solvers (2.35) and (2.36) are going to be applied to the SWE in both 1D (3.1) and 2D (3.8) configurations.

3.3.1 1D numerical scheme

It is possible to express the equations (3.1) and (3.2) in a non-conservative form as in [16]:

$$\frac{d\mathbf{F}(x,\mathbf{U})}{dx} = \left.\frac{\partial \mathbf{F}(x,\mathbf{U})}{\partial x}\right|_{\mathbf{U}=const} + \left.\frac{\partial \mathbf{F}(x,\mathbf{U})}{\partial \mathbf{U}}\right|_{x=const} \frac{\partial \mathbf{U}(x,t)}{\partial x} \tag{3.14}$$

considering the subtlety that $\mathbf{F}(x,\mathbf{U})$ is not only function of $\mathbf{U}$ but also of x. Using (3.14), the 1D shallow water equations can be formulated as follows :

$$\frac{\partial \mathbf{U}(x,t)}{\partial t} + \mathbf{J}(x,\mathbf{U})\frac{\partial \mathbf{U}(x,t)}{\partial x} = \mathbf{H}'(x,\mathbf{U}) \tag{3.15}$$

being $\mathbf{H}'(x,\mathbf{U})$ the vector related with the sources expressed in the non-conservative form:

$$\mathbf{H}'(x,\mathbf{U}) = \mathbf{H}(x,\mathbf{U}) - \left.\frac{\partial \mathbf{F}(x,\mathbf{U})}{\partial x}\right|_{\mathbf{U}=const} \tag{3.16}$$

and $\mathbf{J}$ the Jacobian matrix of the original system

$$\mathbf{J} = \left.\frac{\partial \mathbf{F}}{\partial \mathbf{U}}\right|_{x=const} = \begin{pmatrix} 0 & 1 \\ c^2 - u^2 & 2u \end{pmatrix} \tag{3.17}$$

with $u = Q/A$ and $c = \sqrt{g\,A/B}$ (B is the top width at the free surface).

Following the Leibniz rule, it is possible to express the link between I_1 and I_2 in this manner [35]:

$$\frac{\partial I_1}{\partial x} = I_2 + A\frac{\partial h}{\partial x} \tag{3.18}$$

As stated in [16, 19], there exists a difference between the partial and the total derivatives when discretizing the equation: the discrete increments approach actually the total derivatives and not the partial derivatives. Therefore, prior to discretization, all terms have to be carefully expressed in total derivatives. In particular:

$$\frac{dh}{dx} = \frac{\partial h}{\partial x} + \frac{\partial h}{\partial A}\frac{\partial A}{\partial x} = \frac{\partial h}{\partial x} + \frac{1}{B}\frac{\partial A}{\partial x} \tag{3.19}$$

leading to:

$$\frac{\partial h}{\partial x} = \frac{dh}{dx} - \frac{1}{B}\frac{\partial A}{\partial x} \tag{3.20}$$

From (3.18) and (3.20), the non-conservative source term is expressed as follows:

$$\mathbf{H}'(x,\mathbf{U}) = \mathbf{H}(x,\mathbf{U}) - \left.\frac{\partial \mathbf{F}(x,\mathbf{U})}{\partial x}\right|_{\mathbf{U}=const} = \begin{pmatrix} 0 \\ gA\left(S_0 - S_f - \dfrac{dh}{dx} + \dfrac{1}{B}\dfrac{dA}{dx}\right) \end{pmatrix} \tag{3.21}$$

where the equivalence between the partial and total x-derivatives of the conserved variable A has been used. The Jacobian matrix (3.17) can be diagonalized and the resulting diagonal matrix $\mathbf{\Lambda}$ is formed by the eigenvalues of $\mathbf{J}$, and $\mathbf{P}$ is constructed with its eigenvectors.

$$\mathbf{P} = \begin{pmatrix} 1 & 1 \\ \lambda_1 & \lambda_2 \end{pmatrix}, \quad \mathbf{\Lambda} = \begin{pmatrix} \lambda_1 & 0 \\ 0 & \lambda_2 \end{pmatrix},$$
$$\mathbf{e}_k = \begin{pmatrix} 1 \\ \lambda_k \end{pmatrix}, \quad \lambda_1 = u - c, \quad \lambda_2 = u + c \tag{3.22}$$

The equations in non-conservative form can be discretized in a regular mesh of size Δx by means of the first order explicit scheme. Let consider the interface $i + 1/2$, between cells i and $i + 1$. As stated in (2.43)-(2.56), Roe's linearization [109] allows to express the differences in the conserved variables and in the source terms across the grid edge $i + 1/2$ as a sum of waves:

$$\delta \mathbf{U}_{i+1/2} = \mathbf{U}_{i+1} - \mathbf{U}_i = \sum_{m=1}^{2} (\tilde{\alpha}^m \, \tilde{\mathbf{e}}^m)_{i+1/2},$$
$$(\tilde{\mathbf{H}}' \, \Delta x)_{i+1/2} = \sum_{m=1}^{2} (\tilde{\beta}^m \, \tilde{\mathbf{e}}^m)_{i+1/2} \tag{3.23}$$

with

$$\tilde{\lambda}_1 = \tilde{u} - \tilde{c}, \quad \tilde{\lambda}_2 = \tilde{u} + \tilde{c}, \quad \tilde{\alpha}_1 = \frac{\tilde{\lambda}_2 \, \delta A - \delta Q}{2\tilde{c}}, \quad \tilde{\alpha}_2 = \frac{-\tilde{\lambda}_1 \, \delta A + \delta Q}{2\tilde{c}},$$
$$\tilde{\beta}_1 = -\frac{1}{2\tilde{c}} \left\{ g\tilde{A} \left[\left(\tilde{S}_0 - \tilde{S}_f \right) \Delta x - \delta h + \frac{1}{\tilde{B}} \delta A \right] \right\}, \quad \tilde{\beta}_2 = -\tilde{\beta}_1, \tag{3.24}$$
$$\tilde{u}_{i+1/2} = \frac{\sqrt{A_i} u_i + \sqrt{A_{i+1}} u_{i+1}}{\sqrt{A_i} + \sqrt{A_{i+1}}}, \quad \tilde{c}_{i+1/2} = \sqrt{g \frac{A_i + A_{i+1}}{B_i + B_{i+1}}}$$

where the tilde variables represent an average state at each edge. The average states $\tilde{A}$, $\tilde{B}$, $\tilde{S}_0$ and $\tilde{S}_f$ can be easily defined as arithmetic averages [16] in the conventional formulation.

The contributions due to the fluxes and the source terms can be expressed in a compact formulation as follows:

$$\widetilde{\gamma}^m_{i+1/2} = \left(\widetilde{\alpha} - \frac{\widetilde{\beta}}{\widetilde{\lambda}} \right)^m_{i+1/2} \tag{3.25}$$

Therefore, the first order explicit upwind numerical scheme is formulated [87] according to (2.57) and (2.58):

$$\mathbf{U}^{n+1}_i = \mathbf{U}^n_i - \frac{\Delta t}{\Delta x} \left[\left(\sum_m \tilde{\lambda}^+ \tilde{\gamma} \tilde{\mathbf{e}} \right)^m_{i-1/2} + \left(\sum_m \tilde{\lambda}^- \tilde{\gamma} \tilde{\mathbf{e}} \right)^m_{i+1/2} \right]^n \tag{3.26}$$

where $\tilde{\lambda}^{\pm m}_{i+1/2} = \frac{1}{2}(\tilde{\lambda} \pm |\tilde{\lambda}|)^m_{i+1/2}$ provides the upwind discretization of the flux. Figure 3.2 shows a sketch of the 1D numerical scheme. It illustrates that the in-going contributions from left and right walls are used to update the value of the conserved variables at every cell. The scheme so built has proved to be robust, conservative, well-balanced and positivity preserving [16].

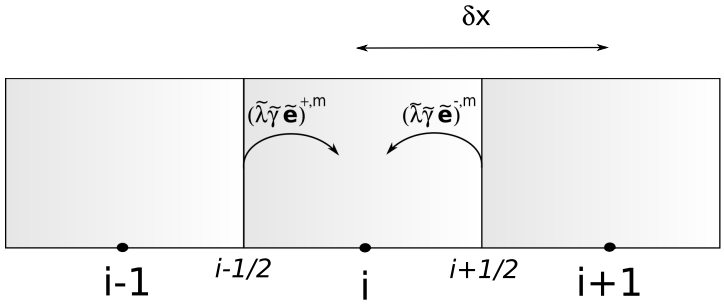

Figure 3.2: Sketch of the 1D numerical scheme

The time step Δt is dynamically chosen following [16]:

$$\Delta t = \text{CFL} \min_{i,m} \left(\frac{\Delta x}{\left|\tilde{\lambda}_m\right|^n_i} \right), \qquad \text{CFL} \leq 1 \tag{3.27}$$

where CFL is the Courant-Friedrich-Lewy number.

3.3.2 2D numerical scheme

It is possible to define a Jacobian matrix of the normal flux in the 2D model:

$$\mathbf{J} = \frac{\partial(\mathbf{E}\cdot\mathbf{n})}{\partial \mathbf{U}} = \begin{pmatrix} 0 & n_x & n_y \\ c^2\, n_x - u\,\mathbf{u}\cdot\mathbf{n} & u\, n_x + \mathbf{u}\cdot\mathbf{n} & u\, n_y \\ c^2\, n_y - v\,\mathbf{u}\cdot\mathbf{n} & v\, n_x & v\, n_y + \mathbf{u}\cdot\mathbf{n} \end{pmatrix} \tag{3.28}$$

with $\mathbf{n} = (n_x,\ n_y)^T$ the outward normal vector, $u = q_x/h$, $v = q_y/h$, $c = \sqrt{g\,h}$ and $\mathbf{u}\cdot\mathbf{n} = u\,n_x + v\,n_y$. Following the same philosophy, the Jacobian matrix (3.28) is diagonalized in terms of matrices $\mathbf{\Lambda}$ and $\mathbf{P}$ formed by its eigenvalues λ_m and eigenvectors $\mathbf{e}_m$ respectively:

$$\mathbf{P} = \begin{pmatrix} 1 & 0 & 1 \\ u - c\,n_x & -c n_y & u + c\,n_x \\ v - c\,n_y & c\,n_x & v + c\,n_y \end{pmatrix}, \quad \mathbf{\Lambda} = \begin{pmatrix} \lambda_1 & 0 & 0 \\ 0 & \lambda_2 & 0 \\ 0 & 0 & \lambda_3 \end{pmatrix},$$

$$\mathbf{e}_1 = \begin{pmatrix} 1 \\ u - c\,n_x \\ v - c\,n_y \end{pmatrix}, \quad \mathbf{e}_2 = \begin{pmatrix} 0 \\ -c\,n_y \\ c\,n_x \end{pmatrix}, \quad \mathbf{e}_3 = \begin{pmatrix} 1 \\ u + c\,n_x \\ v + c\,n_y \end{pmatrix}, \tag{3.29}$$

$$\lambda_1 = \mathbf{u}\cdot\mathbf{n} - c, \quad \lambda_2 = \mathbf{u}\cdot\mathbf{n}, \quad \lambda_3 = \mathbf{u}\cdot\mathbf{n} + c$$

Applying Roe's linearization [109, 110] it is possible to express locally the difference in vector $\mathbf{U}$ across grid edge k projected onto the matrix eigenvectors basis [92]:

$$\delta\mathbf{U}_k = \mathbf{U}_j - \mathbf{U}_i = \widetilde{\mathbf{P}}_k \tilde{\mathbf{A}}_k \tag{3.30}$$

where i, j are the indexes of the cells sharing the edge k and $\tilde{\mathbf{A}}_k = (\tilde{\alpha}_1,\ \tilde{\alpha}_2,\ \tilde{\alpha}_3)^T_k$ contains the set of wave strengths:

$$\tilde{\alpha}_1 = \frac{\delta h}{2} - \frac{1}{2\tilde{c}}\left(\delta\mathbf{q}\cdot\mathbf{n} - \tilde{\mathbf{u}}\cdot\mathbf{n}\,\delta h\right), \quad \tilde{\alpha}_2 = \frac{1}{\tilde{c}}\left[\delta q_y - \tilde{v}\,\delta h)n_x - (\delta q_x - \tilde{u}\,\delta h)n_y\right],$$

$$\tilde{\alpha}_3 = \frac{\delta h}{2} + \frac{1}{2\tilde{c}}\left(\delta\mathbf{q}\cdot\mathbf{n} - \tilde{\mathbf{u}}\cdot\mathbf{n}\,\delta h\right),$$

$$\tilde{u}_k = \frac{\sqrt{h_i}\,u_i + \sqrt{h_j}\,u_j}{\sqrt{h_i}+\sqrt{h_j}}, \quad \tilde{v}_k = \frac{\sqrt{h_i}\,v_i + \sqrt{h_j}\,v_j}{\sqrt{h_i}+\sqrt{h_j}}, \quad \tilde{c}_k = \sqrt{g\,\frac{h_i+h_j}{2}} \tag{3.31}$$

Following the linearization concept, the source term is included in the Riemann solver as a singular source. Considering that source terms are not necessarily constant in time, the following linearization of the non-conservative term is applied as in (2.69) [92]:

$$\mathbf{H}_k^n = \begin{pmatrix} 0 \\ -g\tilde{h}(\delta z + S_{f,\mathbf{n}})n_x \\ -g\tilde{h}(\delta z + S_{f,\mathbf{n}})n_y \end{pmatrix} \tag{3.32}$$

The source term is next projected onto the matrix eigenvectors basis [92]

$$\tilde{\mathbf{H}}_k = \widetilde{\mathbf{P}}_k\tilde{\mathbf{B}}_k \tag{3.33}$$

where $\tilde{\mathbf{B}}_k = (\tilde{\beta}_1,\ \tilde{\beta}_2,\ \tilde{\beta}_3)_k^T$ contains the source strengths:

$$\tilde{\beta}_1 = -\frac{1}{2c}(\delta z + S_{f,\mathbf{n}}), \quad \tilde{\beta}_2 = 0, \quad \tilde{\beta}_3 = -\tilde{\beta}_1 \tag{3.34}$$

where $\tilde{\mathbf{u}}\cdot\mathbf{n} = \tilde{u}\,n_x + \tilde{v}\,n_y$, $\delta\mathbf{q}\cdot\mathbf{n} = \delta q_x\,n_x + \delta q_y\,n_y$ and the averages states at each wall k are represented with the tilde variables. $S_{f,\mathbf{n}}$ accounts for the discretized and projected friction term, which is expressed as follows [92]:

$$S_{f,\mathbf{n}} = \frac{\overline{n}^2\ \tilde{\mathbf{u}}\mathbf{n}\ \min(|u_i|,|u_j|)}{\max(h_i,h_j)^{4/3}}d_n \tag{3.35}$$

where $\overline{n} = \frac{1}{2}(n_i + n_j)$ is the averaged Manning's coefficient and d_n is the normal distance between cell centers. The contributions due to the fluxes and the source terms are combined in a compact expression:

$$\widetilde{\gamma}_k^m = \left(\widetilde{\alpha} - \frac{\widetilde{\beta}}{\widetilde{\lambda}} \right)_k^m \tag{3.36}$$

and defining $(\widetilde{\lambda}^-)_k^m$ as

$$(\widetilde{\lambda}^-)_k^m = \frac{1}{2}(\widetilde{\lambda} - |\widetilde{\lambda}|)_k^m \tag{3.37}$$

the 2D numerical upwind explicit scheme is formulated using the finite volume approach for the updating of a single cell whose area is A_i, dealing with the contributions that arrive to the cell [89]:

$$\mathbf{U}_i^{n+1} = \mathbf{U}_i^n - \frac{\Delta t}{A_i} \sum_{k=1}^{NE} \sum_{m}^{3} \left[(\tilde{\lambda}^- \tilde{\gamma} \tilde{\mathbf{e}})_k^m l_k \right]^n \tag{3.38}$$

In this expression, N_E indicates the number of edges in cell i and l_k is the length of each edge (see Figure 3.3). This scheme has been proved to be robust, conservative, well-balanced and positivity preserving over irregular bed [92].

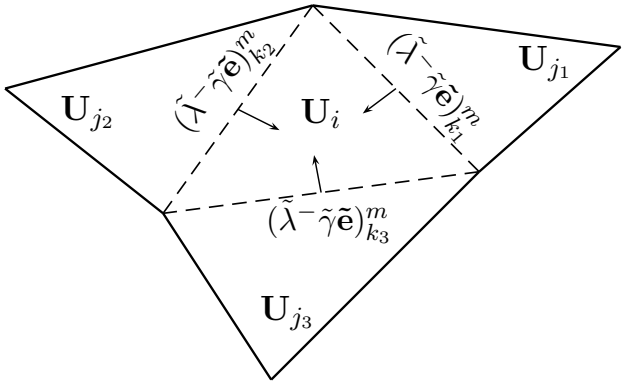

Figure 3.3: Sketch of the 2D numerical discretization

When considering unstructured meshes in the 2D scheme, a distance χ_i is defined by using the area of the cell as well as the length of the k edges:

$$\chi_i = \frac{A_i}{\max_{k=1,N_E} \; l_k} \tag{3.39}$$

Therefore, the time step is again chosen by using the following rule [92]:

$$\Delta t = \text{CFL}\ \frac{\min(\chi_i, \chi_j)}{\max_m |\tilde{\lambda}^m|} \qquad \text{CFL} \leq 0.5 \tag{3.40}$$

Although it is worth noting that the CFL value could be chosen over this value in certain triangular Delaunay meshes, it should preferable remain under the value of 0.5 in the 2D model.

3.3.3 Entropy fix

Roe's scheme may produce non-physical results due to the procedure of linearization. To avoid this, the version of the Harten-Hyman entropy fix [118] is used in this work. It is formulated without loss of generality for the edge k, between cells i and j.

Let define $\lambda_i^m = \lambda^m(\mathbf{U}_i)$ and $\lambda_j^m = \lambda^m(\mathbf{U}_j)$. In the case of a transonic rarefaction where $\lambda_i^m < 0 < \lambda_j^m$, the jump associated to $\widetilde{\lambda}_k^m$ is decomposed into two new jumps,

$$\bar{\lambda}_k^m = \lambda_i^m \frac{(\lambda_j^m - \widetilde{\lambda}_k^m)}{(\lambda_j^m - \lambda_i^m)} \qquad \widehat{\lambda}_k^m = \lambda_j^m \frac{(\widetilde{\lambda}_k^m - \lambda_i^m)}{(\lambda_j^m - \lambda_i^m)} \tag{3.41}$$

with $\bar{\lambda}_k^m + \widehat{\lambda}_k^m = \widetilde{\lambda}_k^m$, and $\bar{\lambda}_k^m < 0$ and $\widehat{\lambda}_k^m > 0$ by definition.

This idea can be applied to the decomposition of the source term associated to β_k^m into two new values, $\bar{\beta}_k^m$ and $\widehat{\beta}_k^m$. As the amount of source term has to be conservative, the splitting must satisfy $\bar{\beta}^m + \widehat{\beta}^m = \beta^m$. In order to avoid undesirable results and reduction of the time step size [92], the choice used is

$$\bar{\beta}^m = \beta^m \qquad \widehat{\beta}^m = 0 \tag{3.42}$$

that preserves the stability region in (3.40), simply replacing $\widetilde{\lambda}_k^m$ by $\bar{\lambda}_k^m$ [92].

3.3.4 Boundary conditions

Boundary conditions discretization becomes a very important issue when designing a finite volume scheme. In the case of a hyperbolic system, the theory of characteristics provides clear information about the number of external boundary conditions to be

imposed at the inlet or at the outlet domain [67]. The set of possibilities is illustrated for the 1D case in Figure 3.4 and can be summarized as follows [20, 13]:

1. Subcritical inlet flow: One of the variables is enforced and the other is calculated numerically.

2. Supercritical inlet flow: All the variables have to be imposed, no information is provided from the inner cells.

3. Subcritical outlet flow: As in the subcritical inlet flow, one of the variables is required to complete the information at the boundary cell.

4. Supercritical outlet flow: No extra information apart from that computed numerically is needed.

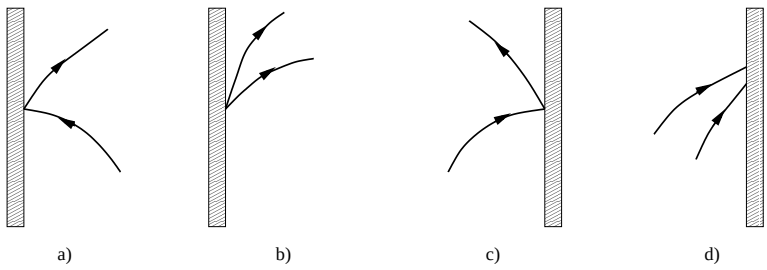

Figure 3.4: Type of 1D open boundaries: a) Subcritical inlet, b) Supercritical inlet, c) Subcritical outlet, d) Supercritical outlet

It it worth remarking that boundary conditions are enforced by requiring that the boundary cells adopt the desired values of the imposed variables.

The extension of the philosophy presented above in the 1D case for the 2D shallow water system is not a straightforward procedure. The characterisation of the flow regime at the inlet or outlet boundary is not an easy task and it requires to convert cross section average quantities such as discharge or water surface level to water depth or velocity at each cell. Additionally, in realistic problems with irregular and complex geometries, the distribution of these average quantities demands a fine treatment. This was precisely carried out in [90].

When dealing with closed or solid boundaries, the 2D scheme requires that no flow must cross the boundary, i.e., $\mathbf{u} \cdot \mathbf{n} = 0$ where $\mathbf{u}$ is the cell velocity and $\mathbf{n}$ is the

solid outward normal direction. It is imposed in the cell velocity once the contributions coming from the inner walls have been computed and added to the cell. The conservation is also ensured in all kind of flow conditions.

3.4 Solute transport

The study of solute transport phenomena and river mixing has become a great concern in hydraulic and environmental problems. A solute is defined as any substance that is advected by water flows. In fact, a solute may be not only a reactive pollutant such as fertilizer or pesticide, but also dissolved gasses or tracer substances. The interest is usually put on the time evolution of a solute concentration within a complex hydrodynamic system, that is, given the solution concentration at a specific time and space, the aim is to know the spatial distribution of the solute concentrations at some future time. This physical process is modelled by means of the advection equation and can incorporate the effect of reaction (with the water and with other solutes) and solute diffusion. It can be coupled with both 1D and 2D hydrodynamic equations detailed above.

3.4.1 Governing equations

For the sake of clarity, the transport of only one solute is presented coupled to each model, even though it is possible to define more than one solute and to establish connections between them. It is worth noting that the solute transport equations will be expressed in a conservative form, assuming that the velocities and the water depth could not vary smoothly in space and time.

3.4.1.1 1D shallow water equations with solute transport

The 1D shallow water equations and the solute transport can be expressed coupled in a single system of equations:

$$\mathbf{U} = \begin{pmatrix} A \\ Q \\ A\phi \end{pmatrix}, \quad \mathbf{F} = \begin{pmatrix} Q \\ \frac{Q^2}{A} + gI_1 \\ Q\phi \end{pmatrix}, \quad \mathbf{H} = \begin{pmatrix} 0 \\ g\left[I_2 + A\left(S_0 - S_f\right)\right] \\ 0 \end{pmatrix}$$
$$\mathbf{R} = \begin{pmatrix} 0 \\ 0 \\ -KA\phi \end{pmatrix} \quad \mathbf{D} = \begin{pmatrix} 0 \\ 0 \\ \frac{\partial}{\partial x}\left[DA\frac{\partial \phi}{\partial x}\right] \end{pmatrix} \tag{3.43}$$

where the third equation in (3.43) represents the transport of a substance with a cross-section average concentration of ϕ, an uptake constant K and diffusion coefficient of D.

3.4.1.2 2D shallow water equations with solute transport

Correspondingly, the 2D shallow water model with solute transport can be written in a unique coupled system:

$$\frac{\partial \mathbf{U}}{\partial t} + \frac{\partial \mathbf{F}(\mathbf{U})}{\partial x} + \frac{\partial \mathbf{G}(\mathbf{U})}{\partial y} = \mathbf{H}(\mathbf{U}) + \mathbf{R}(\mathbf{U}) + \mathbf{D}(\mathbf{U}) \tag{3.44}$$

where

$$\mathbf{U} = (h, q_x, q_y, h\phi)^T$$

$$\mathbf{F} = \left(q_x, \frac{q_x^2}{h} + \frac{1}{2}gh^2, \frac{q_x q_y}{h}, h\phi u\right)^T, \qquad \mathbf{G} = \left(q_y, \ \frac{q_x q_y}{h}, \ \frac{q_y^2}{h} + \frac{1}{2}gh^2, \ h\phi v\right)^T$$

$$\mathbf{H} = \left(0, \ gh(S_{0x} - S_{fx}), \ gh(S_{0y} - S_{fy}), \ 0\right)^T \tag{3.45}$$

and ϕ is the depth-average solute concentration. The source terms associated to the solute transport equation are expressed as follows:

$$\mathbf{R} = (0, 0, 0, -Kh\phi)^T \qquad \mathbf{D} = \left(0, 0, 0, \overrightarrow{\nabla}(Dh\overrightarrow{\nabla}\phi)\right)^T \tag{3.46}$$

where K is the uptake constant and D is an empirical diffusion matrix.

3.4.2 Numerical scheme

In the present work, the solute transport has been considered leaving aside the consideration concerning diffusion terms. However many strategies such as splitting and computing separately the advection and the diffusion terms or solving the diffusion implicitly [91, 95], have been developed to avoid small values in the time step size due to the combination of the CFL and Peclet number.

The numerical resolution of the solute transport equation under an explicit finite volume method is frequently performed by solving the depth-averaged concentration apart from the shallow water equations, that is, using a simpler decoupled algorithm. The scheme is easy: once the hydrodynamic equations have been solved, the corresponding substances or solutes are advected with these flow field quantities previously computed. However, careless numerical techniques lead to numerical troubles and do not preserve the conservation property [95], providing non-physical results in certain cases.

In order to get a fully conservative method, the complete system including the hydrodynamic and the transport equations is considered. Mathematically, the complete system conserves the hyperbolicity property, implying the existence of a 3×3 or 4×4 Jacobian matrix for the 1D or the 2D model respectively. On this basis we can apply the procedure described above, allowing a Roe's local linearization and expressing the contributions that arrive to the cell as a sum of waves. This scheme guarantees the conservation but it can lead to unbounded values in the final solute concentration in extreme cases. For this purpose, a strategy that avoids these situations by enforcing a conservative redistribution of the solute mass fluxes was proposed in [90].

It is feasible to decouple the solute transport equation from the hydrodynamic system in a conservative way as in [29], using a high resolution scheme that provides bounded solutions. However the time step is restricted to achieve the max-min property. A different technique is used in this work for the solute transport. A thorough analysis of the augmented Riemann solver, considering all the set of possible approximate solutions in all kind of different flow situations for the volumetric concentration was presented in [98]. This huge analysis allowed to define in essence a single numerical flux $q^{\downarrow}$, directly related to the Roe's linearization, which is able to completely decouple the solute transport from the hydrodynamic system in a

conservative way.

In the 1D framework, $q^{\downarrow}$ at interface $i+1/2$ (between cells i and $i+1$) is defined as:

$$q^{\downarrow}_{i+1/2} = Q_i + \sum_{m=1}^{2} \left(\widetilde{\lambda}^{-} \; \widetilde{\gamma} \; \widetilde{\mathbf{e}}_1 \right)^{m}_{i+1/2} \tag{3.47}$$

and the numerical scheme for the solute transport equation becomes:

$$(A\phi)^{n+1}_i = (A\phi)^n_i - \frac{\Delta t}{\Delta x} \left[(q\phi)^{\downarrow}_{i+1/2} - (q\phi)^{\downarrow}_{i-1/2} \right] \tag{3.48}$$

where

$$\phi^{\downarrow}_{i+1/2} = \begin{cases} \phi_i & if \quad q^{\downarrow}_{i+1/2} > 0 \\ \phi_{i+1} & if \quad q^{\downarrow}_{i+1/2} < 0 \end{cases} \tag{3.49}$$

In the 2D configuration, the ideas are extended by projecting the problem onto the normal direction of the edge k separating cells i and j. Therefore,

$$q^{\downarrow}_k = q_i + \sum_{m=1}^{3} \left(\widetilde{\lambda}^{-} \; \widetilde{\gamma} \; \widetilde{\mathbf{e}}_1 \right)^{m}_{k} \tag{3.50}$$

where $q_i = (h\mathbf{un})_i$ and the numerical scheme for the solute transport equation is written as:

$$(h\phi)^{n+1}_i = (h\phi)^n_i - \frac{\Delta t}{A_i} \sum_{k=1}^{N_E} (q\phi)^{\downarrow}_k l_k \tag{3.51}$$

where

$$\phi^{\downarrow}_k = \begin{cases} \phi_i & if \quad q^{\downarrow}_k > 0 \\ \phi_j & if \quad q^{\downarrow}_k < 0 \end{cases} \tag{3.52}$$

From a physical point of view, the new solute mass at a fixed cell can be merely seen as exchanging water volumes with certain concentration through the neighbouring walls and mixing them (finite volume Godunov's type method) with the former mass existing in the previous time (Figure 3.5). According to this philosophy, the outlet

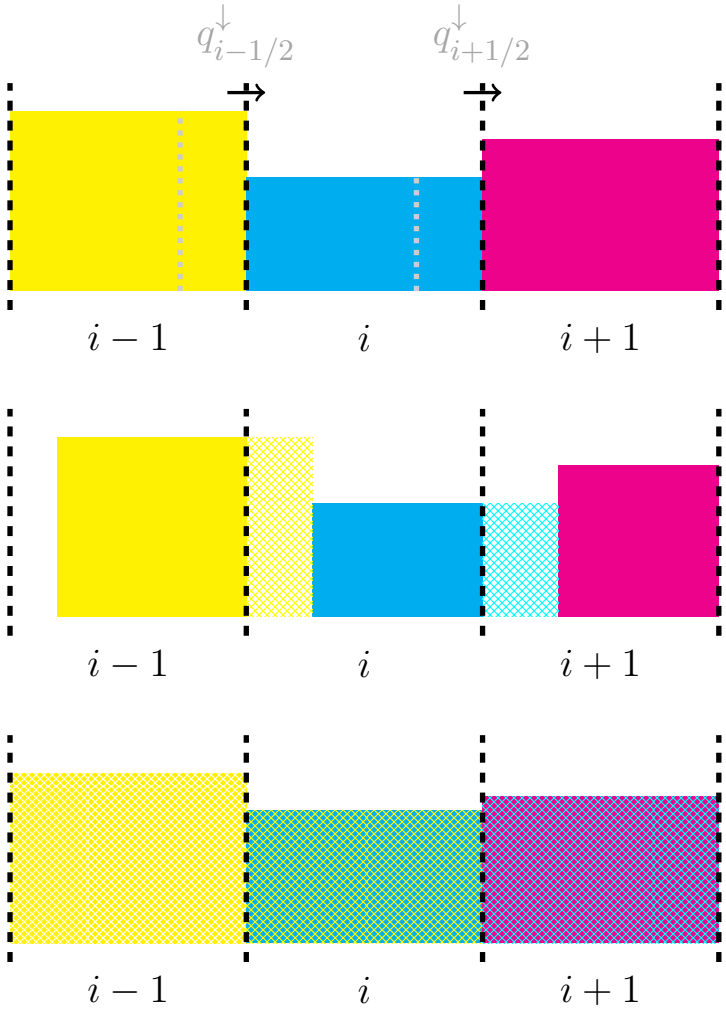

Figure 3.5: Physical representation of mass solute exchange for the novel solute transport technique with $q^{\downarrow}_{i-1/2}, q^{\downarrow}_{i+1/2} > 0$

boundary cells will require a special treatment when applying this technique. As the concept of numerical flux has been recovered in such way for the solute transport equation, it is necessary to define a numerical flux also at the outlet boundary wall in order to ensure the solute conservation. For that purpose, $q^{\downarrow} = (h\mathbf{un})_{BC}$ and $\phi^{\downarrow} = \phi_{BC}$ are defined at the boundary wall for the updating of the boundary cell BC (Figure 3.6).

As shown, the formulation in both 1D and 2D cases reduces to computing a numerical flux $q^{\downarrow}$ using the already computed averaged values at each edge for the hydrodynamic part. Apart from ensuring a perfect conservation and bounded non-oscillatory solutions [98], the simple discretization decreases substantially the num-

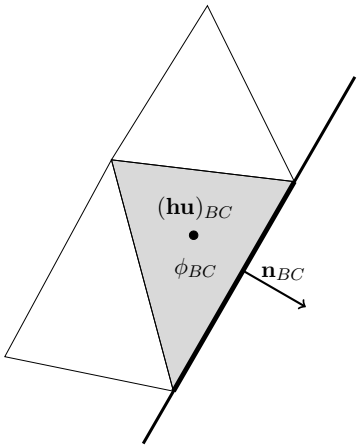

Figure 3.6: Numerical flux at the outlet boundary cell for the solute transport

ber of computations that would be necessary for the complete coupled system.

Chapter 4

Source terms, time step size and wet/dry treatment

The numerical treatment of source terms in the context of upwind schemes has been widely discussed in the literature during the last decade. Given a numerical scheme in a finite volume approach, the main focus has been put on elucidating how the source term discretization affects the numerical solution. In the particular case of a system of hyperbolic conservation laws, the preservation of the steady-state property such as still water equilibrium has been widely analysed when developing new techniques to discretize the source terms. An upwind discretization of the source terms has been generally adopted [122, 50]. However, these careful analysis developed for the preservation of steady states, may produce unsatisfactory results when dealing with unsteady scenarios, mainly related to the stability condition and the automatic computation of the time step size.

The numerical treatment of wet/dry fronts was considered a secondary issue before the development and the popularity of 2D models. However, when they emerged two decades ago, the tracking of a flooding advance over complex and irregular topographies was poorly captured. Furthermore, spurious oscillations and extreme velocities appeared frequently in the vicinity of wet/dry fronts leading to wrong and non-physical numerical results. Much efforts have been done mainly in the 2D framework in the last decade [6, 62, 64, 73] always based on the construction of well-balanced schemes able to preserve steady state of still water in the presence of irregular complex geometries. Other approaches related to semi-explicit high-resolution techniques [26] or high-order discontinuous-Galerkin methods [131] to ensure positivity preserving schemes have been explored in the context of well-balanced property.

Realistic configurations usually involve strong favourable and adverse slopes and high roughness that represent a challenge when trying to predict the evolution in space and time of a flooding event. In fact, wet/dry interfaces are considered as moving boundaries in the two dimensional depth-averaged shallow models and their resolution entails considerable difficulties: small water depths near dry cells can lead to numerical instabilities, non-physical high velocities or negative water depths.

The problem has been faced from different points of views: Liang et al. [75, 74] balanced the slope source terms by multiplying an average of water levels and a difference of bottom elevation on the faces. In [23, 37, 30, 99] a null velocity at the wet cell of the wet/dry front is considered, in order to compute the fluxes and source terms as usual. From the conservation property, Brufau et al. [13, 14] proposed a new intuitive way of locally redefining the bottom level difference across the corresponding interfaces to guarantee the equilibrium condition. A cell was considered as dry if its water depth was under 10^{-6} m.

This chapter emphasizes the idea of a correct bed slope and friction treatment from the study of the local Riemann Problem inside the augmented Roe's solver and applies these ideas to the correct strategy to handle wet/dry interfaces.

4.1 Source terms limitation

There are many situations such as transient flow over complex bed and/or friction surfaces in which the source terms play a leading role over the convective terms. In these scenarios, negative water depths in wet/dry or even in wet/wet problems and unrealistic non-physical solutions can appear due to the wrong estimation of the source amount, not only of the bed slope but also of the friction terms even when using the upwind discretization. The current tendency to avoid these unrealistic numerical solutions is reducing the time step size until the problems disappear. However, this approach could lead to decrease the time step size in many orders of magnitude hence rising the number of time steps done, and consequently the physical time needed to compute the solution. Therefore, a good philosophy could be to adopt a correct estimation of the source amount instead of reducing the time step size. This may help to reproduce accurately the expected numerical solution with a considerable saving in the computational time.

These non-physical situations were already detected by Murillo et al. [97] and Burguete et al. [17]. In the second one, the friction term discretization was analysed and a limitation in the time step size was added to the classical CFL condition in order to prevent producing a change of sign in the water velocity in cases of high relative roughness. In [97], the bed slope terms are mainly examined, using scalar equations with source terms as a first step. The reasoning is performed by evaluating a parameter that measures the relative influence of the source terms over the convective part. If the source terms dominates the flux, a limitation in time step is proposed according to the jump in the conserved variable.

Another possibility consists of inspecting the approximate augmented solutions presented in chapter 2, for the SWE [92, 93] and to transform the physical constraints such as the positivity of the water depth into mathematical requirements over the intermediate star states that are part of the average approximate solution. This procedure, which is essentially related to the basic stability condition in the homogeneous case, is adopted in this work.

Without loss of generality, the analysis is first presented for the 1D SWE over irregular geometries for the subcritial case. The reason is intrinsically related to the nature of the Godunov cell averaging method in supercritical flow, that avoids negative values in the water depth since the bed slope source term does not participate in the updating of the water depth [13]. The proposed fix will be only applied to wet/wet problems with inadequate estimation of source amount. Wet/dry fronts will be later examined. A second analysis will be carried out for the correction of the friction terms, which will be applied to all kind of flow regimes (subcritical and supercritical) and situations (wet/wet and wet/dry).

Following the derivation of the finite volume approach and Roe's linearization previously done, the upwind first order numerical method was expressed:

$$\mathbf{U}_i^{n+1} = \mathbf{U}_i^n - \frac{\Delta t}{\Delta x}\left[\left(\sum_m \tilde{\lambda}^+\tilde{\gamma}\tilde{\mathbf{e}}\right)_{i-1/2}^m + \left(\sum_m \tilde{\lambda}^-\tilde{\gamma}\tilde{\mathbf{e}}\right)_{i+1/2}^m\right]^n \tag{4.1}$$

for the updating of a single cell i from time t^n to time $t^{n+1} = t^n + \Delta t$ according to the contributions from left and right edges. It exists however another point of view based on Godunov's approach, which consists of cell-averaging the intermediate star quantities that appear in the Riemann Problem to obtain a new piecewise solution

in time t^{n+1}. It can be easily derived from (4.1) for a subcritical situation ($\tilde{\lambda}_1 < 0$, $\tilde{\lambda}_2 < 0$). In that case:

$$\mathbf{U}_i^{n+1} = \mathbf{U}_i^n - \frac{\Delta t}{\Delta x}\left[\left(\tilde{\lambda}_2^+ \tilde{\gamma}_2 \tilde{\mathbf{e}}\right)_{i-1/2} - \left(\tilde{\lambda}_1^- \tilde{\gamma}_1 \tilde{\mathbf{e}}\right)_{i+1/2}\right]^n \tag{4.2}$$

where $\mathbf{U} = (A, Q)^T$. From (2.61):

$$\begin{aligned} \mathbf{U}_i^* &= \mathbf{U}_i^n + (\tilde{\gamma}_1 \tilde{\mathbf{e}})_{i+1/2} \rightarrow (\tilde{\gamma}_1 \tilde{\mathbf{e}})_{i+1/2} = \mathbf{U}_i^* - \mathbf{U}_i^n \\ \mathbf{U}_i^{**} &= \mathbf{U}_i^n - (\tilde{\gamma}_2 \tilde{\mathbf{e}})_{i-1/2} \rightarrow (\tilde{\gamma}_2 \tilde{\mathbf{e}})_{i-1/2} = \mathbf{U}_i^n - \mathbf{U}_i^{**} \end{aligned} \tag{4.3}$$

and (4.2) becomes:

$$\mathbf{U}_i^{n+1} = \mathbf{U}_i^n - \frac{\Delta t}{\Delta x}\left[(\tilde{\lambda}_2)^+_{i-1/2}(\mathbf{U}_i^n - \mathbf{U}_i^{**}) - (\tilde{\lambda}_1)^-_{i+1/2}(\mathbf{U}_i^* - \mathbf{U}_i^n)\right] \tag{4.4}$$

The sketch of the updating (4.4) of cell i from left and right contributions is displayed in Figure 4.1. Finally, gathering correctly the terms:

$$\mathbf{U}_i^{n+1}\Delta x = \mathbf{U}_i^{**}(\widetilde{\lambda}^2_{i-1/2}\Delta t) + \mathbf{U}_i^n(\Delta x - \widetilde{\lambda}^2_{i-1/2}\Delta t + \widetilde{\lambda}^1_{i+1/2}\Delta t) + \mathbf{U}_i^*(-\widetilde{\lambda}^1_{i+1/2}\Delta t) \tag{4.5}$$

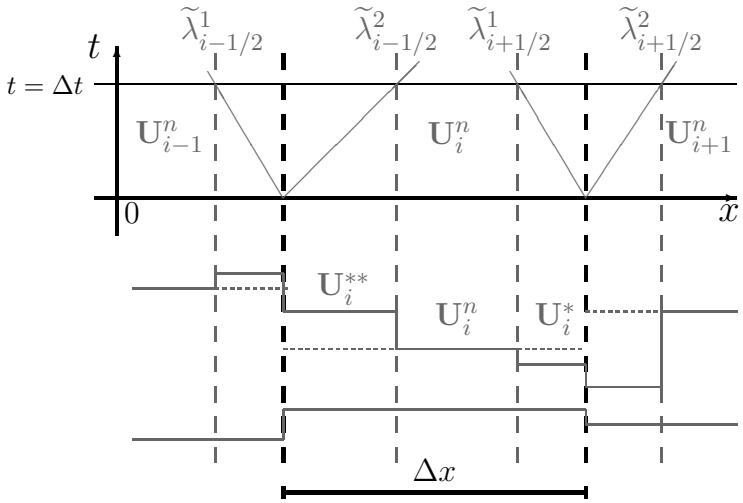

Figure 4.1: Control volume in the Godunov method

4.1.1 Bed slope limitation

Non-negative values of wetted area in the intermediate states A_i^{**} and A_i^* are sought in order to ensure a non-negative cell-averaged solution $\mathbf{U}_i^{n+1}$. With that goal, let consider the Riemann Problem at the edge $i+1/2$ and the approximate solution given in (2.60) and (2.61). For the sake of clarity, sub-indexes referred to average quantities (tilde variables) at edge $i+1/2$ are eliminated. Considering $\widetilde{e}_1^1 = 1$ and $\widetilde{\lambda}^1 < 0$, the positivity requirement over A_i^*:

$$A_i^* = A_i^n + (\widetilde{\gamma})_{i+1/2}^1 = A_i^n + \widetilde{\alpha}^1 - \left(\frac{\widetilde{\beta}}{\widetilde{\lambda}}\right)^1 \geq 0 \tag{4.6}$$

constrains the amount of source for $\widetilde{\beta}^1$

$$\widetilde{\beta}^1 \geq \left(A_i^n + \widetilde{\alpha}^1\right)\ \widetilde{\lambda}^1 = \widetilde{\beta}_{min}^1 \tag{4.7}$$

Remembering now that $\widetilde{e}_1^2 = 1$ and $\widetilde{\lambda}^2 > 0$, the derivation of the constraint for β_2 is straightforwardly achieved:

$$A_{i+1}^{**} = A_{i+1}^n - (\widetilde{\gamma})_{i+1/2}^2 = A_{i+1}^n - \widetilde{\alpha}^2 + \left(\frac{\widetilde{\beta}}{\widetilde{\lambda}}\right)^2 \geq 0 \rightarrow \widetilde{\beta}^2 \geq \left(-A_{i+1}^n + \widetilde{\alpha}^2\right)\ \widetilde{\lambda}^2 = \widetilde{\beta}_{min}^2 \tag{4.8}$$

Therefore:

- If $A_i^* < 0$ and $A_{i+1}^{**} > 0$, $\widetilde{\beta}^1$ is redefined using (4.7), not only ensuring conservation, i.e., $\widetilde{\beta}^2 = -\widetilde{\beta}^1$ but also a non-negative value A_{i+1}^{**}:

$$\widetilde{\beta}^1 = \begin{cases} \widetilde{\beta}_{min}^1 & \text{if} \quad -\widetilde{\beta}_{min}^1 \geq \widetilde{\beta}_{min}^2 \\ \widetilde{\beta}^1 & \text{otherwise} \end{cases}, \qquad \widetilde{\beta}^2 = -\widetilde{\beta}^1 \tag{4.9}$$

- If $A_i^* > 0$ and $A_{i+1}^{**} < 0$, $\widetilde{\beta}^2$ is redefined according to (4.8):

$$\widetilde{\beta}^2 = \begin{cases} \widetilde{\beta}_{min}^2 & \text{if} \quad -\widetilde{\beta}_{min}^2 \geq \widetilde{\beta}_{min}^1 \\ \widetilde{\beta}^2 & \text{otherwise} \end{cases}, \qquad \widetilde{\beta}^1 = -\widetilde{\beta}^2 \tag{4.10}$$

With this redistribution of the source terms, the appearances of negative water depths in wet/wet problems are eliminated. They are mainly related to the advancing of a slow flow over strong bed slope gradients. The cases where both $A_i^* < 0$ and $A_{i+1}^{**} < 0$ are not considered. Rare exceptions near the "vacuum state" or where there is a strong expansion may produce negative values hence the proposed solution consists of reducing the time step size.

4.1.2 Friction limitation

The other unrealistic solution that should be avoided is related to the infeasibility of the flow resistance (friction terms) to change the sign of the velocity within one time step. Firstly, as the source terms are due to bed slope and friction terms, we can split them into a sum of two components:

$$\beta^m = \beta_F^m + \beta_S^m \tag{4.11}$$

where β_S^m accounts for the bed slope terms and β_F^m includes the friction terms. When analizing the RP at interface $i+1/2$, as stated in [93], the intermediate stars states referred to the discharge are equal $Q_i^* = Q_{i+1}^{**}$ in both subcritical or supercritical situations and can be expressed:

$$Q_i^* = Q_i^n + (\widetilde{\gamma}\widetilde{e}_2)^1 = Q_i^n + \widetilde{\alpha}^1\widetilde{\lambda}^1 - \widetilde{\beta}^1 \tag{4.12}$$

According to (4.11), a new quantity can be defined, isolating the bed slope effects and disregarding the friction contributions:

$$Q_i^\nabla = Q_i^n + \widetilde{\alpha}^1\widetilde{\lambda}^1 - \widetilde{\beta}_S^1 \tag{4.13}$$

In case that $Q_i^\nabla Q_i^* < 0$ the effect of friction terms is overestimated to the extent that flow could move back, resulting in an impossible situation. Accordingly, the friction terms should be redefined as:

$$\widetilde{\beta}_F^1 = \begin{cases} Q_i^\nabla & \text{if} \quad Q_i^\nabla Q_i^* < 0 \\ \widetilde{\beta}_F^1 & \text{otherwise} \end{cases}, \qquad \widetilde{\beta}_F^2 = -\widetilde{\beta}_F^1 \tag{4.14}$$

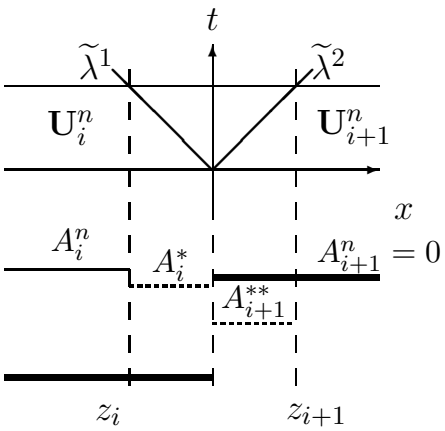

Figure 4.2: Sketch of the intermediate states in the (x,t) plane for the subcritical case. Wet/dry interfaces and negative value in the intermediate state A_{i+1}^{**}.

in order to ensure a non-negative value in Q_i^*. These cheap and simple corrections when discretizing the source terms allow to build robust solutions recovering the conventional CFL condition, avoiding large reductions in the time step size to ensure positivity solutions [93].

4.2 Wet/dry treatment

The advances suggested in [92] are applied in this work for the numerical treatment of wet/dry interfaces. Considering again the Riemann Problem at the interface $i+1/2$, let assume that i is the wet cell and $i+1$ is the dry cell (water depth under the machine accuracy). Negative water depth or wetted area values can appear in cell $i+1$ due to the Godunov's cell-averaging process. The direct responsible for this undesirable phenomenon is the intermediate value A_{i+1}^{**} as illustrated in Figure 4.2.

Considering that cell $i+2$ is also dry, the contributions from the right edge $i+3/2$ are null hence applying (4.5) over cell $i+1$, in the particular case of the wetted area, results:

$$\begin{aligned} A_{i+1}^{n+1}\Delta x &= A_{i+1}^{**}(\widetilde{\lambda}_{i+1/2}^2\Delta t) + A_{i+1}^n(\Delta x - \widetilde{\lambda}_{i+1/2}^2\Delta t + \widetilde{\lambda}_{i+3/2}^1\Delta t) + A_{i+1}^*(-\widetilde{\lambda}_{i+3/2}^1\Delta t) \\ &= A_{i+1}^{**}(\widetilde{\lambda}_{i+1/2}^2\Delta t) < 0 \end{aligned} \tag{4.15}$$

Regarding (4.15), the time step should be reduced to zero in order to achieve a non-negative value. As this option is considered as absurd, it is automatically left aside.

Therefore, the unique physical solution satisfying the positivity of the solution consists of considering the edge $i+1/2$ as a solid wall, i.e., the information should not cross this interface in the current time step. In order for the scheme to remain mass conservative, the information related to the mass that the numerical method foresees to be sent to the cell $i+1$ is reflected and necessarily sent to the cell i (see Figure 4.3). The contributions related to the momentum are disregarded. Additionally, null normal velocity to the edge is enforced to ensure conservation.

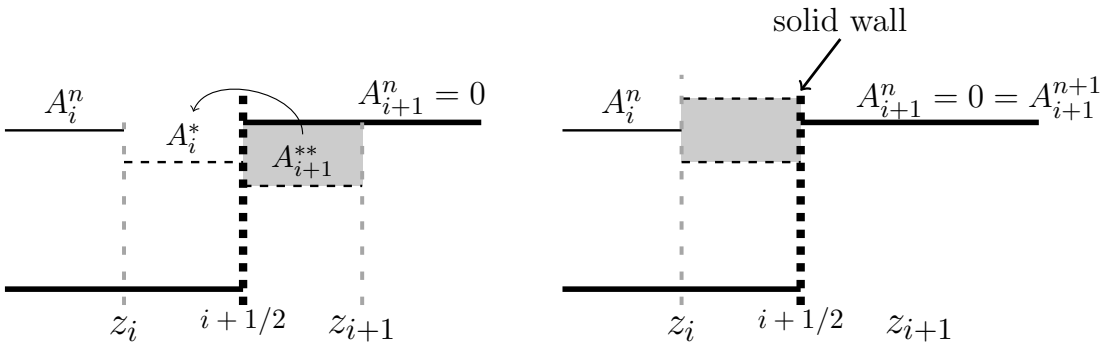

Figure 4.3: Wet/dry treatment

As an example, the expression for the updating of the cross section wetted area at cells i and $i+1$ (assuming that the cell $i+2$ is also dry) is addressed:

$$A_i^{n+1} = A_i^n - \frac{\Delta t}{\Delta x}\left[\left(\sum_m \tilde{\lambda}^+\tilde{\gamma}\tilde{\mathbf{e}}\right)^m_{i-1/2} + \left(\sum_m \tilde{\lambda}^-\tilde{\gamma}\tilde{\mathbf{e}}\right)^m_{i+1/2} + \left(\sum_m \tilde{\lambda}^+\tilde{\gamma}\tilde{e}_1\right)^m_{i+1/2}\right]^n$$

$$A_{i+1}^{n+1} = 0 \tag{4.16}$$

Although this technique seems 'a priori' to be sophisticated, it becomes nevertheless simple and clear when the algorithm goes over the computational walls or edges and decides to which cell the contributions should be sent. It can be summarized in the Algorithm 1.

Algorithm 1 Compute and send the fluxes

for $k = 0$ to $NWALLS$ **do**
  Compute the average tilde values at each wall: $\widetilde{\lambda}_k^m$, $\widetilde{\alpha}_k^m$, $\widetilde{\beta}_k^m$, $\widetilde{\mathbf{e}}_k^m$
  Friction terms redistribution according to (4.14)
  Bed slope wet/wet redistribution according to (4.9) and (4.10)
  Compute A_i^* and A_{i+1}^{**}

  if ($A_i^* < 0$ and $A_i^n = 0$) **then**
    Send mass contributions to cell i+1
  else
    if ($A_{i+1}^{**} < 0$ and $A_{i+1}^n = 0$) **then**
      Send mass contributions to cell i
    else
      Send mass/momentum contributions according to the sign of $\widetilde{\lambda}_k^m$ (upwind)
    end if
  end if
end for

As shown, the problem has been deeply studied in this work from a one dimensional point of view. However, it is feasible to extend all the reasoning and strategies specified above to the 2D framework. As stated before, the extension is achieved by projecting the local Riemann Problem to the normal direction given by the computational edge or wall and simply replacing in the previous analysis the edge $i + 1/2$, the cells i, $i + 1$, the wetted area A and the discharge Q by the edge k, the cells i, j, the water depth h and the unit discharge q respectively. This extension is extensively described in [92, 93].

Chapter 5

Pressure source term integration: formulation

The source terms included in the shallow water formulation (both in 1D and 2D versions) can be split into friction terms and pressure terms. Pressure terms are related to bed variations in the 2D model and to bed and width changes in the 1D model.

The differential shallow water equations are valid on the hypothesis of continuous and differentiable solution and they do not make sense for non-differentiable solutions or in the presence of discontinuities. However, practical and realistic scenarios such as channels with an important bed slope, rivers flowing in mountain valleys, profound excavations or sills describe situations in which the bed may be discontinuous and the water depth comparable with the bed step. Apart from that, the finite volume method represents in particular the topography into piecewise constant functions in each cell, a feature that enables the incessant appearance of these previously mentioned discontinuities. Therefore, a wrong discretization in the pressure terms for these cases could lead to wrong and non-physical solutions that could erroneously predict the flow conditions.

As described in the previous chapter, different limitations in the bed slope such as (4.9) and (4.10) and in the frictions terms (4.14) are required to prevent non-physical numerical solutions and to avoid undesirable reductions in the time step size. However, this strategy is actually independent of what is developed in this chapter: the correct integration of pressure terms in the context of discontinuous solutions and the adequate choice to model and discretize the physical phenomena that are taking place. For the sake of clarity, friction terms will be omitted.

The focus will be consequently put on the computation of the pressure integral

$$T = \int_S \left(\frac{p_b}{\rho_w} \right) dS \tag{5.1}$$

where S is the surface over which the pressure forces are not null. As an example, Figure 5.1 shows a sudden width variation in a rectangular channel (left) and in a trapezoidal channel (right) with a bed step.

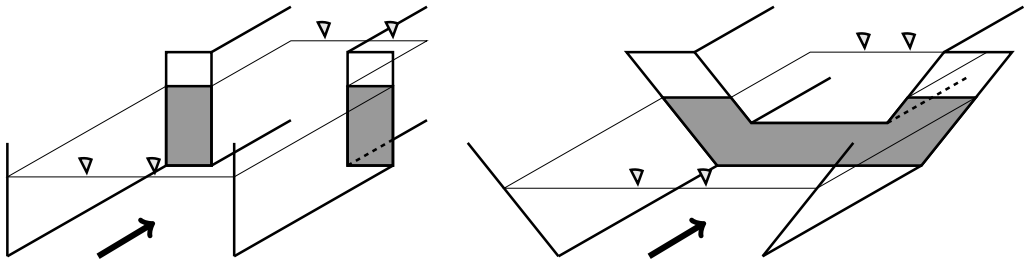

Figure 5.1: Sudden narrowing in a rectangular channel (left) and in a trapezoidal channel with an adverse bed step (right). The shadow surface represents the surface S over which the integral pressure is performed

This topic is not new and many papers can be found in the literature regarding different approaches of the Riemann Problem over a bed step. Firstly, it is mainly accepted that there exists a stationary wave positioned over the bed step which accounts for a jump discontinuity in the flow variables [111, 3, 48]. However, there is awareness that existence and uniqueness of solutions are not guaranteed and some assumptions must be done. The physical principles connecting the flow variables are controversial and two essential schools of thought can be distinguished: one based on mass and energy conservation over the bed step and the other based on mass and momentum conservation.

The former approach states that the energy conservation must be used as a closure when the slope becomes infinite, that is, in a bed step [3, 15]. However, as known, energy losses and dissipation exist from a physical point of view due to flow recirculating processes or in the presence of hydraulic jumps for instance, and momentum conservation equations should be recovered. On the other hand, mass an momentum point of view with a hydrostatic pressure distribution at the bed step is found in [8, 111, 92, 33]. A careful analysis is performed over an infinitesimal control volume including the step where the multiplicity of solutions is avoided by imposing a constraint over the energy across the step, which must be dissipated

according to these authors. Other works as [69] presented a detailed description of the Riemann Problem over a step, providing existence and uniqueness under certain energy assumptions.

It is notable that, apart from maintaining the well-balanced or C-property as stated in chapter 4, several numerical solvers are concerned about an adequate source term discretization in the presence of bed discontinuities. Stelling et al. [113] designed a numerical scheme able to switch between momentum conservation or energy head conservation depending on the flow conditions. In Murillo et al. [96], energy constant states are prioritized when possible so that the numerical integration of bed slope terms is combined with energy constraints to construct a robust energy balanced method.

In the present work, the derivation of the differential and integral discretizations for the bed slope source terms is presented from a control volume point of view. As the integral formulation of the shallow water equations, which allows to correctly resolve a bed or narrowing discontinuity, implies an assumption on the pressure which is not always valid for all situations, the expression will be formulated in a general way, leaving open the possibility of choosing one or another approach. Although all the previous works found in the literature only consider 1D rectangular constant width cases or 2D simple configurations, the analysis will be firstly performed over these geometries and subsequently extended to one dimensional cases over abrupt width variations and cumbersome cross sections bathymetry.

5.1 1D rectangular cross section

The 1D SWE can be expressed in a rectangular cross section configuration, assuming constant width along the rectangular channel and neglecting the friction losses:

$$\frac{\partial}{\partial t}\begin{pmatrix} h \\ hu \end{pmatrix} + \frac{\partial}{\partial x}\begin{pmatrix} hu \\ hu^2 + \frac{1}{2}gh^2 \end{pmatrix} = \begin{pmatrix} 0 \\ \frac{p_b}{\rho_w} \end{pmatrix} \tag{5.2}$$

where h represents the water depth, u the depth averaged component of the velocity vector, g is the acceleration of the gravity, p_b is the pressure source term along the bottom and ρ_w the density of water. According to (3.2) and (3.3), and assuming

$I_2 = 0$ (rectangular constant width channel), $\dfrac{p_b}{\rho_w} = -gh\dfrac{\partial z_b}{\partial x}$.

Let consider a control volume delimited by x_L and x_R as in Figure 5.2, where p_L and p_R are the resultants of the pressure distributions on sections left and right respectively and T illustrates the pressure force along the bed step.

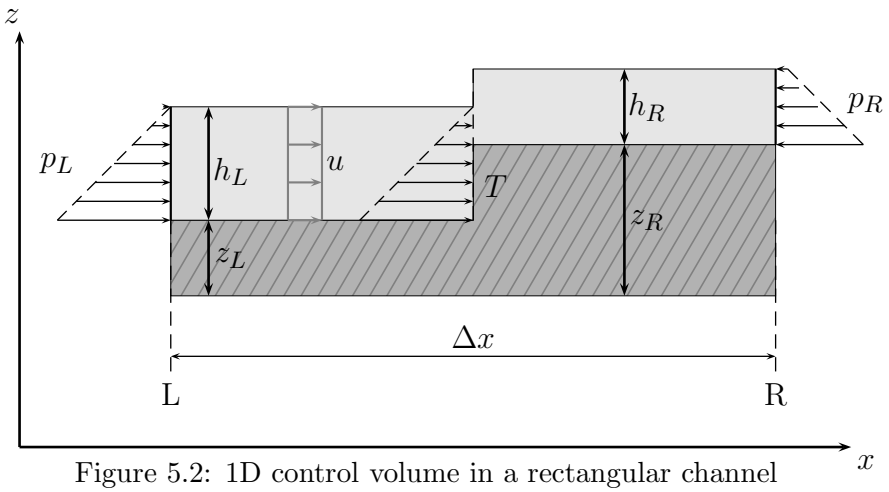

Figure 5.2: 1D control volume in a rectangular channel

As stated before, when dealing with abrupt or sudden variations, the integral formulation of the shallow water equations is required to be able to evaluate the behaviour of the solution. They are expressed as follows:

$$\begin{gathered}\int_{x_L}^{x_R}\left(h(x,t^{n+1})-h(x,t^n)\right)dx+\int_{t^n}^{t^{n+1}}\left(hu(x_R,t)-hu(x_L,t)\right)dt=0\\ \int_{x_L}^{x_R}\left(hu(x,t^{n+1})-hu(x,t^n)\right)dx+\\ +\int_{t^n}^{t^{n+1}}\left(\left(hu^2+\frac{1}{2}gh^2\right)_{x_R,t}-\left(hu^2+\frac{1}{2}gh^2\right)_{x_L,t}\right)dt=\int_{t^n}^{t^{n+1}}\underbrace{\int_S\left(\frac{p_b}{\rho_w}\right)dS}_{T}\end{gathered} \tag{5.3}$$

where S represents the bed step surface. As a matter of fact, these equations represent the formulation of the mass and momentum conservation over the control volume of fluid illustrated in Figure 5.2. In order to examine them, it is possible to choose a system of reference that moves with the speed of the discontinuity located between x_L and x_R in t^n. With this assumption, the time derivatives of the integral

terms in (5.3) become null and the Rankine-Hugoniot conditions are derived:

$$\begin{aligned} [hu]_{x_L}^{x_R} &= 0 \\ \left[\left(hu^2 + \frac{1}{2}gh^2\right)\right]_{x_L}^{x_R} &= \int_{z_L}^{z_R} \left(\frac{p_b}{\rho_w}\right) dz \end{aligned} \tag{5.4}$$

where the brackets $[\cdot]$ represent the jump discontinuity and z_L, z_R indicate the elevations to the left and right sides (respectively) of the bottom discontinuity. The integral of the bottom pressure is a question of interest [92].

5.1.1 Differential formulation

The first approach can be derived from the differential expression (3.2) and (3.3). It is based on the assumption that the variations in the existing variables are smooth inside the control volume and the pressure is hydrostatic. The pressure integral related to the bottom change can be easily approximated as:

$$\int_{z_L}^{z_R} \frac{p_b}{\rho_w} = -gh\frac{\partial z_b}{\partial x} \tag{5.5}$$

and the discretization results consequently a straightforward estimation

$$\int_{z_L}^{z_R} \frac{p_b}{\rho_w} = -gh\frac{\partial z_b}{\partial x} \approx T_{diff} = -g\widetilde{h}\frac{\delta z}{\Delta x} \tag{5.6}$$

where $\widetilde{h} = \dfrac{h_L + h_R}{2}$ and $\delta z = z_R - z_L$. This formulation, which will be referred with the sub-index $diff$, is the most exploited in the literature although it may produce inaccurate results in the presence of big discontinuities [92].

5.1.2 Integral formulation

The second approach or integral formulation consists of performing an accurate evaluation of the pressure integral of (5.4), assuming discontinuities not only in the water level surface but also in the bed level. In the same way, an assumption of the pressure distribution has to be done. The lack of experimental studies related to this

topic prevents a reliable choice of the pressure distribution based on experimental data. Nonetheless, a hydrostatic assumption is adopted in this work, keeping in mind that this hypothesis may be valid for a wide range of situations but not for all [111]. Therefore, the pressure integral (5.4) is approximated by:

$$\int_{z_L}^{z_R} \frac{p_b}{\rho_w} = -g \int_0^{z^\star} (h^\star - \eta) d\eta \tag{5.7}$$

where $z^\star$ and $h^\star$ have to be determined. Different flow situations can be considered depending on the sign of the bed discontinuity, that is, and upward or a downward step and the water depths or levels on both sides.

Two particular situations can be singled out in which the height of the bed step is greater than or equal to the level in contact to the step. These cases are illustrated in Figures 5.3 and 5.4 for adverse and favourable bed step respectively. The left state is coloured in blue while the right state is in red. The yellow surface with a filled line pattern shows the surface on the step over which the integral is performed.

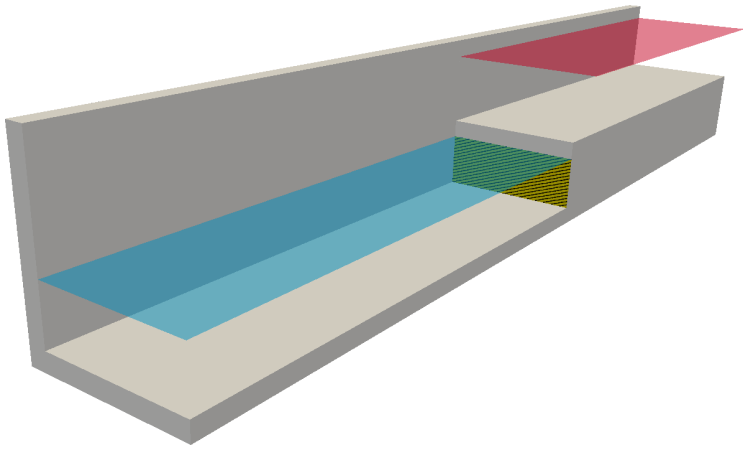

Figure 5.3: Adverse bed step ($\delta z \geq 0$) in a rectangular channel with $d_L < z_R$

It is possible to formulate what is illustrated in the mentioned figures:

- If $\delta z \geq 0$ and $d_L < z_R$ then $z^\star = h_L$ and $h^\star = h_L$ and

$$T_{int} = -g \int_0^{h_L} (h_L - \eta) d\eta \tag{5.8}$$

- If $\delta z \leq 0$ and $d_R < z_L$ then $z^\star = h_R$ and $h^\star = h_R$ and

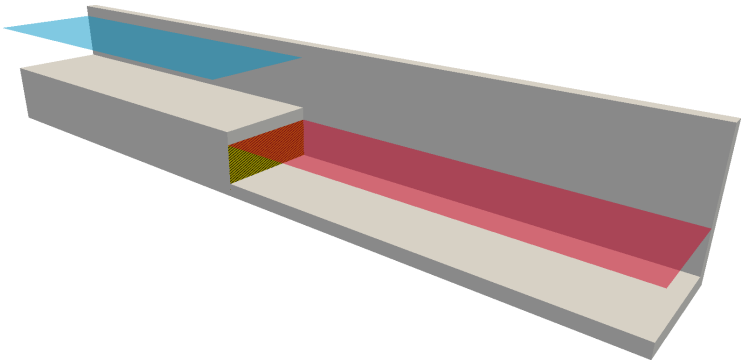

Figure 5.4: Favourable bed step ($\delta z \leq 0$) in a rectangular channel with $d_R < z_L$

$$T_{int} = -g \int_0^{h_R} (h_R - \eta) d\eta \tag{5.9}$$

where $d = h + z$ is the level surface.

When the level of the side in contact to the step is greater than the step height, the surface over which the pressure force is exerted will be related to the height of the step as illustrated in Figures 5.5 and 5.6 (yellow surface with line pattern), that is, $z^\star = \delta z$.

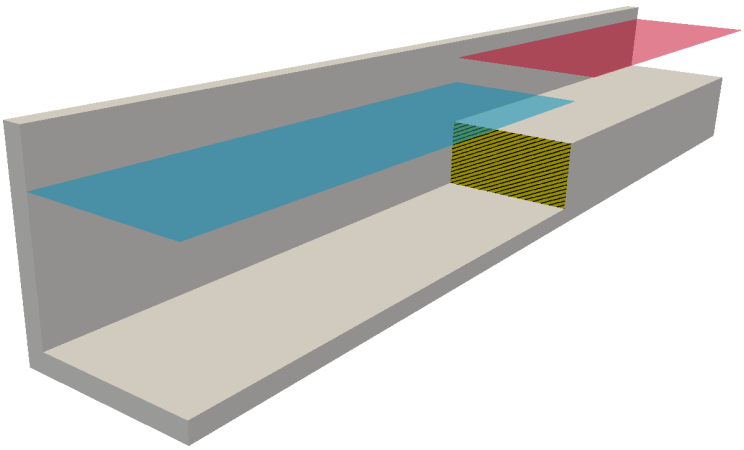

Figure 5.5: Adverse bed step ($\delta z \geq 0$) in a rectangular channel with $d_L \geq z_R$

However, the difficulty resides in the estimation of $h^\star$. In [92, 96, 93, 111], $h^\star$ is chosen according to the sign of the bed step discontinuity:

$$h^\star = \begin{cases} h_L & \text{if } \delta z \geq 0 \\ h_R & \text{if } \delta z < 0 \end{cases} \tag{5.10}$$

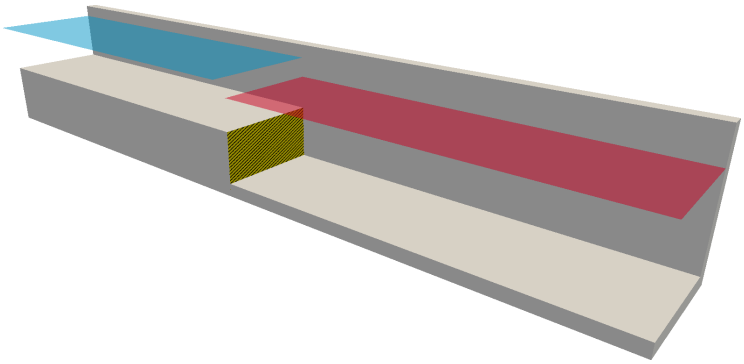

Figure 5.6: Favourable bed step ($\delta z \leq 0$) in a rectangular channel with $d_R \geq z_L$

while in [113], $h^\star$ is assumed as a linear combination of the right and left states:

$$h^\star = \gamma h_L + (1-\gamma) h_R \tag{5.11}$$

with $0 \leq \gamma \leq 1$.

In the present work, the choice of $h^\star$ will be open for these situations. Mathematically, the limit when x_L approaches x_R leads to an indeterminate form in the pressure integral of (5.4). Furthermore, although the hypothesis that considers the lower side of the step as the direct responsible for the pressure force is reasonably consistent [92], there is no experimental evidence of this exactly because of this a moderate position has been adopted in this dissertation.

All the possible situations can be condensed in the following formula, which refer to the integral formulation of the source term in the presence of a bed step in a rectangular channel with constant width (sub-index *int*):

$$T_{int} = -g \int_0^{z^\star} (h^\star - \eta) d\eta = -g z^\star (h^\star - \frac{z^\star}{2}) \tag{5.12}$$

where

$$h^\star = \begin{cases} h_L & \text{if } \delta z \geq 0 \text{ and } d_L < z_R \\ h_R & \text{if } \delta z < 0 \text{ and } d_R < z_L \\ f(h_L, h_R, \delta z) & \text{otherwise} \end{cases} \qquad z^\star = \begin{cases} h_L & \text{if } \delta z \geq 0 \text{ and } d_L < z_R \\ h_R & \text{if } \delta z < 0 \text{ and } d_R < z_L \\ \delta z & \text{otherwise} \end{cases} \tag{5.13}$$

5.2 1D irregular cross section

Let consider the 1D shallow water equations omitting the influence of friction source terms:

$$\frac{\partial}{\partial t}\begin{pmatrix} A \\ Q \end{pmatrix} + \frac{\partial}{\partial x}\begin{pmatrix} Q \\ \dfrac{Q^2}{A} + gI_1 \end{pmatrix} = \begin{pmatrix} 0 \\ gI_2 + gAS_0 \end{pmatrix} \tag{5.14}$$

and a control volume similar to that considered for the rectangular cross section case, bounded by x_L and x_R. Integral relationships can be established for system (5.14) for the propagation of a discontinuity initially located between x_L and x_R:

$$\begin{gathered} \int_{x_L}^{x_R} \left(A(x,t^{n+1}) - A(x,t^n)\right) dx + \int_{t^n}^{t^{n+1}} \left(Q(x_R,t) - Q(x_L,t)\right) dt = 0 \\ \int_{x_L}^{x_R} \left(Q(x,t^{n+1}) - Q(x,t^n)\right) dx + \\ + \int_{t^n}^{t^{n+1}} \left(\left(\frac{Q^2}{A} + gI_1\right)_{x_R,t} - \left(\frac{Q^2}{A} + gI_1\right)_{x_L,t} \right) dt = \int_{t^n}^{t^{n+1}} \underbrace{\int_S \left(\frac{p_b}{\rho_w}\right) dS}_{T} \end{gathered} \tag{5.15}$$

where T condenses the terms $gI_2 + gAS_0$ into a pressure integral over the bottom surface S . Analogously, the Rankine-Hugoniot conditions are expressed:

$$\begin{gathered} [Q]_{x_L}^{x_R} = 0 \\ \left[\left(\frac{Q^2}{A} + gI_1\right)\right]_{x_L}^{x_R} = \int_S \left(\frac{p_b}{\rho_w}\right) dS \end{gathered} \tag{5.16}$$

From the original conservative differential formulation, as described in (3.14), it is feasible to obtain the non-conservative formulation

$$\frac{\partial \mathbf{U}(x,t)}{\partial t} + \mathbf{J}(x,\mathbf{U})\frac{\partial \mathbf{U}(x,t)}{\partial x} = \mathbf{H}'(x,\mathbf{U}) \tag{5.17}$$

where

$$\mathbf{H}'(x,\mathbf{U}) = \mathbf{H}(x,\mathbf{U}) - \left.\frac{\partial \mathbf{F}(x,\mathbf{U})}{\partial x}\right|_{\mathbf{U}=const} = gI_2 + gAS_0 - g\left.\frac{\partial I_1}{\partial x}\right|_{\mathbf{U}=const} \tag{5.18}$$

5.2.1 Differential formulation

The differential formulation assumes smooth variations in the conserved variables as well as in the bottom surface. It is worth remarking that only under this hypothesis, the Leibnitz rule [35] is used in (3.18). As the discrete increments approach actually the total derivatives instead of the partial derivatives, all terms have to be carefully expressed in total derivatives (as stated in [16, 19, 86]) as in (3.19) to arrive to this expression:

$$\mathbf{H}'(x,\mathbf{U}) = \begin{pmatrix} 0 \\ gA\left(-\dfrac{dz_b}{dx} - \dfrac{dh}{dx} + \dfrac{1}{B}\dfrac{dA}{dx}\right) \end{pmatrix} \tag{5.19}$$

where the partial and total x-derivatives applied over the conserved variables are equivalent. It is important to remark the appearance of the term $\dfrac{1}{B}\dfrac{dA}{dx}$, ignored in the majority of the 1D shallow water models.

The differential way of discretizing (5.19) is carried out by approximating the derivatives as discrete increments and the values at each interface as the average of the states right and left. Consequently,

$$T_{diff} = g\widetilde{A}\left(-\frac{\delta z}{\delta x} - \frac{\delta h}{\delta x} + \frac{1}{\widetilde{B}}\frac{\delta A}{\delta x}\right) \tag{5.20}$$

where $\widetilde{A} = \dfrac{1}{2}(A_L + A_R)$, $\delta z_b = z_R - z_L$, $\delta h = h_R - h_L$, $\widetilde{B} = \dfrac{1}{2}(B_L + B_R)$ and $\delta A = A_R - A_L$.

Although the assumption of smooth variations does not apply in every case, the differential formulation is the most used for the 1D shallow water equations over irregular geometries.

5.2.2 Integral formulation

The assumptions lying beneath the differential formulation are not always valid and must be re-analysed. In particular, over irregular geometries and/or abrupt variations in the river bed bathymetry, the hypotheses related to gradually varied functions and variables is wrong and another approach has to be considered.

As in the previous analysis for the rectangular cross section channel, an assumption for the pressure distribution has be to be adopted. Although it is well known that a hydrostatic pressure distribution does not cover all possible flow conditions, it is able to approximate correctly a wide range of situations. Therefore, assuming a hydrostatic pressure distribution, it is possible to express T in (5.15) as:

$$T = \underbrace{\int_0^{z^\star} (h^\star - \eta)\ \sigma^\star(\eta)\ d\eta}_{T_b} + \underbrace{\int_{z_1^{\star\star}}^{z_2^{\star\star}} (h^{\star\star} - \eta)(\sigma_R(\eta) - \sigma_L(\eta))\ d\eta}_{T_w} \tag{5.21}$$

where σ is the width.

T_b accounts for pressure term related to the bottom and seems to be very similar to that analysed for the rectangular case. As in the previous simplified case, the choice of $z^\star$ will be given by the sign and the relative height of the bed step with respect to the water depth on both sides of the discontinuity. The choice of $\sigma^\star$ will be correspondingly determined by the sign of the bed step, that is, the width of the side which is in contact to the surface. Furthermore, $h^\star$ will be open as in the rectangular case, following the same argument. Therefore T_b is compactly written:

$$T_b = \int_0^{z^\star} (h^\star - \eta)\ \sigma^\star(\eta)\ d\eta \tag{5.22}$$

where

$$h^\star = \begin{cases} h_L & \text{if } \delta z \geq 0 \text{ and } d_L < z_R \\ h_R & \text{if } \delta z < 0 \text{ and } d_R < z_L \\ f(h_L, h_R, \delta z) & \text{otherwise} \end{cases} \qquad \sigma^\star = \begin{cases} \sigma_L & \text{if } \delta z \geq 0 \\ \sigma_R & \text{if } \delta z < 0 \end{cases}$$

$$z^\star = \begin{cases} h_L & \text{if } \delta z \geq 0 \text{ and } d_L < z_R \\ h_R & \text{if } \delta z < 0 \text{ and } d_R < z_L \\ \delta z & \text{otherwise} \end{cases} \tag{5.23}$$

On the other hand, T_w is the pressure term due to the width variation on both sides of the discontinuity and is not null in the presence of an abrupt contraction or enlargement of a channel or river. Figure 5.7 shows an adverse step followed by a narrowing in a trapezoidal channel (left) and a triangular channel (right). The surface in yellow with black diagonal lines illustrates the surface over which the integral pressure is performed.

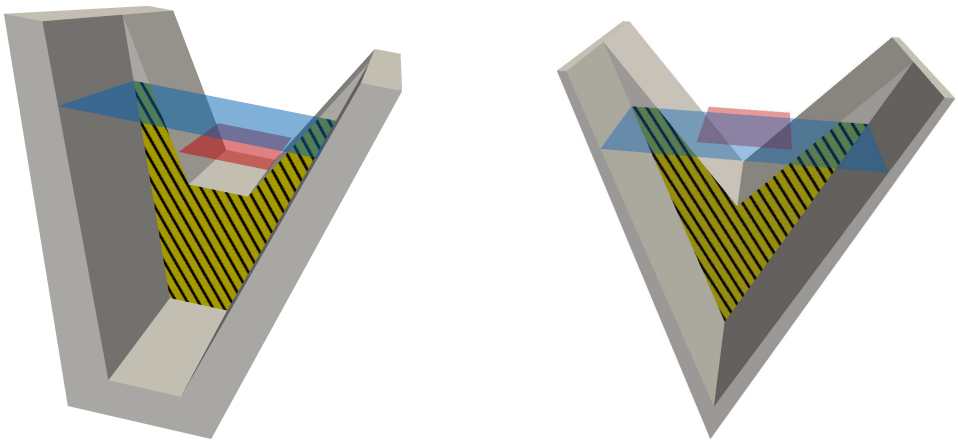

Figure 5.7: Adverse step and narrowing in a trapezoidal channel (left) and a triangular channel (right)

The computation of T_w requires to know not only the limits $z_1^{\star\star}$ and $z_2^{\star\star}$ but also the value of $h^{\star\star}$. The value of $h^{\star\star}$ will be open in this work as we are not able to exactly determine it when dealing with a discontinuity in the free surface. However, the limits of the integral can be characterized depending not only on the bed step but also on the width variation signs.

Four possibilities arise, which are going to be illustrated by means of a rectangu-

lar channel (for simplicity) with a positive/negative bed step and a sudden narrow/enlargement. As in the previous figures, the left states are plotted in blue and the right states are coloured in red. Furthermore, the yellow surfaces filled with a pattern will refer to the surface over which each pressure term is integrated: T_b in black squares and T_w in straight lines.

1. Case 1: $\delta z \geq 0$ and $\delta\sigma \leq 0$. An adverse step combined with a sudden narrowing.

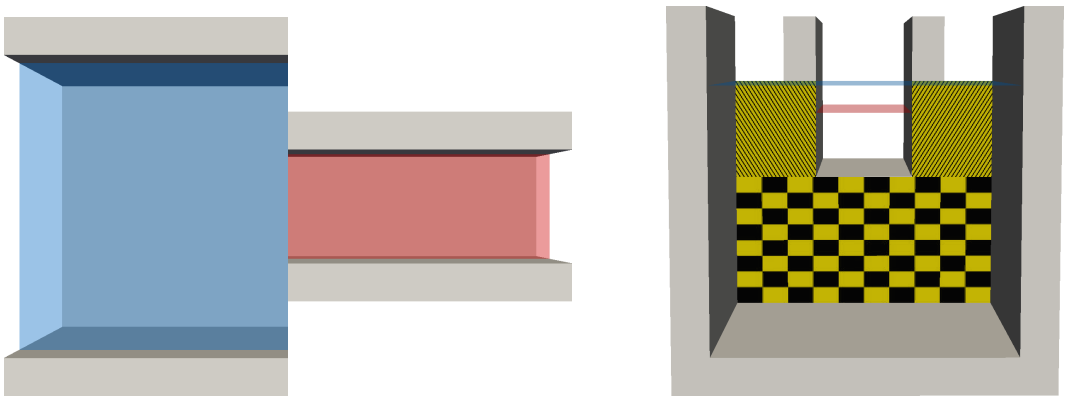

Figure 5.8: Plant view (left) and front view (right) of case 1: $\delta z \geq 0$ and $\delta\sigma \leq 0$

In this case $z_1^{\star\star} = \delta z$ and $z_2^{\star\star} = h_L$.

2. Case 2: $\delta z \geq 0$ and $\delta\sigma \geq 0$. An adverse step combined with a sudden enlargement.

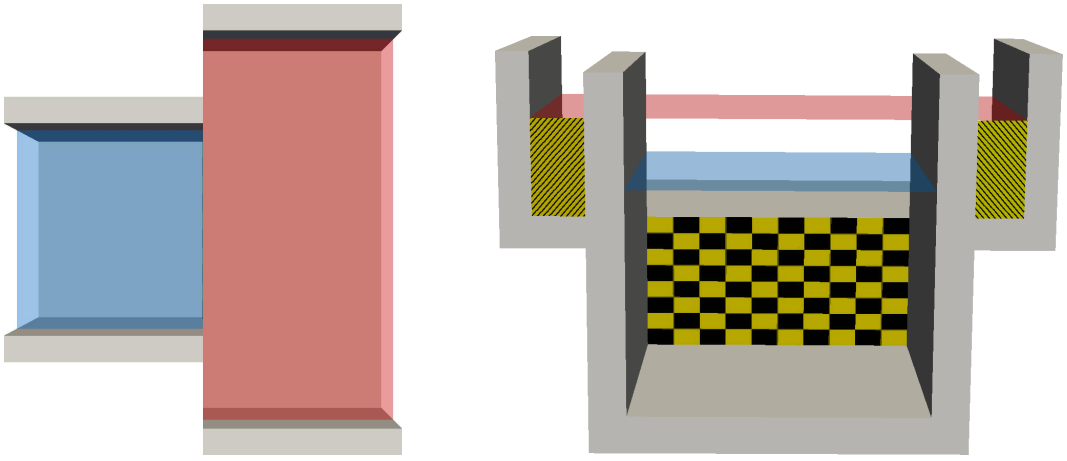

Figure 5.9: Plant view (left) and front view (right) of case 2: $\delta z \geq 0$ and $\delta\sigma \geq 0$

In this case $z_1^{\star\star} = 0$ and $z_2^{\star\star} = h_R$.

3. Case 3: $\delta z \leq 0$ and $\delta\sigma \leq 0$. A favourable step combined with a sudden narrowing.

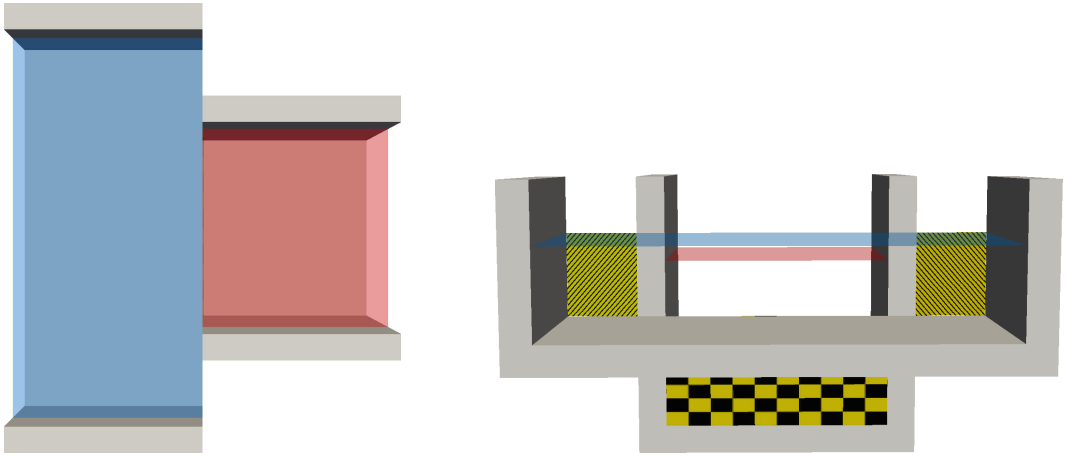

Figure 5.10: Plant view (left) and front view (right) of case 3: $\delta z \leq 0$ and $\delta\sigma \leq 0$

In this case $z_1^{\star\star} = 0$ and $z_2^{\star\star} = h_L$.

4. Case 4: $\delta z \leq 0$ and $\delta\sigma \geq 0$. A favourable step combined with a sudden enlargement.

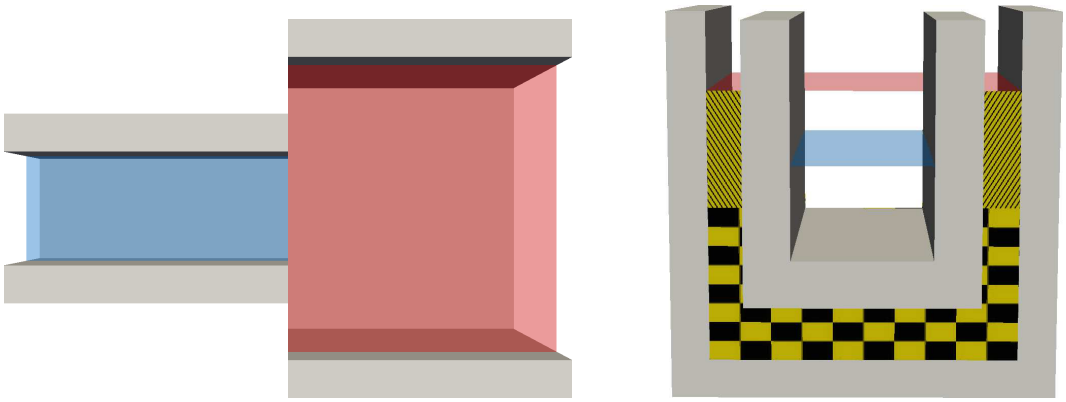

Figure 5.11: Plant view (left) and front view (right) of case 4: $\delta z \leq 0$ and $\delta\sigma \geq 0$

In this case $z_1^{\star\star} = \delta z$ and $z_2^{\star\star} = h_R$.

As stated before, the value of $h^{\star\star}$ remains open in this work. However, it can be chosen according to the bed step sign, that is, from the side which is in contact to the

bed step or simply averaging the left and right free surface levels of the discontinuity.

This analysis is extended in a general way for irregular geometries and the formulation of the pressure width term is compactly expressed as follows:

$$T_w = \int_{z_1^{\star\star}}^{z_2^{\star\star}} (h^{\star\star} - \eta)(\sigma_R(\eta) - \sigma_L(\eta))\ d\eta \tag{5.24}$$

where

$$h^{\star\star} = f(h_L, h_R, \delta z) \quad z_1^{\star\star} = \begin{cases} 0 & \text{if } \delta z \delta\sigma \geq 0 \\ \delta z & \text{if } \delta z \delta\sigma < 0 \end{cases} \quad z_2^{\star\star} = \begin{cases} h_R & \text{if } \delta\sigma \geq 0 \\ h_L & \text{if } \delta\sigma < 0 \end{cases} \tag{5.25}$$

5.2.2.1 Numerical approach: hydraulic table

In a general case involving irregular cross sections, the numerical approximation of T requires the computation of the various integrals of the form

$$I = \int_{a_1}^{a_2} (a_3 - \eta)\sigma(\eta)\ d\eta \tag{5.26}$$

which can be an arduous task in irregular topographies. Hydraulic tables will be helpful for this issue.

The numerical resolution of the 1D SWE far from academic configurations, i.e., in realistic test cases (rivers) with complex cross sections, requires the use of hydraulic relations between the variables that participate in the computation. In order to achieve a bijective association between them, the procedure consist of constructing one hydraulic table for each section. Therefore, given a cross section defined by N points (see Figure 5.12), and once the elevation points are reordered from the lowest z_0 to the highest z_N, the goal is to fill a table composed by N rows and six columns with the following information:

$$z_k \quad h_k \quad \sigma_k \quad dBz_k \quad A_k \quad W_k \tag{5.27}$$

where z_k is the level, h_k is the water depth, σ_k is the width, dBz_k is the side slopes, A_k is the wetted area and W_k represents the following integral

$$W(z) = \int_0^{z_k} \eta\sigma(\eta)d\eta \tag{5.28}$$

which will be useful to compute the pressure integral (5.26).

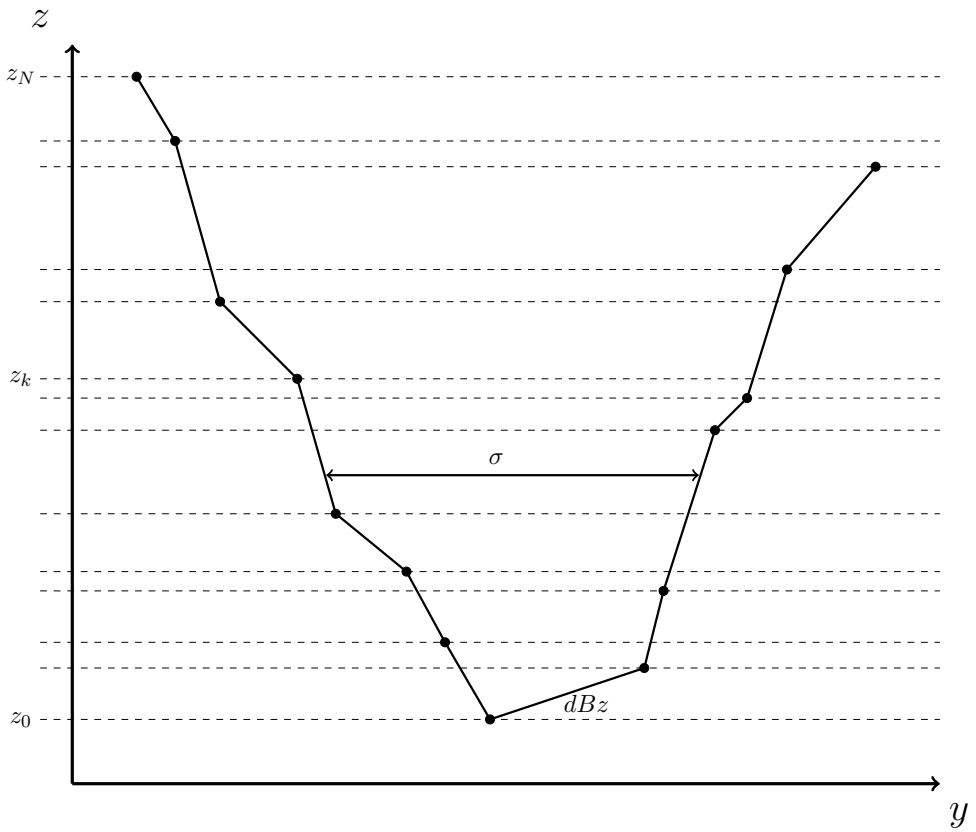

Figure 5.12: 1D cross section. Construction of the hydraulic table

With the following relation

$$\sigma_{k+1} = \sigma_k + dBz_k(z_{k+1} - z_k) \tag{5.29}$$

it is possible to obtain the consequent expressions for A and W:

$$A_{k+1} = A_k + \int_{z_k}^{z_{k+1}} \sigma(\eta) = \int_{z_k}^{z_{k+1}} [\sigma_k + dBz_k(\eta - z_k)]\, d\eta = A_k + \sigma_k\eta + \frac{1}{2}dBz_k(\eta - z_k)^2)\Big|_{z_k}^{z_{k+1}} = A_k + \sigma_k(z_{k+1} - z_k) + \frac{1}{2}dBz_k(z_{k+1} - z_k)^2 \tag{5.30}$$

$$W_{k+1} = W_k + \int_{z_k}^{z_{k+1}} \eta\ \sigma(\eta) d\eta = W_k + \int_{z_k}^{z_{k+1}} \left[\eta(\sigma_k - dBz_k z_k) + \eta^2 dBz_k)\right] d\eta =$$
$$W_k + \frac{1}{2}(\sigma_k - dBz_k z_k)(z_{k+1}^2 - z_k^2) + \frac{1}{3}(z_{k+1}^3 - z_k^3) dBz_k =$$
$$W_k + \left[\frac{1}{2}\sigma_k(z_{k+1} + z_k) + \frac{1}{6}(2z_{k+1}^2 - z_{k+1}z_k - z_k^2) dBz_k\right](z_{k+1} - z_k) \tag{5.31}$$

In the knowledge that $h_k = z_k - z_0$ and

$$h_0 = A_0 = \sigma_0 = 0 \tag{5.32}$$

the hydraulic table can be easily constructed using the geometric information that allows to calculate dBz. As a consequence of this, the computation of the integral I in (5.26) becomes a systematic procedure.

As mentioned above, the discretization of the pressure integral $T = T_b + T_w$ will actually approach the terms $gI_2 + gAS_0$ related to the change in width and bottom respectively. However, from the non-conservative formulation in (5.18), $g\dfrac{\partial I_1}{\partial x}\Big|_{A=const}$ must be discretized and evaluated correctly. Being a partial derivative, the strategy consist of converting this quantity into total derivative by means of:

$$\frac{dI_1}{dx} = \frac{\partial I_1}{\partial x}\Big|_{A=const} + \frac{\partial I_1}{\partial A}\frac{\partial A}{\partial x} = \frac{\partial I_1}{\partial x}\Big|_{A=const} + \frac{A}{B}\frac{\partial A}{\partial x} \tag{5.33}$$

where B is the top width of the free surface. Providing the partial derivatives applied over the conserved variables are equivalent to the total derivatives, the following expression can be written for the discretization of the term $g\dfrac{\partial I_1}{\partial x}\Big|_{A=const}$:

$$\frac{\partial I_1}{\partial x}\Big|_{A=const} \approx \frac{1}{\Delta x}\left(\delta I_1 - \frac{\widetilde{A}}{\widetilde{B}}\delta A\right) \tag{5.34}$$

where $\delta I_1 = (I_1)_R - (I_1)_L$, $\delta A = A_R - A_L$, $\widetilde{A} = \dfrac{1}{2}(A_R + A_L)$ and $\widetilde{B} = \dfrac{1}{2}(B_R + B_L)$.

Chapter 6

Pressure source term integration: Test cases

The behaviour of the numerical solution using the differential and integral formulations is tested through different test cases in this chapter. Many of them have analytical solutions, nevertheless there are other whose exact or analytical solutions depend on assuming certain hypothesis of the energy over bed steps that are not analysed in this work. Furthermore, the integral formulation requires the choice of the free parameters in several situations. For the sake of simplicity, an average between left and right states is considered.

Different configurations are firstly investigated to corroborate the well-balanced property in the case of still water with a complex topography or width variations. They have exact solution which is the initial condition and their description is summarized in Table 6.1. All of them represent a channel 100 m long, with closed boundaries at $x = 0\ m$ and at $x = 100\ m$ and with a null Manning coefficient. The simulations are performed with a spatial discretization of $\Delta x = 1\ m$ until $t = 100\ s$.

Test Case	Cross Section	Discontinuity	Description
1	Rectangular	x=50 m	Adverse Bed step
2	Rectangular	x=50 m	Narrowing
3	Trapezoidal	x=35 m	Favourable Bed step
		x=70 m	Enlargement
4	Trapezoidal	x=50 m	Adverse Bed step + Enlargement
5	Irregular	x=50 m	Sudden change in section

Table 6.1: Test cases 1-5: still water under sudden bed and width variations

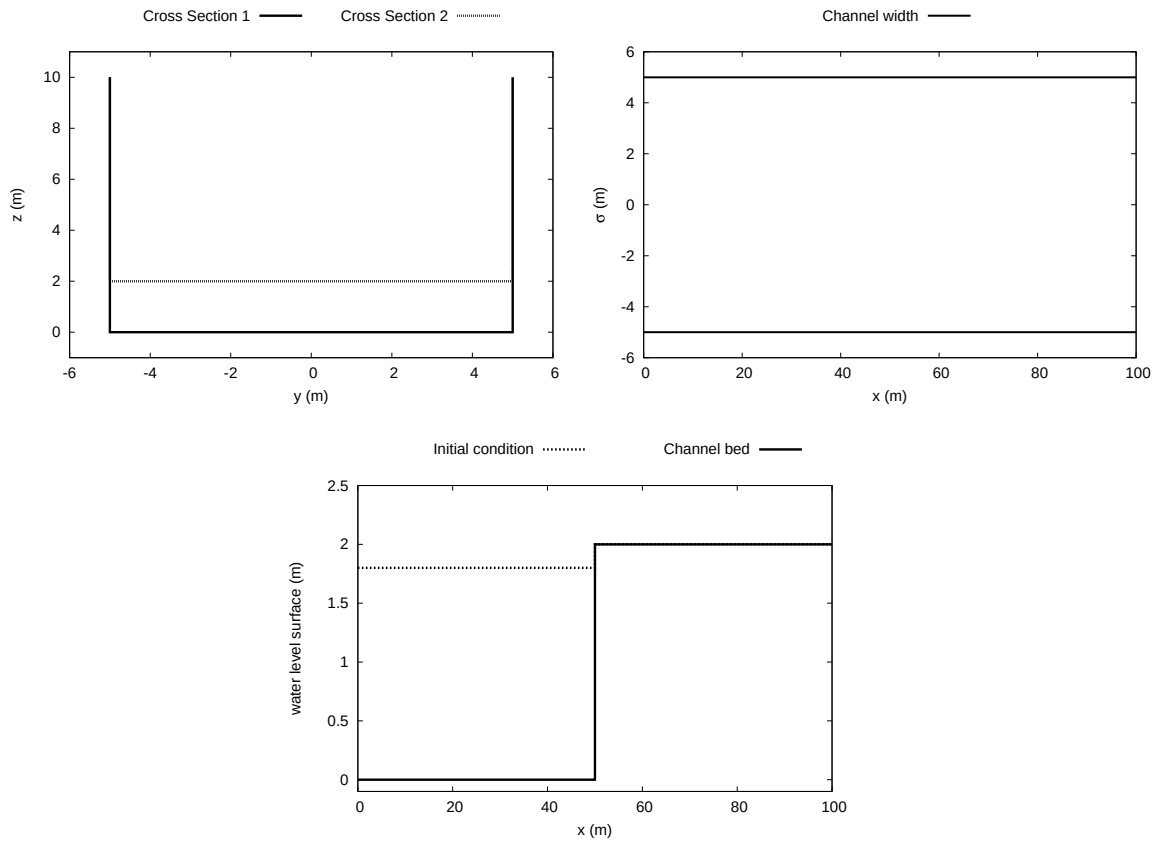

Figure 6.1: Test case 1: Cross sections (upper left), longitudinal profile of the width (upper right) and initial condition and bed level (lower middle)

Test case 1 consists of a rectangular channel with a constant width of $10m$ and a bed step of 2 m located at $x = 50$ m (see Figure 6.1).

$$z(x) = \begin{cases} 0 & \text{if } x < 50 \ m \\ 2 & \text{if } x \geq 50 \ m \end{cases} \tag{6.1}$$

The initial condition is still water with a discontinuity in the water level surface $d = h + z$ defined as:

$$d(x, 0) = \begin{cases} 1.8 & \text{if } x < 50 \ m \\ 0 & \text{if } x \geq 50 \ m \end{cases} \tag{6.2}$$

The final state at $t = 100$ s is plotted in Figure 6.2. The water should remain quiescent (left) with a constant level of $d = 1.8$ m at the left side of the discontinuity.

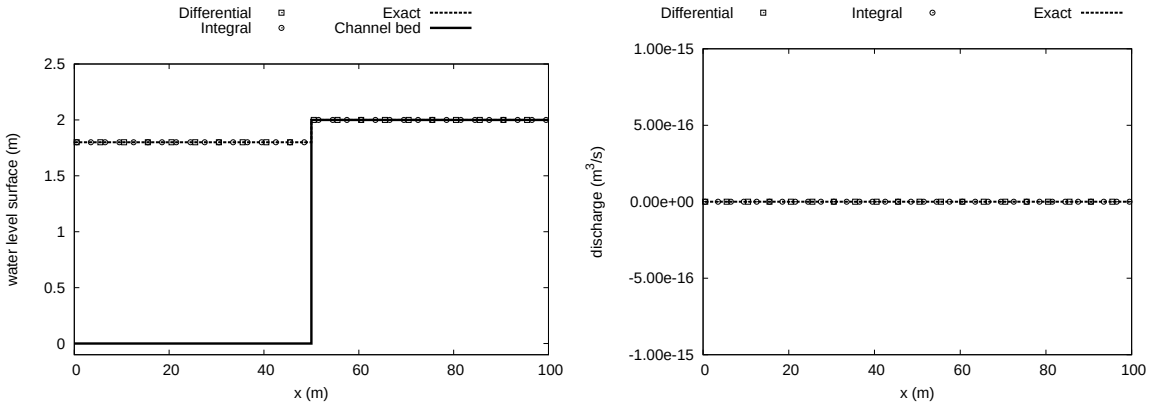

Figure 6.2: Test case 1: Longitudinal profile of water level surface (left) and discharge (right)

Futhermore, the discharge (right) is null below the machine accuracy.

In the second test case, a flat rectangular channel is considered in which a sudden narrowing from a cross sections of 10 m width to 5 m width takes place at $x = 50\ m$:

$$\sigma(x) = \begin{cases} 10 & \text{if } x < 50\ m \\ 5 & \text{if } x \geq 50\ m \end{cases} \tag{6.3}$$

The initial condition consists of a still constant water level surface of 1 m. The detail of this test case 2 is condensed in Figure 6.3.

After the simulation time, the water is consequently at rest as displayed in Figure 6.4 using both the differential and integral formulations.

Test case 3 considers a trapezoidal cross section channel (see Figure 6.5, left) with two abrupt discontinuities. The first corresponds to a bed step discontinuity located at $x = 35\ m$ and the second is a sudden cross section enlargement at $x = 70\ m$:

$$z(x) = \begin{cases} 0.6 & \text{if } x < 30\ m \\ 0 & \text{if } x \geq 30\ m \end{cases} \qquad \sigma(x) = \begin{cases} 10 & \text{if } x < 70\ m \\ 15 & \text{if } x \geq 70\ m \end{cases} \tag{6.4}$$

The initial condition is water at rest with a constant level of $d = 1\ m$. The set-up of the case is plotted in Figure 6.5.

The numerical results achieved by both the differential and the integral formulations are displayed in Figure 6.6 for the water level surface (left) and the discharge (right). As expected, the water remains at rest.

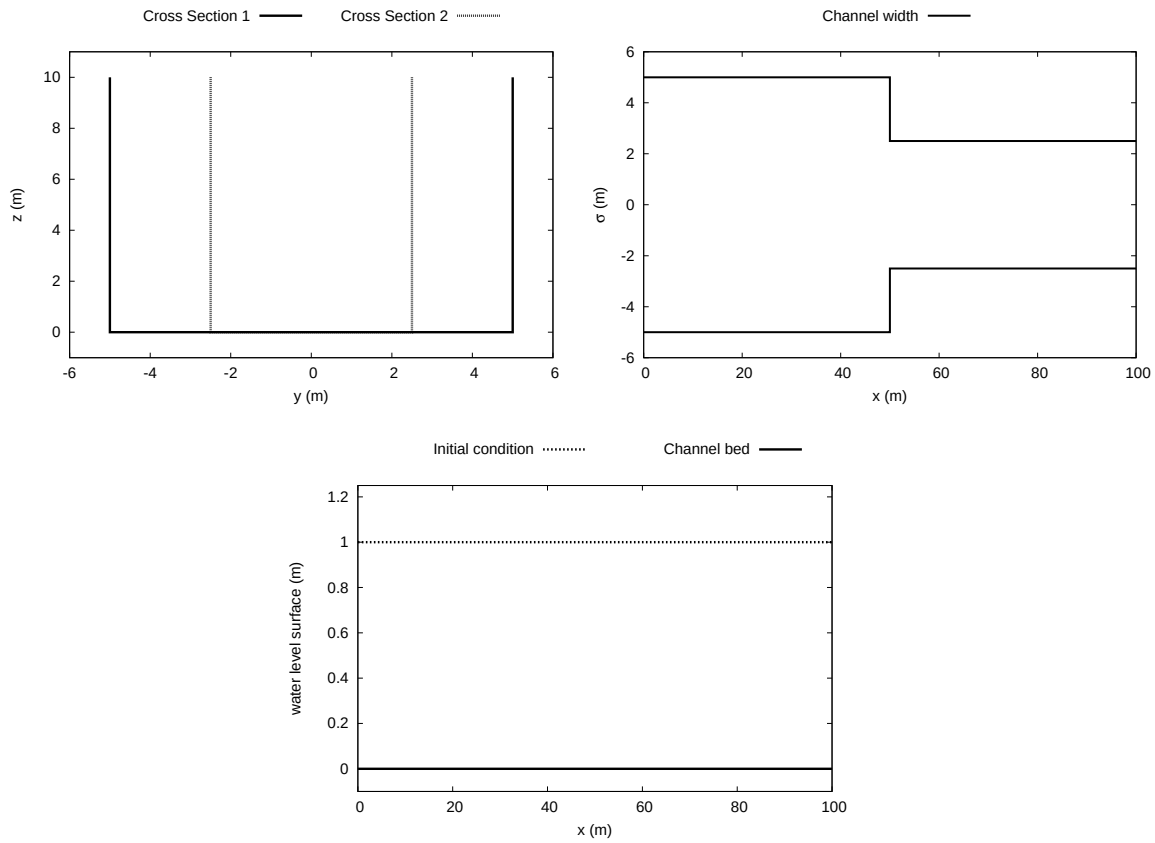

Figure 6.3: Test case 2: Cross sections (upper left), longitudinal profile of the width (upper right) and initial condition and bed level (lower middle)

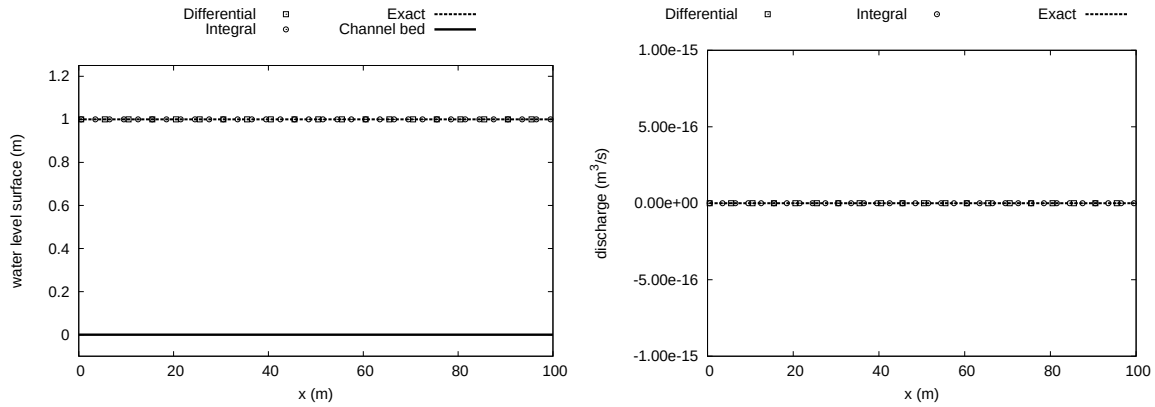

Figure 6.4: Test case 2: Longitudinal profile of water level surface (left) and discharge (right)

Test case 4 represents a trapezoidal channel with a combined bed and width discontinuity located at $x = 50\ m$ given by:

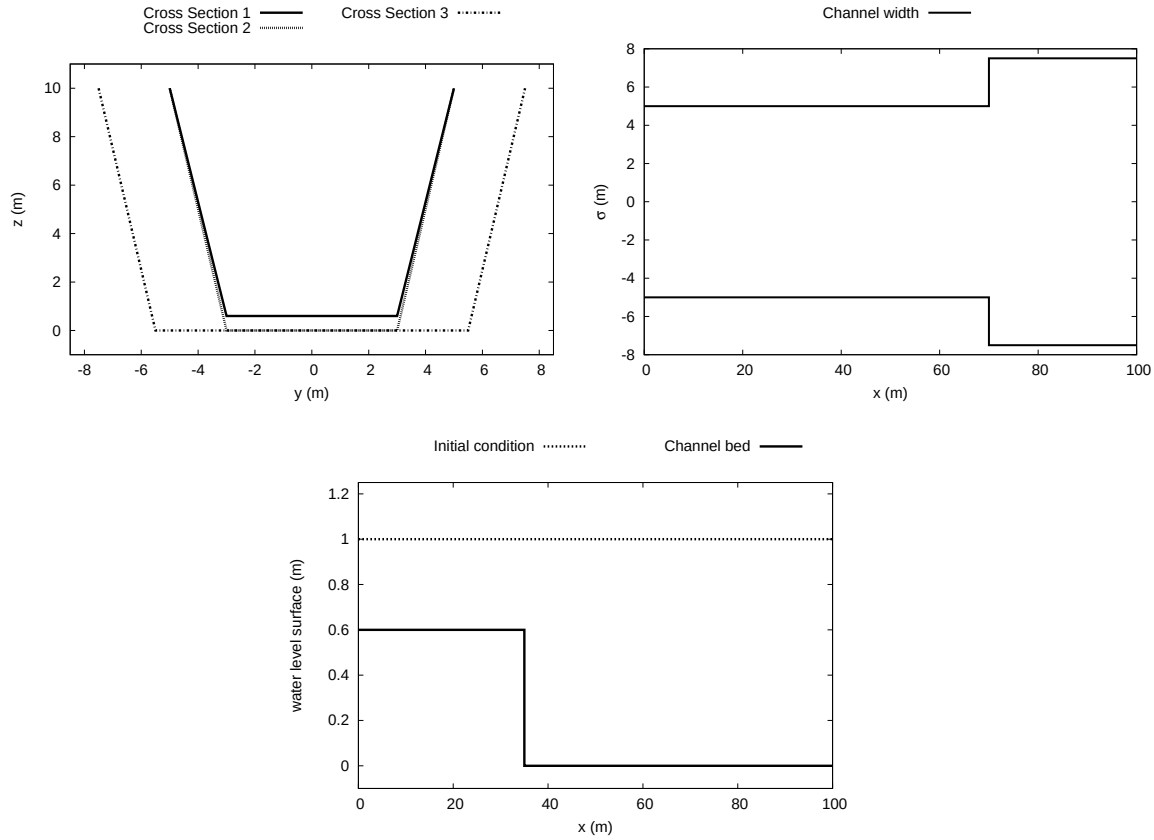

Figure 6.5: Test case 3: Cross sections (upper left), longitudinal profile of the width (upper right) and initial condition and bed level (lower middle)

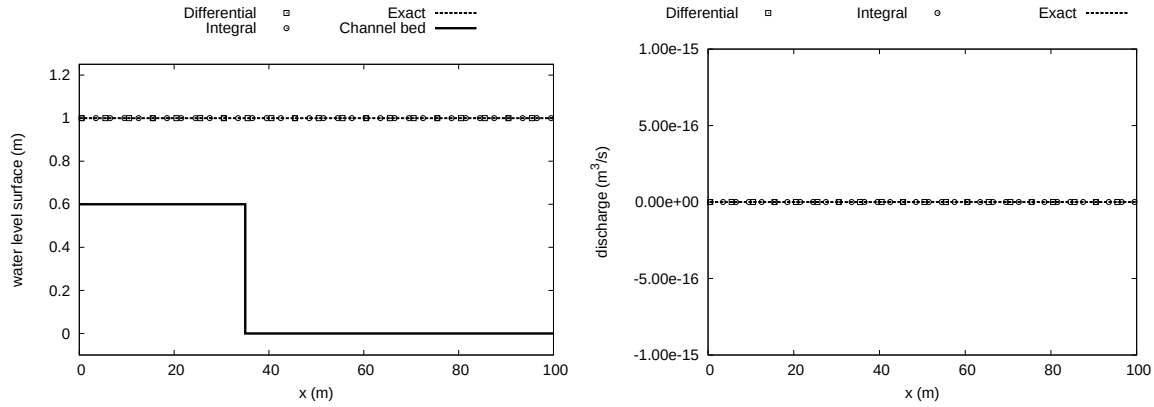

Figure 6.6: Test case 3: Longitudinal profile of water level surface (left) and discharge (right)

$$z(x) = \begin{cases} 0 & \text{if } x < 50m \\ 1.2 & \text{if } x \geq 50m \end{cases} \qquad \sigma(x) = \begin{cases} 10 & \text{if } x < 50m \\ 15 & \text{if } x \geq 50m \end{cases} \tag{6.5}$$

The initial condition are still water with a constant level of $d = 2\ m$. The cross sections, the longitudinal profiles for the width variation and for the bed level as well as the initial condition are shown in Figure 6.7. Analogously to the previous cases, the numerical results displayed in Figure 6.8 demonstrate again the well-balanced property in the case of sudden both bed and width variations.

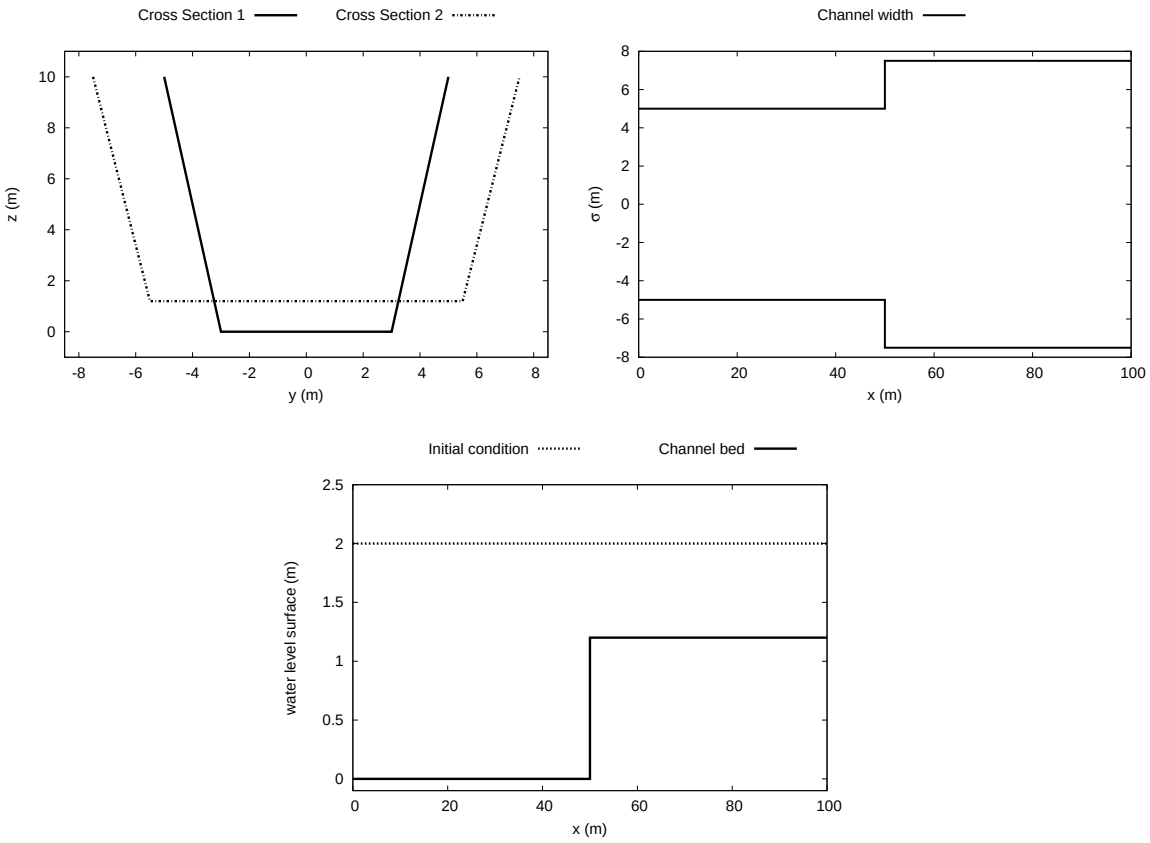

Figure 6.7: Test case 4: Cross sections (upper left), longitudinal profile of the width (upper right) and initial condition and bed level (lower middle)

In order to evaluate the still water property for the integral formulation with completely irregular cross sections, test case 5 considers a reach of a channel/river with a winding cross section that changes suddenly at $x = 50\ m$ becoming another cross section completely different. Not only the lowest point of the section changes but also the width, as plotted in Figure 6.9 (upper left and right). In this figure the initial condition is also displayed (lower middle), which consists of a constant still water level of $d = 3\ m$.

Despite the irregular geometries, the well-balanced property is also satisfied for this

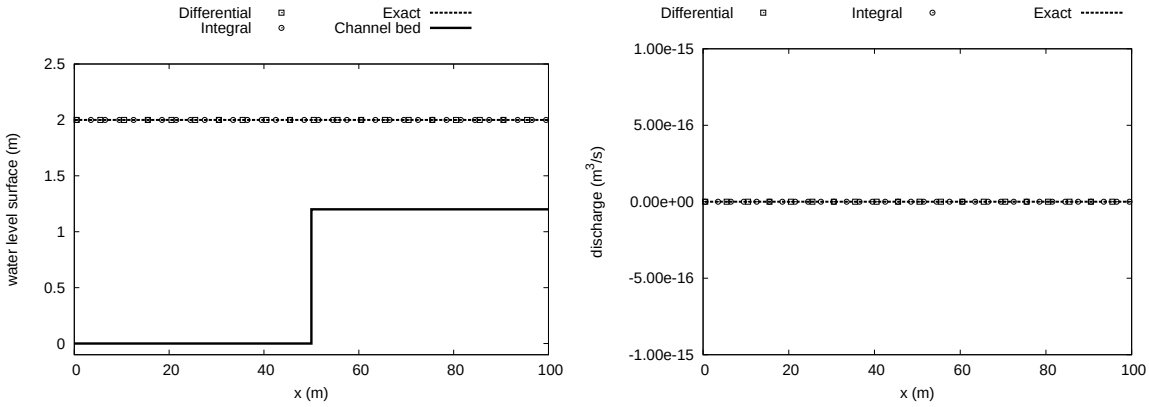

Figure 6.8: Test case 4: Longitudinal profile of water level surface (left) and discharge (right)

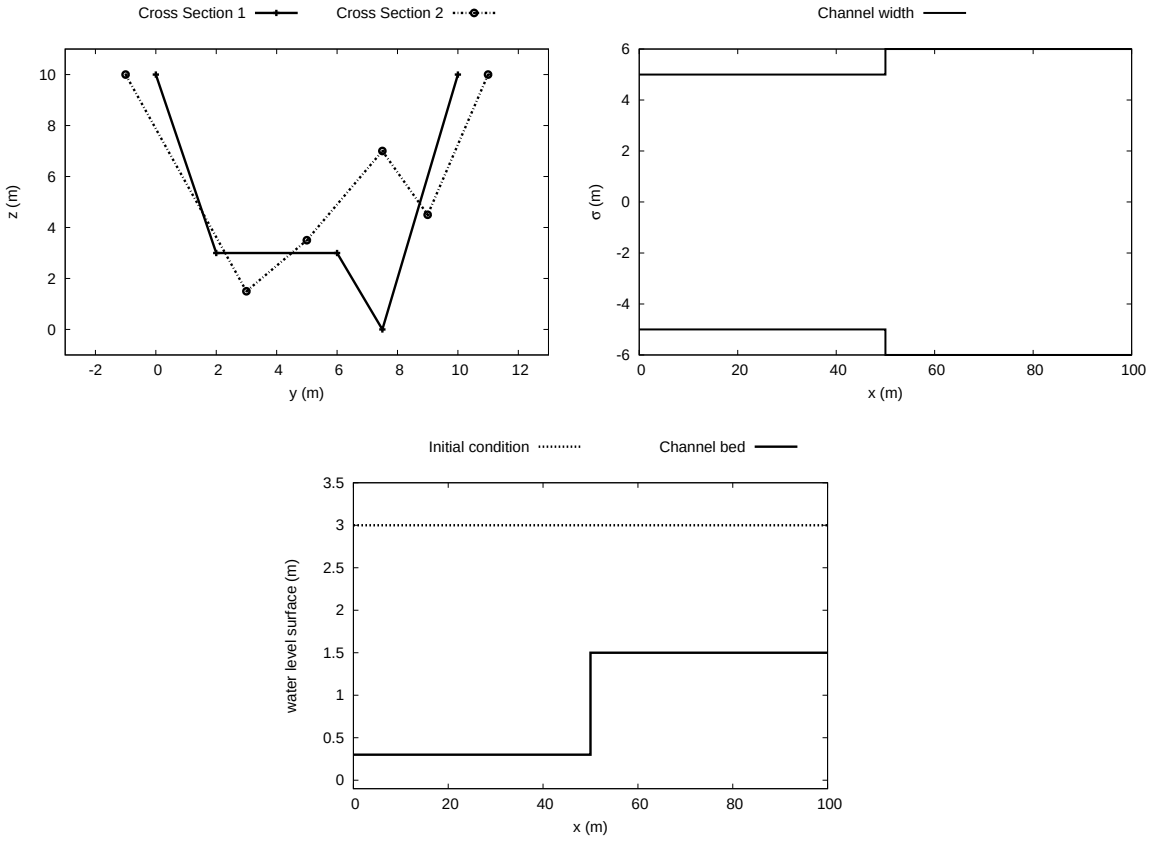

Figure 6.9: Test case 5: Cross sections (upper left), longitudinal profile of the width (upper right) and initial condition and bed level (lower middle)

test case (Figure 6.10), with both integral and differential formulations, achieving a constant water level surface and discharge all over the domain in the order of the

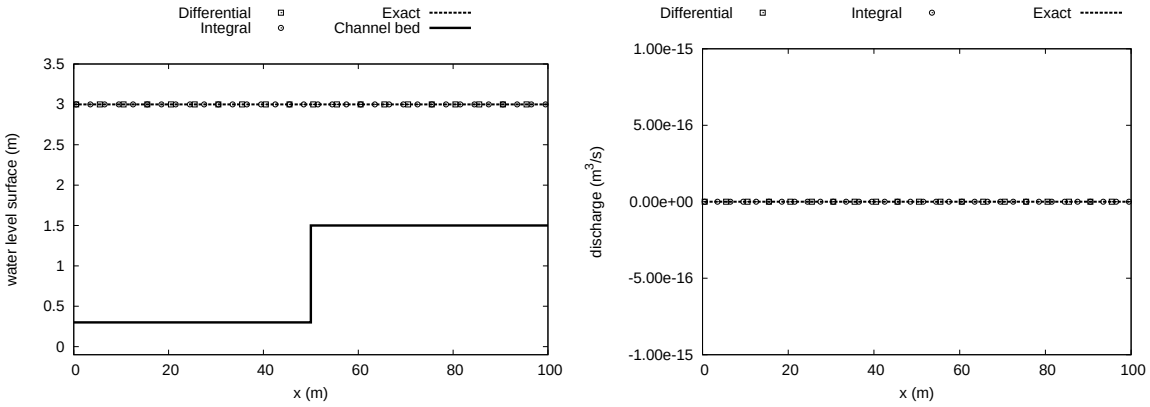

Figure 6.10: Test case 5: Longitudinal profile of water level surface (left) and discharge (right)

machine accuracy.

Although this five test cases presented above could seem simple and easy-to-achieve, a careless discretization of the source term leads instantaneously to spurious oscillations and non-physical solutions like moving water from the previous configurations.

With these verifications, the integral formulation is able to preserve the well-balanced property in the case of still water. Let consider now two of the problems that were firstly proposed by MacDonald in [78] and after extended in [79]. They represent academic 1D configurations for open channel flow supplied with analytical solution in the steady state. The first one (test case 6) consists of a trapezoidal channel 300 m long with a bed level in the form of several concatenated smooth dunes. A constant Manning friction coefficient of $n = 0.03\ s/m^{1/3}$ is imposed all over the domain. The inlet boundary condition corresponds to a constant discharge of 20 m^3/s and a fixed water depth $h_{out} = 0.71\ m$ is considered as outlet boundary. The analytical solution for the water depth is given by:

$$h(x) = 0.71 + 0.25sin\left(\frac{2\pi x}{300}\right) \tag{6.6}$$

and it corresponds to an entirely subcritical case. The discretization is done by means of a regular mesh of size $\Delta x = 1.0\ m$ and the simulation is carried out until $t = 2000\ s$. The results in terms of water level surface and discharge along the domain are plotted in Figure 6.11. Although the water level as well as the bed level are differentiable and smooth, the integral formulation approximates very well the

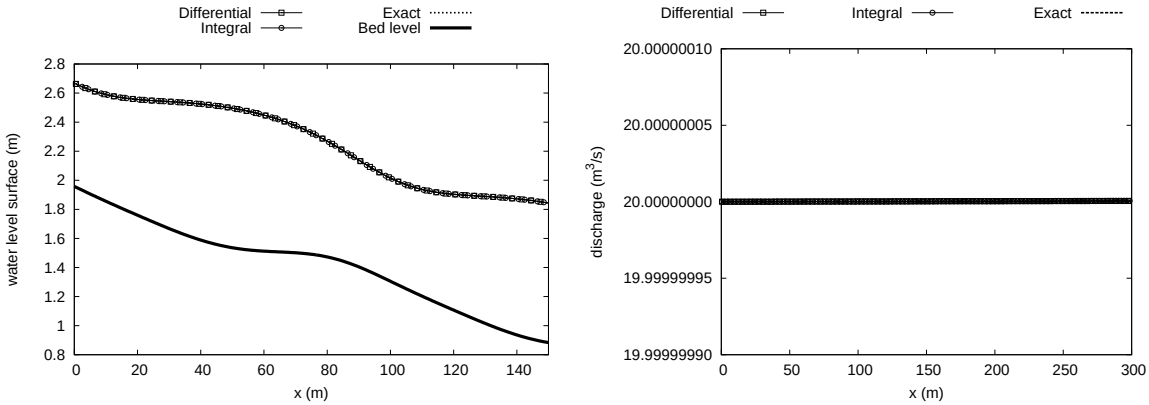

Figure 6.11: Test case 6: Longitudinal profile of water level surface (left) and discharge (right)

exact solution.

The second MacDonald-type case which will be called test case 7, consists of a rectangular 10 m width channel of a length of 150 m. The analytical solution for the water depth is of the form:

$$h(x) = 0.741617 - \frac{0.25}{tanh(3)} tanh\left(3\frac{x-50}{50}\right) \tag{6.7}$$

and it changes smoothly from subcritical to supercritical flow before a sudden transition again to subcritical via a hydraulic jump. A Manning coefficient of $n = 0.03\ s/m^{1/3}$ is used, a constant discharge of 20 m^3/s is enforced at the inlet and a constant water depth of $h_{out} = 1.700225\ m$ is imposed as outlet boundary. The domain is discretized into 150 cells ($\Delta x = 1.0\ m$) and the simulation time is set to $t = 4000\ s$. The results are shown in Figure 6.12. It is worth remarking the peak in the discharge when a hydraulic jump occurs, which is reproduced in both integral and differential formulations. It is related to the Roe's solver and the upwind discretization.

The error in norm L_1 achieved by both formulations in test cases 7 and 8 is also examined. Table 6.2 shows that the error produced by each discretization for the water surface elevation and for the discharge are very similar and anyhow in the same order of magnitude.

Therefore, the integral formulation has been demonstrated to behave at least as well as the differential formulation not only in still water cases but also under smooth

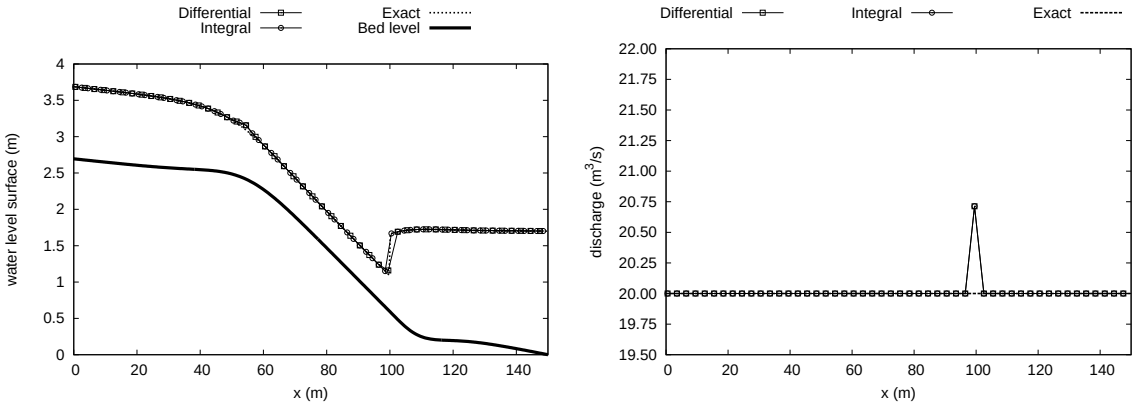

Figure 6.12: Test case 8: Longitudinal profile of water level surface (left) and discharge (right)

Test Case	Variable	Integral L_1 error	Differential L_1 error
7	h	6.096e-05	6.050e-05
	Q	3.260e-10	2.636e-10
8	h	4.335e-03	4.335e-03
	Q	4.754e-03	4.754e-03

Table 6.2: Test cases 7-8: L_1 error for h and Q

assumptions in steady states.

Test case 9 consists of a steady flow over a bump. The rectangular channel has a length of 6 m, a constant width of 0.24 m and the bottom level is characterized as follows:

$$z(x) = \begin{cases} 0.13 & \text{if } x < 3.25\ m \\ 0.13 - 0.0472(x - 3.25) & \text{if } x \geq 3.25\ m \end{cases} \tag{6.8}$$

A semicircular obstacle with a length of 0.317 m and a height of 0.073 m is placed at $x = 0.97\ m$. From a constant water depth as initial condition, an inlet discharge of 4 m^3/h is introduced until the steady state is reached. A free outlet boundary and a constant Manning roughness coefficient of $n = 0.0115\ s/m^{1/3}$ is imposed, and the domain is divided into 300 regular cells each 0.02 m. The results in terms of longitudinal profile of water level surface as well as discharge are shown in Figure 6.13.

As observed, the location of the hydraulic jump is slightly different when comparing

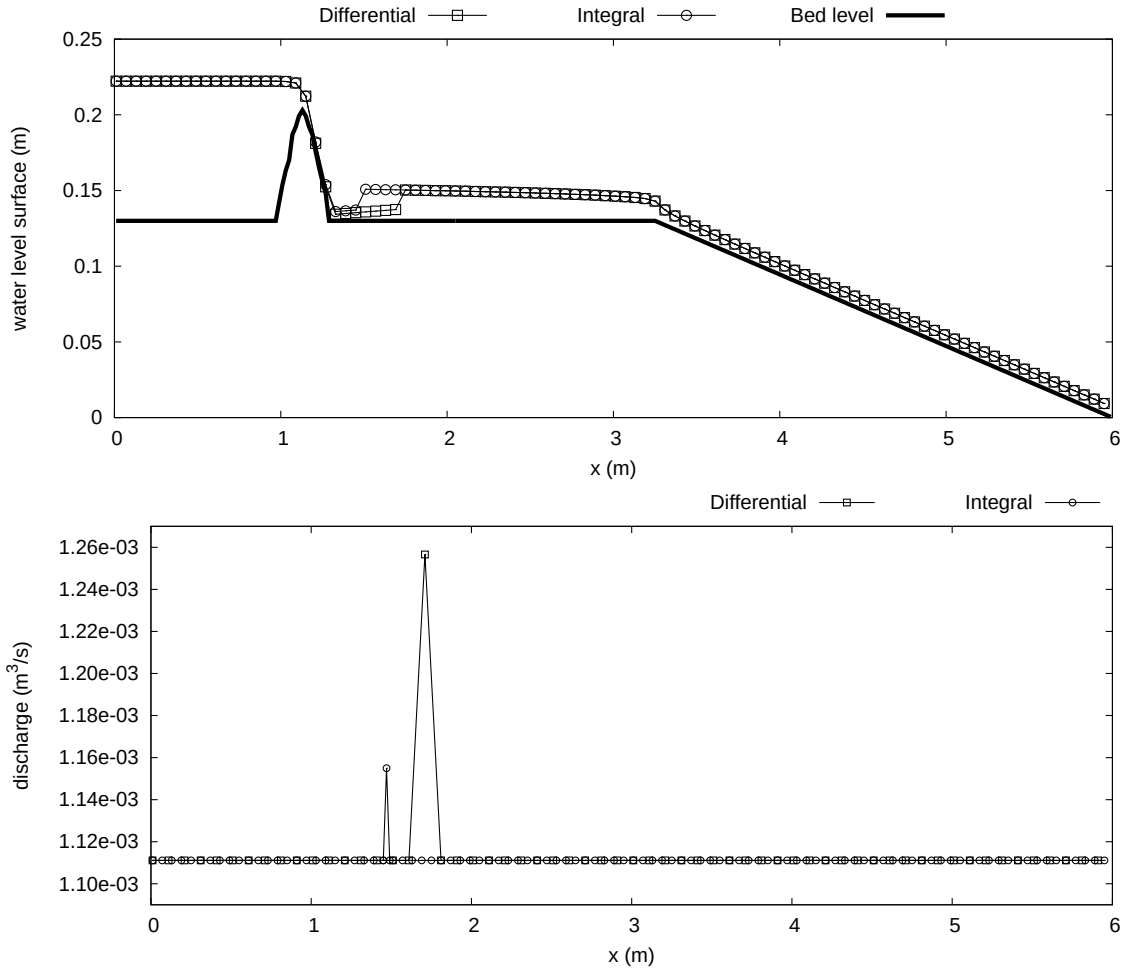

Figure 6.13: Test case 9: Longitudinal profile of water level surface (left) and discharge (right)

the differential and the integral discretization. It is due to how the formulation is perceiving the bump and performing the pressure integral mentioned in the previous chapter. The peak in the discharge corresponds again to the hydraulic jump.

Furthermore, an inaccurate source term integration could contribute to the appearance of negative water depth values, which are unacceptable for the numerical method. In this case, the time size is chosen as half the previous one and the variables are again computed. This procedure is repeated until the value of the water depth is positive or null.

The evolution of the time step size for both integral and differential approaches during the first 50 seconds is displayed in Figure 6.14. The reason for plotting only the first 50 seconds is easy: the convergence from the initial condition to the

steady state condition is critical and after that the time step size remains almost constant. As can be observed, the number of reductions with the integral formulation is considerable fewer than the differential approach, making faster the computation of the former one.

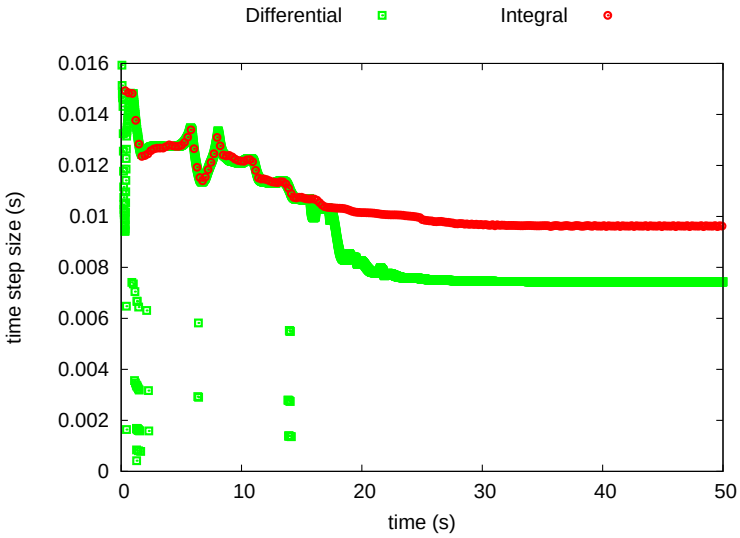

Figure 6.14: Test case 9: Evolution of the time step size

Test cases 10-12 illustrate different dam-break problem types, i.e, problems defined by discontinuous free surface initial conditions. The evolution in time of this kind of conditions generates unsteady flow [92] that is going to be anaylsed. Although several authors propose exact solutions for the dam break problems over a bed step, these exact solutions are based on assuming certain hypothesis over the pressure and the energy through the bed step. As there still exists some controversy about this topic, no exact solution related to this kind of problems is provided in this work.

The geometry of test case 10 is the same as that in test case 3, that is, a trapezoidal channel with a discontinuity in the bed step at $x = 35\ m$ and a sudden width expansion at $x = 70\ m$. The initial condition is given by:

$$h(x) = \begin{cases} 0.6 & \text{if } x < 30\ m \\ 0.3 & \text{if } x \geq 30\ m \end{cases} \tag{6.9}$$

and is plotted in Figure 6.15. The numerical results achieved by both the differential and the integral formulations at $t = 4\ s$ and at $t = 18\ s$ are displayed in Figure 6.16 for the water surface elevation and in Figure 6.17 for discharge.

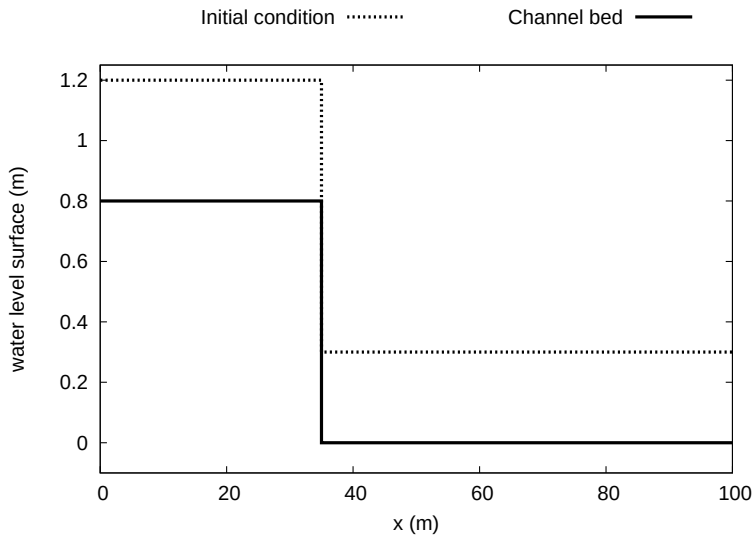

Figure 6.15: Test case 10: Bed level and initial condition

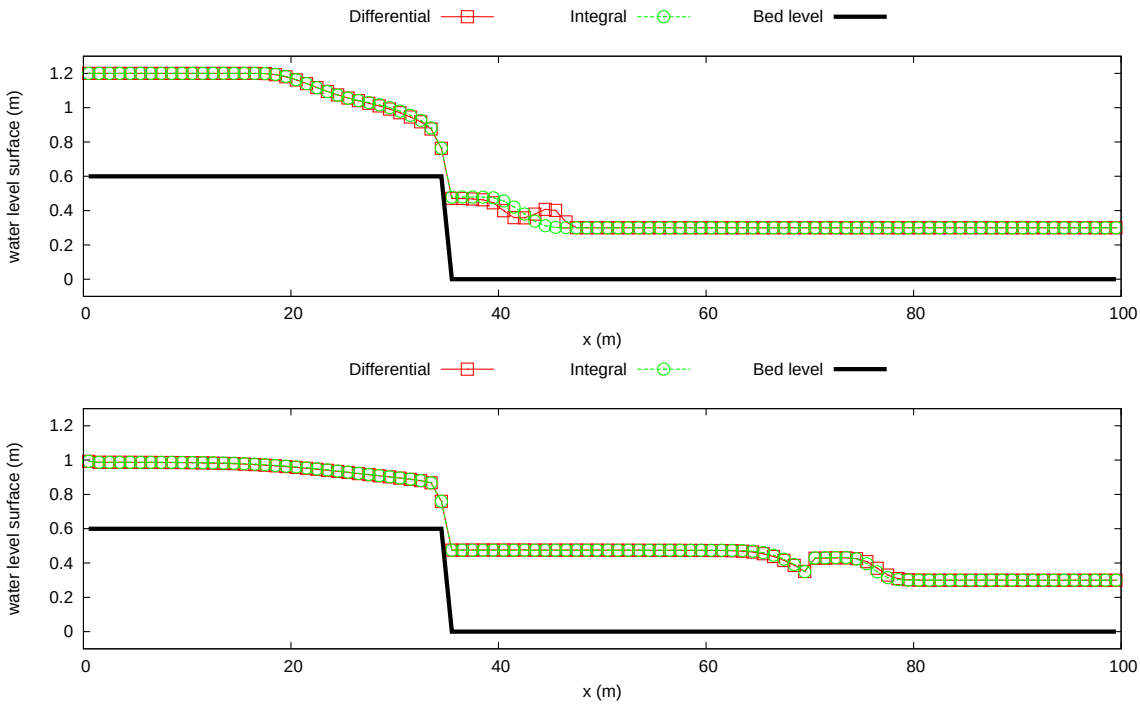

Figure 6.16: Test case 10: Longitudinal profile of water level surface at $t = 4\ s$ (upper) and at $t = 18\ s$ (lower)

A rarefaction is moving back and a shock is propagated forward from $x = 30\ m$ while two different steady discontinuities related to the bottom and the width variation are devised at $x = 35\ m$ and at $x = 70\ m$ respectively. As can be seen, the differential and the integral formulation are moderately similar, above all at the

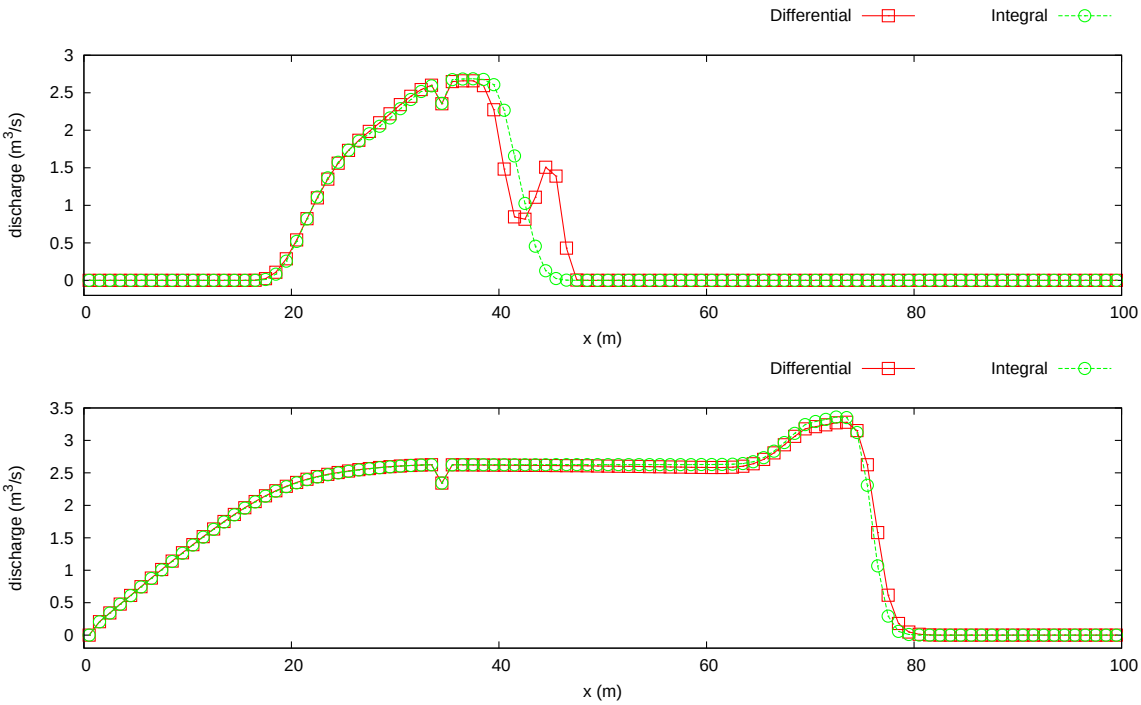

Figure 6.17: Test case 10: Longitudinal profile of discharge at $t = 4\ s$ (upper) and at $t = 18\ s$ (lower)

beginning of the dambreak problem. Although there is not any evidence about the exact solution, the integral formulation seems to be more physically reliable while in the differential formulation a steepened wave appears just after the shock that could be a consequence of a overestimation of the pressure term related to the bottom.

Test cases 11 and 12 adopt the geometry and topography of test case 4 hence a trapezoidal channel with a discontinuity at $x = 50\ m$ consisting of an adverse bed step of 1.2 m and a sudden enlargement are considered. For test case 11, the initial condition (Figure 6.18) is expressed as follows:

$$d(x) = h(x) + z(x) = \begin{cases} 2 & \text{if } x < 30\ m \\ 0.8 & \text{if } x \geq 30\ m \end{cases} \tag{6.10}$$

Therefore, the discontinuity at the free surface is placed at the same location as the bottom and width discontinuities. The results for the water surface elevation and for the discharge at $t = 1\ s$ and $t = 3\ s$ are plotted in Figures 6.19 and 6.20 respectively. As can be seen, the differential and integral formulations produce again different numerical results.

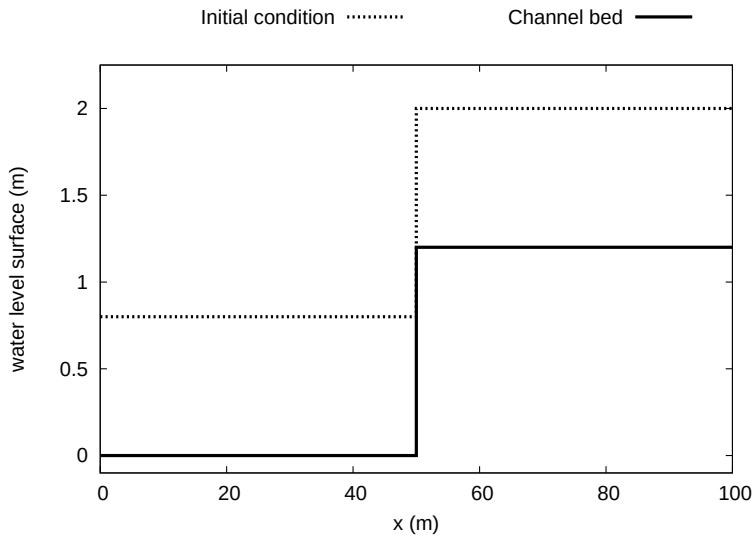

Figure 6.18: Test case 11: Bed level and initial condition

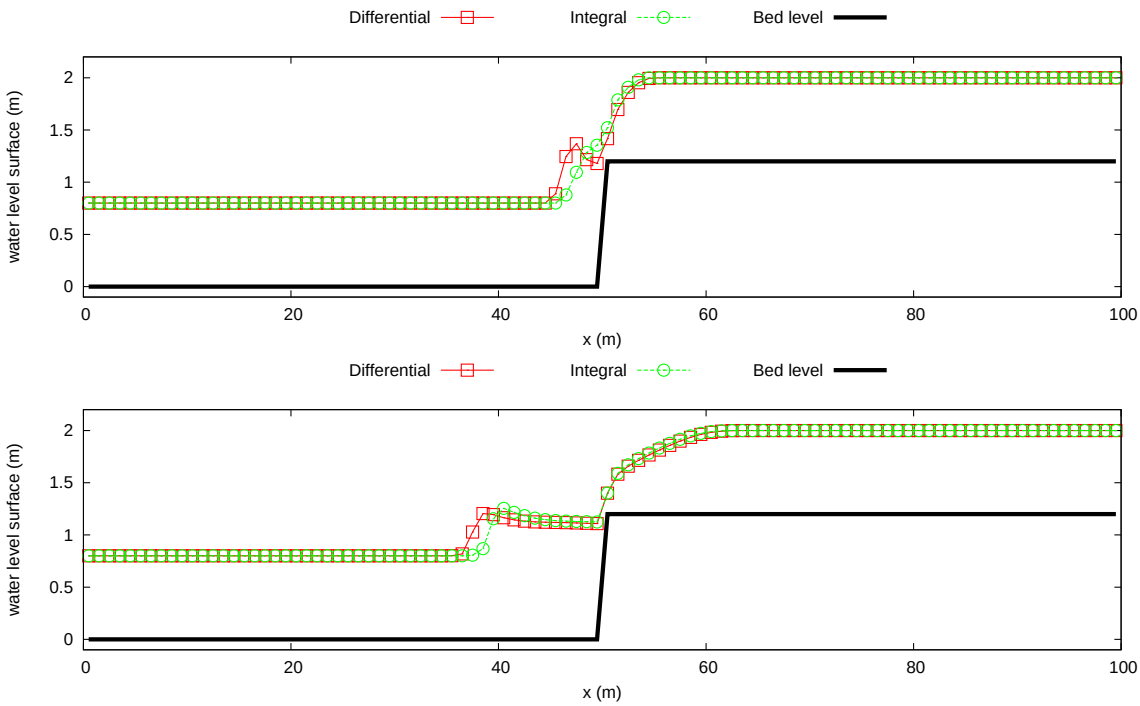

Figure 6.19: Test case 11: Longitudinal profile of water level surface at $t = 1\ s$ (upper) and at $t = 3\ s$ (lower)

The initial condition for test case 12 consists of two concatenated dam-break problems (see Figure 6.21), upstream ($x = 20\ m$) and just over ($x = 50\ m$) the bottom-width discontinuity respectively:

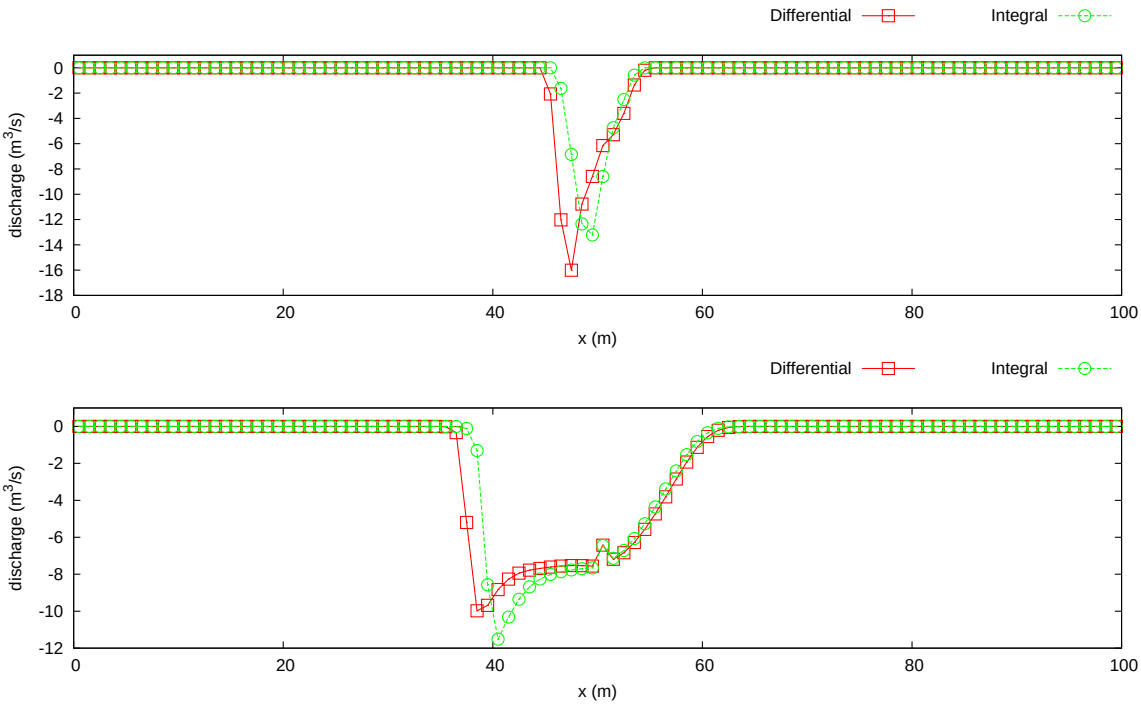

Figure 6.20: Test case 11: Longitudinal profile of discharge at $t = 1\ s$ (upper) and at $t = 3\ s$ (lower)

$$d(x) = h(x) + z(x) = \begin{cases} 1.5 & \text{if } x < 20\ m \\ 0.5 & \text{if } 20\ m \leq x < 50\ m \\ 1.7 & \text{if } x \geq 50\ m \end{cases} \tag{6.11}$$

For both the differential and integral formulation, Figure 6.22 shows the numerical results at $t = 1\ s$ and at $t = 3\ s$ for the water level surface while Figure 6.23 displays the longitudinal profile for the discharge.

At $x = 20\ m$, a rarefaction moves back and a shock front moves forward while at the same time, at $x = 50\ m$, a rarefaction propagates to the end of the channel and a shock develops in the other direction. The differences between both formulations are highlighted, although the integral formulation is able to provide a numerical solution smoother than the differential approach.

The last test case considered in this section (test case 13) represents a triangular/trapezoidal channel of length 1000 m characterized by the following bottom geometry:

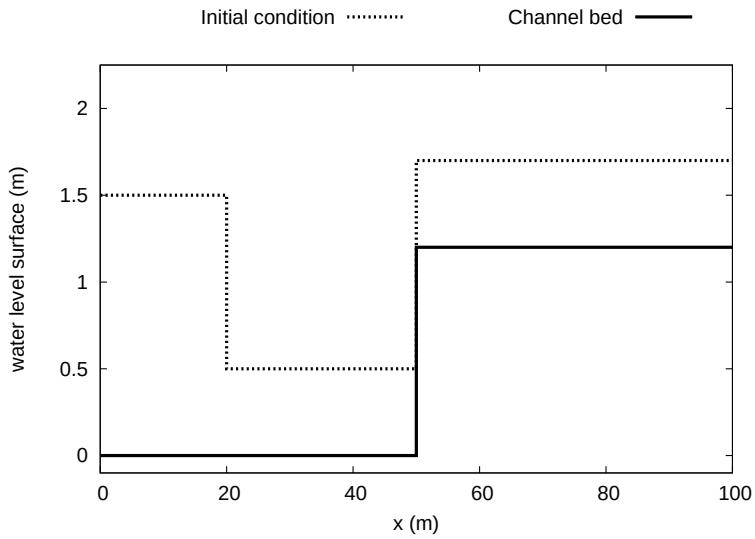

Figure 6.21: Test case 12: Bed level and initial condition

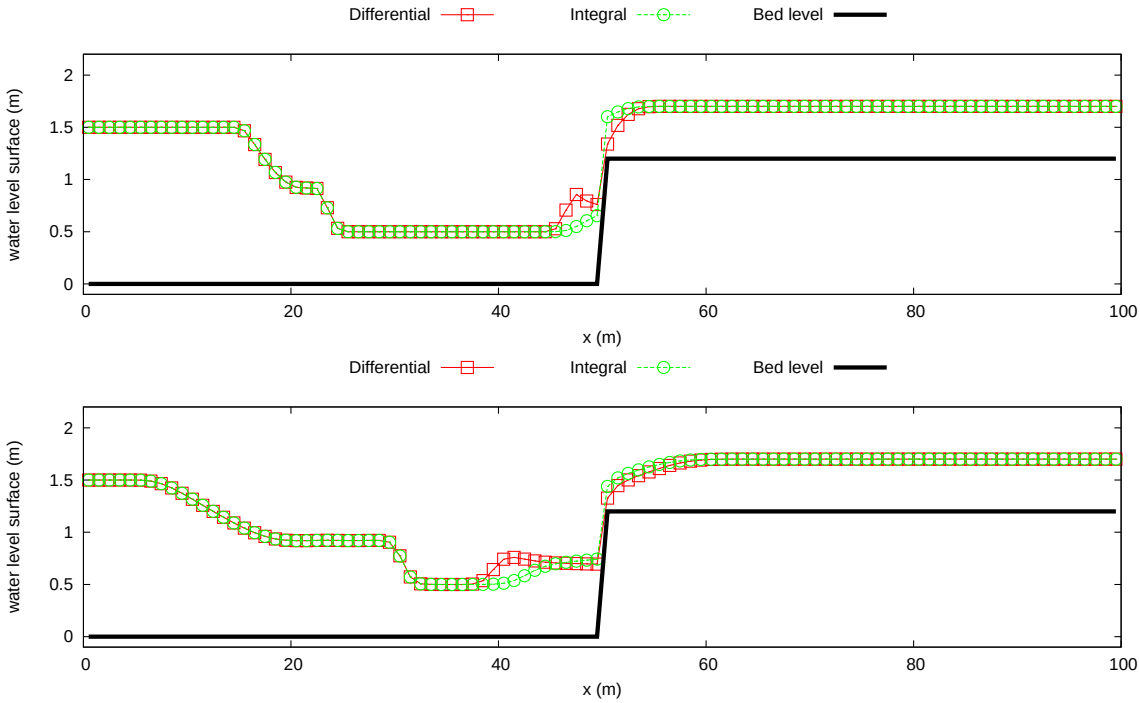

Figure 6.22: Test case 12: Longitudinal profile of water level surface at $t = 1\ s$ (upper) and at $t = 3\ s$ (lower)

$$z(x) = \begin{cases} 0.0 & \text{if } x < 250\ m \\ 0.5 - 0.0004(x - 250) & \text{if } x \geq 250\ m \end{cases} \tag{6.12}$$

Therefore, the channel has an abrupt discontinuity at $x = 250\ m$ and afterwards a

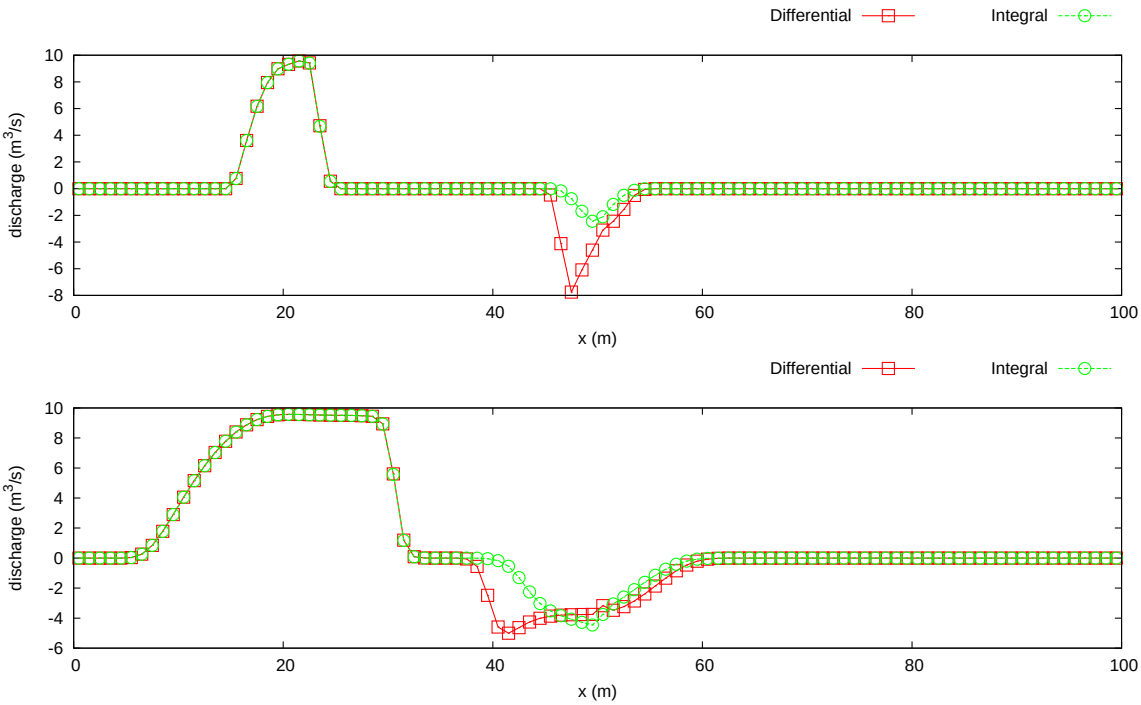

Figure 6.23: Test case 12: Longitudinal profile of discharge at $t = 1\ s$ (upper) and at $t = 3\ s$ (lower)

smooth bottom favourable slope. The cross section evolution along the longitudinal coordinate is plotted in Figure 6.24: the channel has a triangular section at the beginning with the same slope from the left and the right side (section 1), that changes suddenly at $x = 250\ m$ and becomes asymmetric (section 2). Afterwards, it changes smoothly to turn into a trapezoidal section at the end of the channel (cross section 3).

In this test case, the convergence to a steady state of 1 m^3/s is sought. It is a challenging test case because of the rapid varying flow over a bed step and the appearance of wet/dry fronts. A Manning coefficient of $n = 0.01 s/m^{1/3}$ is set constant for all the channel and a free boundary condition is enforced at the outlet. The initial condition (see Figure 6.25) is still water depth defined by:

$$h(x) = \begin{cases} 0.5 & \text{if } x < 250\ m \\ 0 & \text{if } x \geq 250\ m \end{cases} \tag{6.13}$$

The domain is discretized in 1000 cells with $\Delta x = 1\ m$ and the simulation is carried out until steady state is reached. The numerical results achieved by the integral

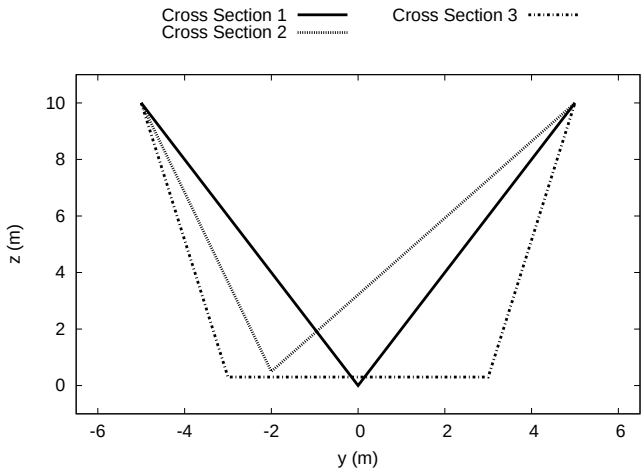

Figure 6.24: Test case 13: Cross sections

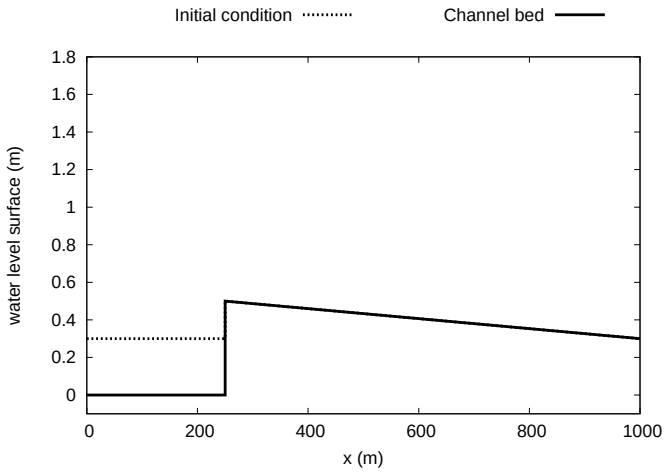

Figure 6.25: Test case 13: Bed level and initial conditions

and the differential formulation are displayed in Figure 6.26 and Figure 6.27 for the water surface elevation and for the discharge respectively.

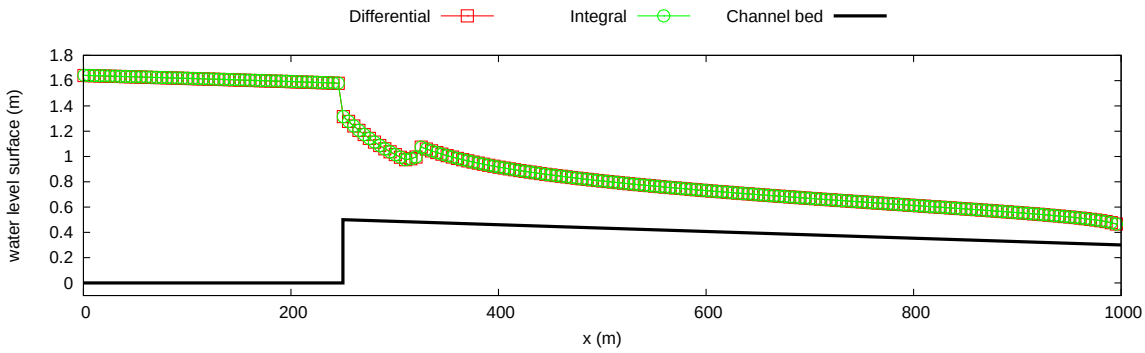

Figure 6.26: Test case 13: Longitudinal profile of water level surface

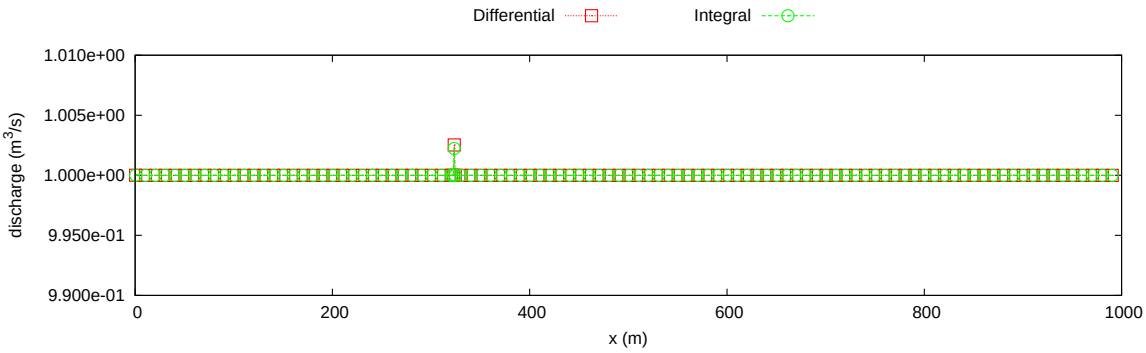

Figure 6.27: Test case 13: Longitudinal profile of discharge

A hydraulic jump develops after the bed step (close to $x = 325\ m$) and is reflected in the peak produced by both formulations in the discharge profile. As can be observed, there are not many differences between integral and differential formulations in the final state. However, the convergence to steady state is not achieved in the same manner. As stated before, the appearance of negative values of water depth can be dramatic and, although they should have been reduced with the techniques to avoid non-physical values, the proposed solution when they appear consist of reducing the time step until the water depth becomes positive or null.

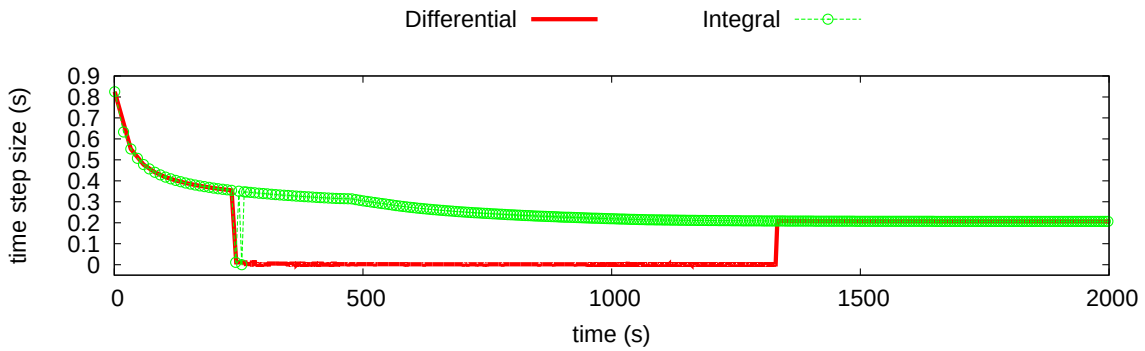

Figure 6.28: Test case 13: Evolution of the time step size

In this case, an incorrect estimation of the source term could lead to minuscule time step sizes as displayed in Figure 6.28 for the differential formulation. This fact makes consequently the simulation slower. As an example, while the simulation using the integral formulation is carried out in 11 seconds, the simulation with the differential formulation spends 386 seconds to reach the final steady state. This problem was also reported in [92] inside the two dimensional framework.

Chapter 7

Conclusions

A review of scalar and systems of conservation laws has been developed. The differential and integral formulation for these hyperbolic conservation laws as well as several concepts such us the Riemann Problem are introduced. The Roe's Approximate Riemann Solver is presented for the homogeneous case and the augmented version of the scheme is proposed for system of conservation laws with source terms. Furthermore, approximate Riemann solutions are proposed for the 1D and the 2D case, exploring all the possibilities related to the eigenvalues.

Being the shallow water equations a system of conservation laws with source terms, they are a good candidate to apply the previous ideas developed in a general manner. Both the 1D and 2D shallow water equations are presented in chapter 3. The numerical scheme applied to the hydrodynamic equations is explained, paying attention to the boundary conditions and the entropy fix. The solute transport equations are presented coupled to the hydrodynamic system and a technique consisting of decoupling the solute equations in a conservative way is illustrated.

The focus is subsequently put on the source term treatment and the wet/dry fronts. Taking into account the ideas of the approximate Riemann solutions, it is feasible to limit and distribute intelligently the source term amount when discretizing the equations in order to reduce the number of negative values of water depth and to entirely avoid the non-physical solutions. The wet/dry fronts are examined from the same point of view and an algorithm is proposed to limit and distribute the numerical flux in the wet/dry interfaces to remain the scheme conservative.

A novel source term discretization coming from the integral formulation of the conservative equations is presented. In contrast to the classical approach, called here differential formulation, the integral formulation is able to better approximate the

flow through discontinuities, where the differential formulation is not valid at all. This integral approach is firstly presented in a 1D rectangular cross section configuration for the flow over a bed step. These ideas can be extended to the 2D shallow water equations. It is worth noting that a parameter is left open in this work when performing the integral of the pressure related to the bottom step due to the controversial in the literature about the flow over a step.

The extension to the 1D shallow water equations with irregular geometries is deeply analysed in section 5.2. The differential formulation is presented before, remarking the extra term that appear when passing to the non-conservative formulation. The propagation of discontinuities should be studied from the integral point of view hence the integral formulation is developed for irregular geometries. As performing the pressure integrals implies again doing several assumptions on the energy through a discontinuity, a free parameter is again left open in this work. Hydraulic tables are used to implement these pressure integrals related to the bottom and the width variations.

Finally, the advances related to the source term discretization are applied to different test cases to corroborate the well-balanced property, the validity of the integral formulation under smooth conditions and the behaviour of both differential and integral formulations in the case of sudden strong discontinuities not only related to the bottom level but also to the width contractions or expansions. Although analytical solutions for these kind of problems are open, the integral formulation seems to be more robust in the presence of abrupt discontinuities and is able to compute the numerical solution using time step sizes bigger than the differential formulation.

Part II

Large Time Step upwind explicit scheme (CFL >1)

Introduction

According to the discretization of the temporal derivative, there exist two main classes of numerical methods: implicit and explicit schemes. Implicit schemes offer unconditional numerical stability at the extra cost of having to deal with the resolution of an algebraic system. In fact, the updating of a variable in the following time step in the implicit schemes will depend not only on the value of the variable in the previous time step but also on the value at the current time. On the other hand, conceptual simplicity is the most valuable characteristic of explicit schemes. Variables are updated taking into account the information at the previous time step. However, the size of the time step is restricted by stability reasons to fulfil the CFL condition when dealing with a hyperbolic system of conservation laws.

When dealing with the shallow water equations, the great majority of the schemes have been developed using a explicit technique. However, different approaches in the 1D, 2D and 3D frameworks for implicit or semi-implicit models have been explored during the last decades. In [18] a 1D robust implicit scheme is presented for the simulation of river hydraulics. Several corrections are done related to the numerical resolution (bidiagonal and tridiagonal) of the complete system concerning implicit and semi-implicit schemes with suitable CFL numbers. Following this philosophy, in [34] the focus is put on the adopting semi-implicit schemes with local CFL numbers and equivalent cross sections which are computationally saving, to improve efficiency in real engineering problems. In the 2D framework, Casulli [25] proposed a semi-explicit finite difference scheme analysing which terms have to be discretized in an explicit or implicit way. Different improvements and modifications of this method related to high-order and discontinuous-Galerkin schemes can be found in [42, 116]. On the same way, 3D semi-implicit approaches have been carried out in [27, 28].

It is possible to relax the condition over the time step size when using explicit schemes. A generalization of the first order Goudnov's explicit upwind scheme , modified to allow large time steps, was explored by Leveque [70, 71] (Large Time Step, LTS) first in the scalar non-linear case and then adapted to systems of equa-

tions. It is stable for CFL values larger than 1 and provides accurate and correct solutions of shocks. Some difficulties can be met when a rarefaction is present in the solution so that adjustments are necessary. Other class of large time step explicit schemes based on TVD properties [57] have been analysed and tested mainly for the scalar equations or systems of equations without source terms. These will not be considered in the present work.

Engineering applications related with atmospheric dynamics [102] and Euler equations [106, 107] have been recently published. Apart from retaining most of the advantages offered by explicit schemes, they are able to increase not only the efficiency in terms of computational burden, but also the accuracy of the numerical results. As long as fewer time steps are required to complete the simulation, the numerical diffusion associated with the numerical scheme is reduced, obtaining more accurate results.

The shallow water equations, being a hyperbolic system of partial differential equations, are also a good candidate for the application of the LTS scheme. A deep analysis of the application of this kind of LTS scheme to scalar equations and systems of conservation laws with source terms can be found in [87] with a particular application to the 1D shallow water equations.

As related before, the source term treatment and the boundary conditions discretization are crucial to allow stability in presence of large CFL values in realistic cases. On the one hand, the idea of using a stationary jump discontinuity representing the source term in the Riemann solution [52] and the corresponding augmented approximate Riemann solvers for the shallow water equations [92] is incorporated to the LTS scheme.

On the other hand, the boundary conditions discretization is another issue of importance in the development of a numerical model. In the context of the shallow water equations, open boundaries and closed boundaries can appear and must be explored. From the structure of the LTS scheme, information is transmitted not only to the immediate neighbouring cells but also to a number of other cells growing as the CFL value increases. Therefore, some information can cross the boundaries and a careful consideration is required in order to reproduce all kind of scenarios such as subcritical, supercritical and closed boundaries.

Before applying the LTS scheme to the 1D shallow water equations, the discretiza-

tion is described first, for 1D scalar equations with and without source terms. In the non-linear case, the treatment of the rarefaction waves is explored. Then, the scheme is extended to 1D systems of equations, in particular to solve the 1D shallow water equations where bed slope and friction source terms are incorporated into the proposed procedure. This method is proposed to be a general tool for solving the 1D shallow water equations for open channel and river flow problems, allowing the increase of the CFL value when possible. However, several issues that were totally solved in the context of the first order upwind scheme such as wet/dry fronts or the entropy correction have to be analysed.

The extension of the LTS scheme to the 2D shallow water equations was firstly mentioned in [94]. Other recent applications in connection with atmospheric dynamics [102] and Euler equations [106] have been extended to more than one dimension using the dimensional splitting technique. In this work, the extension of the mentioned LTS scheme to the 2D shallow water equations is firstly achieved by means of this dimensional splitting procedure on structured grids. While the advances related to source term discretization are preserved, boundary conditions require some adjustments concerning the dimensional splitting procedure and the characteristic line information. Then a novel technique is proposed to formulate the Large Time Step scheme on triangular grids, accounting for the maximum information allowed to be sent from each computational wall and defining appropriate paths to send the information across them.

Another issue of importance that appears explicitly in the 2D shallow water system is the formulation of wet/dry fronts. The proper discretization of wet/dry fronts to ensure positivity without drastic time step reduction below the CFL condition was presented in [92, 93] and detailed in part I. The extension of the LTS scheme to situations with wet/dry fronts in 1D was previously discussed in [87] suggesting to recover the conventional first order upwind scheme in those cases. When moving to 2D models of inundation problems, the likely presence of wet/dry fronts requires another approach. The definition of wet/dry solid interfaces and the correct sending of information should lead to an adequate wet/dry treatment, not excessively restricting the time step size and avoiding the appearance of negative water depth values.

Chapter 8

LTS scheme for 1D scalar equations

8.1 Scalar equations

8.1.1 Linear scalar equation

The basic ideas underlying the Large Time Step (from now on LTS) scheme can be introduced by examining first the linear scalar equation,

$$\frac{\partial u}{\partial t} + \frac{\partial f(u)}{\partial x} = 0 \tag{8.1}$$

where u is the conserved variable and $f(u)$ is a linear function, $f(u) = \lambda u$, $\lambda = constant$.

The numerical resolution of (8.1) by means of the first order upwind finite volume method scheme can be written as follows:

$$u_i^{n+1} = u_i^n - \frac{\Delta t}{\Delta x}(\delta f^+_{i-1/2} + \delta f^-_{i+1/2}) \tag{8.2}$$

This is a finite volume point of view centered at the cells which accumulates the

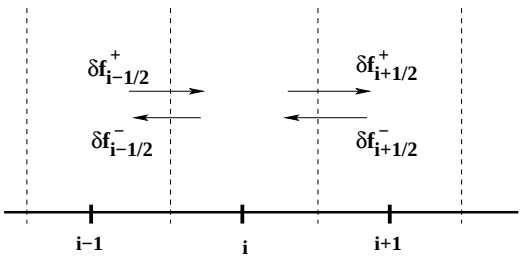

Figure 8.1: Contributions from left and from right in cell i

arriving signals to update the value of the function at every cell. There is another way to consider this situation by looking where the signals go from each interface [70]. For example, at interface $(i, i+1)$ the quantity $\nu\ \delta u_{i+1/2}$, where $\nu = \dfrac{\Delta t}{\Delta x}\lambda$ can be defined and it is sent according to the sign of λ following the algorithm:

$$\begin{array}{ll} \text{if } \lambda > 0 \Rightarrow \nu\ \delta u_{i+1/2} & \text{updates } i+1 \\ \\ \text{if } \lambda < 0 \Rightarrow \nu\ \delta u_{i+1/2} & \text{updates } i \end{array} \tag{8.3}$$

Both versions of the scheme are equivalent if

$$CFL = \frac{\Delta t}{\Delta x}\lambda \leq 1 \tag{8.4}$$

The second approach is nevertheless preferable to extend the scheme to CFL > 1. As described by Leveque [70], the extension of the scheme to larger time steps is achieved by allowing each wave or signal to propagate independently from all other waves according to the following algorithm:

If $\lambda > 0$

$$\begin{array}{ll} \delta u_{i+1/2} & \text{updates } i+1, \cdots, i+\mu_{i+1/2} \\ (\nu-\mu)\ \delta u_{i+1/2} & \text{updates } i+\mu_{i+1/2}+1 \end{array} \tag{8.5}$$

If $\lambda < 0$

$$\begin{array}{ll} \delta u_{i+1/2} & \text{updates } i, \cdots, i+\mu_{i+1/2}+1 \\ (\nu-\mu)\ \delta u_{i+1/2} & \text{updates } i+\mu_{i+1/2} \end{array} \tag{8.6}$$

where $\mu = int(\nu)$. Figure 8.2 shows how the information is sent from interface $(i, i+1)$ to the involved cells when $\lambda > 0$ (a) and when $\lambda < 0$ (b).

The proposed scheme is explicit and remains conservative. This is the basic formulation of what is called LTS scheme in this work. It is important to remark that if CFL $\leqslant 1$ the scheme becomes the original first order explicit upwind scheme (8.2).

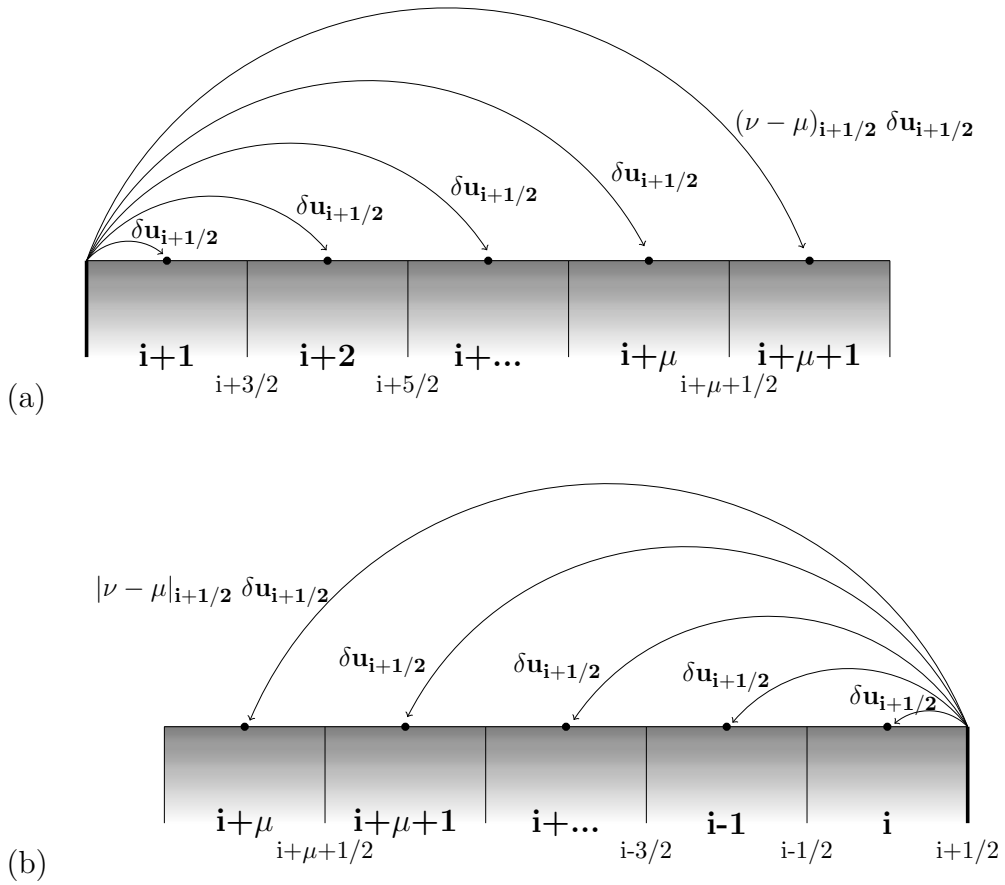

Figure 8.2: Scheme of the contributions from intercell *i+1/2* for $\lambda > 0$ (a) and for $\lambda < 0$ (b)

8.1.2 Non-linear scalar equation

Consider now the conservation law:

$$\frac{\partial u}{\partial t} + \frac{\partial f(u)}{\partial x} = 0 \tag{8.7}$$

where $f(u)$ is a convex non-linear function of u. So that:

$$\lambda = \frac{df}{du} \qquad \lambda = \lambda(u). \tag{8.8}$$

which is no longer constant. The LTS scheme, when applied to (8.7), requires the definition of an approximate advection celerity at the intercell as follows:

$$\widetilde{\lambda}_{i+1/2} = \frac{f(u_{i+1}) - f(u_i)}{u_{i+1} - u_i} \tag{8.9}$$

Certain new elements appear in this case that are going to be explored using the Burgers equation as an example.

8.1.2.1 Burgers equation and the Riemann Problem

The inviscid Burgers equation is a particular case of scalar conservation law of the type (8.7) with $f(u) = \frac{1}{2}u^2$. This equation can be written as

$$\frac{\partial u}{\partial t} + \frac{\partial}{\partial x}\left(\frac{u^2}{2}\right) = 0 \qquad \text{or} \qquad \frac{\partial u}{\partial t} + u\frac{\partial u}{\partial x} = 0 \tag{8.10}$$

Considering the following initial value problem or Riemann Problem (RP)

$$u(x,0) = \begin{cases} u_L & if \quad x < 0 \\ u_R & if \quad x > 0 \end{cases} \tag{8.11}$$

two different situations appear depending on the relative value of u_L and u_R. When $u_L > u_R$ a right moving shock develops (see Figure 8.3). Otherwise, the solution of the RP consists of a smooth rarefaction wave connecting the two constant states u_L an u_R.

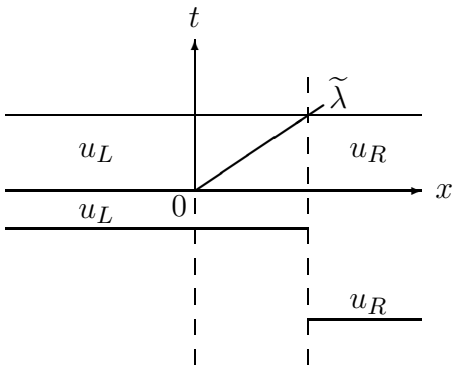

Figure 8.3: Discontinous solution of (8.11) when $u_L > u_R$

As described in [70, 71], the LTS scheme can be used to provide an accurate and correct solution of shocks. In presence of a rarefaction, the explicit upwind scheme

replaces several characteristic lines with a single line and only one intermediate state u^* is defined (see Figure 8.4 (a)). This approximation is effective in the conventional upwind explicit method but can fail when using CFL > 1. The proposed LTS includes several intermediate states $u_1^*, ..., u_{N_p}^*$

$$u_j^* = \frac{(N_p - j)u_L + ju_R}{N_p} \qquad j = 1, \cdots, N_p \tag{8.12}$$

corresponding to several discontinuities travelling at different speeds (Figure 8.4(b)). The required number of discontinuities N_p is related with the strength of the RP. A good approximation could be:

$$N_p = int(\frac{\delta u\ \Delta t}{\delta x}) \tag{8.13}$$

where $\delta u = u_R - u_L$. The proposed way of handling rarefaction waves is always conservative.

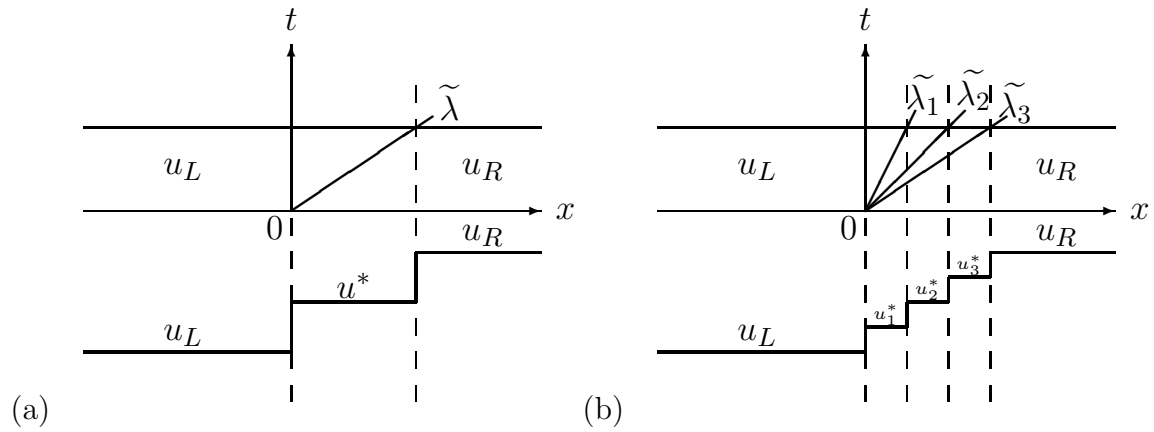

Figure 8.4: (a) Classical treatment of rarefaction waves in the upwind scheme; (b) Splitting treatment of rarefaction waves in the LTS scheme

In order to illustrate the performance of LTS in presence of a rarefaction, consider (8.10) with the initial data:

$$u(x,0) = \begin{cases} 1.0 & if \quad x < 50.0 \\ 4.0 & if \quad x > 50.0 \end{cases} \tag{8.14}$$

The exact solution for this case is

$$u(x,t) = \begin{cases} 1.0 & if \quad \frac{x}{t} \leq 1.0 \\ \frac{x}{t} & if \quad 1.0 < \frac{x}{t} < 4.0 \\ 4.0 & if \quad \frac{x}{t} \geq 4.0 \end{cases} \tag{8.15}$$

Figure 8.5(a) shows the exact solution at $t = 5s$ together with the numerical results obtained with the LTS scheme on a regular mesh of $\Delta x = 1.0$. The discretization of the rarefaction in a single wave has been used and different CFL values are associated to different number of time steps (TS) as summarized in Table 8.1. Only in the case of CFL=1.0 an accurate solution is achieved although using 20 TS.

Figures 8.5(b) and 8.5(c) show the exact solution at $t = 5s$ and the numerical results obtained with the LTS scheme on the same grid, now supplied with the splitting wave treatment. Different CFL values have been used and are summarized in Table 8.1. The number of time steps used to compute the numerical solution and the number of pieces N_p the discontinuity has been split into are also indicated.

The larger the CFL value is, the more accurate the numerical solution is. Moreover, in this problem there is no upper bound in the choice of the CFL value apart from that imposed by the finite length of the computational domain. Only one time step, of size equal to the total simulation time, can provide the exact solution when the simulation time is less than the time required for the wave to reach the boundaries. In that case, the maximum CFL value would be built with the time increment equal to the total computational time.

	CFL value	**Time steps (TS)**	$\mathbf{N_p}$
No splitting waves	1.0	20	-
	2.0	10	-
	4.0	5	-
	10.0	2	-
	20.0	1	-
Splitting waves	1.0	20	1
	2.0	10	2
	4.0	5	3
	10.0	2	7
	20.0	1	15

Table 8.1: Summary of numerical solutions

(a)

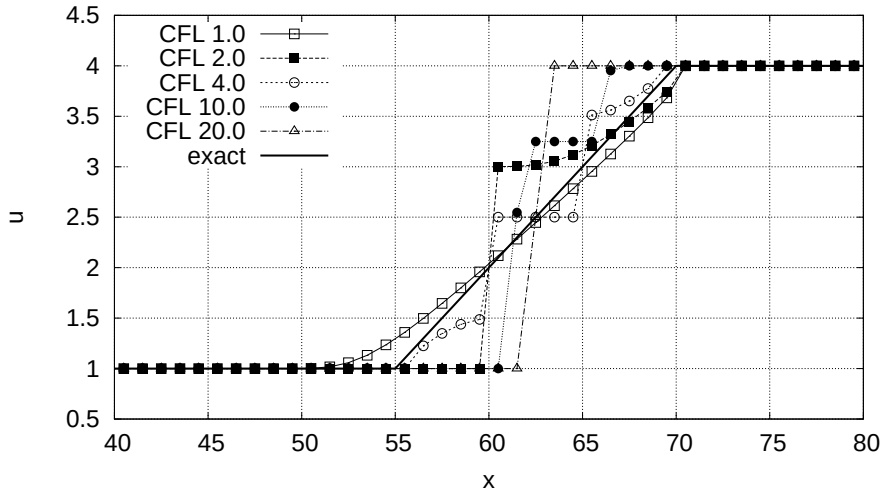

(b)

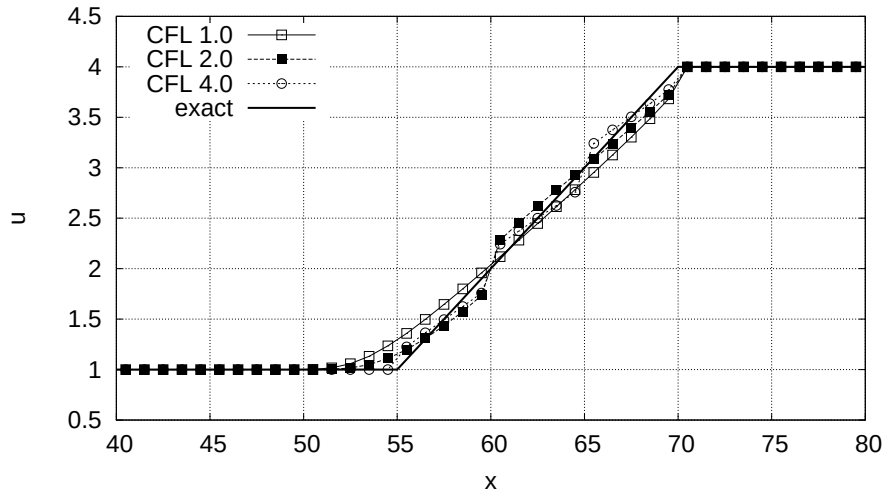

(c)

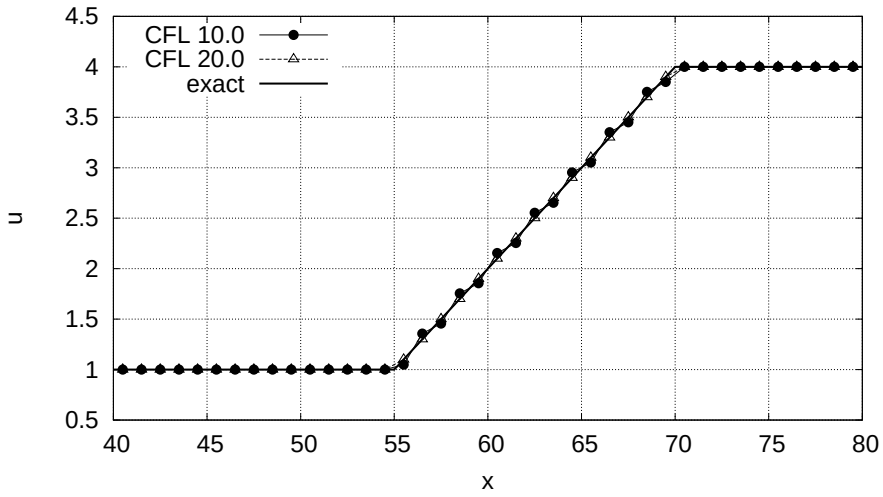

Figure 8.5: Exact and numerical solution of (8.10) (a) No splitting rarefaction wave; (b),(c) Splitting rarefaction wave

8.1.3 Non-linear scalar equation with source terms

Consider now the nonlinear scalar equation with source terms:

$$\frac{\partial u}{\partial t} + \frac{\partial f(u)}{\partial x} = s \tag{8.16}$$

where s is a source term and the local RP:

$$u(x,0) = \begin{cases} u_L = u_i & if \quad x < 0 \\ u_R = u_{i+1} & if \quad x > 0 \end{cases} \tag{8.17}$$

According to Roe's approach and following the ideas developed in Part I, section 2, the solution of the RP is achieved from an approximate solution $\hat{u}(x,t)$ of the locally linearized problem that must fulfil the Consistency Condition [72]. Integrating over a suitable control volume $[-\frac{\Delta x}{2}, \frac{\Delta x}{2}] \times [0, \Delta t]$

$$\int_{\frac{-\Delta x}{2}}^{\frac{\Delta x}{2}} \hat{u}(x,\Delta t)dx = \Delta x\ (u_{i+1}^n + u_i^n) - (f(u_{i+1}^n) - f(u_i^n))\Delta t + s_{i+1/2}\Delta t \tag{8.18}$$

For the last integral involving the source term s, the following linearization in time is assumed

$$\int_0^{\Delta t} \int_{\frac{-\Delta x}{2}}^{\frac{\Delta x}{2}} s(x,t)\, dx\, dt = \int_{\frac{-\Delta x}{2}}^{\frac{\Delta x}{2}} s(x,0)\, dx = s_{i+1/2} \tag{8.19}$$

Following [92], a weak solution of the linear RP in (8.16),(8.17) that satisfies (8.18) in the case $\widetilde{\lambda}_{i+1/2} > 0$ was proposed [92]:

$$\hat{u}(x,t) = \begin{cases} u_i & if \quad x < 0 \\ u_{i+1}^{**} & if \quad 0 < x < \widetilde{\lambda}_{i+1/2}\, t \\ u_{i+1} & if \quad x > \widetilde{\lambda}_{i+1/2}\, t \end{cases} \tag{8.20}$$

where $\widetilde{\lambda}$ is the advection velocity as in (8.9). Note that one wave is associated to the celerity $\widetilde{\lambda}$ and the other wave is steady and also that

$$u_{i+1}^{**} = u_{i+1} - (\widetilde{\theta}\delta u)_{i+1/2} \tag{8.21}$$

with

$$\widetilde{\theta}_{i+1/2} = 1 - \frac{s_{i+1/2}}{f(u_{i+1}) - f(u_i)} \tag{8.22}$$

measuring the relative influence of the source and flux terms

Figure 8.6 is a sketch of the approximate solution when $\widetilde{\lambda}_{i+1/2} > 0$.

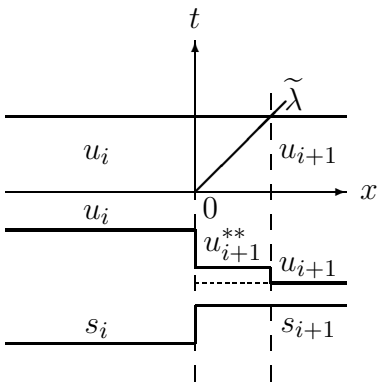

Figure 8.6: Approximate solution for $\hat{u}(x,t)$.

In case that $\widetilde{\lambda}_{i+1/2} < 0$, the procedure is analogous, and the approximate solution is:

$$\hat{u}_(x,t) = \begin{cases} u_i & if \quad x < \widetilde{\lambda}_{i+1/2}\, t \\ u_i^* & if \quad \widetilde{\lambda}_{i+1/2}\, t < x < 0 \\ u_{i+1} & if \quad x > 0 \end{cases} \tag{8.23}$$

with

$$u_i^* = u_i + (\widetilde{\theta}\delta u)_{i+1/2} \tag{8.24}$$

Therefore, the LTS scheme could be written as follows:

If $\widetilde{\lambda}_{i+1/2} > 0$

$$\begin{array}{ll} (\widetilde{\theta}\ \delta u)_{i+1/2} & \text{updates } i+1, \cdots, i+\mu_{i+1/2} \\ (\nu-\mu)_{i+1/2}\ (\widetilde{\theta}\ \delta u)_{i+1/2} & \text{updates } i+\mu_{i+1/2}+1 \end{array} \tag{8.25}$$

If $\widetilde{\lambda}_{i+1/2} < 0$

$$\begin{array}{ll} (\widetilde{\theta}\ \delta u)_{i+1/2} & \text{updates } i, \cdots, i+\mu_{i+1/2}+1 \\ (\nu-\mu)_{i+1/2}\ (\widetilde{\theta}\ \delta u)_{i+1/2} & \text{updates } i+\mu_{i+1/2} \end{array} \tag{8.26}$$

where $\nu_{i+1/2} = \dfrac{\widetilde{\lambda}\Delta t}{\Delta x}$ and $\mu_{i+1/2} = int(\nu_{i+1/2})$

8.1.3.1 First approach: application to Burger's equation with source terms

Consider Burgers's equation including source terms as in [92]:

$$\frac{\partial u}{\partial t} + \frac{1}{2}\frac{\partial u^2}{\partial x} = -u\frac{\partial z}{\partial x} \tag{8.27}$$

with the initial data

$$u(x,0) = u_o(x) = \begin{cases} u_L & if \quad x < 0 \\ u_R & if \quad x > 0 \end{cases} \qquad z(x) = \begin{cases} z_L & if \quad x < 0 \\ z_R & if \quad x > 0 \end{cases} \tag{8.28}$$

The same RP in [92] are going to be presented here, using $\Delta x = 1$ at $t = 15s$. The source term discretization used is

$$s_{i+1/2} = -\frac{1}{2}(u_{i+1} + u_i)(z_{i+1} - z_i) \tag{8.29}$$

enforcing equilibrium in steady states [92]. All the cases are summarized in Table 8.2. More information about the nature and the exact solution of each test case can be found in [92].

Figures 8.7–8.9 plot the results for each test case using different values of CFL. The source term is represented in dashed line, the numerical solutions with CFL=1.0 using $(-\triangle-)$, the numerical solution with CFL=5.0 using $(-\square-)$ and that with CFL=30.0 using $(-\circ-)$. They are compared with the exact solution (——).

Note that CFL=30.0 is the largest value possible leading to one single time step. As can be observed, these test cases are very extreme, particularly the cases 5 and 6 where the source term dominate the convective term. The numerical solution from

Table 8.2: Summary of test cases.

Test case	u_L	u_R	z_L	z_R
1	2.0	1.0	0.0	0.5
2	2.0	1.0	0.0	-0.5
3	1.0	2.0	0.5	0.0
4	1.0	2.0	0.0	0.5
5	2.0	1.0	0.0	1.5
6	1.0	2.0	1.5	0.0

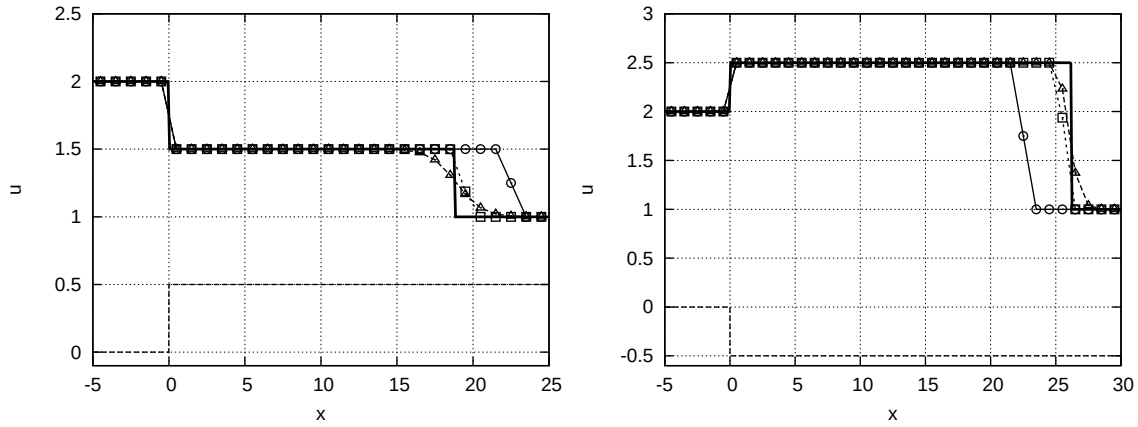

Figure 8.7: Exact (——) and computed solutions at $t = 15s$ for test case 1 (left) and test case 2 (right) using CFL=1.0 ($-\triangle-$), CFL=5.0 ($-\square-$) and CFL=30.0 ($-\circ-$)

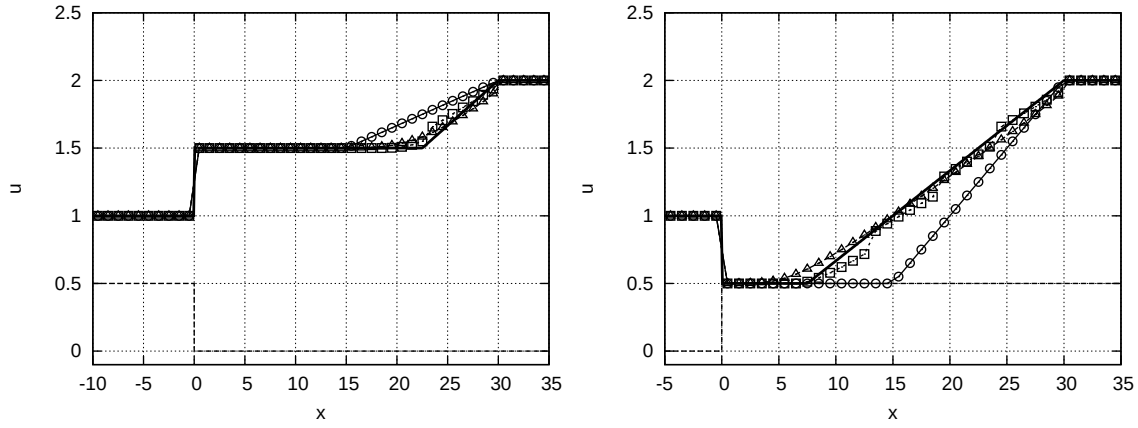

Figure 8.8: Exact (——) and computed solutions at $t = 15s$ for test case 3 (left) and test case 4 (right) using CFL=1.0 ($-\triangle-$), CFL=5.0 ($-\square-$) and CFL=30.0 ($-\circ-$)

the LTS scheme when using CFL>1 is able to approximate the classical upwind explicit (FOU) scheme using CFL=1.0, mainly in the test cases 1, 2, 3 and 4, but is

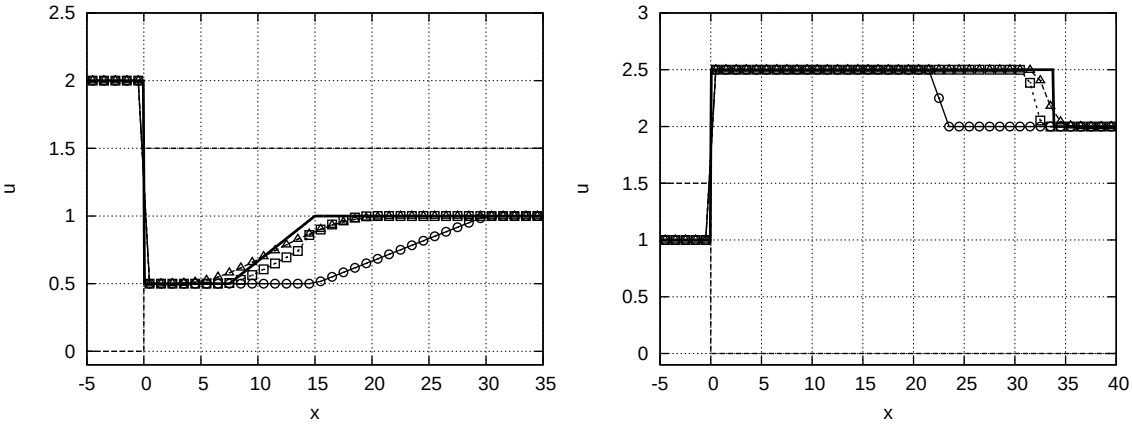

Figure 8.9: Exact (—) and computed solutions at $t = 15s$ for test case 5 (left) and test case 6 (right) using CFL=1.0 ($-\triangle-$), CFL=5.0 ($-\square-$) and CFL=30.0 ($-\circ-$)

not able to approximate the exact solution in a single time step. The main advantage of the LTS scheme is that the time step is not restricted by the CFL condition allowing large Δt values. From FOU, the speed celerity $\widetilde{\lambda}$ is estimated as in the homogeneous case (8.9). The fact is that, in several situations with large source terms that influence the convective term, using the LTS scheme, this linearization could lead to a wrong solution because of an overestimation or underestimation of this value. A way to overcome this situation is proposed.

8.1.3.2 Accurate estimation of the wave celerity

Let s_e be the exact value of the integral of the source term in the control volume

$$s_e = \int_0^{\Delta t} \int_{\frac{-\Delta x}{2}}^{\frac{\Delta x}{2}} s \, dx \, dt \tag{8.30}$$

A better wave celerity $\hat{\lambda}_{i+1/2}$ can be estimated by using directly the information provided by the analytical solution, constructed by means of the appropriate Rankine-Hugoniot (hereafter RH) conditions.

Assuming the RP in (8.17), a weak solution satisfying (8.18) for the case $\hat{\lambda}_{i+1/2} > 0$ is proposed (the case $\hat{\lambda}_{i+1/2} < 0$ is analogous):

$$\hat{u}(x,t) = \begin{cases} u_i & if \quad x < 0 \\ u_{i+1}^{**} & if \quad 0 < x < \hat{\lambda}_{i+1/2}\, t \\ u_{i+1} & if \quad x > \hat{\lambda}_{i+1/2}\, t \end{cases} \tag{8.31}$$

Figure 8.10 is a sketch of the approximate solution in this situation. Enforcing Rankine-Hugoniot conditions across the two waves:

$$\begin{cases} f(u_{i+1}) - f(u_{i+1}^{**}) = \hat{\lambda}_{i+1/2}(u_{i+1} - u_{i+1}^{**}) \\ f(u_{i+1}^{**}) - f(u_i) - s_e = \lambda_s(u_{i+1}^{**} - u_i) = 0 \end{cases} \tag{8.32}$$

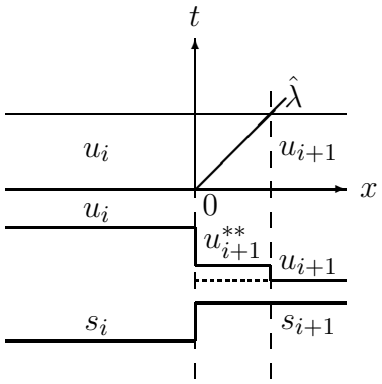

Figure 8.10: Approximate solution for $\hat{u}(x,t)$.

where $\lambda_s = 0$ is the wave celerity associated to the steady discontinuity at $x = 0$. The first RH condition leads to:

$$\hat{\lambda}_{i+1/2} = \frac{f(u_{i+1}) - f(u_{i+1}^{**})}{u_{i+1} - u_{i+1}^{**}} \tag{8.33}$$

In order to apply the method described in (8.25) and (8.26), the consistency condition using the exact integration of the source term over the control volume (8.18) must be checked. Taking into account the second RH condition in (8.32) :

$$s_e = f(u_{i+1}^{**}) - f(u_i) \tag{8.34}$$

Using definitions (8.21), (8.33) and (8.34):

$$\hat{\lambda}_{i+1/2}\,\widetilde{\theta}_{i+1/2}\,\delta u = \hat{\lambda}_{i+1/2}\left(\frac{u_{i+1}-u^{**}_{i+1}}{\delta u}\right)\delta u = \frac{f(u_{i+1})-f(u^{**}_{i+1})}{u_{i+1}-u^{**}_{i+1}}(u_{i+1}-u^{**}_{i+1}) =$$

$$f(u_{i+1}) - f(u^{**}_{i+1}) - f(u_i) + f(u_i) = \delta f_{i+1/2} - s_e \tag{8.35}$$

Hence the consistency of our numerical scheme is proved. Next step is to replace $\widetilde{\lambda}$ by $\hat{\lambda}$ in (8.25) and (8.26) leading to the following algorithm:

If $\hat{\lambda}_{i+1/2} > 0$

$$\begin{array}{ll} (\widetilde{\theta}\,\delta u)_{i+1/2} & \text{updates } i+1,\cdots,i+\mu_{i+1/2} \\ (\nu-\mu)_{i+1/2}\,(\widetilde{\theta}\,\delta u)_{i+1/2} & \text{updates } i+\mu_{i+1/2}+1 \end{array} \tag{8.36}$$

If $\hat{\lambda}_{i+1/2} < 0$

$$\begin{array}{ll} (\widetilde{\theta}\,\delta u)_{i+1/2} & \text{updates } i,\cdots,i+\mu_{i+1/2}+1 \\ |\nu-\mu|_{i+1/2}\,(\widetilde{\theta}\,\delta u)_{i+1/2} & \text{updates } i+\mu_{i+1/2} \end{array} \tag{8.37}$$

where $\nu_{i+1/2} = \dfrac{\hat{\lambda}\Delta t}{\Delta x}$ and $\mu_{i+1/2} = int(\nu_{i+1/2})$

8.1.3.3 Second approach: application to the Burgers equation with source terms

Considering (8.27), the RP in (8.28) and the test cases in table 8.2, the performance of the first and second approaches of the wave celerity is evaluated at $t = 15s$ and computed with $\Delta x = 1$. The same source term discretization as in (8.29) is used, representing it in dashed line. The numerical solutions with CFL=1.0 ($-\triangle-$), with CFL=30.0 using $\widetilde{\lambda}$ as wave celerity ($-\circ-$) and with CFL=30.0 using $\hat{\lambda}$ as wave celerity ($-\bullet-$) are going to be compared with the exact solution (——) in Figures 8.11–8.13. Also the splitting rarefaction treatment as explained in (8.12) has been used for computing the numerical solutions with the LTS scheme.

The main conclusion is that the LTS scheme, including a good source term treatment is less diffusive than the conventional explicit upwind scheme and it can be able to

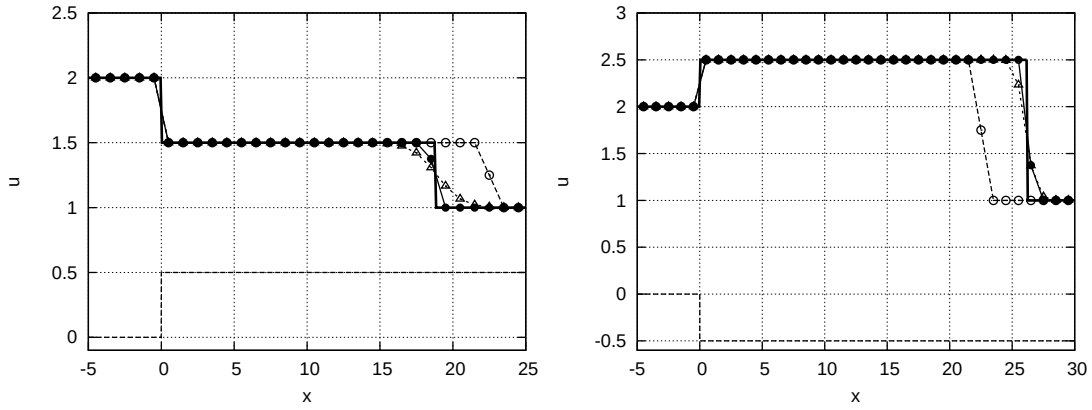

Figure 8.11: Exact (——) and computed solutions at $t = 15s$ for test case 1 (left), and test case 2 (right) using CFL=1.0 ($-\triangle-$), CFL=30.0 with $\widetilde{\lambda}$ as wave celerity ($-\circ-$) and CFL=30.0 with $\hat{\lambda}$ as wave celerity ($-\bullet-$)

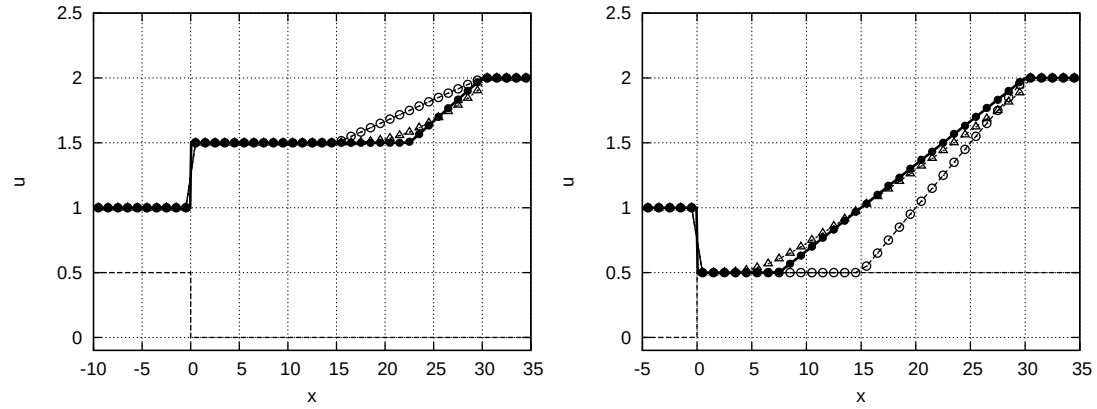

Figure 8.12: Exact (——) and computed solutions at $t = 15s$ for test case 3 (left), and test case 4 (right) using CFL=1.0 ($-\triangle-$), CFL=30.0 with $\widetilde{\lambda}$ as wave celerity ($-\circ-$) and CFL=30.0 with $\hat{\lambda}$ as wave celerity ($-\bullet-$)

reproduce the exact solution. However, if no correction in the estimation of the wave celerity is applied, the numerical solution is not able to approximate the exact solution. Maybe, when using the FOU scheme there is no noticeable difference between the two approaches of the wave celerity, because the method is forced to work with small time steps but the LTS scheme allows larger time steps, and therefore important error is introduced if a careless estimation of the wave celerity is applied. Note that this improvement has been possible in the particular case of a scalar equation with known exact solution.

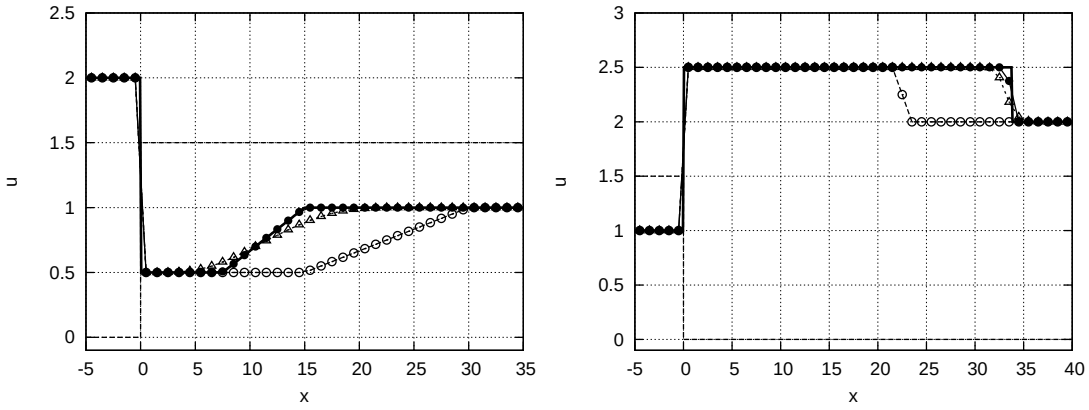

Figure 8.13: Exact (—) and computed solutions at $t = 15s$ for test case 5 (left), and test case 6 (right) using CFL=1.0 ($-\triangle-$), CFL=30.0 with $\widetilde{\lambda}$ as wave celerity ($-\circ-$) and CFL=30.0 with $\hat{\lambda}$ as wave celerity ($-\bullet-$)

Chapter 9

LTS scheme for the 1D shallow water equations

9.1 1D systems of conservation laws with source terms

The extension of the proposed LTS scheme to systems of equations with source terms is discussed in this section. A 2×2 hyperbolic nonlinear system of equations can be expressed in the form

$$\frac{\partial \mathbf{U}}{\partial t} + \frac{\partial \mathbf{F}}{\partial x} = \mathbf{S} \tag{9.1}$$

where $\mathbf{U}$ is the vector of conserved variables, $\mathbf{F}$ is the vector of fluxes of these conserved variables and $\mathbf{S}$ represents the vector of source terms. A Jacobian matrix $\mathbf{J}$ can be defined

$$\mathbf{J} = \frac{d\mathbf{F}}{d\mathbf{U}} \tag{9.2}$$

The strictly hyperbolicity property of the system ensures that the two eigenvalues λ^1, λ^2 of the Jacobian are real and different and it is possible to define two matrices $\mathbf{P} = (\mathbf{e}^1, \mathbf{e}^2)$ and $\mathbf{P}^{-1}$, with $\mathbf{e}^1, \mathbf{e}^2$ the eigenvectors of $\mathbf{J}$, achieving the diagonalization:

$$\mathbf{J} = \mathbf{P}\mathbf{\Lambda}\mathbf{P}^{-1} \tag{9.3}$$

Provided that Roe's linearization [109] is used to uncouple the homogeneous part of

the system, an approximate Jacobian matrix $\tilde{\mathbf{J}}_{i+1/2}$ can be built whose eigenvalues $\widetilde{\lambda}^1, \widetilde{\lambda}^2$ and eigenvectors $\widetilde{\mathbf{e}}^1, \widetilde{\mathbf{e}}^2$ allow to express the difference in vector $\mathbf{U}$ as well as in the linearized source term $\mathbf{S}_{i+1/2}$:

$$\delta\mathbf{U}_{i+1/2} = \sum_{m=1}^{2} (\alpha\ \widetilde{\mathbf{e}})_{i+1/2}^{m} \qquad \mathbf{S}_{i+1/2} = \sum_{m=1}^{2} (\beta\ \widetilde{\mathbf{e}})_{i+1/2}^{m} \tag{9.4}$$

Therefore, the first order upwind (FOU) explicit scheme can be written as in Part I, 2.57:

$$\mathbf{U}_i^{n+1} = \mathbf{U}_i^n - \frac{\Delta t}{\Delta x}\left((\delta\mathbf{F} - \mathbf{S})_{i-1/2}^{+} + (\delta\mathbf{F} - \mathbf{S})_{i+1/2}^{-}\right)^n \tag{9.5}$$

where

$$(\delta\mathbf{F} - \mathbf{S})_{i+1/2}^{\pm} = \sum_{m=1}^{2} \left(\widetilde{\lambda}^{\pm}\ \widetilde{\gamma}\ \widetilde{\mathbf{e}}\right)_{i+1/2}^{m} \qquad \tilde{\gamma}_{i+1/2}^{m} = \left(\tilde{\alpha} - \frac{\tilde{\beta}}{\tilde{\lambda}}\right)_{i+1/2}^{m} \tag{9.6}$$

Following the analogy developed for the expression of the LTS scheme for the scalar case, it can be formulated for systems of conservation laws as follows:

If $\widetilde{\lambda}_{i+1/2} > 0$

$$\begin{array}{ll} (\gamma\ \widetilde{\mathbf{e}})_{i+1/2}^{m} & \text{updates } i+1, \cdots, i+\mu_{i+1/2} \\ (\nu-\mu)_{i+1/2}^{m}\,(\gamma\ \widetilde{\mathbf{e}})_{i+1/2}^{m} & \text{updates } i+\mu_{i+1/2}+1 \end{array} \tag{9.7}$$

If $\widetilde{\lambda}_{i+1/2} < 0$

$$\begin{array}{ll} (\gamma\ \widetilde{\mathbf{e}})_{i+1/2}^{m} & \text{updates } i, \cdots, i+\mu_{i+1/2}+1 \\ (\nu-\mu)_{i+1/2}^{m}\,(\gamma\ \widetilde{\mathbf{e}})_{i+1/2}^{m} & \text{updates } i+\mu_{i+1/2} \end{array} \tag{9.8}$$

where $\nu_{i+1/2}^{m} = \dfrac{\Delta t}{\Delta x}\widetilde{\lambda}_{i+1/2}^{m}$ and $\mu_{i+1/2}^{m} = int(\nu_{i+1/2}^{m})$. It is worth indicating that the assumption of Leveque's original LTS scheme consisting of a linear interaction between the waves underlies the proposed LTS scheme, introducing also some source of inaccuracy and the risk of losing robustness (TVD property) in the presence of strong discontinuities. However, other approaches considering the formulation of the non-linear interactions of waves in terms of colliding times and distances are also explored in the literature (see [106],[107]).

9.2 Application to the 1D shallow water equations

The 1D shallow water equations are a good candidate to apply these techniques. As a reminder, they are written in a differential conservative form as follows:

$$\mathbf{U} = \begin{pmatrix} A \\ Q \end{pmatrix}, \quad \mathbf{F} = \begin{pmatrix} Q \\ \frac{Q^2}{A} + gI_1 \end{pmatrix} \quad \mathbf{S} = \begin{pmatrix} 0 \\ g\left[I_2 + A\left(S_0 - S_f\right)\right] \end{pmatrix} \tag{9.9}$$

The approximate Jacobian $\widetilde{\mathbf{J}}$ is

$$\tilde{\mathbf{J}}_{i+1/2} = \begin{pmatrix} 0 & 1 \\ \widetilde{c}^2 - \widetilde{u}^2 & 2\widetilde{u} \end{pmatrix}_{i+1/2} \tag{9.10}$$

with [16]

$$\widetilde{c} = \sqrt{g\frac{(A/b)_i + (A/b)_{i+1}}{2}} \quad \widetilde{u} = \frac{Q_{i+1}\sqrt{A_{i+1}} + Q_i\sqrt{A_i}}{\sqrt{A_{i+1}} + \sqrt{A_i}} \tag{9.11}$$

where b is the top width. The resulting set of approximate eigenvalues and eigenvectors is

$$\begin{aligned} \widetilde{\lambda}^1 &= \widetilde{u} - \widetilde{c} \qquad \widetilde{\lambda}^2 = \widetilde{u} + \widetilde{c} \\ \widetilde{\mathbf{e}}^1 &= \begin{pmatrix} 1 \\ \widetilde{u} - \widetilde{c} \end{pmatrix} \qquad \widetilde{\mathbf{e}}^2 = \begin{pmatrix} 1 \\ \widetilde{u} + \widetilde{c} \end{pmatrix} \end{aligned} \tag{9.12}$$

Different questions related to the nature of the 1D shallow water equations arise such as the rarefaction splitting technique or the boundary conditions.

9.2.1 Rarefaction splitting treatment

Using the LTS scheme (9.7), (9.8), when a rarefaction appears in the context of the SWE, it can be split in several waves travelling at different speeds ensuring exact

conservation in the sense of Roe. This is demonstrated here in the particular case of a rarefaction wave split in two pieces.

When representing a rarefaction through a unique wave $\tilde{\lambda}$ at interface $i+1/2$, the quantity $(\nu\gamma\tilde{e})_{i+1/2} = \dfrac{\tilde{\lambda}_{i+1/2}\Delta t}{\Delta x}(\gamma\tilde{e})_{i+1/2}$ is sent. The aim of the splitting is originating two waves, $\tilde{\lambda}^a_{i+1/2}$ and $\tilde{\lambda}^b_{i+1/2}$, that, in order to be conservative verify

$$\frac{\tilde{\lambda}_{i+1/2}\Delta t}{\Delta x}(\gamma\tilde{e})_{i+1/2} = \frac{\tilde{\lambda}^a_{i+1/2}\Delta t}{\Delta x}(\gamma^a\tilde{e})_{i+1/2} + \frac{\tilde{\lambda}^b_{i+1/2}\Delta t}{\Delta x}(\gamma^b\tilde{e})_{i+1/2} \tag{9.13}$$

Therefore enforcing

$$(\tilde{\lambda}\gamma)_{i+1/2} = (\tilde{\lambda}^a\gamma^a)_{i+1/2} + (\tilde{\lambda}^b\gamma^b)_{i+1/2} \tag{9.14}$$

According to (9.14), the definition of $\gamma^a_{i+1/2}$ and $\gamma^b_{i+1/2}$ follows

$$\gamma^a_{i+1/2} = \gamma_{i+1/2}\left(\frac{\tilde{\lambda}^b - \tilde{\lambda}}{\tilde{\lambda}^b - \tilde{\lambda}^a}\right)_{i+1/2} \qquad \gamma^b_{i+1/2} = \gamma_{i+1/2}\left(\frac{\tilde{\lambda} - \tilde{\lambda}_a}{\tilde{\lambda}^b - \tilde{\lambda}^a}\right)_{i+1/2} \tag{9.15}$$

There is some freedom for the choice of $\tilde{\lambda}^a_{i+1/2}$ and $\tilde{\lambda}^b_{i+1/2}$ for example, they could be defined as follows:

$$\tilde{\lambda}^a_{i+1/2} = \varepsilon\ (\lambda_i + \tilde{\lambda}_{i+1/2}) \qquad \tilde{\lambda}^b_{i+1/2} = (1-\varepsilon)\ (\lambda_{i+1} + \tilde{\lambda}_{i+1/2}) \tag{9.16}$$

where ε is a free parameter (preferably close to 0.5). The choice of the number of pieces N_p that the rarefaction is split into is again related to the integer part of the wave strength, that is,

$$N_p \approx int\left(\frac{\gamma_{i+1/2}\tilde{e}_1\ \Delta t}{\Delta x}, \frac{\gamma_{i+1/2}\tilde{e}_2\ \Delta t}{\Delta x}\right) \tag{9.17}$$

As mentioned above, this procedure has been described for the splitting of a wave into two waves in a conservative way. When splitting the wave in a general number of pieces N_p, the strategy could become tedious. An alternative way consisting of using the previous information is adopted in this work. Given N_p, computed with an equality in (9.17), it is rounded to a number of the form $\overline{N_p} = 2^k$ being k an integer. Therefore, the procedure reduces to apply the previous algorithm recursively (each

wave into two sub-waves, each sub-wave into two sub-sub-waves and so on) to split the initial wave into a number of travelling waves $\overline{N_p}$, similar to the strength of the wave.

9.2.2 Boundary conditions

The boundary conditions dicretization is another issue of importance and requires a careful consideration. In the context of the shallow water equations, open boundaries and closed boundaries can appear and are going to be analyzed.

In the case of open boundaries, two flow situations can be distinguished: subcritical and supercritical. When dealing with a supercritical outlet boundary, no external information is required. In fact, the boundary cell receives the information coming from the inner cells according to the scheme provided in (9.7) and (9.8). If some of the contributions cross the boundary they are stored at inlet and outlet 'ghost bags' in order to control the conservation property but they do not affect the updated solution of the boundary cell (Figure 9.1).

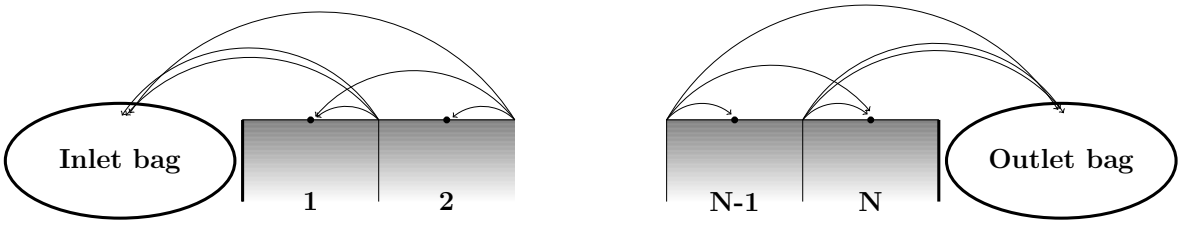

Figure 9.1: Open boundaries in the LTS scheme

In case of having subcritical inlet or outlet boundary, one variable is externally imposed as physical boundary conditions and the other variable is calculated using the updating information arriving from the inner interfaces. Also some of the contributions cross the boundary, so they are stored as in the supercritical case.

At closed boundaries, two possible techniques are proposed: an accumulation technique and a reflection technique. Consider the downstream boundary at node N (the reasoning for the upstream boundary is analogous) and the information from edge *i+1/2* ($\widetilde{\lambda}_{i+1/2} > 0$). If $i+\mu_{i+1/2}+1 > N$, some of the contributions from *i+1/2* go out of the downstream end of the domain. As the solid wall condition requires that no information crosses the boundary and the method must remain conservative, the

accumulation technique stores these contributions at the downstream boundary cell N as shown in Figure 9.2 (a). On the other hand, the reflection technique considers the downstream outlet edge as a mirror, sending the information that would cross the boundary back to the corresponding cell. It can be seen in Figure 9.2 (b).

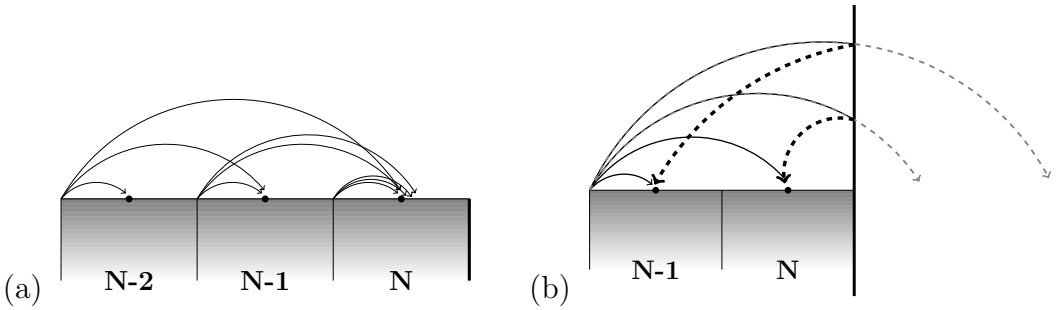

Figure 9.2: Closed boundary treatment: (a) Accumulation technique and (b) Reflection technique

9.2.3 Entropy fix, source terms, CFL limit and the choice of the target CFL

The LTS scheme formulated in this work is actually an alteration of the basic Roe scheme where larger CFL values can be used. As it is well known, the basic explicit scheme requires some kind of correction in order to avoid non-physical situations near sonic points. This correction, called entropy fix, must also be applied in the proposed LTS scheme. The version of the Harten-Hyman entropy fix [118], detailed in Part I, section 3.3.3 has been adopted.

As detailed in the previous chapters, an upwind discretization for the source term related not only with the bed slope but also with the friction term is adopted according to [92] . This treatment is able to satisfy the preservation of steady-states in the context of the shallow water equations providing discrete evaluations of the source term that ensure energy dissipating solutions when demanded. Also the wet/dry front has been formulated following [92], avoiding the appearance of negative values of water depth. A more accurate estimation of the wave celerities in presence of strong source terms or big discontinuities could be based on the three Rankine-Hugoniot conditions associated to the approximate solution, according to the idea suggested in the non-linear scalar case. However, due to the mutual dependence

between the waves celerities and the intermediate states $\mathbf{U}^*$ and $\mathbf{U}^{**}$, there is not a simple or straightforward procedure [111] to achieve an accurate solution at very high CFL numbers (associated to only one or two time steps in total). Therefore, instead of seeking a correction in the wave speeds in presence of strong source terms or big discontinuities, the present work is focused on applying a reduction on the CFL value. This is next explained.

A parameter that includes the influence not only of the size of the discontinuity in the water cross section but also of the initial values is considered as proposed in [97]:

$$\xi_1 = \frac{min_i\{|A_i|, |A_{i+1}|, |\delta A_{i+1/2}|\}}{|\delta A_{i+1/2}|} \qquad 1 \leq i \leq N \tag{9.18}$$

where $0 \leq \xi_1 \leq 1$. Also, a second parameter ξ_2 is defined incorporating the equivalent influence of the bed slope source term as follows:

$$\xi_2 = \frac{min_i\{|d_i|, |d_{i+1}|, |\delta d_{i+1/2}|\}}{|\delta d_{i+1/2}|} \qquad 1 \leq i \leq N \tag{9.19}$$

where $0 \leq \xi_2 \leq 1$ and $d = h + z$ is the water surface level. Let ξ be the minimum of these two parameters,

$$\xi = min(\xi_1, \xi_2) \tag{9.20}$$

If A or d are gradually varied functions, $\xi = 1$ and it is not necessary to diminish the CFL value. Otherwise, a reduction in the CFL initial value, i.e., in the time step, is required in order to achieve a good solution. In this work, the value $\xi = 0.25$ is proposed as a limit. Under this value, the CFL number will be reduced to 1.0 recovering the original Roe's method and over this value, a linear interpolation between 1.0 and the CFL number chosen initially according to the parameter ξ is submitted. Therefore, the final CFL value (CFL_l) can be expressed as follows:

$$\text{CFL}_l = \begin{cases} 1.0 & if \quad \xi < 0.25 \\ 1.0 + \dfrac{\text{CFL} - 1.0}{0.75}(\xi - 0.25) & if \quad \xi \geq 0.25 \end{cases} \tag{9.21}$$

An alternative way to proceed could be to establish the limit in $\xi = 1.0$. Under this number the CFL value will be reduced to 1.0. Also in the case where a flow regime

transitions occur (mainly in hydraulic jumps) the CFL number is reduced to ensure the correct solution of the problem.

The initially chosen CFL value is a very important part in the LTS scheme because it is responsible not only for an accurate and non-oscillatory numerical solution but also for the computational speed. It is not clear 'a priori' what is the optimum CFL target in each case, but some factors should be taken into account when choosing it and there are some restrictions and recommendations to be made. One of them is the number of cells, and there is an obvious geometrical restriction in that the CFL value must be less than the number of cells involved. The performance of the LTS scheme shows that the information is sent to a number of neighbouring cells according to the CFL value, so that if no restriction is imposed over the ratio CFL/number of cells, the relevant information is lost through the boundaries. Apart from that, in the case of convergence to steady states, a suitable choice for the target CFL value could be one order of magnitude below the number of cells. In cases of convergence to discontinuous steady state, the initial CFL target value will be internally reduced by the proposed algorithm (9.21), slowing accordingly the speed of the calculation but not affecting the global stability. In unsteady flow simulations, the time stepping does not work as an iterative method and the recommendation is to choose a CFL target value two orders of magnitude below the number of cells.

9.3 Numerical results

A set of cases is proposed in this chapter to test the proposed LTS scheme in 1D shallow water context. Steady and unsteady scenarios are considered and different problems where the bed slope and the friction terms play a leading role are analysed.

9.3.1 Test case 1: Subcritical dambreak

This test case is firstly proposed with the intention of examining the performance of the rarefaction splitting technique. A flat frictionless rectangular channel 100 m long, 1 m wide is considered, with initial conditions of zero velocity and a discontinuity in the water level surface

$$h(x, t = 0) = \begin{cases} 4m & \text{if} \quad x < 50\text{m} \\ 1m & \text{if} \quad x > 50\text{m} \end{cases} \tag{9.22}$$

Two numerical solutions using the LTS scheme computed with CFL=5.0 and $\Delta x = 1.0m$ are compared with the exact solution (——). The results from the LTS scheme with rarefaction splitting are plotted using $(- \bullet -)$, those from the LTS without splitting are plotted using $(- \circ -)$ in Figure 9.3 (upper) and (lower) for the water depth and discharge respectively after $t = 3s$. Although oscillations appear in the presence of the shock wave in both numerical solutions, the LTS scheme using the split rarefactions is more accurate than the LTS scheme without the splitting treatment.

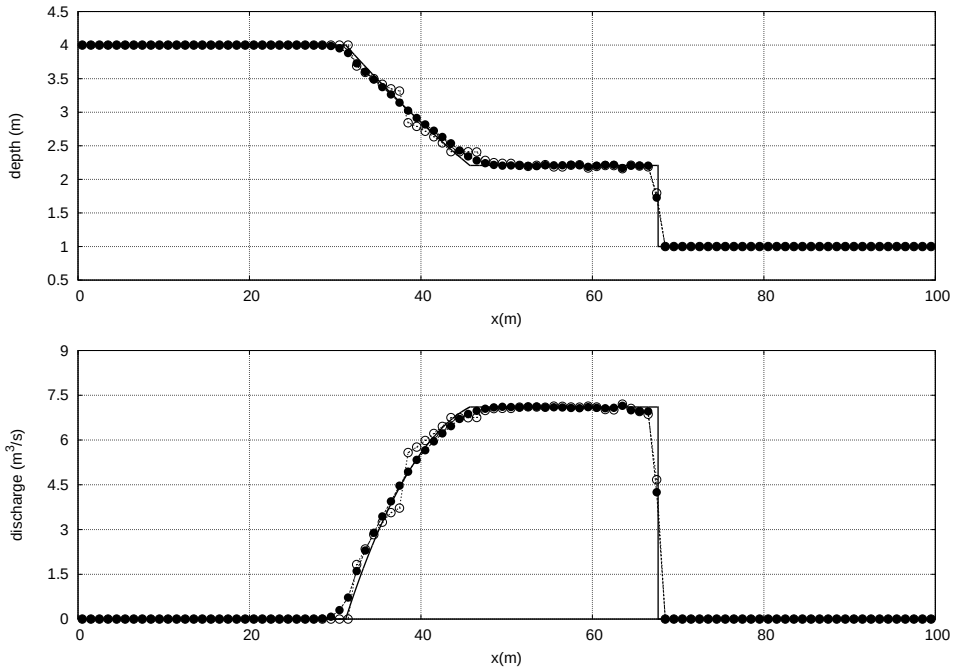

Figure 9.3: Test case 1: Exact (——) and numerical solutions at $t = 3s$ for the depth (upper), and the discharge (lower) using splitting $(- \bullet -)$ and no splitting $(- \circ -)$ rarefaction treatment

9.3.2 Test case 2: Dambreak with closed boundaries

Test case 2 deals with the same geometry and initial conditions as the previous test case and its main purpose is to evaluate the performance of the accumulation

and reflection technique proposed when dealing with closed boundaries. Thus, solid walls at $x = 0\ m$ and at $x = 100\ m$ are considered.

After several seconds the shock and the rarefaction waves arrive to the end of the domain and rebound. The numerical solutions with the LTS scheme are computed again with CFL=5.0 and $\Delta x = 1.0m$. The two ways of dealing with the closed boundaries, accumulation ($-\circ-$) and reflection ($-\bullet-$) technique are compared with the exact solution (——) at t=10.5s (Figure 9.4) and at t=16.5 (Figure 9.5) for the water depth (left) and for the discharge (right)).

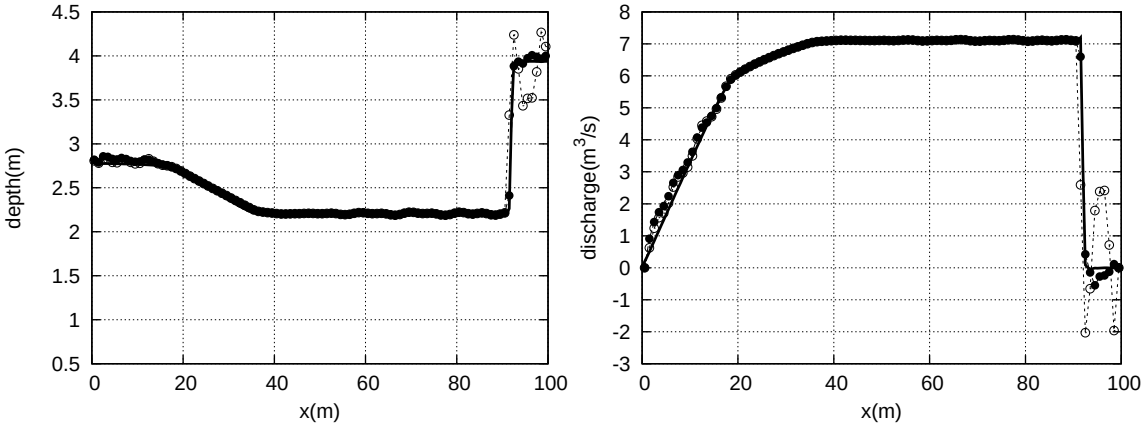

Figure 9.4: Test case 2: Exact (——) and numerical solutions at $t = 10.5s$ for the depth (left) and the discharge (right) using the accumulation ($-\circ-$) and reflection ($-\bullet-$) technique

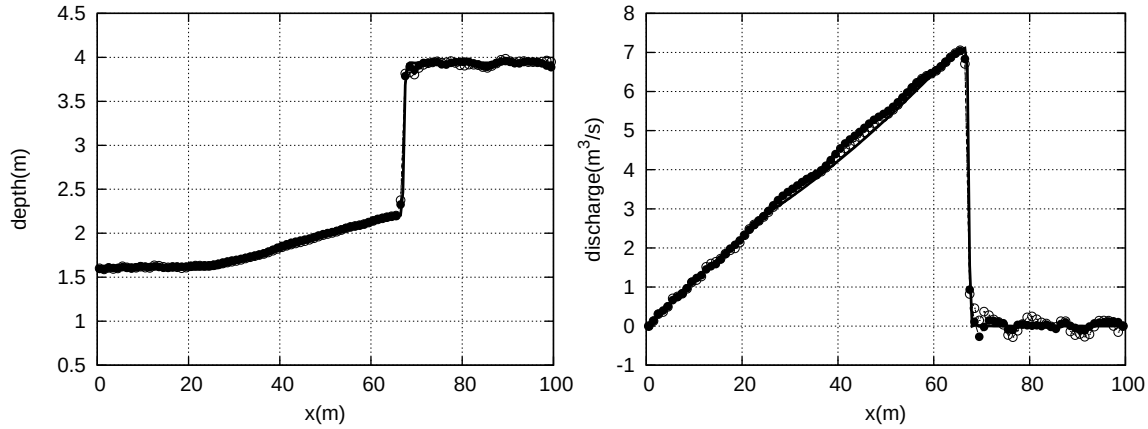

Figure 9.5: Test case 2: Exact (——) and numerical solutions at $t = 16.5s$ for the depth (left) and the discharge (right) using the accumulation ($-\circ-$) and reflection ($-\bullet-$) technique

The results highlight that the reflection technique achieves more accurate solutions than the accumulation technique mainly near the time when the waves collide with the solid walls. After the reflection, the two techniques provide similar results. Therefore, the reflection technique is preferred here because the LTS scheme using very large CFL numbers in closed boundaries could lead the boundary cells to accumulate excessive information in a time step producing oscillations and non-physical situations.

9.3.3 Test case 3, 4 and 5: application to steady flow with source terms

Three examples from [79, 78], considering open channel flow with analytical solutions, are used here. They both apply a Manning friction coefficient $n = 0.03$, have been simulated with $\Delta x = 1.0$ and the inlet discharge is 20 m^3/s. In test case 3 the flow is subcritical all along the 150 m length and the 10 m wide rectangular channel. The downstream boundary condition is a fixed height. The steady water depth is:

$$h(x) = 0.8 + 0.25\ exp\left(33.75\left(\frac{x}{150} - 0.5\right)^2\right) \tag{9.23}$$

Test case 4 corresponds to a trapezoidal channel with 10 m bottom width and 200 m length. The side slope of the channel is 2, and there is not downstream boundary condition. Hence, a smooth transition between subcritical flow upstream (at the first half of the reach) and supercritical flow downstream (at the second half) takes place. Here, the steady water depth is expressed as follows:

$$h(x) = 0.706033 - 0.25\ tanh\left(\frac{x - 100}{50}\right) \tag{9.24}$$

In test case 5, the 10 m wide rectangular channel steepens and then flattens out again along the 150 m lenght. The solutions changes smoothly from subcritical flow to supercritical flow at $x = 50m$. After it return via a hydraulic jump to subcritical flow at $x = 100m$. The downstream boundary condition is a fixed height of 1.700225 m and the steady water depth is:

$$h(x) = 0.741617 - \frac{0.25}{tanh(3)}\, tanh\left(3\frac{x-50}{50}\right) \tag{9.25}$$

The results for these test cases can be observed in Figures 9.6, 9.7 and 9.8 where the numerical solution using CFL = 60.0 ($-\circ-$) is compared with the exact solution (——). The bed level is represented in dashed line.

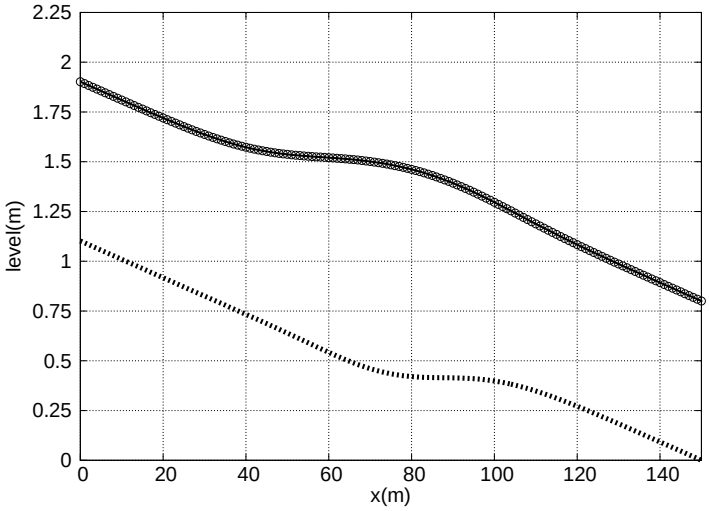

Figure 9.6: Test case 3: Exact (——) and numerical ($-\circ-$) solution using CFL 60.0

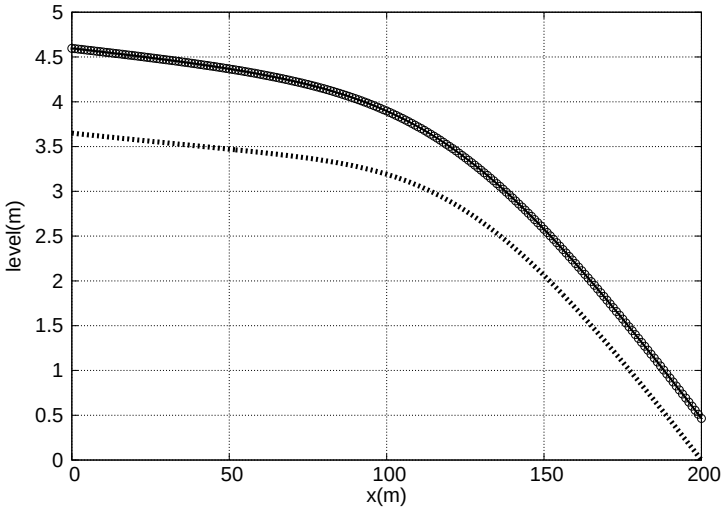

Figure 9.7: Test case 4: Exact (——) and numerical ($-\circ-$) solution using CFL 60.0

The results indicate that the LTS scheme is really valid for computing steady states with very large CFL numbers only accessible for the implicit methods. In fact, the

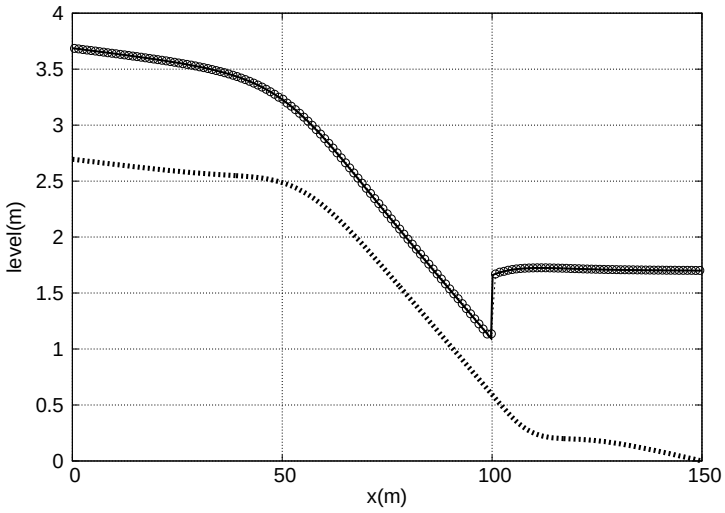

Figure 9.8: Test case 5: Exact (——) and numerical ($-\circ-$) solution using CFL 60.0

L_1-error obtained for the discharge is in the order or magnitude of the machine accuracy for test cases 4 and 5 (10^{-16}) and 3.12×10^{-3} due to the wrong peak generated in the upwind Roe's scheme in the presence of hydraulic jumps (see part I).

The CFL limiter presented before is also activated in order to ensure the correct solution of the numerical approach. Figure 9.9 provides the information about the evolution of the time step in each test case.

The time step value using CFL=1.0 in test case 1 is near 0.18 in comparison with the LTS scheme using CFL=60.0 where the time step value is near 8.91. In the second test case, the time step using CFL 1.0 is near 0.16 whereas using CFL=60.0, after several oscillations related with the CFL limiter and the smooth transition, arrives to 7.95 approximately. In test case 3 a hydraulic jump occurs, and the CFL value is suddenly limited to 2.0, so there is no much difference between the time step in the LTS scheme using CFL=60.0 (the actual CFL value used is near 2.0) and the conventional explicit upwind method with CFL=1.0.

9.3.4 Test cases 6-11: application to dambreak problem over a step

The unsteady flow induced by and ideal dambreak is the most widely used test case for numerical schemes of the kind considered here. Combining it with large

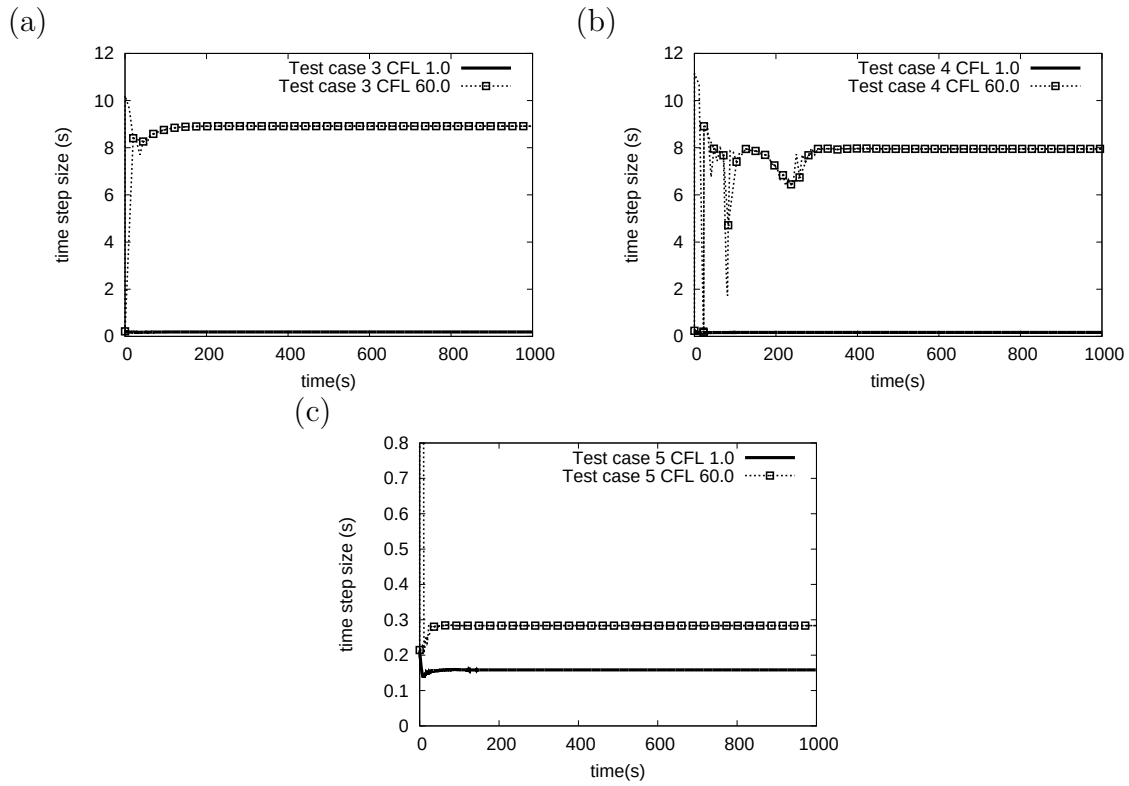

Figure 9.9: Evolution of the time step: (a) test case 3, (b) test case 4 and (c) test case 5

source terms represented by discontinuous bed becomes a powerful tool to evaluate how robust and accurate a numerical scheme can be. The results are going to be presented as follows: the numerical solution provided by the LTS scheme with CFL=5.0 ($-\bullet-$) is compared with the numerical solution obtained with the FOU (first order upwind) scheme with CFL=1.0 ($-\circ-$) and also with the exact solution of each problem (—).

As detailed in part I, due to the controversy around the integration of the bed step in a dambreak problem, there exists multiplicity of solutions. For these test cases, the philosophy followed by Murillo in [92] is adopted: assuming a piecewise representation of the bed level and a hydrostatic pressure distribution, the force exerted over the bed step is enforced to depend only on the free surface side in contact to the bed step. This hypothesis acts as a closure for the dambreak problem over a bed step and allows to deduce analytical solutions for these kind of situations. The same philosophy when computing the numerical solution is adopted for the bed slope source term not only for the LTS scheme but also for the FOU scheme.

The geometry of all of them is a rectangular frictionless 100m long channel with a

bottom step at $x = 0$ and a variable height at each side of the bed discontinuity. All of this test cases are included in [92] and more information about the nature and the exact solution can be found there. The test cases computed here are summarised in Table 9.1 and do not include wet/dry front since, in those cases, the LTS simply reduces to the FOU scheme.

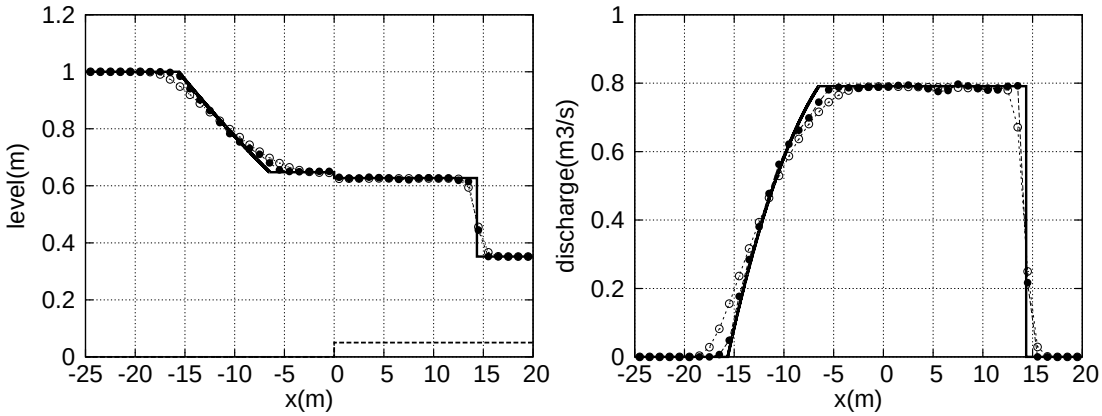

Figure 9.10: Test case 6: Exact (—) and numerical solutions at $t = 5s$ using CFL=1.0 ($-\circ-$) and CFL=5.0 ($-\bullet-$) for the water level surface (left) and the discharge (right)

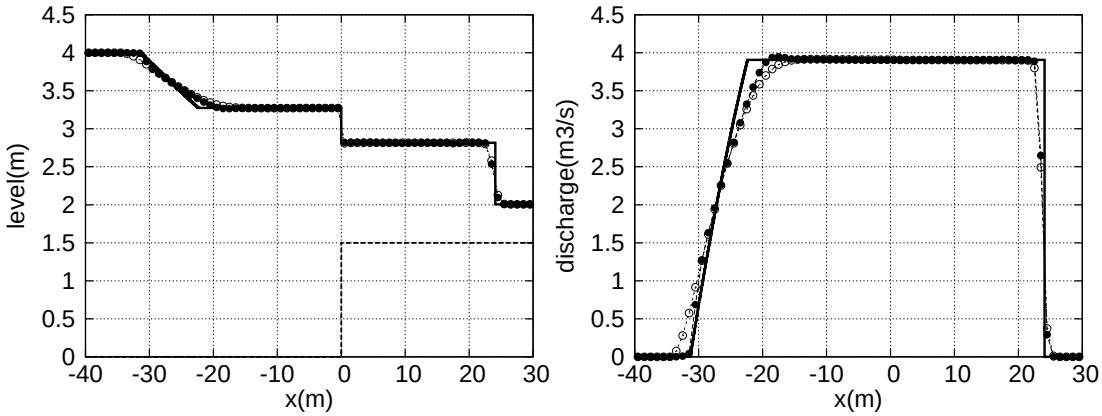

Figure 9.11: Test case 7: Exact (—) and numerical solutions at $t = 5s$ using CFL=1.0 ($-\circ-$) and CFL=5.0 ($-\bullet-$) for the water level surface (left) and the discharge (right)

All the numerical solutions are computed with $\Delta x = 1.0$. Also, for the numerical solution provided by the LTS scheme, the parameter ξ in (9.20) using to reduce the time step at big discontinuities has been applied.

The results are presented in the form of plots of the water level surface and discharge for each test case (Figures 9.10–9.15). The topography is represented in dashed line.

Table 9.1: Summary of test cases.

Test Case	h_L	h_R	u_L	u_R	z_L	z_R
6	1.0	0.30179953	0.0	0.0	0.0	0.05
7	4.0	0.50537954	0.1	0.0	0.0	1.5
8	2.5	2.49977381	1.5	0.0	0.0	0.25
9	1.5	0.16664757	2.0	0.0	0.0	2.0
10	1.0	0.04112267	0.2	0.0	0.25	0.0
11	0.6	0.02599708	0.35	0.0	1.2	0.0

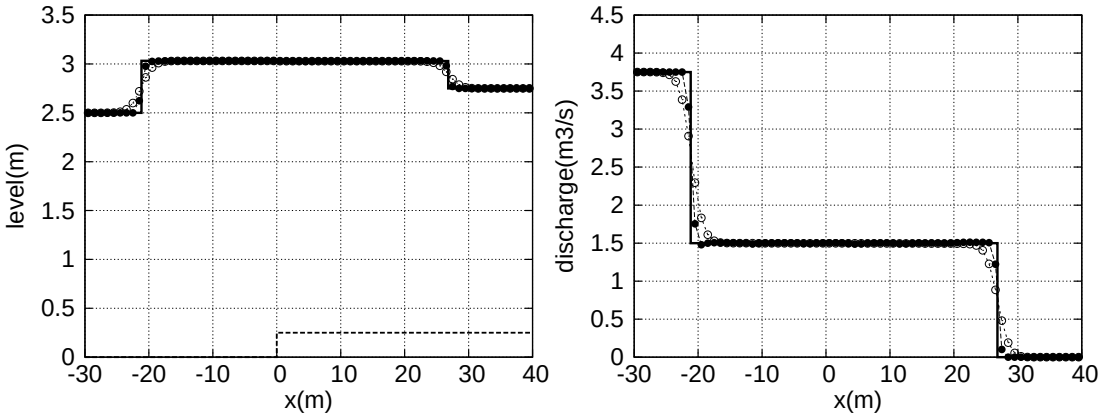

Figure 9.12: Test case 8: Exact (—) and numerical solutions at $t = 5s$ using CFL=1.0 ($-\circ-$) and CFL=5.0 ($-\bullet-$) for the water level surface (left) and the discharge (right)

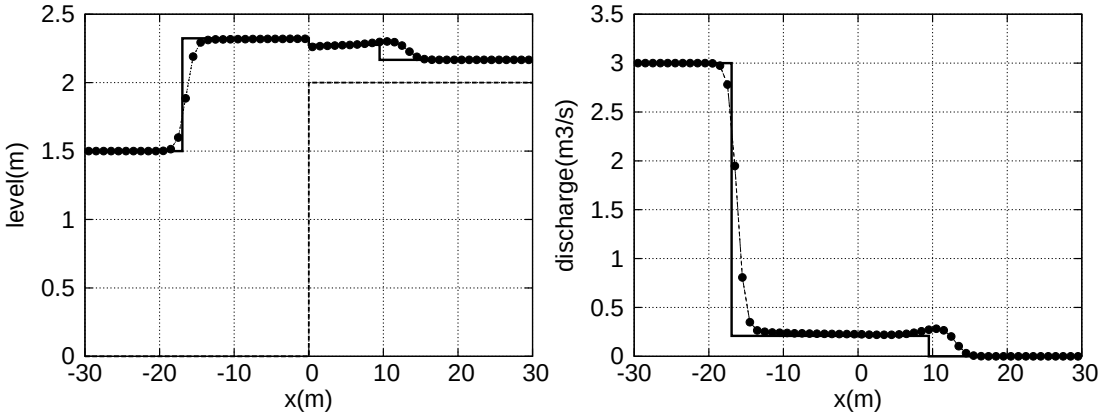

Figure 9.13: Test case 9: Exact (—) and numerical solutions at $t = 5s$ using CFL=1.0 ($-\circ-$) and CFL=5.0 ($-\bullet-$) for the water level surface (left) and the discharge (right)

The test cases proposed here are really extreme cases where the source term plays a leading role. Also discontinuities in the initial height and discharge make these situations in fact suitable to examine the power of a numerical method.

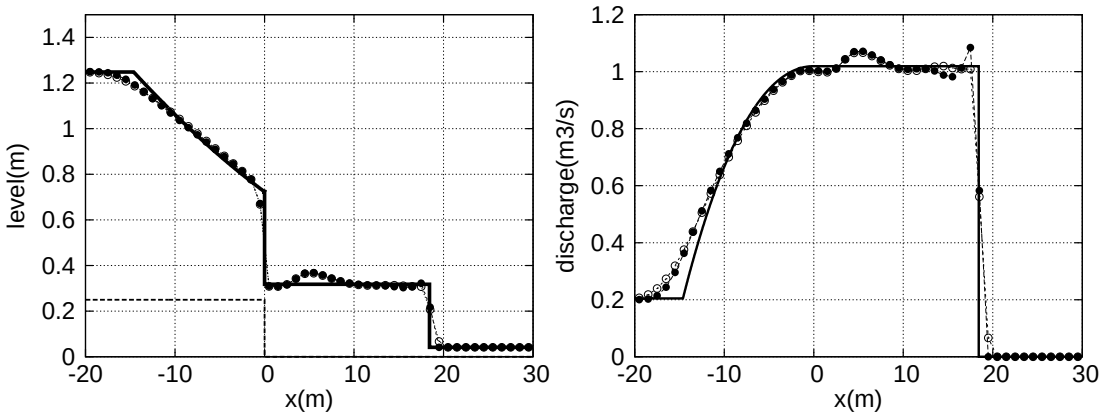

Figure 9.14: Test case 10: Exact (—) and numerical solutions at $t = 5s$ using CFL=1.0 ($-\circ-$) and CFL=5.0 ($-\bullet-$) for the water level surface (left) and the discharge (right)

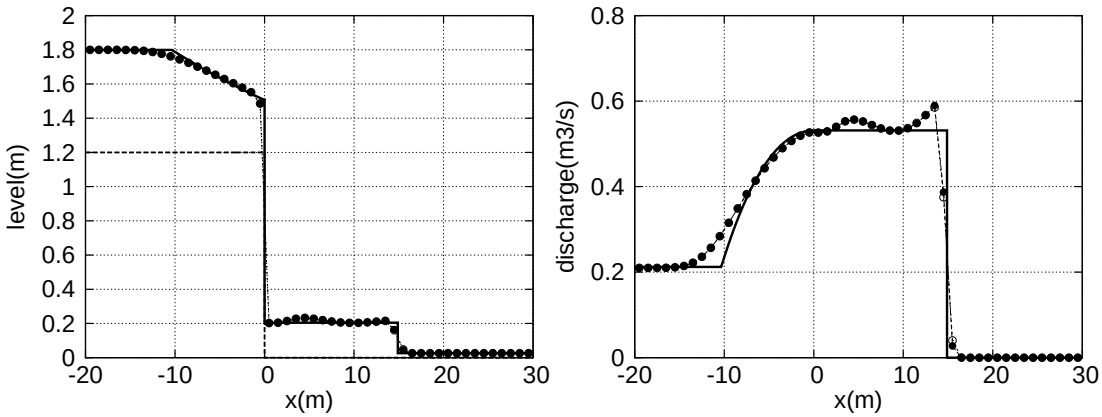

Figure 9.15: Test case 11: Exact (—) and numerical solutions at $t = 5s$ using CFL=1.0 ($-\circ-$) and CFL=5.0 ($-\bullet-$) for the water level surface (left) and the discharge (right)

The results provided by the LTS scheme are as good or more accurate than those from the FOU scheme. As the time steps are larger, less of them are necessary to compute the numerical solution, so it is less diffusive. Moreover, the influence of ξ is presented above all in test cases 9, 10 and 11 where this parameter is frequently less than 1 (and generally less also than 0.25). The aim of the parameter ξ is to detect when a strong discontinuity or large source term are present and to be able to generalise the LTS scheme. The examples show that in the extreme test cases, the CFL number is reduced when a large discontinuity is present. For all test cases the number of time steps necessary to compute the numerical solution is indicated in Table 9.2. Figure 9.16 (a) and (b) shows also the evolution of the time step for test cases 6,7,8 and 9,10,11 respectively using the LTS and FOU scheme. The shading symbols represents the conventional upwind explicit scheme and the empty symbols

the LTS scheme.

Test case	LTS scheme	FOU scheme
6	5	19
7	12	34
8	8	33
9	30	30
10	19	25
11	16	20

Table 9.2: Test cases 6-11: Time steps done by each numerical method

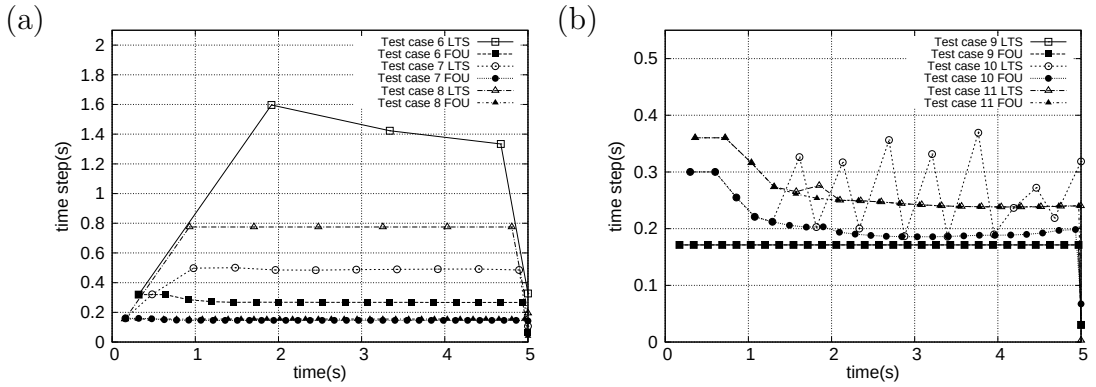

Figure 9.16: Evolution of the time step (a) for test cases 6, 7, 8 and (b) for test cases 9, 10, 11

9.3.5 Test case 12: unsteady flow over complex topography

A rectangular channel 1500m long with strong changes in breadth and bed slope (see Figure 9.17) as used in [122] is next considered.

The initial conditions are zero flow and 12m uniform surface level. The boundary conditions are an upstream time-variable height

$$h(0,t) = 12.0 + 4 + 4\,\sin\left(\frac{(t-10800)\pi}{21600}\right) \tag{9.26}$$

and a downstream zero-flow. The exact solution and more information about this test case can be found in [65] or [122]. In figure 9.18, the numerical solutions at t=10800s, computed on a regular 1500-cell grid with target values of CFL=1.0

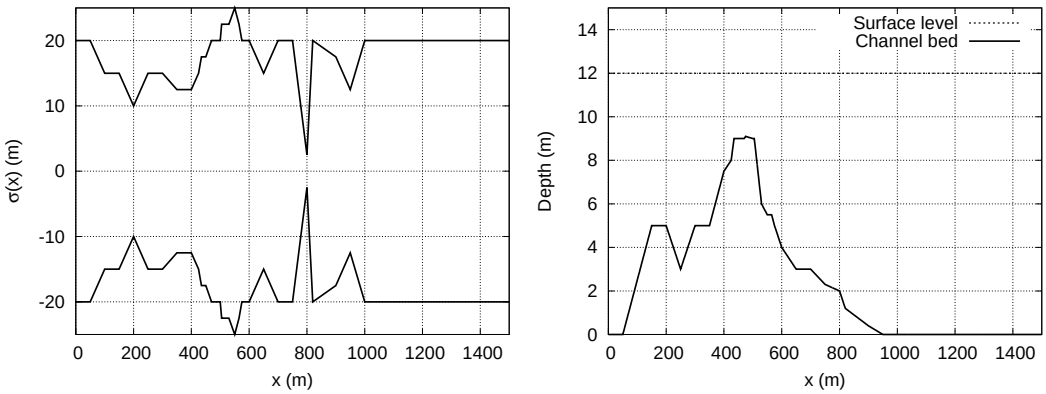

Figure 9.17: Breadth and bed variation for the complex topography test case

$(-\circ-)$, CFL=3.59 $(-\triangle-)$ and CFL=7.18 $(-\square-)$ are compared with the exact solution (—) in terms of longitudinal profile of water surface level and unit discharge all along the channel.

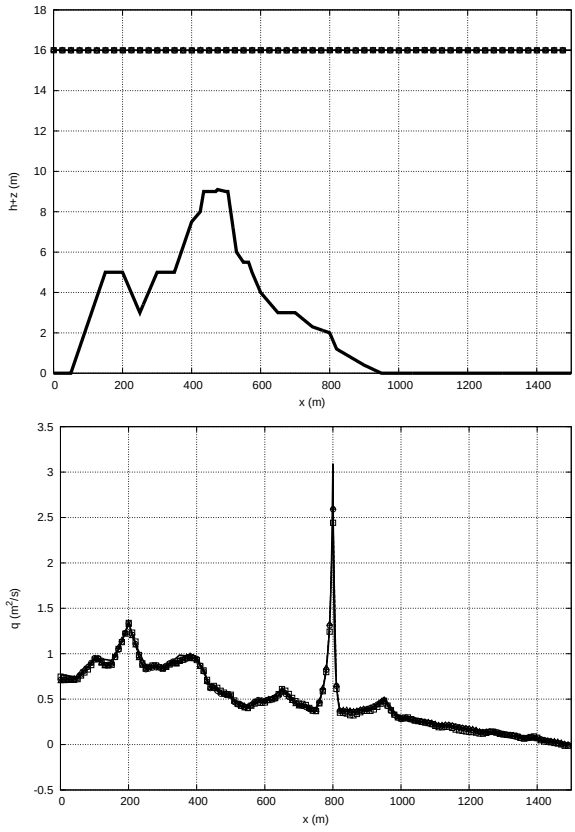

Figure 9.18: Exact (—) and numerical solutions at $t = 10800s$ using target values of CFL=1.0 $(-\circ-)$, CFL=3.59 $(-\triangle-)$ and CFL=7.18 $(-\square-)$ for the water level surface (left) and the discharge (right)

The use of CFL>1 with the LTS scheme implies a reduction in the computational time. However, due to the flow conditions induced by the rapidly varying irregular geometry, the parameter ξ suggested in Section 9.2.3 forces the target CFL to be re-adjusted ensuring an accurate and stable numerical solution. Figure 9.19 shows the time evolution of the actual time step size used by the method in the numerical simulation with target CFL=1.0 (—), CFL=3.59 (−△−) and CFL=7.18 (−□−). As can be seen, in the case of using target values of CFL=3.59 and CFL=7.18, the time step value is frequently reduced to that of CFL=1.0 according to the ξ parameter.

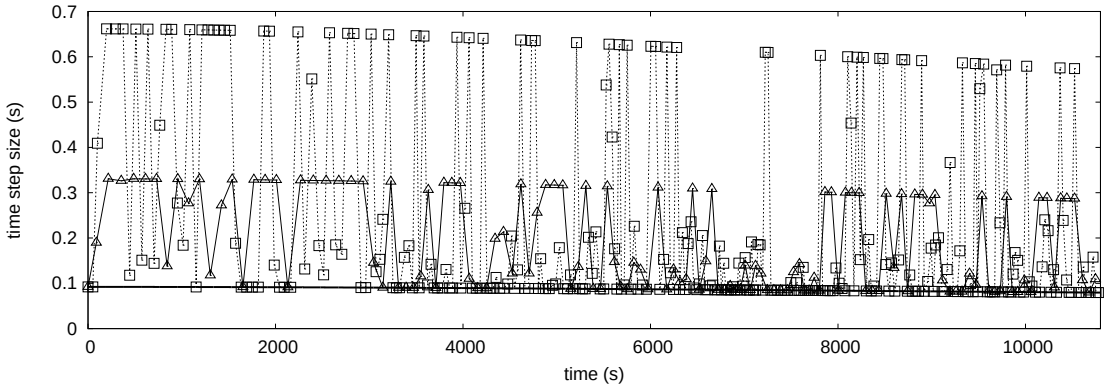

Figure 9.19: Time evolution of the time step with target values of CFL=1.0 (—), CFL=3.59 (−△−) and CFL=7.18 (−□−)

Therefore, a computational gain is achieved when increasing the target value of CFL but it is not proportional to the CFL value itself because of the discontinuities in the solution. In order to assert this, Table 9.3 shows the total CPU time used by the computations based on the three different target CFL values and the respective speed-up achieved. The real computational gain should be 3.59 in the case of CFL=3.59 and 7.18 in the case of CFL=7.18. However, the presence of discontinuities and the complexity of the topography reduce the time step according to the parameter ξ and makes the speed-up to be 2.268 and 2.67 respectively instead.

CFL	**CPU time (s)**	**Speed-up**
1.0	701	-
3.59	309	2.268
7.18	262	2.67

Table 9.3: CPU time and speed-up

Chapter 10

LTS scheme for 2D scalar equations

10.1 2D scalar equation

In order to introduce the 2D LTS scheme, the 2D linear scalar equation is used:

$$\frac{\partial u}{\partial t} + \nabla \cdot \mathbf{f}(u) = 0\,, \qquad \mathbf{f}(u) = (f_x, f_y)\,, \tag{10.1}$$

where u represents the conserved variable and $\mathbf{f}(u)$ is a linear function, $\mathbf{f} = \boldsymbol{\lambda} u$ and $\boldsymbol{\lambda} = (\lambda_x, \lambda_y)$ is constant. The first order upwind (FOU) explicit scheme can be formulated for the updating of cell i, by means of the in-going contributions that arrive to the cell:

$$u_i^{n+1} = u_i^n - \frac{\Delta t}{\Omega_i} \sum_{k=1}^{N_E} (\boldsymbol{\lambda} \cdot \mathbf{n})_k^- \; \delta u_k l_k \tag{10.2}$$

where $\delta u_k = u_j^n - u_i^n$ and i, j are the indexes of the cells sharing edge k. Being an explicit scheme, the time step for the conventional FOU approach is restricted by stability reasons in order to fulfil the CFL condition, which will be expressed later for square and triangular grids. This stability condition can be relaxed in the case of 2D problems and two techniques will be used in this work depending on the geometry of the mesh: when dealing with a structured square grid, a dimensional splitting technique will be adapted to the LTS scheme whereas a novel original technique is proposed to extend the LTS scheme in the case of triangular unstructured grids.

10.2 2D LTS scheme on square grids

10.2.1 Dimensional splitting

One general method to accomplish the 2D extension is the dimensional splitting where the equations are simplified to solve them many times in a 1D configuration and to project onto the grid following the space directions. The procedure is very easy to follow in a quadrilateral Cartesian structured mesh. In order to solve (10.1) let π_x denote the evolution operator in the x direction

$$\frac{\partial u}{\partial t} + \frac{\partial f_x}{\partial x} = 0 \tag{10.3}$$

and $\mathcal{R}^x_\tau$ the numerical resolution of (10.3) by means of the chosen solver with a time step size of τ (analogously for the y-component). The Strang splitting formulation [115] can be expressed as follows:

$$u(x,y)^{n+1} = [\pi_x \mathcal{R}^x_{\Delta t/2} \circ \pi_y \mathcal{R}^y_{\Delta t} \circ \pi_x \mathcal{R}^x_{\Delta t/2}]^n \,. \tag{10.4}$$

As the interfaces are looped over in the x- or y-direction, a 1D problem is considered when running along a row or a column respectively. Therefore, the computational time is increased compared to (10.2) because of the cost of covering twice all the edges of each of the main directions.

When dealing with the same numerical scheme to solve the problems in both directions, the resulting solution could be influenced by the mesh. For example, if the chosen solver is the FOU scheme and the Strang splitting formulation is used literally as expressed in (10.4), the particular problem in x-direction is being solved twice with a time step size of exactly half of that for the y-direction: hence the numerical results will be more diffusive in the x-direction. In order to improve the Strang splitting technique, the solution proposed in this work consists of distributing the numerical diffusion due to the chosen solver alternating the x- and the y-directions in (10.4). Therefore, the numerical solution will be computed for example as follows:

$$u(x,y)^{n+1} = \begin{cases} [\pi_x \mathcal{R}^x_{\Delta t/2} \circ \pi_y \mathcal{R}^y_{\Delta t} \circ \pi_x \mathcal{R}^x_{\Delta t/2}]^n & \text{if } n \text{ is even} \\ [\pi_y \mathcal{R}^y_{\Delta t/2} \circ \pi_x \mathcal{R}^x_{\Delta t} \circ \pi_y \mathcal{R}^y_{\Delta t/2}]^n & \text{if } n \text{ is odd} \end{cases} \tag{10.5}$$

where n is the index of the time step. This combined strategy can handle any numerical scheme to solve the one-dimensional problems associated with the splitting formulation. The time step is usually defined as follows in the particular case of a quadrilateral structured mesh whose elements have length l and area Ω:

$$\Delta t = CFL \frac{\Omega / l}{\boldsymbol{\lambda} \cdot \mathbf{n}} \tag{10.6}$$

With this definition of the time step size, the CFL number is chosen equal or below 0.5 in the case of the FOU scheme on square grids. However, it is feasible to relax this CFL number, allowing to select larger values and consequently, increasing the time step size.

The LTS scheme explained before in the 1D configuration is a good candidate to be implemented inside this combined dimensional splitting technique. While the simplicity of solving 1D equations and the advances related to boundary conditions and source terms are preserved, the disadvantage of the computational time associated with the splitting formulation is significantly reduced because of using large time step sizes in the numerical resolution of the equations. In consequence, the 2D LTS scheme for the scalar equation is formulated simply by splitting each time step into three "sub-steps" and applying the procedure described in (8.5) and (8.6), replacing Δx by Ω / l. It is summarized in the following algorithm for the n even case:

Step 1

- Compute the discrete values at each computational interface and determine the time step size using (10.6).
- Send the x-direction contributions with time step $\Delta t/2$ according to (8.5) and (8.6), only from interfaces for which $\mathbf{n} = (n_x, 0)$ (where $n_x = \pm 1$).
- Update boundaries and cells.

Step 2

- Compute the discrete values at the computational interfaces for which $\mathbf{n} = (0, n_y)$ (where $n_y = \pm 1$).

- Send the y-direction contributions with time step Δt according to (8.5) and (8.6), only from interfaces for which $\mathbf{n} = (0, n_y)$ (where $n_y = \pm 1$).
- Update boundaries and cells.

Step 3

- Compute the discrete values at each computational interfaces for which $\mathbf{n} = (n_x, 0)$ (where $n_x = \pm 1$).
- Send the x-direction contributions with time step $\Delta t/2$ according to (8.5) and (8.6), only from interfaces for which $\mathbf{n} = (n_x, 0)$ (where $n_x = \pm 1$).
- Update boundaries and cells.

A corresponding algorithm is applied for n odd.

10.2.1.1 Boundary conditions for the scalar case

The boundary conditions treatment has to be reconsidered if formulating a LTS scheme. In particular, when combining large time steps with time-dependent boundary conditions, a special handling is necessary in order to be accurate.

Characteristic line analysis is a useful tool to determine how many cells are involved in the boundary stencil. The CFL value chosen for the computation gives the information about the number of cells in the interior to be updated with information coming from the boundaries. In fact, this number of boundary cells is related to the integer part of the target CFL value,

$$\mu_{CFL} = int(CFL)\,. \tag{10.7}$$

Moreover, in the case of considering non-integer CFL values, the solution proposed is to consider the last cell ($\mu_{CFL}+1$) "partially" as a boundary cell and the fraction of the boundary information used to be the decimal part of the CFL number.

Once the number of boundary cells is determined, the information to be updated at each cell is obtained from the extrapolation of the boundary information through the characteristic lines. This treatment can be understood as the imposition of ghost cells, considered in [57] or [106] in the context of LTS schemes.

Apart from that, the imposition of boundary conditions on 2D structured grids using the LTS scheme is performed by taking into account the dimensional splitting. Note that each sub-iteration inside a complete time step that solves the 1D sub-problem must be considered as an independent computation. Therefore, boundary cells have to be updated after each sub-step inside the dimensional splitting, hence improving accuracy.

10.2.2 Numerical results

10.2.2.1 Test case 1: Pure advection simulation of a circular shape

A circular shape advection test case is proposed in order to evaluate the performance of the LTS scheme in combination with the dimensional splitting. A square domain $[0, 330\,\mathrm{m}]^2$ discretized on a fine quadrilateral mesh of 108 900 cells is chosen for this test case, where a circular shape of radius 25 m, centered at (50,50) is set as the initial condition:

$$u(x, y, 0) = \begin{cases} 1.0 & \text{if} \quad \sqrt{(x-50)^2 + (y-50)^2} \leq 25 \\ 0.0 & \text{otherwise}\,. \end{cases} \tag{10.8}$$

A constant advection velocity of $\boldsymbol{\lambda} = (1, 1)$ and open boundaries are set all over the domain and the numerical results are examined after t=200 s. The conventional upwind scheme (FOU) with a CFL=0.5 is compared with the LTS scheme with different CFL numbers in Figure 10.1. Using even CFL values, the exact solution is achieved hence odd CFL numbers (1.0, 5.0, 25.0, 75.0 and 151.0) have been chosen in this case. Results highlight that the higher the CFL value chosen, the more accurate the numerical solution is. There are several reasons for this. The main reason is that characteristics are straight lines of constant slope, the temporal error is almost negligible and therefore the spatial accuracy dominates the temporal accuracy. As a consequence, when increasing the CFL number, fewer time steps are done, hence the numerical diffusion associated with the scheme (only first-order accurate) decreases. Apart from that, there is no upper limit to the choice of the CFL number in this case.

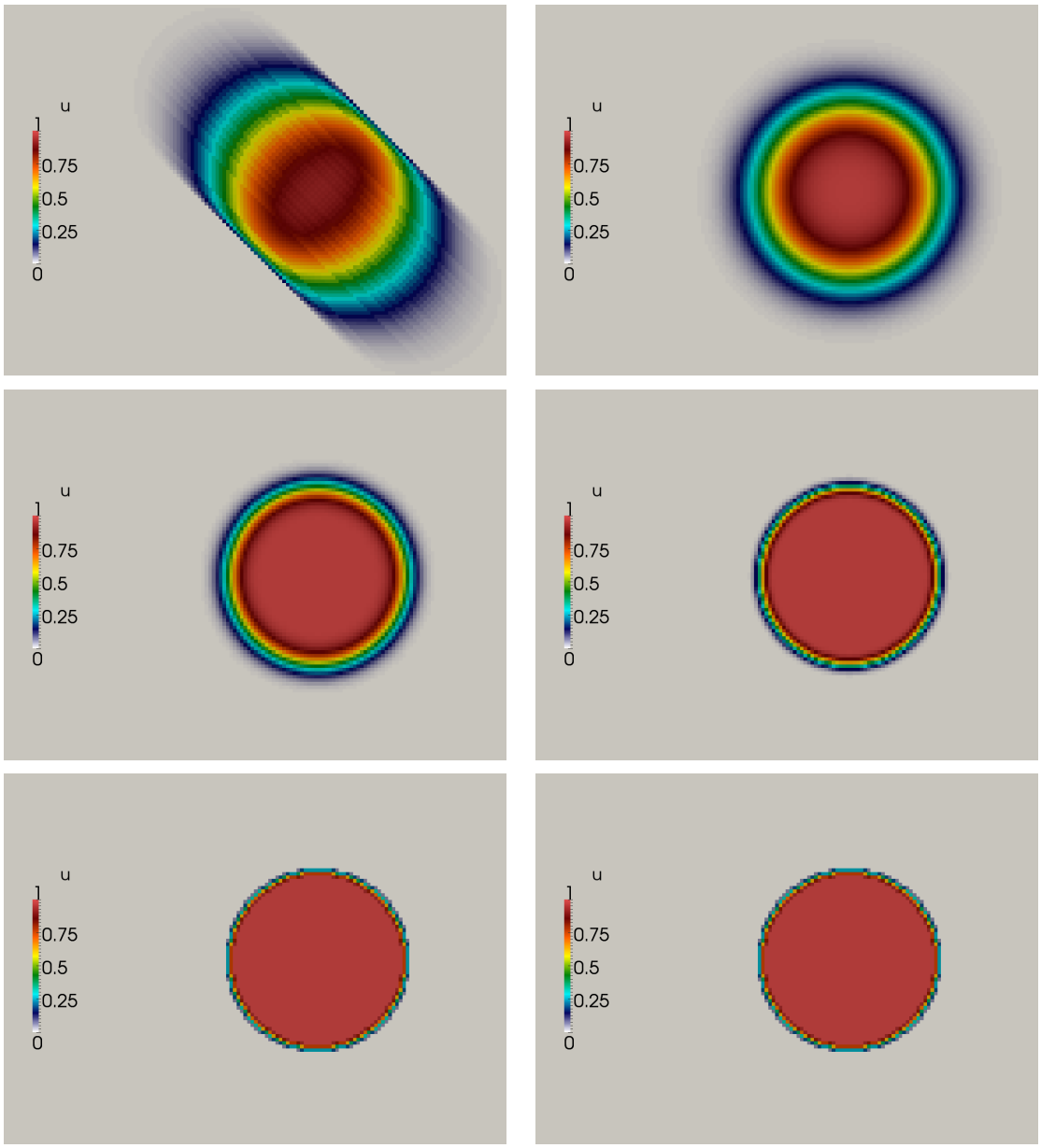

Figure 10.1: Numerical results for test case 1: FOU scheme CFL 0.5 (upper left), LTS CFL 1.0 (upper right), LTS CFL 5.0 (middle left), LTS CFL 25.0 (middle right), LTS CFL 75.0 (lower left) and LTS CFL 151.0 (lower right)

10.2.2.2 Test case 2: Advection simulation for a rotating cone

A square 2 m × 2 m domain discretized using 8 464 cells (92 × 92) is used as a quadrilateral structured mesh to simulate the circular advection of a "cone" defined as follows [63]:

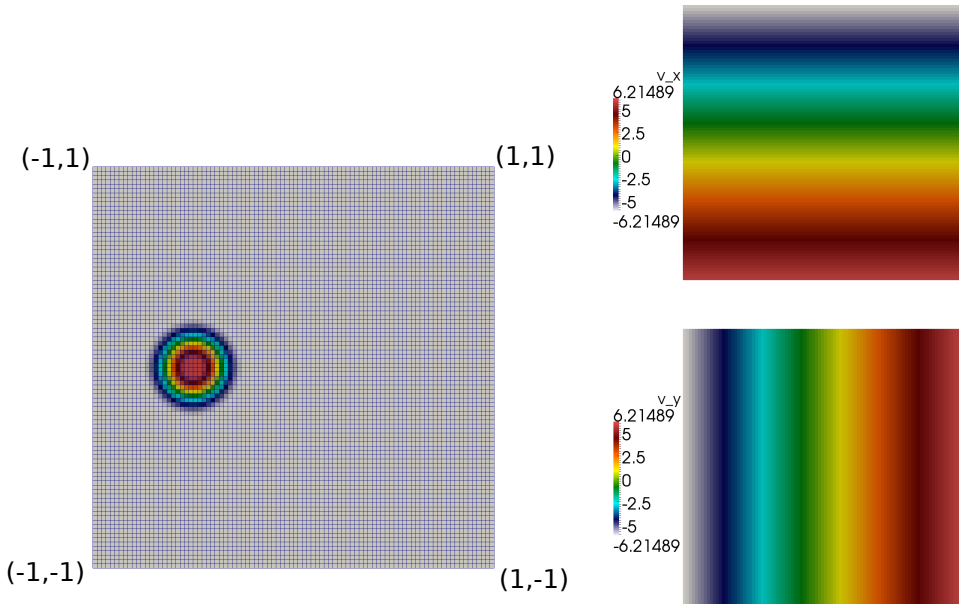

Figure 10.2: Test case 2: Initial condition and detail of the quadrilateral structured mesh (left) and velocity field (right) in x-direction (upper) and in y-direction (lower)

$$u(x,y,0) = \begin{cases} \cos^2(2\pi r) & r \leq 0.25 \\ 0.0 & \text{otherwise}\,, \end{cases} \tag{10.9}$$

where $r = \sqrt{(x+0.5)^2 + y^2}$. The mesh and the initial conditions, as well as the non-constant velocity field, $\boldsymbol{\lambda} = (-2\pi y, 2\pi x)$, are plotted in Figure 10.2. After one period T (where T=1 s in this case), the cone should return to its original position, recovering the initial condition. Also the analytical solution at times T/4, T/2 and 3T/4 can be easily computed.

The numerical results computed with the FOU scheme with a CFL=0.5 and with the LTS scheme with CFL numbers of 1.0, 3.0, 10.0, 20.0 and 60.0 are shown in Figure 10.3 at T=1. The peak value of each numerical scheme is also highlighted at the top of each figure.

As can be seen, the FOU scheme is not able to reproduce very well the rotating cone due to the excessive loss of information coming from the numerical diffusion. Even the LTS scheme with a CFL of 1.0 approximates better the solution, though it is still not very accurate. When increasing the CFL value, two phenomena occur. Firstly, the peak value, one indicator of the accuracy of the numerical solution, increases because the time step size is bigger and fewer steps are required to compute the

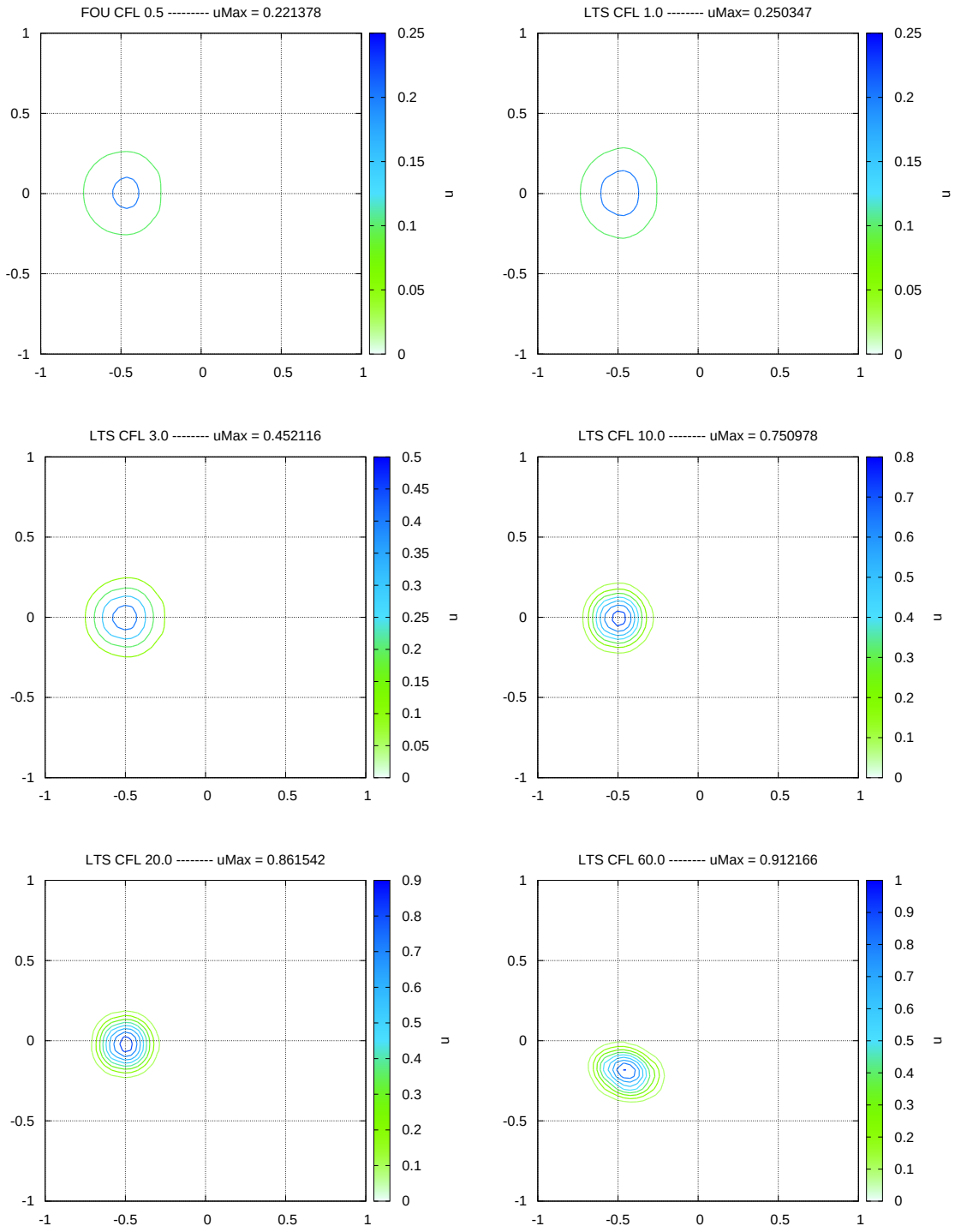

Figure 10.3: Numerical results for test case 2 at t=T: FOU scheme CFL 0.5 (upper left), LTS CFL 1.0 (upper right), LTS CFL 3.0 (middle left), LTS CFL 10.0 (middle right), LTS CFL 20.0 (lower left) and LTS CFL 60.0 (lower right)

solution. It is worth remarking that the numerical results improve on those obtained in [63] where a sophisticated 2D TVD method is used. On the other hand, the solution is deviating due to the non-uniform velocity field. As fewer time steps are done, the larger magnitude of the time steps means that the dimensional splitting loses too much information about the velocity field to be able to follow completely the correct "pathway". This deviation is most obvious when using the LTS scheme with a CFL of 60.0, but it is also visible to a lesser extent when the same scheme is applied with with a CFL of 20.0.

In order to evaluate the quality of the results more fully, the L_1 error between the numerical and the exact solution is plotted in Figure 10.4.

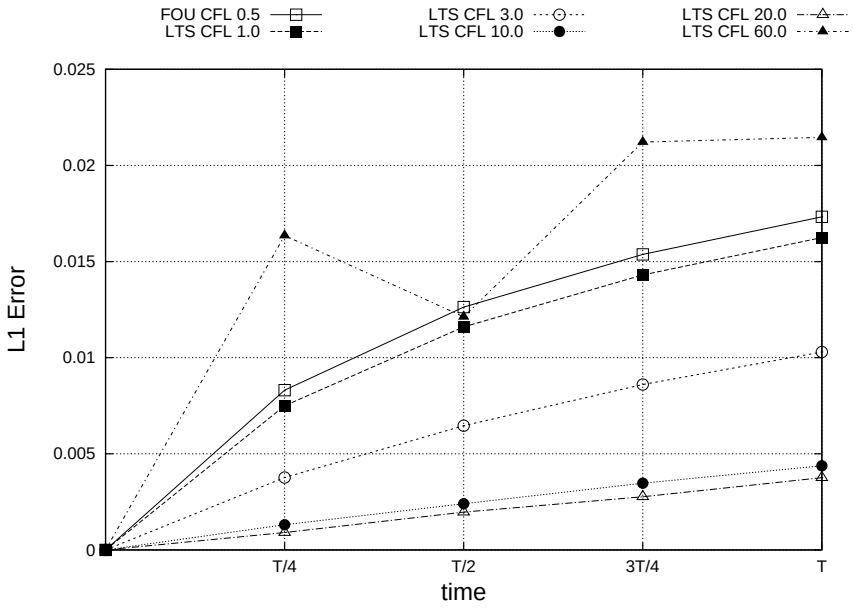

Figure 10.4: Test case 2: L_1 errors for the LTS scheme using different CFL numbers.

The LTS scheme with CFL=20.0 is the most accurate in terms of this norm, providing the best results. Also, as could be conjectured from examining Figure 10.3, the least accurate choice is the LTS with a CFL=60.0, even though it achieves the highest peak value. It is not able to reproduce either the exact location or the shape of the rotating cone due to the fact that it is losing important information related to the velocity field when doing these huge time steps.

The optimal CFL value is therefore a question of interest. It is not known *a priori* what this optimum is, that is, from which CFL value the accuracy starts to decrease. Four different quadrilateral meshes, derived by uniform mesh refinement (as

described by grid refinement 1, Table 10.1), have been used to clarify which CFL value computes the most accurate solution.

Mesh	Number of elements
1	92×92=8464
2	184×184=33856
3	368×368=135424
4	736×736=541696

Table 10.1: Test case 2. Grid refinement 1. Meshes and elements.

At t=T, the comparison between the numerical solutions computed by the four grids using different CFL values has been carried out. The results in terms of the L_1 norm are shown in Table 10.2. The symbol "-" in Table 10.2 indicates that the results achieved in these cases are the same as for the previous CFL number.

Mesh	CFL	L_1	Peak value	Mesh	CFL	L_1	Peak value
1	20.0	**2.08e-03**	0.862	3	20.0	6.37e-04	0.968
1	30.0	5.12e-03	0.893	3	30.0	**6.00e-04**	0.977
1	40.0	1.22e-02	0.924	3	40.0	8.40e-04	0.983
1	60.0	2.15e-02	0.912	3	60.0	1.21e-03	0.988
1	100.0	2.51e-02	0.867	3	100.0	3.55e-03	0.993
1	160.0	-	-	3	160.0	1.23e-02	0.995
2	20.0	1.46e-03	0.937	4	20.0	3.06e-04	0.984
2	30.0	**1.42e-03**	0.954	4	30.0	2.37e-04	0.988
2	40.0	2.99e-03	0.963	4	40.0	**2.23e-04**	0.992
2	60.0	4.76e-03	0.971	4	60.0	4.37e-04	0.994
2	100.0	1.57e-02	0.978	4	100.0	1.17e-03	0.996
2	160.0	2.51e-02	0.964	4	160.0	2.92e-03	0.998

Table 10.2: Test case 2. Grid refinement 1. Comparison between CFL values and error norms on each mesh.

When increasing the number of grid cells, the error in the L_1 norm decreases, hence ensuring the convergence. Moreover, the peak value increases not only when refining the mesh but also when increasing the CFL value due to the fact that fewer time steps are done, making the scheme less diffusive and allowing higher peak values.

When observing the error in the L_1 norm, it is clear that very large CFL values increase the error. However, it is also clear that an optimal CFL value exists for which the error is minimal. This optimal CFL number is related not only to the spatial operator (first order) but also to the mesh, being higher when it is refined. For example, for mesh 1, the optimum value is close to 20.0, for mesh 2 and 3, between 20.0 and 30.0 and, for mesh 4, between 30.0 and 40.0. In order to check this hypothesis, an exhaustive grid refinement 2 is proposed.

The number of cells of each mesh is summarized in Table 10.3, running each one with different CFL values from CFL=10.0 to CFL=35.0 (0.5 by 0.5).

Mesh	Number of elements
1	50×50=2500
2	55×55=3025
3	60×60=3600
...	...×...=...
99	540×540=291600
100	545×545=297025
101	550×550=302500

Table 10.3: Test case 2. Grid refinement 2. Meshes and elements.

The considerable amount of data is condensed in Figure 10.5 for the L_1 norm, where the error and the CFL value for which the norm is at a minimum are plotted against the square root of the number of cells.

When moving towards the right along the x-axis in Figure 10.5, the number of cells increases hence the accuracy should be (and is) higher. Moreover, the CFL value for computing the numerical solution with less error (cut-off) grows generally when the mesh increases in number of elements. The more direct implication of this resides in the fact that the CFL value can be increased when refining the mesh. It is worth remarking that the CFL cut-off represents the point at which temporal error is dominating spatial error. Being a first order scheme, the temporal error can become quite high and still not dominate the spatial error. Moreover, in case of having a similar test case with more sharply varying advection speeds, this CFL cut-off would be much lower.

A rate of convergence slightly better than first order is observed in Figure 10.6 where

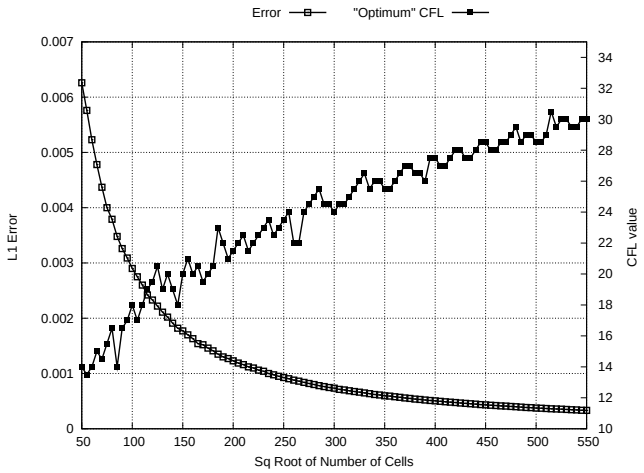

Figure 10.5: Test case 2. Grid refinement 2. Minimum L_1 error, CFL value for this minimum error for each mesh

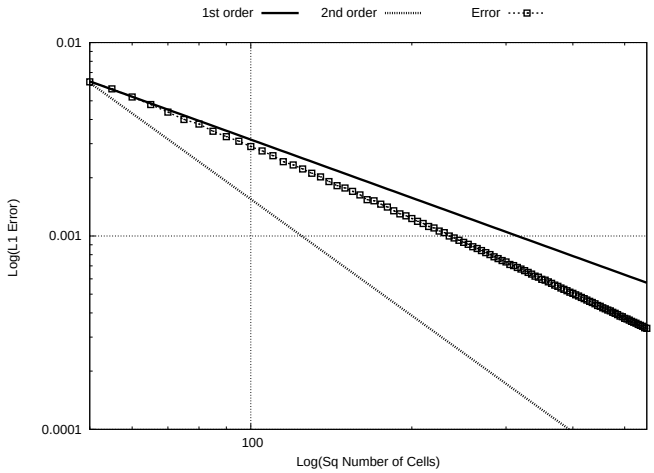

Figure 10.6: Test case 2. Grid refinement 2. Log-log L_1 error

a log-log graph of the error using the optimal values shown in Figure 10.5 and the square root of the number of cells is plotted comparing it with the first order and second order.

10.3 2D LTS scheme on triangular grids

The extension of the LTS scheme to 2D unstructured triangular grids requires a deep awareness of how the numerical scheme is sending the information through the computational edges in the conventional 2D FOU scheme. Not only the wall

orientation of the normal directions in the edges plays an important role but also the disparity of the length of these edges and the cell areas becomes an essential factor when trying to develop the LTS scheme.

The unique approach in this topic was done by Murillo et al. [94], where the scheme was implemented in unstructured triangular grids. The scheme was based on spreading the information from each computational wall to the neighbouring cells according to a criterion related to the cell area of the involved cells. Although the method remained conservative, the computations required cumbersome re-triangularizations in order to allow larger CFL values and to preserve bounded solutions. Consequently, the advantage of using this kind of scheme was reduced.

Another strategy is proposed in this work. A special interest is put on finding the way of packing the information in such a way that allows to compute the numerical solution in Cartesian triangular grids or unstructured Delaunay grids used generally. Besides, the information from each wall or edge will be sent cleverly according to the average discrete velocity at this wall and the orientation of the edges of the neighbouring cells involved.

10.3.1 The idea to pack the information

Let consider here the linear scalar equation in order to simplify the following reasoning:

$$\frac{\partial u}{\partial t} + \boldsymbol{\lambda} \nabla \cdot u = 0 \tag{10.10}$$

where $\boldsymbol{\lambda} = (\lambda_x, \lambda_y)$ is constant. The idea developed in the 1D case or in the dimensional splitting must be modified due to the flow orientation and the geometry of each triangle, as mentioned above. In particular, the definition of the parameters ν_k and δu_k should be reconsidered. In the 1D model, the idea to send the information was based on splitting the total contribution $\nu_k \delta u_k$ in μ_k packages of δu where $\mu_k = int(\nu_k)$ and, what is left, i.e, $(\nu_k - \mu_k)\delta u_k$ to the last cell, so that the scheme remains conservative. In this algorithm underlies the assumption that the information is exchanged through walls whose normal direction and length are always the same. When dealing with triangular cells, this hypothesis is not true and some modifications must be done. In other words, it is necessary to pack the

information in a certain way in order to adapt the LTS scheme to triangular grids. Let consider the edge k shared by cells i and j as displayed in the Figure 10.7, where the normal direction of the edge k, $\mathbf{n}_k$, is defined from cell i to cell j.

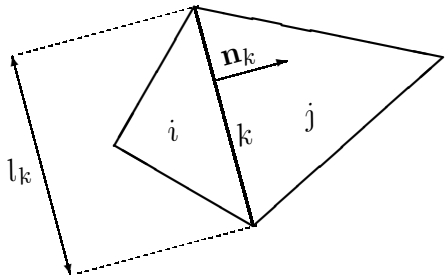

Figure 10.7: Edge k sharing cells i and j

A new quantity L_M^{max} is computed for each computational cell M

$$L_M^{max} = \max_k((\boldsymbol{\lambda}\mathbf{n})^-\ l)_k \qquad k = 1, \cdots N_E \tag{10.11}$$

where N_E is the number of edges in cell M. It is worth noting that L_M^{max} only accounts for the ingoing contributions. This parameter gives an estimation of the maximum amount of information that arrives to the cell from the neighbouring walls and can be used to homogenize or normalize the information sent form each wall by means of ζ_k

$$\zeta_k = \frac{(\boldsymbol{\lambda}\mathbf{n}\ l)_k}{L_M^{max}} \qquad M = \begin{cases} j & \text{if } \boldsymbol{\lambda}\mathbf{n} > 0 \\ i & \text{if } \boldsymbol{\lambda}\mathbf{n} < 0 \end{cases} \tag{10.12}$$

As a matter of fact, this parameter ζ_k provides a measure expressed on a per unit basis of the total amount of information that the wall k is able to send to the neighbouring cell according to its own length and normal direction. It is going to be used to rescale the maximum information to be sent from each wall and to adapt the algorithm to the philosophy developed in the 1D case. So, the quantities δu and ν are re-defined according to this parameter

$$\delta u_k = \zeta_k \, \delta u_{ref,k} \qquad \nu_k = \frac{\nu_{ref,k}}{\zeta_k} \tag{10.13}$$

where $\delta u_{ref,k} = u_j - u_i$ and $\nu_{ref,k} = \dfrac{(\boldsymbol{\lambda}\mathbf{n})_k \Delta t \; l_k}{A_M}$ are the usual definitions for these quantities. As known, the time step size in the case of unstructured grids is restricted by the CFL condition and is chosen as follows:

$$\Delta t = CFL \frac{\min(\chi_i, \chi_j)}{\max_{m=1,2,3} |\widetilde{\lambda}^m|} \qquad \chi_i = \frac{A_i}{\max_{k=1,NE} l_k} \tag{10.14}$$

In the conventional FOU scheme, it is recommended to select a value of CFL=0.5 in general although, according to the computational experience, the CFL value could be chosen close to 1 in the case of unstructured triangular Delaunay grids.

The new redefinition of δu and ν will be the basis of the 2D LTS scheme, which will allow the choice of a larger CFL value. The amount of information is now rescaled according to the maximum allowed in the conventional scheme due to the orientation of the wall edges and the flow direction. Furthermore, the conservation is guaranteed as can be deduced from (10.13).

10.3.2 The idea to send the information

Once the parameters needed for the LTS scheme are normalized at each wall as described in the previous discussion, we are in a position to send the *information*. The main objective will consist of sending the information in an intelligent manner, discriminating between valid (V) or partially valid (PV) and not valid (NV) paths. The 'candidate' paths are constructed by evaluating the discrete average velocity at the edge from which we are sending the information, and computing the dot product between this velocity and the outward neighbour normal directions. These walls are considered as the paths 'candidates' to send the information across them. From each edge, two possible paths arise which are denoted as P_1 and P_2:

$$P_1 = \boldsymbol{\lambda}_k \mathbf{n}_1 \qquad P_2 = \boldsymbol{\lambda}_k \mathbf{n}_2 \tag{10.15}$$

- If $P_1 < 0$, it is labelled as NV and the information is totally sent across

the other wall, i.e., to the neighbouring cell provided by P_2. Moreover, P_2 is labelled as V.

- If $P_2 < 0$, it is labelled as NV and the information is totally sent across the other wall, i.e., to the neighbouring cell provided by P_1. Moreover, P_1 is labelled as V.

- If $P_1 > 0, P_2 > 0$, they are labelled as PV and the information is distributed according to weights θ_1 and θ_2 which are closely related to these dot products:

$$\theta_1 = \frac{P_1}{P_1 + P_2} \qquad \theta_2 = \frac{P_2}{P_1 + P_2} \tag{10.16}$$

The case of both P_1 and P_2 negative is absurd because of geometric considerations. Once the path or paths are discriminated, the procedure is repeated $\mu_k = int(\nu_k)$ times for the subsequent edges which are labelled as V or PV. The last step will follow the same strategy but sending only $(\nu_k - \mu_k)$ times of the information.

Before characterizing the concept of *information*, which has been used up to now in this paragraph, and also before formulating these ideas in a compact algorithm valid for all kind of triangular grids, let consider a toy triangular Cartesian grid and an advection velocity of $\boldsymbol{\lambda} = (2, 1)$. The notation for the normal direction is chosen as follows: $\mathbf{n}_{i,j}$ will represent the outward normal direction from cell i to cell j ; the dot product between these outward directions $\mathbf{n}_{i,j}$ and the velocity will be denoted as P_x. Figure 10.8 shows an sketch of the mesh considered and the reasoning will be referred to this mesh numbering.

Once situated at wall k, let assume the information to send is, for instance, $\nu_k \delta u_k = 3.6\delta u_k$. The algorithm can be summarized in the following steps:

1. Send δu_k to cell 2.

2. Two possibles paths

$$P_1 = \boldsymbol{\lambda}_k \mathbf{n}_{2,4} = 1 \qquad P_2 = \boldsymbol{\lambda}_k \mathbf{n}_{2,3} = 2 \tag{10.17}$$

   - As $P_1, P_2 > 0$, define

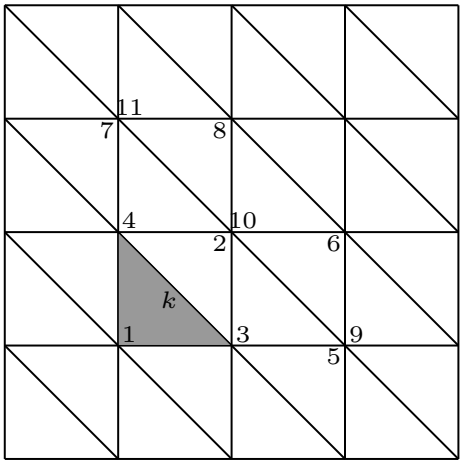

Figure 10.8: Toy triangular Cartesian mesh used to illustrate the procedure to send the information in the 2D LTS scheme

$$\theta_1 = \frac{P_1}{P_1 + P_2} = 1/3 \qquad \theta_2 = \frac{P_2}{P_1 + P_2} = 2/3 \tag{10.18}$$

3. The information is sent according to θ_1 and θ_2: send $\theta_1 \delta u_k$ to cell 4 and $\theta_2 \delta u_k$ to cell 3.

4. Four possibles paths

$$P_{1,1} = \boldsymbol{\lambda}_k \mathbf{n}_{4,7} = -2 \qquad P_{1,2} = \boldsymbol{\lambda}_k \mathbf{n}_{4,8} = 3\frac{\sqrt{2}}{2} \tag{10.19}$$

$$P_{2,1} = \boldsymbol{\lambda}_k \mathbf{n}_{3,5} = -1 \qquad P_{2,2} = \boldsymbol{\lambda}_k \mathbf{n}_{3,6} = 3\frac{\sqrt{2}}{2} \tag{10.20}$$

   - As $P_{1,1} < 0$, the information will be completely sent to cell 6.
   - As $P_{2,1} < 0$, the information will be completely sent to cell 8.

5. Send $\theta_1 \delta u_k$ to cell 6. Send $\theta_2 \delta u_k$ to cell 8.

6. Four possibles paths

$$P_{1,2,1} = \boldsymbol{\lambda}_k \mathbf{n}_{8,11} = 1 \qquad P_{1,2,2} = \boldsymbol{\lambda}_k \mathbf{n}_{8,10} = 2 \tag{10.21}$$

$$P_{2,2,1} = \boldsymbol{\lambda}_k \mathbf{n}_{6,10} = 1 \qquad P_{2,2,2} = \boldsymbol{\lambda}_k \mathbf{n}_{6,9} = 2 \tag{10.22}$$

- As $P_{1,2,1}, P_{1,2,2} > 0$, define

$$\theta_{1,2,1} = \frac{P_{1,2,1}}{P_{1,2,1} + P_{1,2,2}} = 1/3 \qquad \theta_{1,2,2} = \frac{P_{1,2,2}}{P_{1,2,1} + P_{1,2,2}} = 2/3 \quad (10.23)$$

7. The information is sent according to $\theta_{1,2,1}$ and $\theta_{1,2,1}$: send 0.6 $\theta_{1,2,1}\theta_1\delta u_k$ to cell 10 and 0.6 $\theta_{1,2,2}\theta_1\delta u_k$ to cell 11.

- As $P_{2,2,1}, P_{2,2,2} > 0$, define

$$\theta_{2,2,1} = \frac{P_{2,2,1}}{P_{2,2,1} + P_{2,2,2}} = 1/3 \qquad \theta_{2,2,2} = \frac{P_{2,2,2}}{P_{2,2,1} + P_{2,2,2}} = 2/3 \quad (10.24)$$

8. The information is sent according to $\theta_{2,2,1}$ and $\theta_{2,2,1}$: send 0.6 $\theta_{2,2,1}\theta_2\delta u_k$ to cell 9 and 0.6 $\theta_{2,2,2}\theta_2\delta u_k$ to cell 10.

The way of sending the information for this triangular Cartesian grid can be schematized in Figure 10.9.

When dealing with triangular unstructured grids, the information sent to each corresponding valid or partially valid cell L is governed also by the cell area A_L. Following the finite volume approach, the information sent to the involved cell L has to be scaled by $\frac{A_M}{A_L}$ where M is defined in (10.12). Note that this factor is equal to 1 in the case of Cartesian triangular grids.

As can deduced form the previous discussion, the strategy to send adequately the information is not straightforward. The easiest way to understand it is by means of a recursive function able to represent the 'tree structure' that follows the procedure of sending the information. It is summarised in Algorithm 2, which shows the way of sending the total contribution $\nu_k\delta u_k$ from wall k to the cell M and its subsequent neighbouring cells. Figure 10.10 clarifies the neighbouring cells and walls given a wall wc. When handling boundary cells, the procedure becomes simpler because there is no possible choice to send the information far from its unique neighbour.

As a summary, the neighbouring walls that are labelled as valid V or partially valid PV are used to send the information through them; this leads to new neighbouring walls labelled as V or PV... and so on. This strategy will be applied a number of levels or steps equal to $\mu_k = \text{int}(\nu_k)$ and, in the last step, the information has to be sent according to the parameter $(\nu_k - \mu_k)$ as in the 1D LTS scheme.

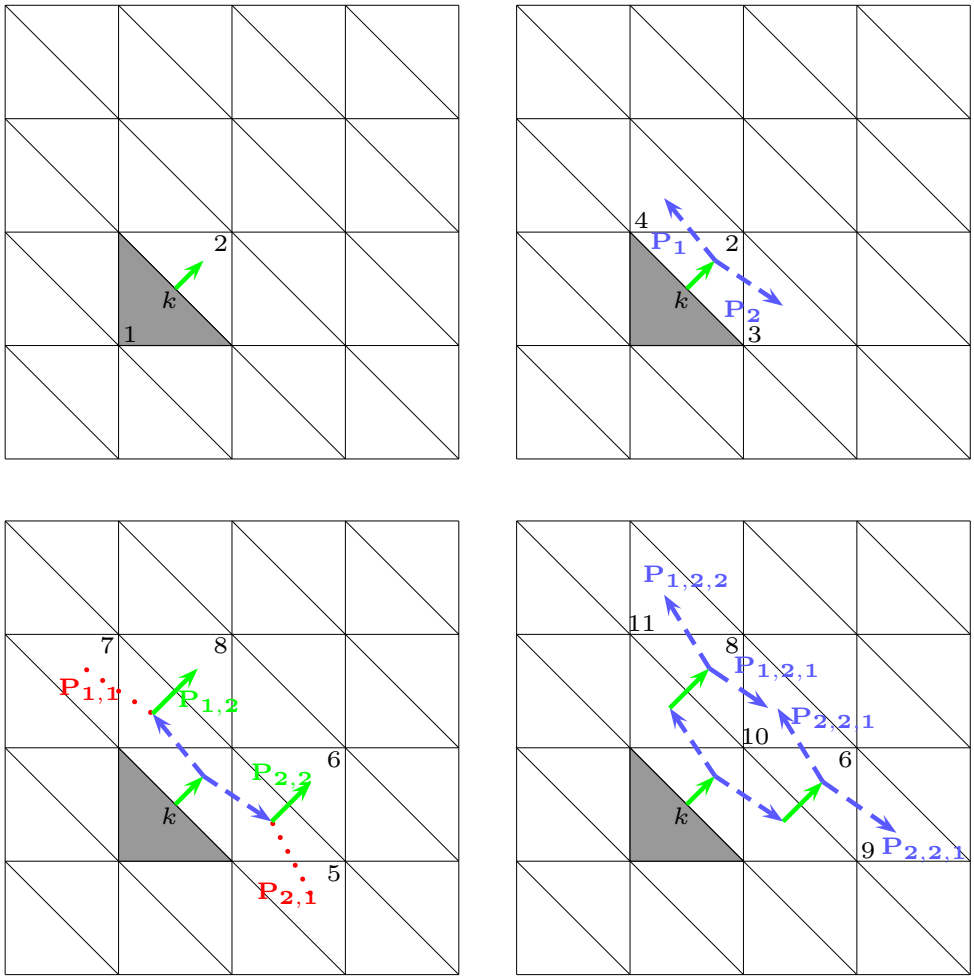

Figure 10.9: Sketch of the procedure for sending the information. Valid V (solid green), partially valid PV (dashed blue) and not valid NV (dotted red)

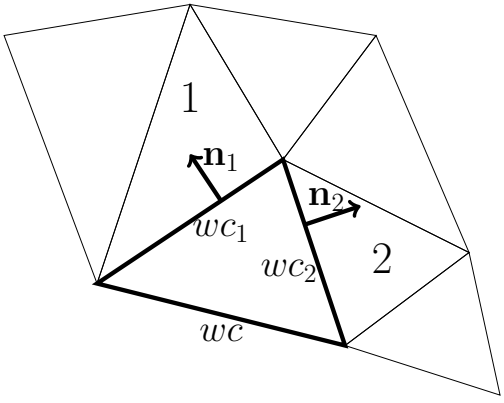

Figure 10.10: Neighbouring cells and walls for wall wc

Algorithm 2 Sending the flux in the 2D LTS scheme

send δu_k to cell M
$contrib$=δu_k
$level$=$\mu_k - 1$
wc=k
sendFlux(wc,$contrib$,$level$)

function sendFlux(wc,$contrib$,$level$)
    if $level \geq 0$ **then**
        set 1 and 2 neighbouring cells of wall wc
        set wc_1 and wc_2 neighbouring walls of wall wc
        evaluate $P_1 = \boldsymbol{\lambda}_k \mathbf{n}_1$ and $P_2 = \boldsymbol{\lambda}_k \mathbf{n}_2$
        label P_1 and P_2 as V, PV and NV according to its own sign.

        if P_1 is V **then**
            if $level > 0$ **then**
                send $\left(contrib \, \dfrac{A_M}{A_1} \right)$ to cell 1
                sendFlux(wc_1, $contrib$, $level - 1$)
            else
                send $\left((\nu_k - \mu_k) \, contrib \, \dfrac{A_M}{A_1} \right)$ to cell 1
            end if
        end if

        if P_2 is V **then**
            if $level > 0$ **then**
                send $\left(contrib \, \dfrac{A_M}{A_2} \right)$ to cell 2
                sendFlux(wc_2, $contrib$, $level - 1$)
            else
                send $\left((\nu_k - \mu_k) \, contrib \, \dfrac{A_M}{A_2} \right)$ to cell 2
            end if
        end if

Algorithm 2 Sending the flux in the 2D LTS scheme (continued)

33: **if** P_1 and P_2 are PV **then**
34: evaluate $\theta_1 = \dfrac{P_1}{P_1 + P_2}$ $\theta_2 = \dfrac{P_2}{P_1 + P_2}$
35: **if** $level > 0$ **then**
36: send $\left(\theta_1 contrib \dfrac{A_M}{A_1}\right)$ to cell 1
37: send $\left(\theta_2 contrib \dfrac{A_M}{A_2}\right)$ to cell 2
38: SENDFLUX(wc_1, $\theta_1 contrib$, $level - 1$)
39: SENDFLUX(wc_2, $\theta_2 contrib$, $level - 1$)
40: **else**
41: send $\left((\nu_k - \mu_k)\ \theta_1 contrib \dfrac{A_M}{A_1}\right)$ to cell 1
42: send $\left((\nu_k - \mu_k)\ \theta_2 contrib \dfrac{A_M}{A_2}\right)$ to cell 2
43: **end if**
44: **end if**
45: **end if**
46: **end function**

10.3.3 Numerical results

10.3.3.1 Test case 1: Pure advection simulation of a rectangular shape in a Cartesian triangular grid

The advection of rectangle defined as (see Figure 10.11, upper left):

$$u(x, y, 0) = \begin{cases} 1.0 & \text{if} \quad 2 \leq x \leq 6, 2 \leq y \leq 4 \\ 0.0 & \text{otherwise}\,. \end{cases} \tag{10.25}$$

with a constant advection velocity $\boldsymbol{\lambda} = (0.5, 1)$ and open boundaries all over the domain is performed in this test case. A domain of $[0, 50] \times [0, 50]$ is discretized into 20000 triangles of area 0.25 m^2. The numerical results after t=35 s achieved by the conventional FOU with CFL=0.5 (Figure 10.11, upper right) are compared with those obtained by the proposed 2D LTS scheme with CFL=2.9 and CFL=6.9 (Figure 10.11, lower left and lower right respectively). Moreover the peak achieved

by each scheme is also highlighted.

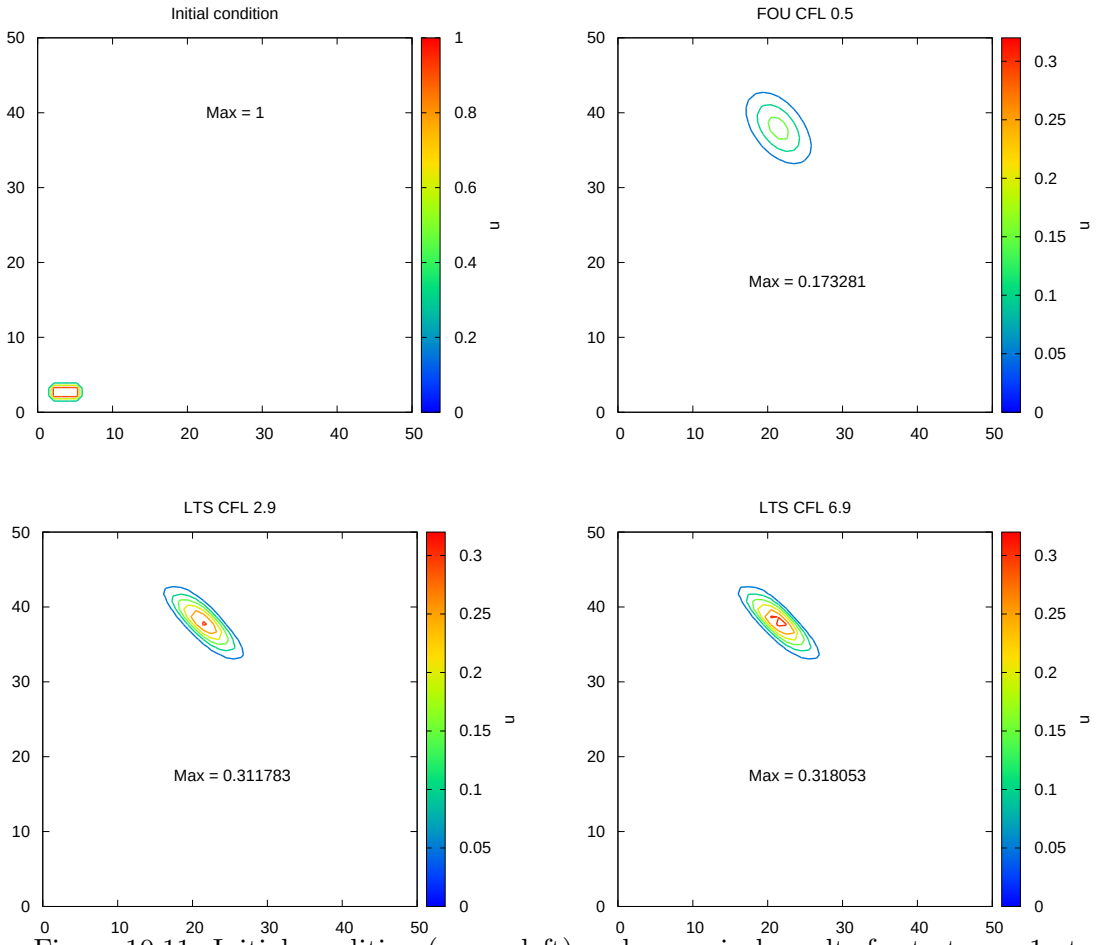

Figure 10.11: Initial condition (upper left) and numerical results for test case 1 at t=35 s: FOU scheme CFL 0.5 (upper right), LTS CFL 2.9 (lower left) and LTS CFL 6.9 (lower right)

As observed, the LTS scheme improves the results obtained by the FOU scheme not only in terms of maximum peak achieved but also in terms of numerical diffusion. The small gain between the results obtained by the LTS with CFL 2.9 and CFL 6.9 is due to the implementation of the 2D LTS scheme. It has been done by giving priority to positivity of the scheme: when a value lower than the initial minimum or greater than the initial maximum is produced, the CFL value is automatically halved in order to ensure a robust scheme. This can be seen as a similar procedure to those performed when negative values in the water depth appear in the context

of the shallow water equations.

10.3.3.2 Test case 2: pure advection of a cone in a unstructured triangular grid

A domain $[-1,3] \times [-1,3]$, discretized into 33632 unstructured triangles is used to perform the advection with $\boldsymbol{\lambda} = (1,1)$ of a cone centered at (-0.65,-0.65) during t=3. The cone is mathematically expressed as follows:

$$u(x,y,0) = \begin{cases} \cos^2(2\pi r) & r \leq 0.25 \\ 0.0 & \text{otherwise}\,, \end{cases} \tag{10.26}$$

Open boundaries are set all over the domain. The initial condition as well as the exact solution are plotted in Figure 10.12, upper left and right respectively. This figure also shows the numerical results achieved by the FOU scheme with CFL=0.9 (middle left) and the mentioned LTS scheme with CFL's 1.5, 3.0 and 4.5 (middle right, lower left and lower right respectively).

Apart from the maximum peak reached by each numerical scheme, the L_1-error is also shown in the middle of each plot. The numerical diffusion, mainly in the direction of the advection velocity, is reduced, achieving a larger value in the cone peak. Accordingly, the L_1-error is diminished when increasing the CFL value.

10.3.3.3 Test case 3: Doswell frontogenesis

An initial condition

$$u(x,y,0) = -tanh\left(\frac{y-4}{8}\right) \tag{10.27}$$

defined in a domain $[0,8] \times [0,8]$ is deformed, influenced by the following velocity field [40, 60]:

$$\boldsymbol{\lambda} = \frac{tanh(d)}{0.385\ d\ cosh^2(d)}(4-y, x-4) \tag{10.28}$$

where d denotes the distance to the center of the domain

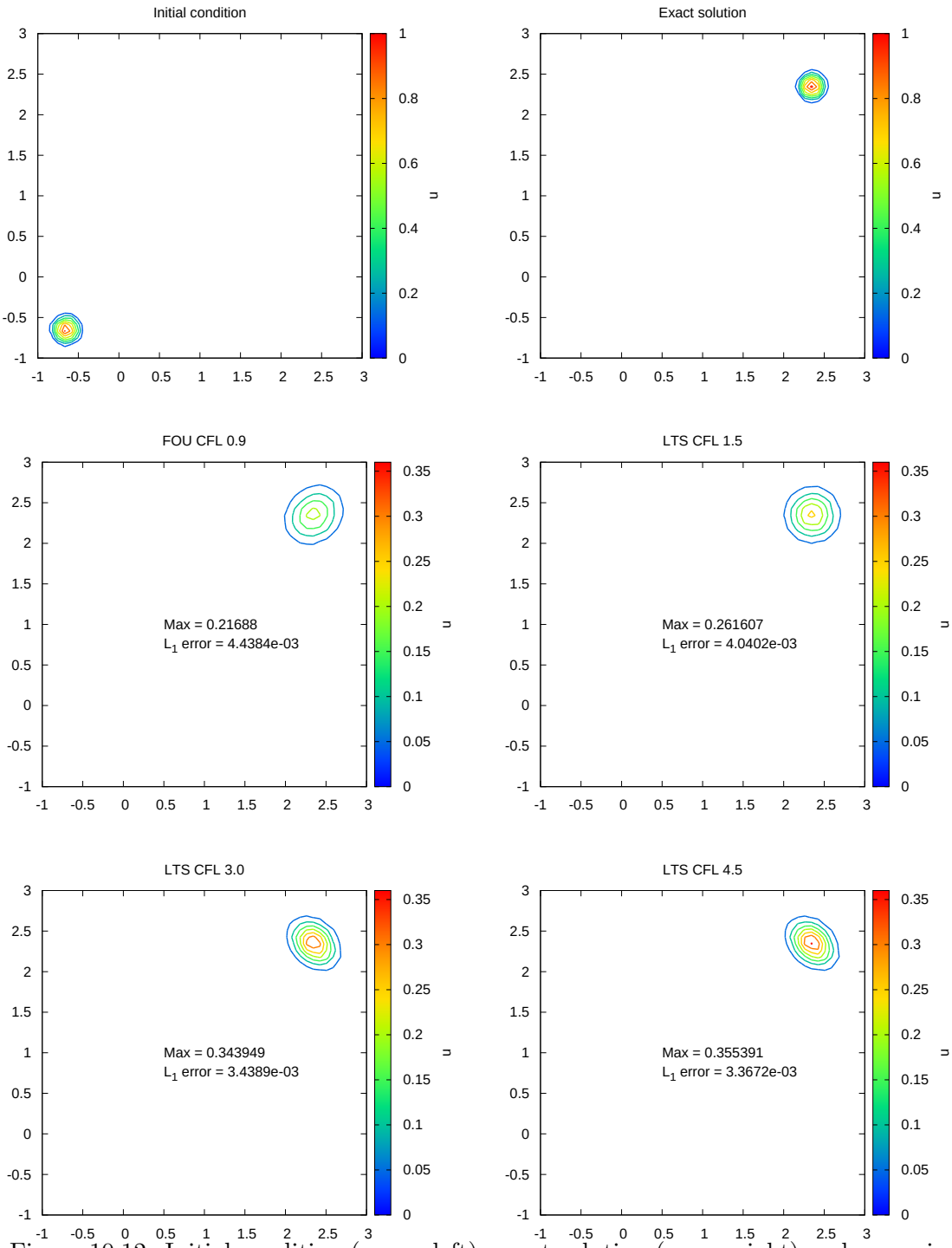

Figure 10.12: Initial condition (upper left), exact solution (upper right) and numerical results for test case 2 at t=3 s: FOU scheme CFL 0.9 (middle left), LTS CFL 1.5 (middle right), LTS CFL 3.0 (lower left) and LTS CFL 4.5 (lower right)

$$d = \sqrt{(x-4)^2 + (y-4)^2} \tag{10.29}$$

The initial condition as well as the velocity field can be observed in Figure 10.13. The domain is discretized into 246453 unstructured triangular cells, open boundaries are assumed all over the domain and the simulation is carried out during t=8. The numerical results are shown in Figure 10.14, where the exact solution (upper left) is compared against the conventional FOU scheme with CFL 0.5 (upper right), the LTS scheme with CFL 5 (lower left) and CFL 20 (lower right).

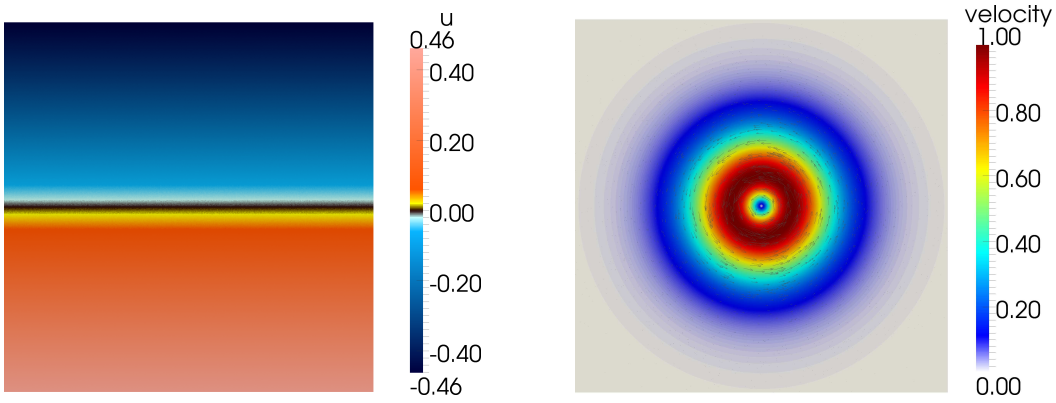

Figure 10.13: Test case 3: Initial condition and velocity field

The results seem to be similar in terms of the general shape of the numerical solution due to the fine discretization of the domain. However, the main differences can be observed in the region close to the center of the spiral, over which a sharper and less diffusive solution is achieved at the same time that the CFL number is increased. The exact solution [40] allows to compute the error in norm L_1 for the mentioned numerical results. Moreover, although it is a short simulation, it is possible to evaluate the computational time spent to compute the solution. Both metrics are condensed in Table 10.4.

	L_1-error	CPU time
FOU CFL 0.5	4.54183e-3	165.24 s
LTS CFL 5.0	4.41325e-3	25.98 s
LTS CFL 20.0	4.37861e-3	10.2 s

Table 10.4: Test case 3: L_1-error and CPU time achieved by each numerical scheme

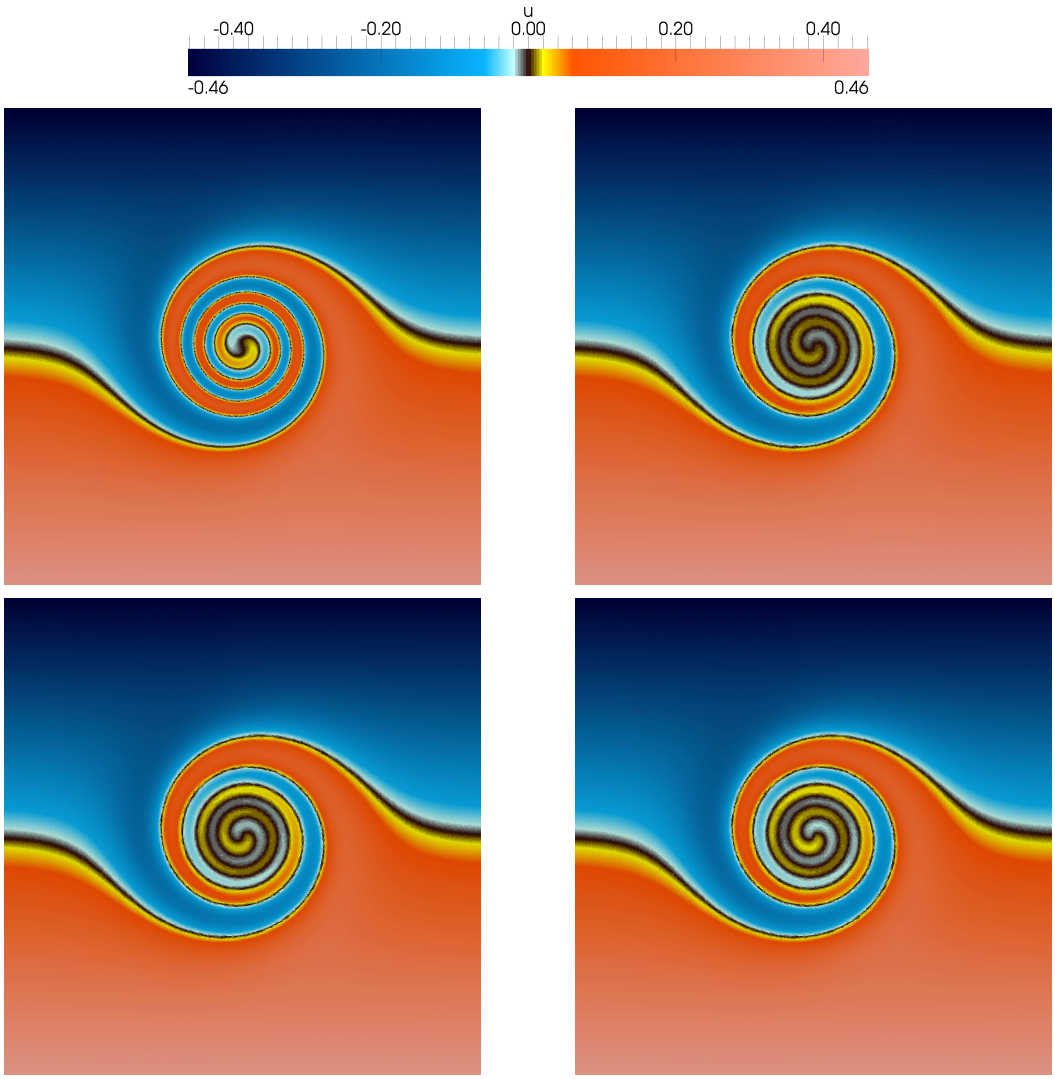

Figure 10.14: Test case 3: Exact solution (upper left) and numerical results achieved by the FOU scheme with CFL 0.5 (upper right) and the LTS scheme with CFL 5 (lower left) and CFL 20 (lower right) at t=8

Observing the table and admitting that the error in norm L_1 decreases slowly and does not scale at all with the CFL value, it can be concluded that not only a less diffusive solution is achieved when increasing the CFL number but also in less time.

10.3.3.4 Test case 4: 2D Burgers's equation

The 2D Burgers's equation is a non-linear scalar equation that can be formulated from (10.1), assuming $\mathbf{f}(u) = (u^2/2, u^2/2)$. The test case presented here consists of

a initial square (Figure 10.15, left) defined by

$$u(x,y,0) = \begin{cases} 1 & \text{if} \quad x \in (-0.5,0) \text{ and } y \in (-0.5,0) \\ 0 & \text{otherwise} \end{cases} \tag{10.30}$$

in a domain of $[-1,1] \times [-1,1]$ discretized into 61906 triangular unstructured cells with open boundary conditions. The evolution in time of the square shape under the influence of the velocity field induced by the Burgers's equation has exact solution at t=1 (Figure 10.15, right) and can be found in [127].

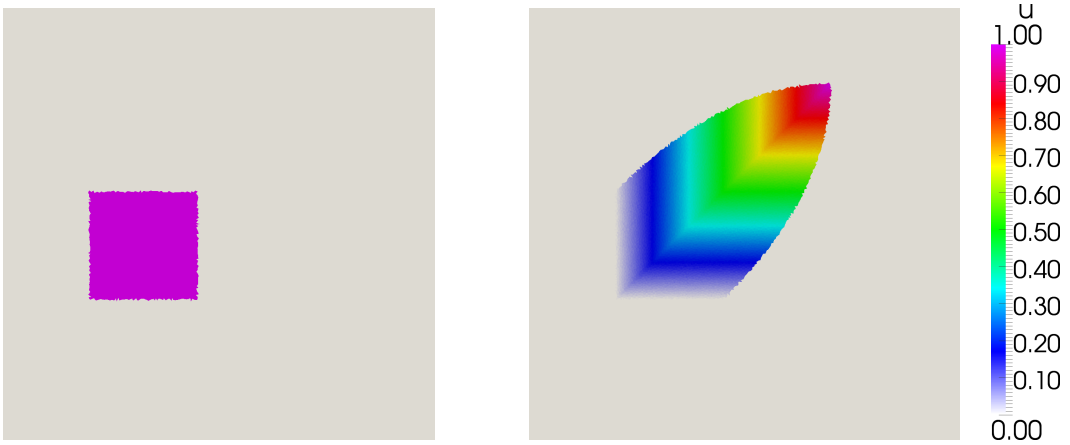

Figure 10.15: Test case 4: Initial condition and exact solution

Figure 10.16 compares the numerical results obtained by the conventional FOU scheme with CFL=0.5 (upper left) with those achieved by the LTS scheme with CFL=2.4 (upper right), CFL=5.1 (lower left) and CFL=8.35 (lower right).

The results in terms of maximum peak and L_1-error with respect to the exact solution are condensed in Table 10.5. As can be deduced form the results, the maximum peak increases when choosing a higher value of the CFL number although the error in norm L_1 does not change accordingly. However, it is worth noting that all the computations performed with the LTS scheme improve the results obtained by the conventional FOU scheme in terms of maximum peak and L_1-error.

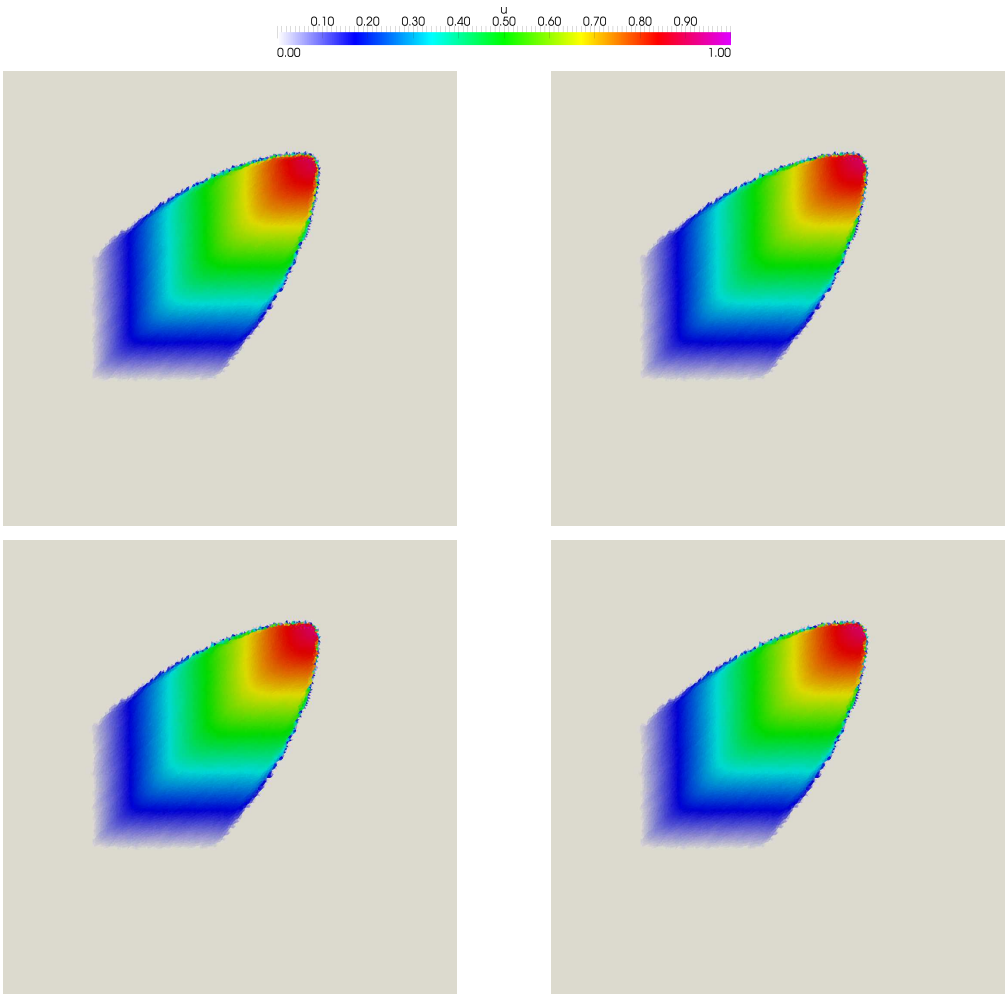

Figure 10.16: Test case 4: Numerical results achieved by the FOU scheme with CFL 0.5 (upper left) and the LTS scheme with CFL 2.4 (upper right), CFL 5.1 (lower left) and CFL 8.35 (lower left)

	Max Peak	L_1-error
FOU CFL 0.5	8.98496e-01	4.30107e-03
LTS CFL 2.4	9.28572e-01	3.79609e-03
LTS CFL 5.1	9.39219e-01	3.81847e-03
LTS CFL 8.35	9.60093e-01	3.75952e-03

Table 10.5: Test case 4: Maximum peak and L_1-error achieved by each numerical scheme

Chapter 11

LTS scheme for the 2D shallow water equations

11.1 2D systems of conservation laws with source terms

A 2D hyperbolic non-linear system of equations with source terms can be written in the form:

$$\frac{\partial \mathbf{U}}{\partial t} + \frac{\partial \mathbf{F}(\mathbf{U})}{\partial x} + \frac{\partial \mathbf{G}(\mathbf{U})}{\partial y} = \mathbf{H}(\mathbf{U}) \tag{11.1}$$

or:

$$\frac{\partial \mathbf{U}}{\partial t} + \nabla \cdot \mathbf{E} = \mathbf{H}\,, \tag{11.2}$$

in which $\mathbf{E}$=($\mathbf{F}, \mathbf{G}$). Equation (11.2) is integrated in a volume or grid cell Ω with area A_i:

$$\frac{\partial}{\partial t} \int_{A_i} \mathbf{U}\, d\Omega + \sum_{k=1}^{N_E} (\delta \mathbf{E} - \mathbf{S})_k \cdot \mathbf{n}_k l_k = 0\,. \tag{11.3}$$

where $\mathbf{n}_k = (n_x, n_y)$ is the outward unit normal vector to cell edge k, $\delta \mathbf{E}_k = \mathbf{E}_j - \mathbf{E}_i$, i and j being the indices of the cells sharing the edge k, l_k is the edge length, N_E is the number of edges in cell i and $\mathbf{S}$ is a suitable matrix accounting for the linearization in time of the vector of source terms.

Applying a Roe's local linearization of the problem at each edge, it is possible to define an approximate Jacobian matrix $\widetilde{\mathbf{J}}_{\mathbf{n},k}$ satisfying:

$$\delta(\mathbf{E}\cdot\mathbf{n})_k = \widetilde{\mathbf{J}}_{\mathbf{n},k}\delta\mathbf{U}_k\,. \tag{11.4}$$

Using two approximate matrices $\widetilde{\mathbf{P}} = (\widetilde{\mathbf{e}}^1, \widetilde{\mathbf{e}}^2, \widetilde{\mathbf{e}}^3)$, and $\widetilde{\mathbf{P}}^{-1}$, built using the eigenvectors of the Jacobian, that diagonalize $\widetilde{\mathbf{J}}_{\mathbf{n},k}$, giving

$$\widetilde{\mathbf{P}}_k^{-1}\widetilde{\mathbf{J}}_{\mathbf{n},k}\widetilde{\mathbf{P}}_k = \widetilde{\mathbf{\Lambda}}_k\,, \tag{11.5}$$

where $\widetilde{\mathbf{\Lambda}}_k$ is a diagonal matrix with eigenvalues $\widetilde{\lambda}_k^m$ in the main diagonal. According to the local linearisation, the conserved variables as well as the source terms are projected onto the matrix eigenvectors basis:

$$\delta\mathbf{U}_k = \widetilde{\mathbf{P}}_k\tilde{\mathbf{A}}_k \qquad (\tilde{\mathbf{S}}\cdot\mathbf{n})_k = \widetilde{\mathbf{P}}_k\tilde{\mathbf{B}}_k \tag{11.6}$$

where $\tilde{\mathbf{A}}_k = (\tilde{\alpha}_1,\ \tilde{\alpha}_2,\ \tilde{\alpha}_3)_k^T$ and $\tilde{\mathbf{B}}_k = (\tilde{\beta}_1,\ \tilde{\beta}_2,\ \tilde{\beta}_3)_k^T$ contain the sets of wave and source strengths, respectively. Therefore, the 2D numerical first order upwind (FOU) scheme can be formulated as follows, dealing with the contributions that arrive to the cell:

$$\mathbf{U}_i^{n+1} = \mathbf{U}_i^n - \frac{\Delta t}{A_i}\sum_{j=1}^{N_E}\sum_{m=1}^{3}\left((\tilde{\lambda}^-\tilde{\gamma}\,\tilde{\mathbf{e}})^m l\right)_k^n\,. \tag{11.7}$$

where $\tilde{\gamma}_k^m = \left(\tilde{\alpha} - \dfrac{\tilde{\beta}}{\tilde{\lambda}}\right)_k^m$.

11.2 Application to the 2D shallow water equations

The two-dimensional shallow water system of equations can be expressed as in (11.1). In particular, $\mathbf{U}$ represents the conserved variables

$$\mathbf{U} = (h,\ q_x,\ q_y)^T\,, \tag{11.8}$$

where q_x and q_y are the unit discharge in the x- and y-direction, respectively, and the fluxes of these variables are given by

$$\mathbf{F} = \left(q_x,\ \frac{q_x^2}{h} + \frac{1}{2} g h^2,\ \frac{q_x q_y}{h} \right)^T , \qquad \mathbf{G} = \left(q_y,\ \frac{q_x q_y}{h},\ \frac{q_y^2}{h} + \frac{1}{2} g h^2 \right)^T , \tag{11.9}$$

where g is the acceleration due to gravity. The source terms of the momentum are due to bed slope and friction

$$\mathbf{H} = \left(0,\ gh(S_{0x} - S_{fx}),\ gh(S_{0y} - S_{fy}) \right)^T , \tag{11.10}$$

The time step size for the standard first order upwind scheme is governed by the discrete wave celerities defined at each computational cell interface and expressed, in the particular case of a quadrilateral structured grid, as

$$\Delta t = \text{CFL} \min_{k,m} \left(\frac{A_i}{l_k \ |\tilde{\lambda}_k^m|} \right) , \qquad CFL \leq 0.5 \, . \tag{11.11}$$

However, its is feasible to extend the ideas developed for the scalar equations either applied over rectangular structured grids or triangular grids and to relax the CFL condition in (11.11) to allow bigger time step sizes. The corresponding procedures that will be later described are based on those explained for the scalar case although several corrections are needed in the context of the shallow water equations.

11.3 2D LTS on square grids

Adopting a correct formulation of the source term discretization as detailed in part I, the restriction in (11.11) can be relaxed when using the 2D LTS scheme and the dimensional splitting technique. Once the time step size is calculated, the procedure consists of computing the contributions at each interface and sending them along the x- or y-direction with their corresponding time step size according to (10.5).

The information is sent from each computational cell interface in a similar way to the 1D case, replacing Δx by A_i/l_k in the case of quadrilateral structured grids. Consequently, in the x-direction, when considering an interface k sharing the cells

i and j, the interface can be relabelled as $i+1/2$ (based on the evolution operator π_x) and cell j as $i+1$, simplifying the notation when referring to the previous or subsequent neighbouring cells. With this notation:

If $\widetilde{\lambda}^m_{i+1/2} > 0$

$$\begin{array}{ll} (\tilde{\gamma}\ \widetilde{\mathbf{e}})^m_{i+1/2} & \text{is subtracted from cells } i+1,\cdots,i+\mu^m_{i+1/2} \\ (\nu-\mu)^m_{i+1/2}\,(\tilde{\gamma}\ \widetilde{\mathbf{e}})^m_{i+1/2} & \text{is subtracted from cell } i+\mu^m_{i+1/2}+1 \end{array} \tag{11.12}$$

If $\widetilde{\lambda}^m_{i+1/2} < 0$

$$\begin{array}{ll} (\tilde{\gamma}\ \widetilde{\mathbf{e}})^m_{i+1/2} & \text{is subtracted from cells } i,\cdots,i+\mu^m_{i+1/2}+1 \\ (\nu-\mu)^m_{i+1/2}\,(\tilde{\gamma}\ \widetilde{\mathbf{e}})^m_{i+1/2} & \text{is subtracted from cell } i+\mu^m_{i+1/2} \end{array} \tag{11.13}$$

where $m=1,2,3$, $\tilde{\gamma}^m_k = \left(\tilde{\alpha}-\dfrac{\tilde{\beta}}{\tilde{\lambda}}\right)^m_k$, $\nu^m_k = \dfrac{\Delta t\ l_k}{A_i}\widetilde{\lambda}^m_k$ and $\mu^m_k = int(\nu^m_k)$. After each sub-iteration inside the whole time step, the cells have to be updated also considering the information from the boundaries. The procedure for one time step is the same as that presented in Section 9, sending the information according to (11.12) and (11.13). Furthermore, the strategy of splitting the rarefaction into several pieces travelling at different speeds is also applied in each of the three sub-iterations. More information can be found in [88].

On the other hand, a parameter ξ was introduced in (9.20) for the 1D analysis to internally reduce the initial target CFL value in the presence of sharp discontinuities or large source terms. The LTS proposed using the splitting technique may produce wrong results in the presence of strong discontinuities in the solution behaving as shocks due to the similarity to the 1D model. To avoid that, at the beginning of every time step the relative size of the discontinuities is evaluated and the target CFL is adjusted accordingly. Then, it is used globally as in any other time step so that the calculations run always with a global time step that is controlled by the most restrictive cell.

The new wet/dry strategy requires a revision of the mentioned parameter in order to avoid undesirable reductions in the target CFL value. In fact, $\xi = min(\xi_1, \xi_2)$, with

$$\xi_1 = \frac{\min_i\{h_i, h_{i+1}, |\delta h_{i+1/2}|\}}{|\delta h_{i+1/2}|}\,, \quad \xi_2 = \frac{\min_i\{|d_i|, |d_{i+1}|, |\delta d_{i+1/2}|\}}{|\delta d_{i+1/2}|} \tag{11.14}$$

for $1 \leq i \leq N$, where h is the water depth, $d = h + z$ is the water surface level and $0 \leq \xi \leq 1$. This parameter ξ gives again a measure of the size of the discontinuity, being closer to 0.0 when the discontinuity is strong and around 1.0 when the variables h and d are smooth or gradually varying.

However, the evaluation of ξ in (11.14) when h_i or h_{i+1} is zero enforces the recovery of the FOU scheme. Therefore, wet/dry fronts must be reformulated inside (11.14) in order to refrain from reducing the CFL initially chosen and a tolerance (TOL) for the variables is proposed. For example, the parameter ξ_1 will only act if

$$\min\{h_i, h_{i+1}, |\delta h_{i+1/2}|\} > TOL\,, \tag{11.15}$$

with an analogous condition imposed for parameter ξ_2, replacing h by d. In this work, $TOL = 0.05\,\mathrm{m}$.

11.4 2D LTS on triangular grids

The philosophy described for the scalar configuration in the case of triangular unstructured grids is extended to the 2D shallow water equations. The total contribution from each wall k shared by cells i and j is

$$\frac{\widetilde{\lambda}_k^m \Delta t\; l_k}{A_M}\,(\tilde{\gamma}\;\widetilde{\mathbf{e}})_k^m \tag{11.16}$$

where

$$M = \begin{cases} j & \text{if } \widetilde{\lambda}_k^m > 0 \\ i & \text{if } \widetilde{\lambda}_k^m < 0 \end{cases} \tag{11.17}$$

is packed according to the maximum allowed quantity that arrives to the cell using the following factor ζ_k

$$\zeta_k = \frac{(\widetilde{\lambda}^m \; l)_k}{L_M^{max}} \tag{11.18}$$

with

$$L_M^{max} = \max_{k,m}(\widetilde{\lambda}^m \; l)_k \qquad k = 1, ..., N_E \quad m = 1, ..., 3 \tag{11.19}$$

Therefore the quantities used to describe the LTS scheme are defined as follows:

$$\nu_k^m = \frac{\widetilde{\lambda}_k^m \Delta t \; l_k}{A_M \zeta_k} \qquad (\tilde{\gamma} \; \widetilde{\mathbf{e}})_k^m = \left(\left(\tilde{\alpha} - \frac{\tilde{\beta}}{\tilde{\lambda}} \right) \; \widetilde{\mathbf{e}} \right)_k^m \zeta_k \tag{11.20}$$

where $m = 1, 2, 3$. With this notation, it is possible to apply the Algorithm 2, expressed for the scalar case, replacing δu_k by $(\tilde{\gamma} \; \widetilde{\mathbf{e}})_k^m$ and $\boldsymbol{\lambda}_k$ by the average velocity $\widetilde{\mathbf{u}}_k = (\tilde{u}, \tilde{v})$. The way of sending the information for the 2D LTS scheme applied to the shallow water equations is included in Algorithm 3.

Algorithm 3 Sending the flux in the 2D SWE LTS scheme

```
send (γ̃ ẽ)_k^m to cell M
contrib=(γ̃ ẽ)_k^m
level=μ_k − 1
wc=k
sendFlux(wc,contrib,level)


function sendFlux(wc,contrib,level)
    if level ≥ 0 then
        set 1 and 2 neighbouring cells of wall wc
        set wc_1 and wc_2 neighbouring walls of wall wc
        evaluate P_1 = u_k n_1 and P_2 = u_k n_2
        label P_1 and P_2 as V, PV and NV according to its own sign.

```

Algorithm 3 Sending the flux in the 2D SWE LTS scheme (continued)

15: **if** P_1 is V **then**
16: **if** $level > 0$ **then**
17: send $\left(contrib \, \frac{A_M}{A_1} \right)$ to cell 1
18: sendFlux(wc_1, $contrib$, $level - 1$)
19: **else**
20: send $\left((\nu_k - \mu_k) \, contrib \, \frac{A_M}{A_1} \right)$ to cell 1
21: **end if**
22: **end if**
23:
24: **if** P_2 is V **then**
25: **if** $level > 0$ **then**
26: send $\left(contrib \, \frac{A_M}{A_2} \right)$ to cell 2
27: sendFlux(wc_2, $contrib$, $level - 1$)
28: **else**
29: send $\left((\nu_k - \mu_k) \, contrib \, \frac{A_M}{A_2} \right)$ to cell 2
30: **end if**
31: **end if**
32:
33: **if** P_1 and P_2 are PV **then**
34: evaluate $\theta_1 = \frac{P_1}{P_1 + P_2} \qquad \theta_2 = \frac{P_2}{P_1 + P_2}$
35: **if** $level > 0$ **then**
36: send $\left(\theta_1 contrib \, \frac{A_M}{A_1} \right)$ to cell 1
37: send $\left(\theta_2 contrib \, \frac{A_M}{A_2} \right)$ to cell 2
38: sendFlux(wc_1, $\theta_1 contrib$, $level - 1$)
39: sendFlux(wc_2, $\theta_2 contrib$, $level - 1$)
40: **else**
41: send $\left((\nu_k - \mu_k) \, \theta_1 contrib \, \frac{A_M}{A_1} \right)$ to cell 1
42: send $\left((\nu_k - \mu_k) \, \theta_2 contrib \, \frac{A_M}{A_2} \right)$ to cell 2
43: **end if**
44: **end if**
45: **end if**
46: **end function**

As a reminder, the contributions from wall k will be sent adequately according the projection of the average velocity $\mathbf{u}_k$ over the candidate neighbouring walls. The dot product between this average velocity and the outward normal direction of this walls will provide a measure of where the information has to be sent. Depending on the sign, valid V, not valid NV and partially valid PV paths are distinguished. The information is sent only across the valid and partially valid walls. Then, the technique is applied over this walls, creating a recursive algorithm that spreads out the information by means of different paths originated at the initial wall k.

11.5 Boundary conditions and wet/dry treatment in the 2D LTS scheme

Boundary conditions are an essential concern and they must be carefully analysed when developing a numerical scheme. Furthermore, as stated in part I, another issue of importance in the 2D shallow water equations is the correct formulation of the wet/dry treatment. The mentioned techniques for the conventional FOU scheme must be adapted to the 2D LTS scheme to avoid instabilities and to prevent negative values of water depth. As the procedure for the boundary conditions and the wet/dry treatment is intrinsically the same for both the square and the triangular configurations, it is presented in a general way in the following sections.

11.5.1 Boundary conditions

The formulation of the boundary conditions in the 2D LTS scheme can be considered as an extension of the treatment described for the 1D framework. In the context of the shallow water equations, open and closed boundaries arise. When dealing with open boundaries, no extra conditions have to be enforced except computing the contributions coming from the inner cells that leave out the domain. In fact, the designed algorithms in the LTS scheme are the responsible for sending the information out of the computational domain and these contributions have to be carefully computed in order to guarantee the mass conservation.

The analysis developed in the 1D configuration in section 9.2.2 revealed that the reflection technique is the adequate strategy to deal with closed boundaries in the

LTS scheme. This technique is also applied to the 2D configuration: each closed boundary wall is considered as a mirror that reflects the contributions and sends them back to the inner cells. In the case of the square grids, the dimensional splitting technique makes the procedure completely equivalent to the 1D configuration, sending back the information to the inner cells in the corresponding row or column.

The case of triangular grids is slightly different due to the multiplicity of paths when sending back the information. As described above, the way of sending the information requires the definition of an average velocity that is projected over the normal direction defined by the candidate edges. The dot product between them determines the paths over which the information is sent. Each path may split into two different paths and so on, creating the structure of an algorithm in the form of a tree. When one of these paths finds a closed boundary wall, the average velocity must be redefined ensuring that the dot product between the initial average velocity and the normal direction of the boundary wall is null. With this redefinition, the path is able to send back the contributions appropriately.

11.5.2 Wet/Dry treatment

The treatment of wet/dry fronts in the LTS scheme was previously mentioned in [87] where a reduction in the time step size is enforced to recover the conventional upwind scheme when a wet/dry front appears in the 1D model. This technique results absurd in the context of the 2D shallow water equations considering that the wet/dry fronts may be entirely present in each time step of this framework. In order to avoid reducing the time step size in all these situations, a short procedure consisting of two steps is proposed in this work, following the reasoning developed in part I. The first step has to be carried out during the computation of the fluxes and it consists of identifying the wet/dry interfaces. Assume that the potential wet/dry front is located at edge k, between cells i and j. The requirement of the positivity of the intermediate states derived from the Riemann Problem (see Figure 11.1) between cells i and j allows the determination of the wet/dry interfaces. These intermediate star states are expressed as follows for the subcritical case:

$$\begin{aligned} \mathbf{U}_i^* &= \mathbf{U}_i^n + (\tilde{\gamma}\widetilde{\mathbf{e}})_k^1 \\ \mathbf{U}_j^{**} &= \mathbf{U}_j^n - (\tilde{\gamma}\widetilde{\mathbf{e}})_k^2 \end{aligned} \tag{11.21}$$

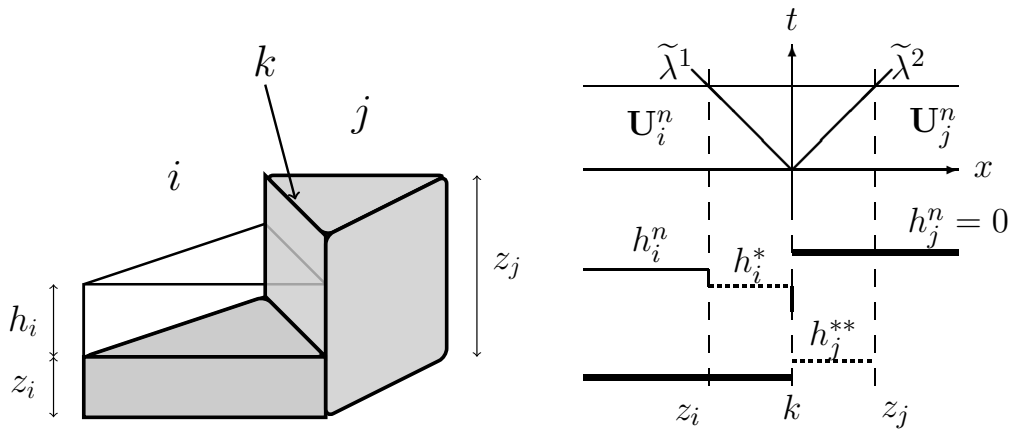

Figure 11.1: Wet/dry front: 3D view (left) and sketch of the Riemann Problem in the (x,t) plane for the subcritical case (right)

A more detailed explanation can be found in part I. In this case, the following rule is adopted:

- If $h_j^n = 0$ and $h_j^{**} < 0$ set k as a solid interface.
- If $h_i^n = 0$ and $h_i^* < 0$ set k as a solid interface.

where h_j^{**} and h_i^* are defined in (11.21).

Once all the contributions are computed and the wet/dry solid interfaces are identified, the second step is applied: the information from each computational edge is sent depending on the character (solid or not solid) of the involved interfaces. Accordingly, before sending to the subsequent cell, if the neighbour wall is identified as a solid interface, the contribution will be reflected and sent back. Otherwise, the information will be sent as usually.

For the sake of clarity, let reduce to the 1D model and consider the interface $i+1/2$ between cells i and $i+1$. Let assume that, for instance, $\nu_{i+1/2} = 4.3$ and the interface $i+5/2$ is labelled as a solid wet/dry interface. The contributions will be typically sent to cell $i+1$ and to cell $i+2$. However, as $i+5/2$ is detected as a solid interface, information cannot pass through this edge and hence is sent back to the corresponding cells as in the reflection technique explained for the in 1D case [87]. It is illustrated in Figure 11.2.

As in the case of closed boundary conditions, the strategy results to some extent different when dealing with triangular grids. The information is sent according

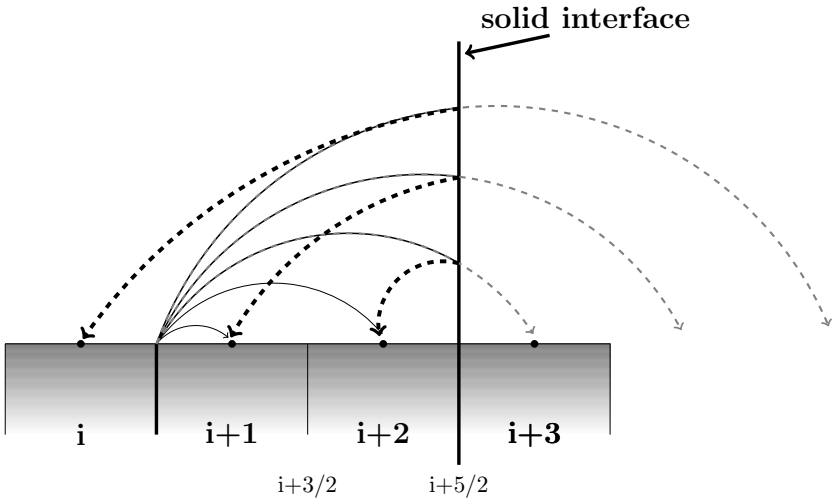

Figure 11.2: Example of the procedure to send the information with a wet/dry solid interface considering a reduced 1D problem

.

to Algorithm 3, unless the corresponding valid or partially valid wall k_s is at the same time labelled as a solid wall. In that case, the average velocity $\widetilde{\mathbf{u}} = (\widetilde{u}, \widetilde{v})$ is redefined enforcing $\widetilde{\mathbf{u}}\ \mathbf{n}_{k_s} = 0$ and the information is sent back, reflecting the waves and creating the same tree algorithm in the opposite direction of the normal direction to the solid wall k_s.

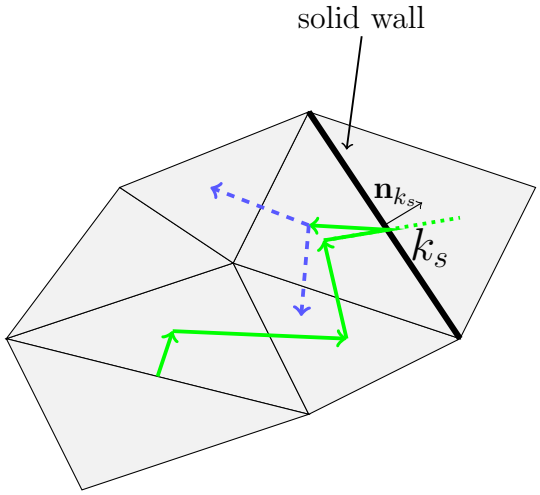

Figure 11.3: Sketch of the procedure to send the information with the interaction of a solid wall

The overall procedure presented here reduces the appearance of negative water depth

values. However, the labelling of the wet/dry interfaces as solid or not comes from a local analysis of the Riemann Problem, but the information is sent far from the neighbouring cells in the LTS scheme. Therefore, the problem of negative values for the water depth is not totally eliminated. In these extreme cases, an option is to reduce the time step to half the size and to recompute.

11.6 Numerical results

In this section, different challenging time-dependent test cases are presented to test the performance of the 2D LTS scheme and to introduce the wet/dry treatment explored in this work. They are performed either on square grids or on triangular grids.

11.6.1 2D LTS on square grids

11.6.1.1 Test case 1: Circular dam break

Dam break problems are widely used to test the behaviour of a numerical scheme. Consider a square frictionless domain $\Omega = [0, 200\,\mathrm{m}]^2$ discretized in a quadrilateral regular mesh of 40 000 cells (200×200) with flat bed and closed boundaries. The initial condition consists of still water of depth 1 m over all the domain except a circular sector in the lower left corner which has a 4 m depth of water (see Figure 11.4):

$$h(x, y, 0) = \begin{cases} 4.0 & \text{if } \sqrt{x^2 + y^2} \leq 100\text{m} \\ 1.0 & \text{otherwise}\,. \end{cases} \tag{11.22}$$

The boundary treatment was previously considered for the 1D shallow water equations. As the information is sent by rows or columns in the 2D LTS scheme, the same technique is adopted. In particular, when dealing with closed boundaries, the reflection technique, that considers the corresponding downstream edge as a mirror and reflects the waves, is utilised in this example. The numerical results achieved by the conventional FOU scheme with a CFL=0.5 are compared with those obtained by the LTS scheme with CFLs of 2.0, 4.0 and 8.0 at $t = 12\,\mathrm{s}$ and $t = 20\,\mathrm{s}$ (Figures 11.5 and 11.6 respectively) for the water depth.

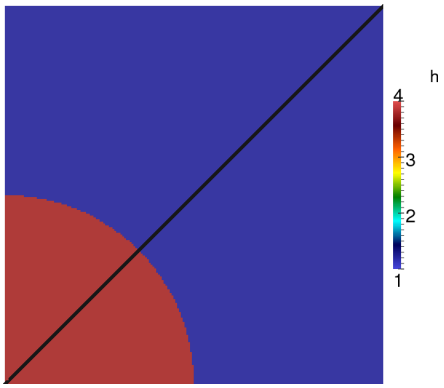

Figure 11.4: Test case 1: Initial state and sampling line

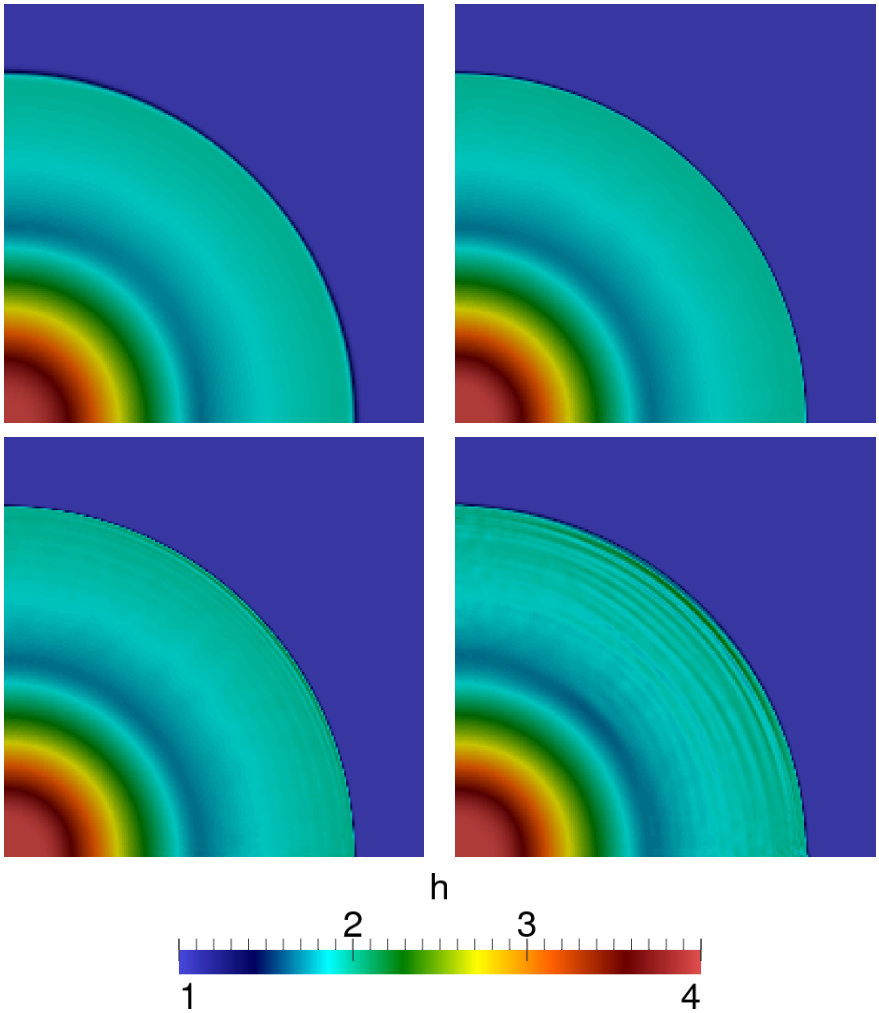

Figure 11.5: Test case 1. Numerical results for water depth at $t = 12\,\mathrm{s}$. FOU CFL 0.5 (upper left), LTS CFL 2.0 (upper right), LTS CFL 4.0 (lower left) and LTS CFL 8.0 (lower right).

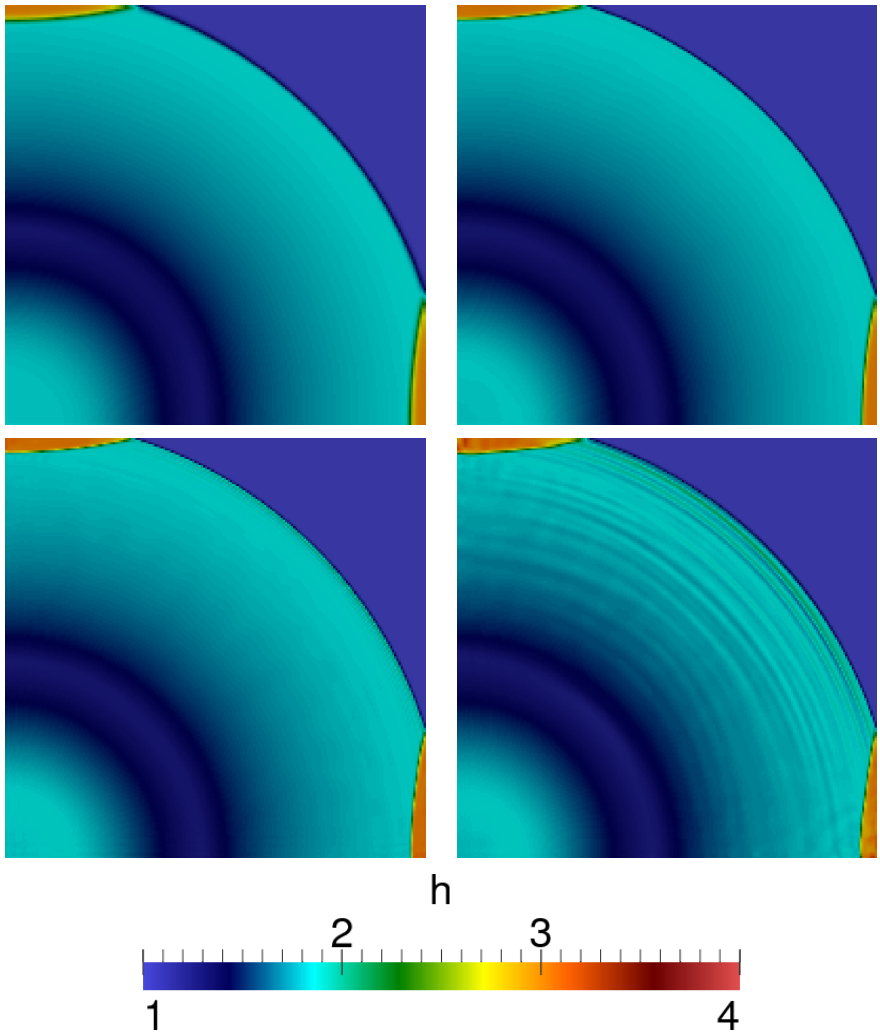

Figure 11.6: Test case 1. Numerical results for water depth at $t = 20\,\mathrm{s}$. FOU CFL 0.5 (upper left), LTS CFL 2.0 (upper right), LTS CFL 4.0 (lower left) and LTS CFL 8.0 (lower right).

Although spurious oscillations are detected near the location of the shock when increasing the CFL number, the solutions seem to be less diffusive, not only in the shock front but also near the rarefaction. In order to corroborate this hypothesis, the comparison through the line plotted in Figure 11.4 is considered, where a high resolution numerical solution (from now on called 'exact') can be computed evaluating the problem as a 1D problem on the radial direction [117]. Figures 11.7 and 11.8 show the exact and numerical results at $t = 12\,\mathrm{s}$ for the water depth and for the x- and y-unit discharge respectively. The LTS scheme becomes visibly less diffusive as the CFL number is increased, although several oscillations appear. However, the

velocity field tends to be more sensitive and larger oscillations near the shock fronts are clearly visible in Figure 11.8.

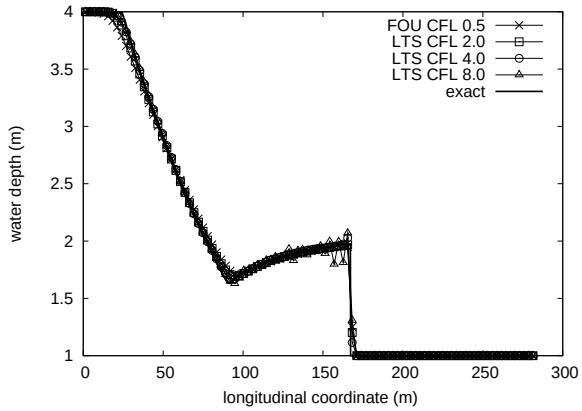

Figure 11.7: Test case 1: Exact and numerical results for water depth at $t = 12\,\mathrm{s}$.

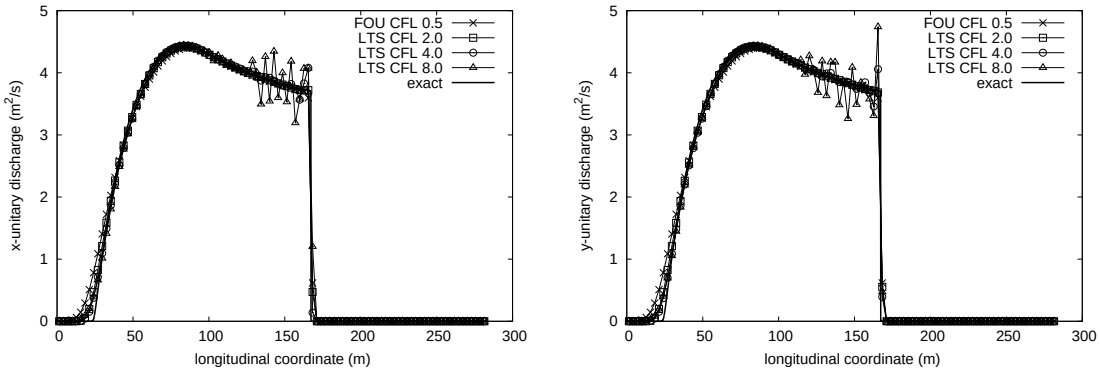

Figure 11.8: Test case 1: Exact and numerical results at $t = 12\,\mathrm{s}$ for x-unit discharge (left) and y-unit discharge (right).

11.6.1.2 Test case 2: Dam break over adverse slope

When incorporating friction and an adverse slope, the dam break problem becomes an example of unsteady flow with source terms. Also, if the initial discontinuity is over a dry bed, the test case contains all the elements that represent a challenge in shallow flow modelling. A test case, consisting of a dam break over dry bed with adverse slope, is performed as a good measure of the behaviour of the wet/dry front treatment in unsteady flow. Consider the same domain and discretization as the previous test case. The friction is modelled now using a Manning friction coefficient

$n = 0.03\,\mathrm{s/m^{\frac{1}{3}}}$. The initial condition and the bed level (see Figure 11.9) are set to

$$h(x,y,0) = \begin{cases} 2.0 & \text{if} \quad \sqrt{x^2+y^2} < 100 \\ 0.0 & \text{if} \quad 100 < \sqrt{x^2+y^2} < \sqrt{2}\ 100.0 \\ 0.0 & \text{if} \quad x > \sqrt{2}\ 100.0\,, \end{cases} \tag{11.23}$$

$$z(x,y) = \begin{cases} 0.0 & \text{if} \quad \sqrt{x^2+y^2} < 100 \\ 0.0 & \text{if} \quad 100 < \sqrt{x^2+y^2} < \sqrt{2}\ 100.0 \\ \dfrac{\sqrt{2(x^2+y^2)}}{100} - 2 & \text{if} \quad x > \sqrt{2}\ 100.0\,. \end{cases} \tag{11.24}$$

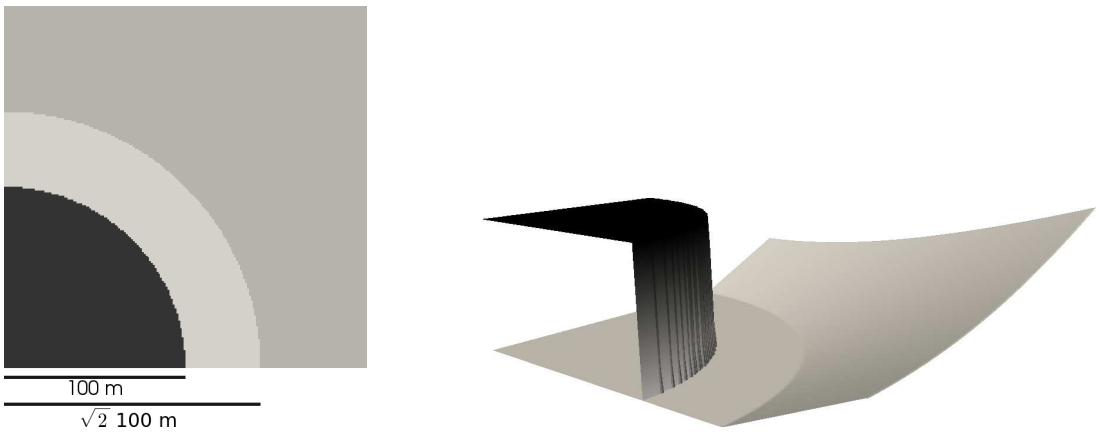

Figure 11.9: Test case 2: Initial condition and bed level. Plan view (left) and 3D view (right).

The convergence to an equilibrium state has been simulated over 40 000 s. The time evolution of the longitudinal profile along the diagonal (as in the previous test case) is plotted in Figure 11.10 at $t = 10\,\mathrm{s}$, $t = 50\,\mathrm{s}$ and $t = 100\,\mathrm{s}$ comparing the numerical results achieved by the FOU scheme and the LTS scheme with an arbitrarily chosen CFL value of 3.7. Also the final state at $t = 40\,000\,\mathrm{s}$ is shown in Figure 11.10 (lower right).

The results illustrate that the location of the wet/dry front is well reproduced by the LTS scheme in comparison with the FOU scheme, as well as the still water surface final state. It is worth remarking that the well-balanced property is demonstrated, as expected, due to the careful discretization of the source terms.

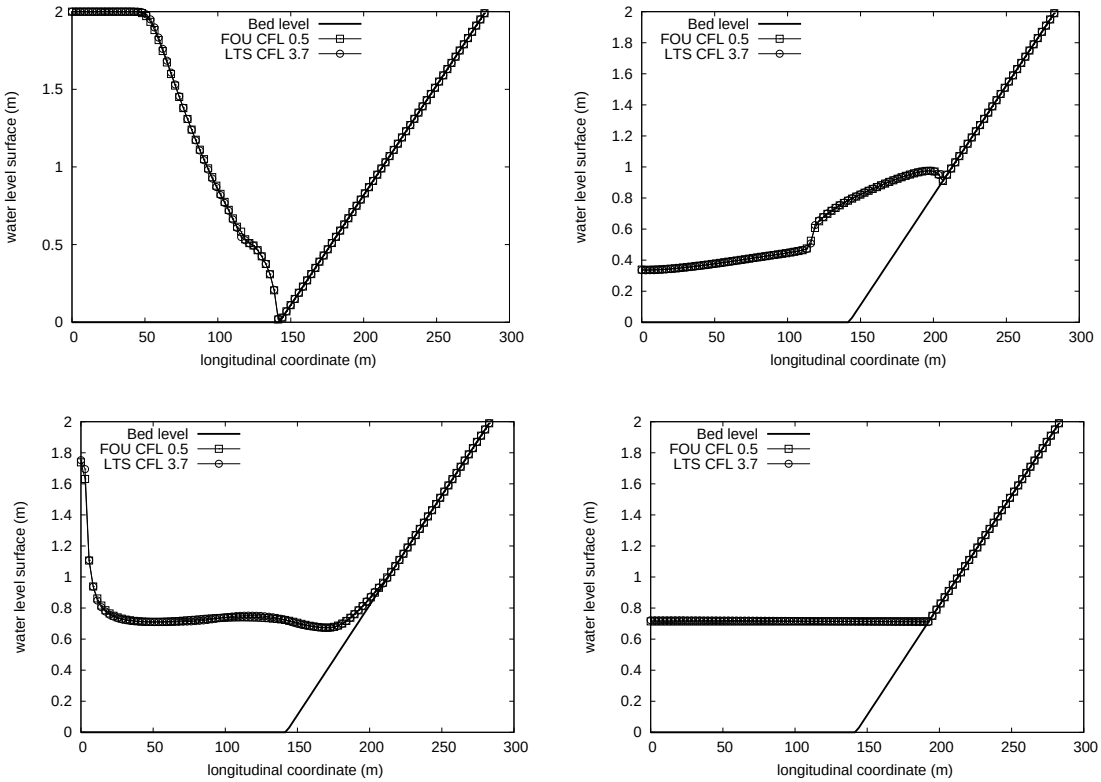

Figure 11.10: Test case 2. Longitudinal profile along the diagonal line achieved by the FOU scheme and the LTS scheme with a CFL of 3.7 at $t = 10\,\mathrm{s}$ (upper left), at $t = 50\,\mathrm{s}$ (upper right), at $t = 100\,\mathrm{s}$ (lower left) and at $t = 40\,000\,\mathrm{s}$ (lower right)

11.6.1.3 Test case 3: tsunami test case

The simulation of a tsunami event modelled in a 1/400 laboratory scale [81, 77] is used to demonstrate the applicability of the LTS scheme to unsteady real problems. Gauging points were located at

$$P1 = (4.52, 2.196)\,, \quad P2 = (4.52, 1.696)\,, \quad P3 = (4.52, 1.196)\,, \tag{11.25}$$

where the evolution in time of the water level surface is registered. Figure 11.11 shows the bathymetry of the reduced model as well as the location of the gauging points mentioned. According to the reported bed material, the friction is modelled with a Manning coefficient of $n = 0.01\,\mathrm{s/m^{\frac{1}{3}}}$. More details about the description and the experimental data can be found in [77, 17].

The initial condition is fixed as a constant water surface level of $h + z = 0.0$ and

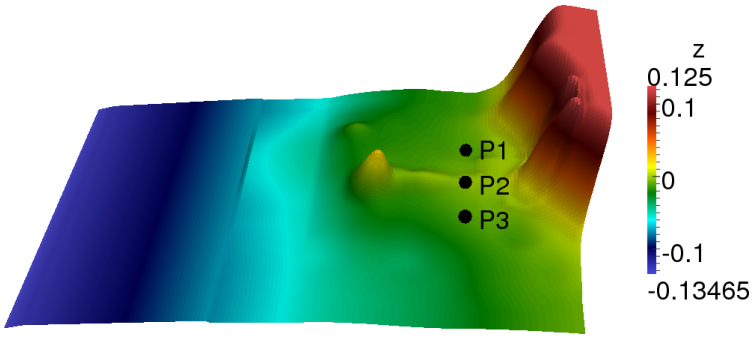

Figure 11.11: Test case 3: Bed elevation and probe locations.

the domain ($[0, 5.488] \times [0, 3.388]$) has been discretized with a mesh of 23 716 cells (196×121). The boundary conditions are considered as closed vertical sidewalls (as in the laboratory model) except the incident wave coming from offshore, defined as a variation in time of the water depth (see Figure 11.13). It is worth remarking that, in this finite volume implementation, the information given as the boundary condition is imposed at the center of the boundary cells.

The numerical simulation has been carried out using the FOU scheme with a CFL=0.5 and the LTS scheme with three different CFL values: 2.4, 4.8 and 7.2. As an example, two states corresponding to times $t = 13\,\mathrm{s}$ and $t = 18\,\mathrm{s}$ are illustrated in Figure 11.12, simulated with the LTS scheme with a CFL=4.8. At $t = 13\,\mathrm{s}$ the shoreline is moving backward due to the depression wave, but by $t = 18\,\mathrm{s}$ the wave has reached the end of the domain and has been reflected.

The time evolution registered experimentally at measured points P1, P2 and P3 is also compared with the numerical results obtained by the FOU scheme and the LTS scheme with the mentioned CFL values in Figure 11.13.

Wet/dry boundaries are present throughout this test case. However, the results achieved by the LTS scheme with different CFL values are very similar to those obtained by the FOU scheme with a CFL=0.5 with respect to the experimental measurements. Also the results achieved by the three different CFL values used for the LTS scheme do not generate 'a priori' many differences. It is due to the internal reduction in the time step size during the computation to avoid negative water depth values.

In order to strengthen this hypothesis, the time evolution L_1-error in these probes P1, P2, and P3 relative to a grid converged solution (the maximum available reso-

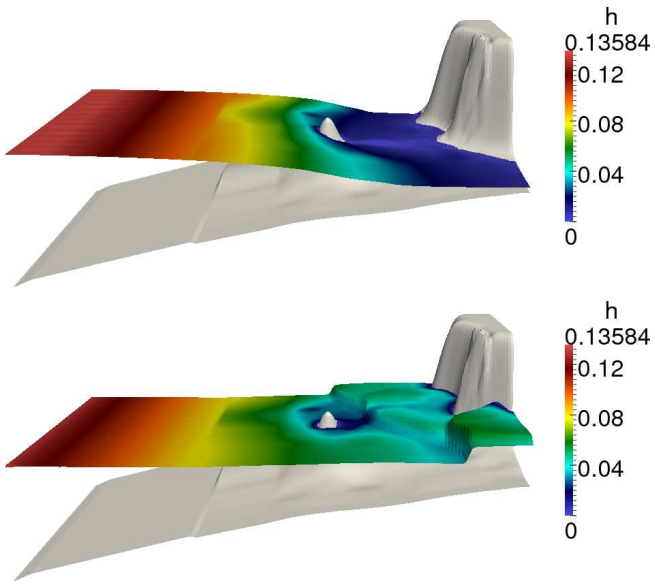

Figure 11.12: Test case 3: 3D plot of the water level surface at $t = 13\,\mathrm{s}$ (upper) and $t = 18\,\mathrm{s}$ (lower)

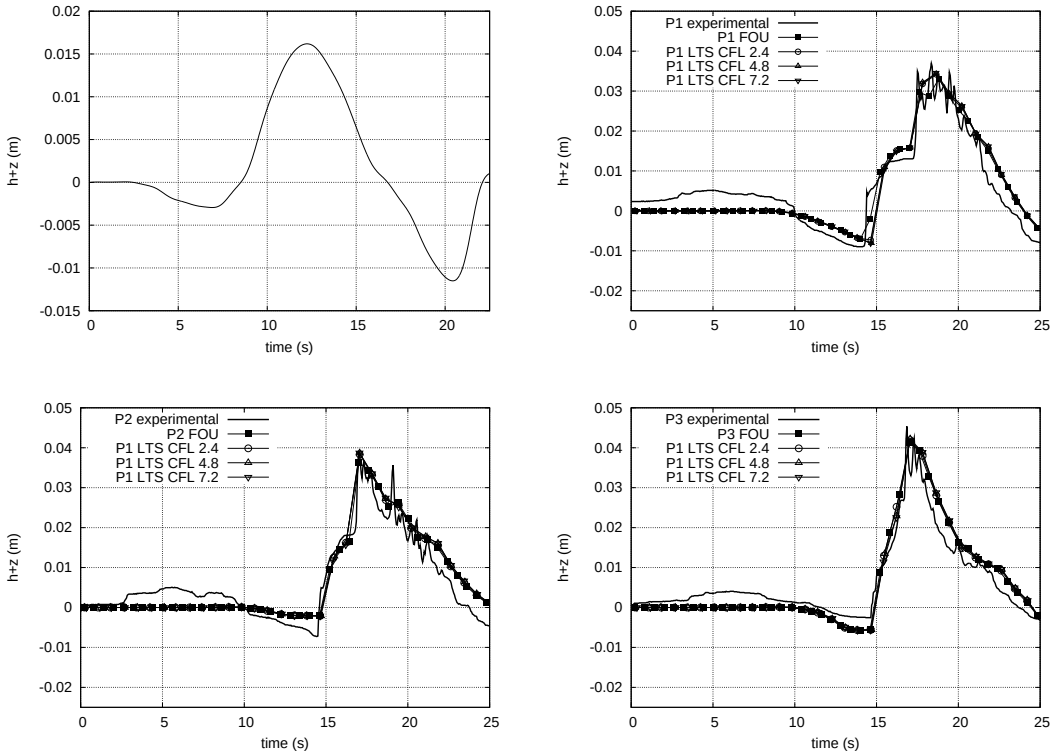

Figure 11.13: Test case 3: Inlet boundary condition (upper left) and experimental vs. numerical results at probe 1 (upper right), probe 2 (lower left) and probe 3 (lower right)

lution data, 392 × 242 cells) is plotted in Figure 11.14. Firstly, as probes are placed in a critical location, just behind the island, with wet/dry transitions, the L_1-error can provide a very local estimation of the error made. Observing the graph, a clear tendency of the error cannot be detected . Results with the LTS CFL 2.4 and even CFL 4.8 improves those obtained by the FOU scheme, mainly at probes P1 and P2. However, P3 registers a better behaviour when using the FOU scheme. Results with the LTS scheme CFL 7.2 are usually worse than with the other schemes. However, the error remains under acceptable values in comparison with the FOU scheme.

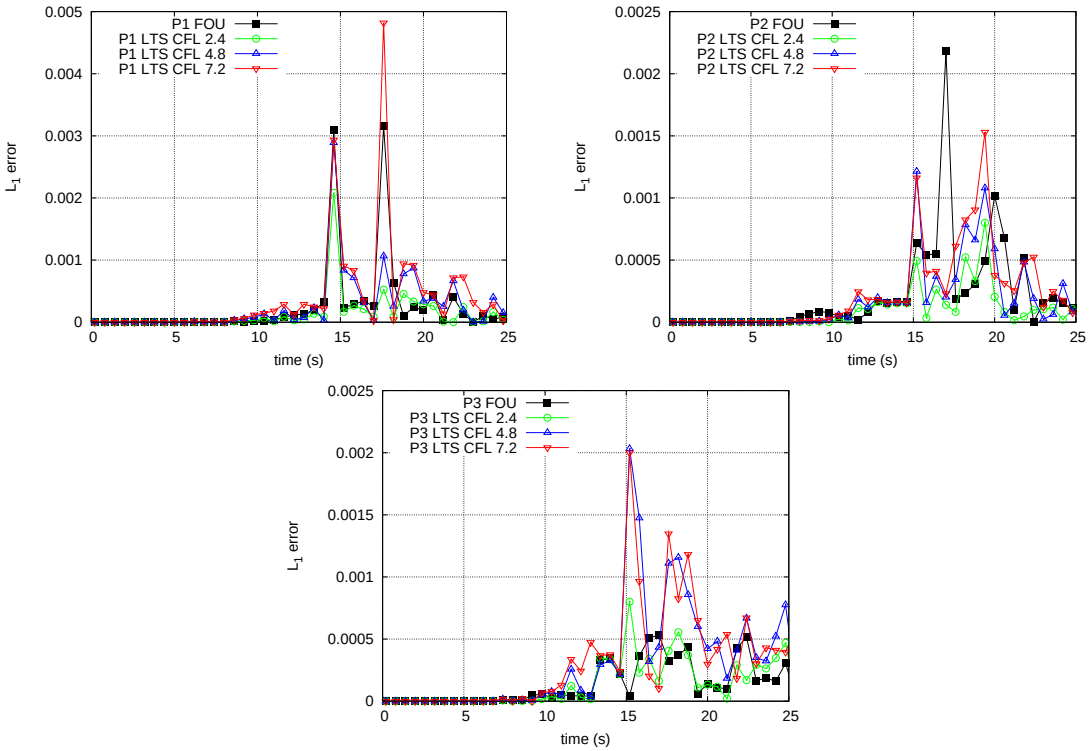

Figure 11.14: Test case 5: L_1-error at probes P1, P2, and P3 relative to a grid converged solution

11.6.1.4 Test case 4: Real world configuration: Ebro river

The proposed LTS scheme is now applied to a realistic test case in order to evaluate its uncertainty in the flooding prediction. For this purpose, a meandering reach of the Ebro river (Spain) is used [89]. The Digital Terrain Model (DTM) including the bathymetry was provided by the Ebro River Basin Administration (www.chebro.es).

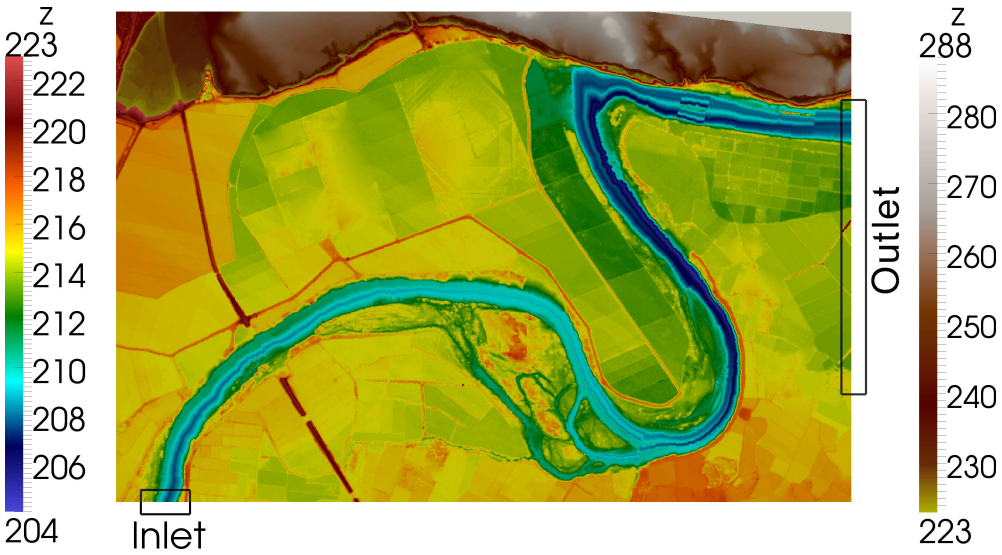

Figure 11.15: Test case 4: Topography and location of the boundaries

The domain ($3 \times 2\ km^2$) is discretized in 300×200 square cells, integrating the information coming from the DTM. This grid will be used for the simulation of a flooding event with the LTS scheme with CFL=4.2 and with the FOU scheme with CFL=0.5. A steady state of 100 m^3/s is computed and set as the initial condition before the flooding event. In fact, the inlet boundary condition consists of a one day abrupt hydrograph raising to 1400 m^3/s in 180 s and decreasing afterwards linearly during the rest of the day (see Figure 11.16, left). With this choice, all kind of scenarios such as sharp shocks, wetting and drying situations, are present. A free flow condition is chosen as the outlet boundary. The location of the inlet and outlet boundary conditions, as well as the topography of the test case are displayed in Figure 11.15. According to the aerial photograph of the domain, a Manning's roughness map is considered, shown in Figure 11.16 (right).

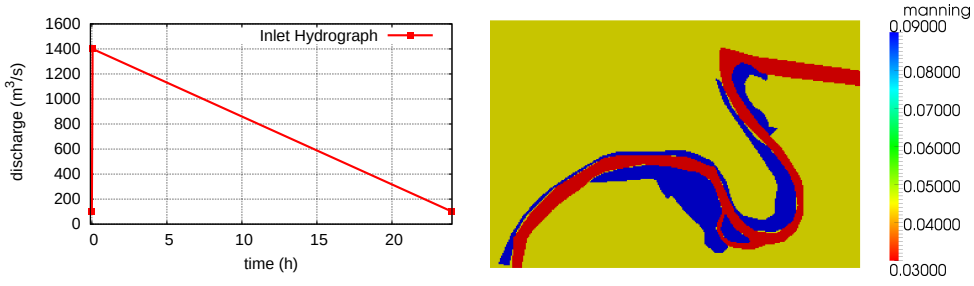

Figure 11.16: Test case 4: Inlet hydrograph and Manning's roughness map

In addition, the simulation of the same configuration with a very fine grid of 1500000

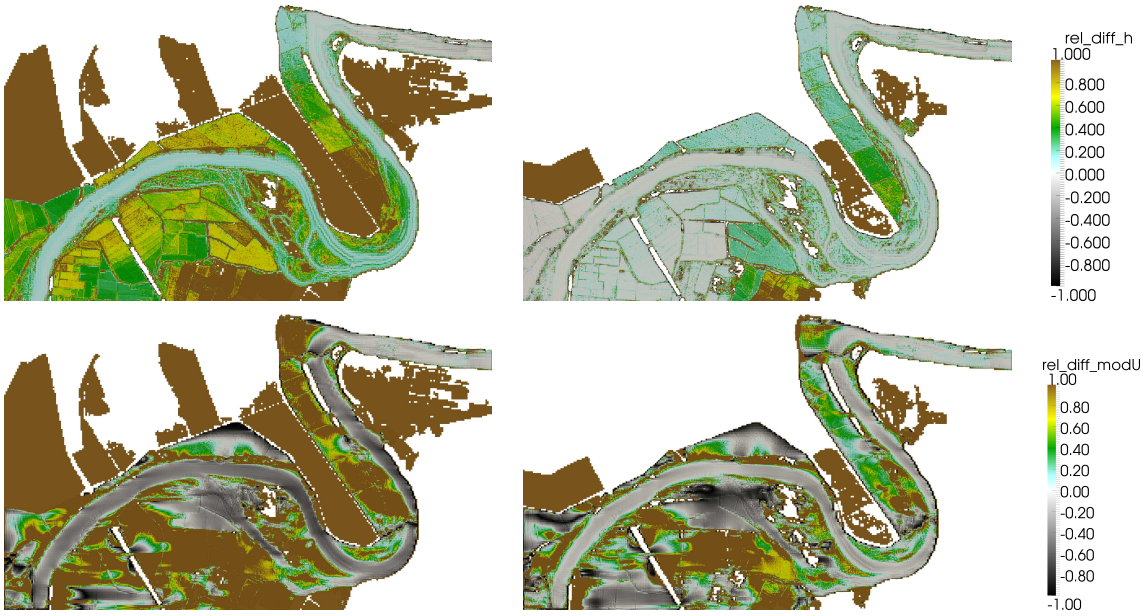

Figure 11.17: Test case 4: Map error of water depth for the FOU scheme (upper left) and for the LTS scheme (upper right) at t=3h. Map error of velocity magnitude for the FOU scheme (lower left) and for the LTS scheme (lower right) at t=3h.

(1500 × 1000) squared cells using the first order upwind scheme with CFL 0.5 is chosen as a reference solution in order to compare the schemes mentioned above. The comparison is firstly done using map errors. Therefore, a mapping from the coarse to the fine grid is performed to be able to extract the spatial distribution of the error. The relative error with respect to the reference solution is analysed for the variables h and velocity magnitude ($modU$). As an example, a map error is included corresponding to t=3h (Figure 11.17) for the FOU scheme (left) and for the LTS scheme (right). The meaning is as follows: 0.0 means no differences, 1.0 has to be understood as the scheme (FOU or LTS) is wetting a cell that is completely dry on the reference solution and -1.0 is a dry zone for the scheme (FOU or LTS) that is wetted on the reference solution.

As can be seen, the error for both schemes is almost totally located at the flood-plain, where the coarse grid is overestimating the flooding area, possibly due to the incorrect definition of levees. It can be concluded that in terms of water depth, at t=3h, the LTS scheme computes a more accurate solution than the FOU scheme. The main factor responsible for this is the wet/dry treatment, which seems to be more restrictive in this situation. The velocity magnitude is overall well-reproduced

in the main river, while the flooding extension overestimates it in the floodplain.

In order to have a quantitative measure of the error, Figure 11.18 shows two graphs. On the left, the evolution of the L_1-error along the domain over the 24h hydrograph is extracted for the water depth and for the velocity magnitude. On the right, the evolution of the flooded area computed by each model is compared against the flooded area achieved by the reference solution.

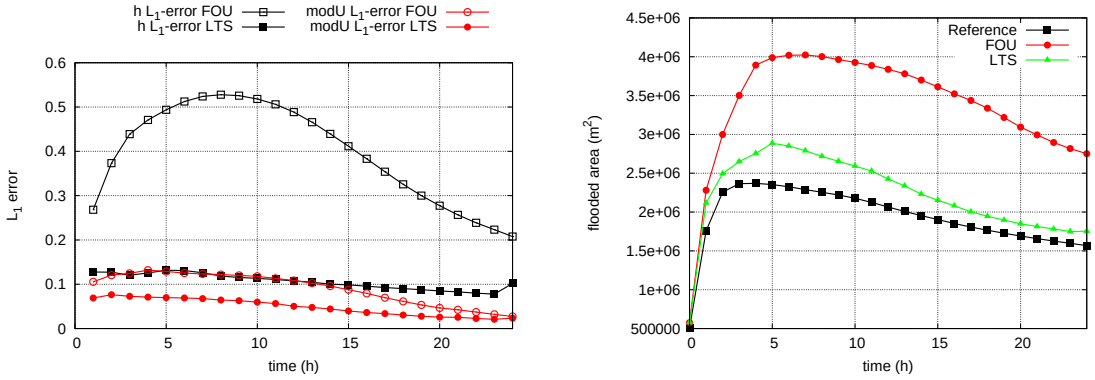

Figure 11.18: Test case 6: Evolution of the L_1-error (left) and flooded area (right) with respect to the reference solution

Observing the figures, the LTS scheme approximates better the results obtained by the reference solution although both models overestimate the flooded area.

11.6.2 2D LTS on triangular grids

11.6.2.1 Test case 5: The spilling of a column of water

The simulation of the flow induced by the spilling of a column of water defined by

$$h(x,y,0) = \begin{cases} 4.0 & \text{if} \quad 45 < x < 55\ , 45 < y < 55 \\ 2.0 & \text{otherwise} \end{cases} \tag{11.26}$$

is performed (see Figure 11.19) over a flat frictionless surface.

It is placed in the middle of a domain $[0, 100] \times [0, 100]$ discretized into 79326 triangular unstructured cells which is assumed to be a closed box, that is, zero flow is enforced all over the right, left, upper and lower boundaries. The simulation is

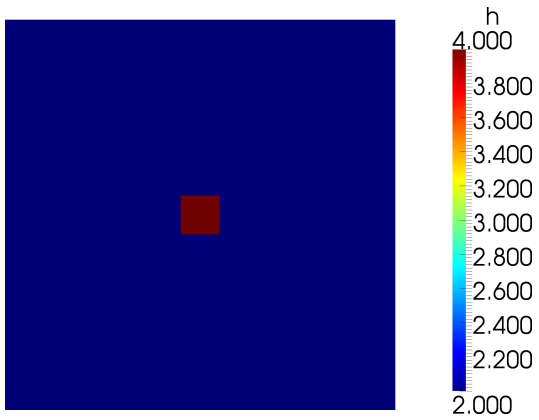

Figure 11.19: Test case 5: Initial condition

carried out during 80 s and the results at t=10 s, t=20 s, t=40 s and t=80 s are displayed in Figure 11.20 for the conventional FOU scheme with CFL 0.9 (left) and for the proposed LTS scheme with CFL 5.0 (right).

A qualitative analysis shows that the numerical diffusion associated to the FOU scheme is widely reduced if using a LTS scheme. Moreover, the technique to manage the closed boundaries seems to be effective due to the absence of oscillations and the large number of rebounds that take place during the simulation. On the other hand, shock and rarefaction are entirely present and interact, and no extra correction is required in the LTS scheme over triangular grids.

11.6.2.2 Test case 6: Dambreak with triangular bump

This test case deals with the simulation of a dambreak over a dry bed with irregular topography. A rectangular cross section channel is considered, 1 m wide and 7 m long, with two triangular bumps with symmetric slopes. More information of the description of the test case is found in [85]. The initial condition is given by

$$h(x,y,0) = \begin{cases} 0.45 & \text{if} \quad x < 2.25 \\ 0 & \text{if} \quad \text{otherwise} \end{cases} \tag{11.27}$$

and is displayed in Figure 11.21 (upper left) in a 3D view with the channel geometry. The domain is discretized into 40033 unstructured triangles and the simulation is carried out during 15 s. Zero flow is assumed all over the boundaries and a constant Manning roughness coefficient of 0.007 $s/m^{1/3}$ is considered according to the ex-

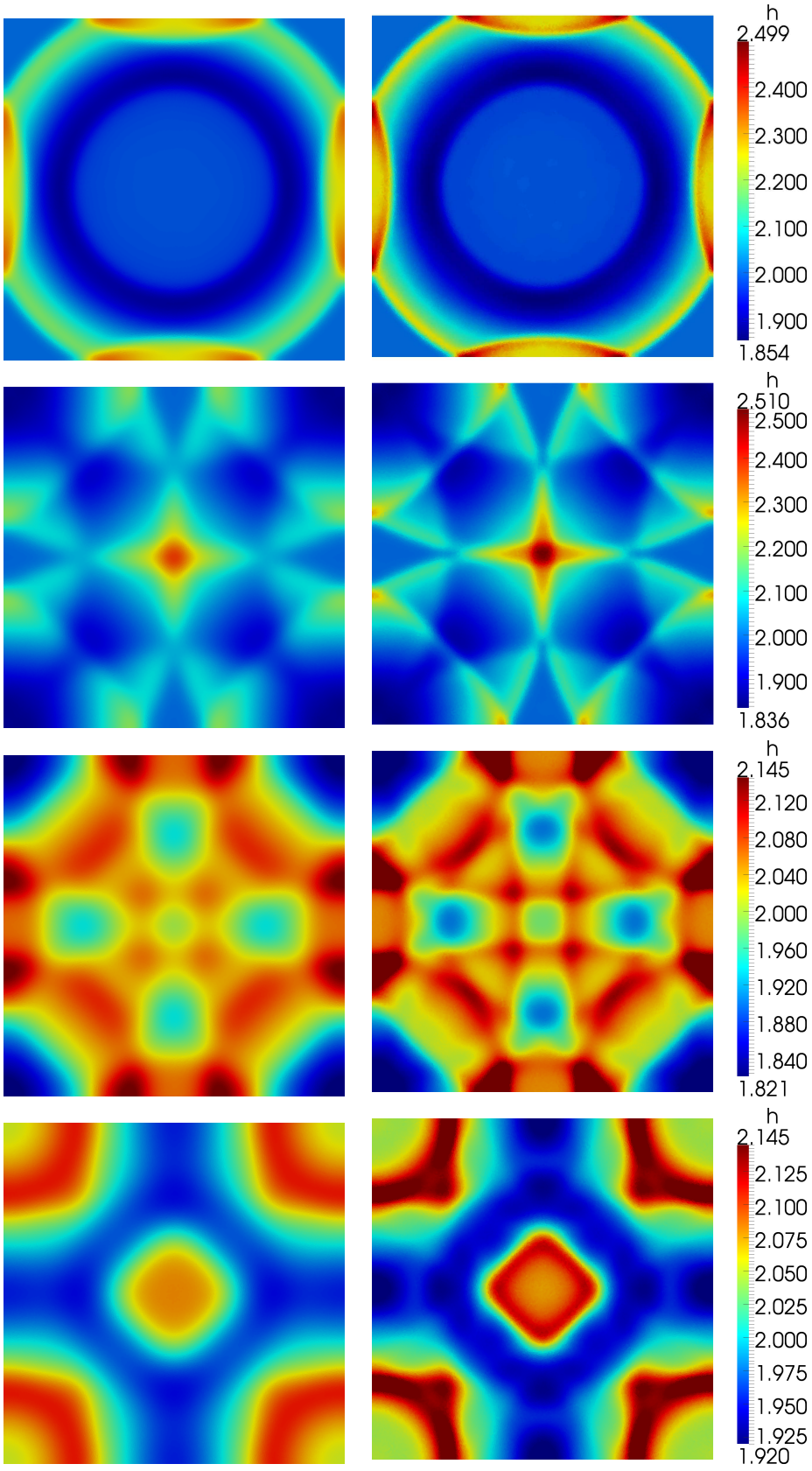

Figure 11.20:]

Test case 5. Numerical results for water depth with FOU CFL 0.9 (left) and LTS CFL 5.0 (right). From upper to lower: t=10 s, t=20 s, t=40 s and t=80 s

perimental specifications. As an example, three snapshots of the complete channel simulated with the LTS scheme with CFL 4.78 at times t=2 s, t=5 s and t=10 s are also shown in (11.21) (upper right, lower left and lower right respectively).

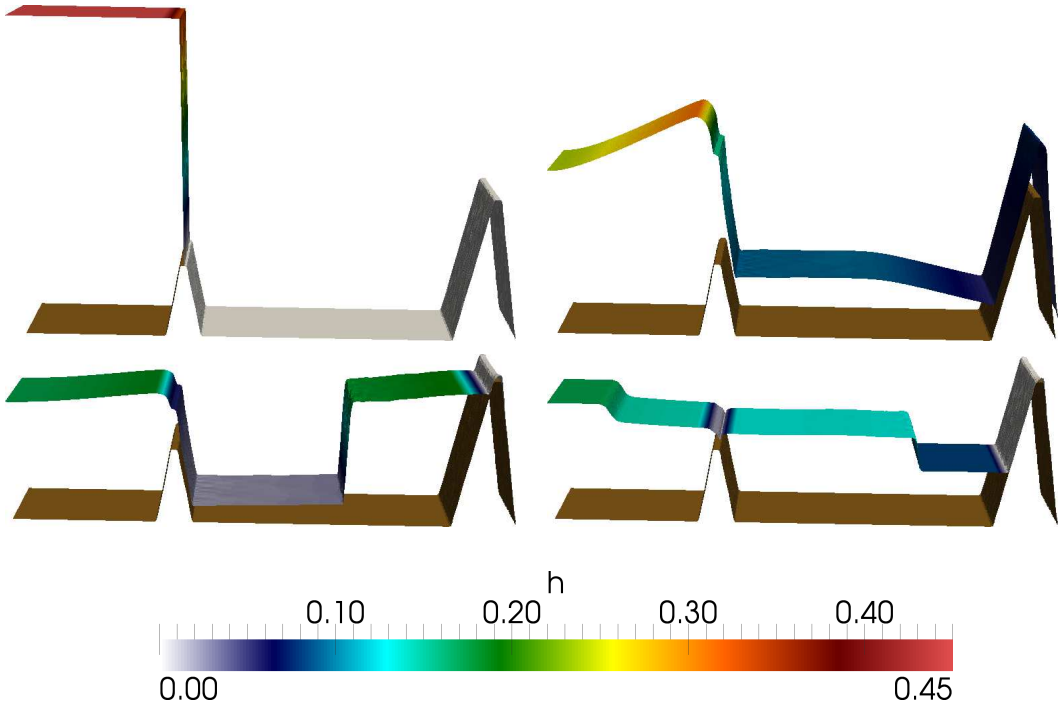

Figure 11.21: Test case 6. Initial condition (upper left) and numerical results achieved by the LTS scheme with CFL 4.78 at times t=2 s (upper right), t=5 s (lower left) and t=10 s (lower right)

On the other hand, the evolution in time of the water depth at points $P_1 = (1.4, 0.5)$, $P_2 = (2.25, 0.5)$ and $P_3 = (4.5, 0.5)$ as well as the velocity in the x-direction at probe P1 is registered. Therefore, the numerical results achieved by the LTS scheme with a value of CFL=4.78 and the FOU scheme with CFL 0.5 are compared with those experimental measurements (see Figure 11.22).

Numerical results and experimental measurements have a good agreement. Although several differences are present, maybe related to the nature of the equations and the hydrostatic hypothesis assumed by the 2D shallow water equations, the overall behaviour of the numerical results is very similar to the recorded data. As a consequence, the LTS scheme is proved to be able to handle wet/dry boundaries in unsteady situations, with complex topography.

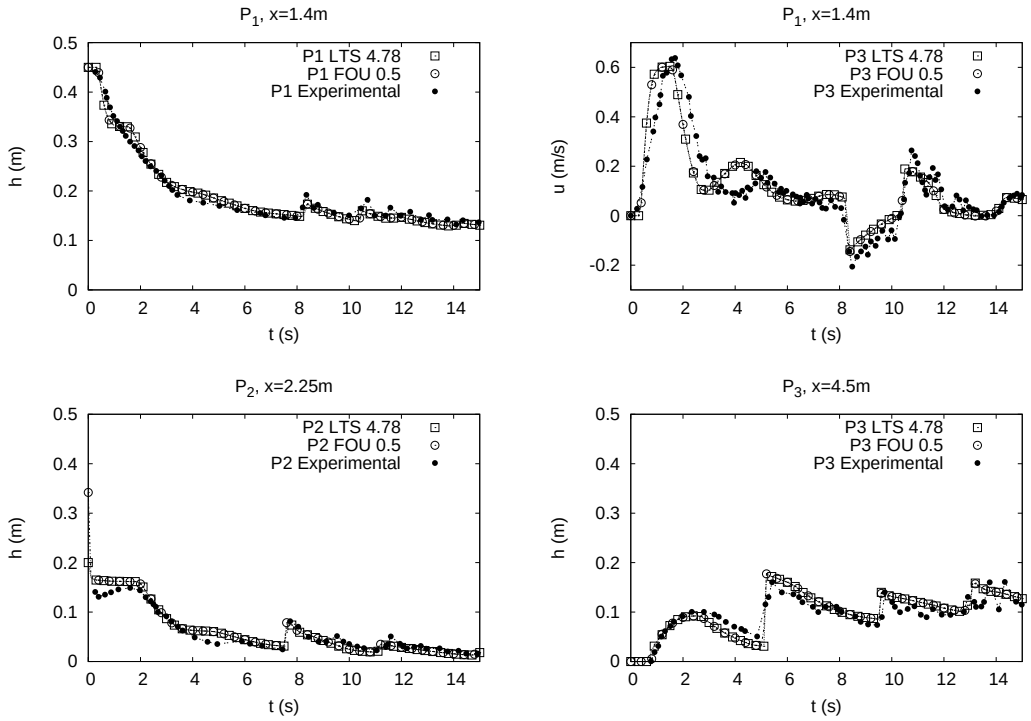

Figure 11.22: Test case 6: Experimental measurements and numerical results achieved by the FOU scheme with CFL 0.5 and the LTS scheme with CFL 4.78. Evolution in time of water depth at probe P1 (upper left), velocity at probe P1 (upper right) and water depth at probes P2 and P3 (lower left and lower right respectively)

11.6.2.3 Test case 7: Filling depressions

The last test case performed with the 2D LTS scheme with unstructured triangular grid consists of a square $2000\,m \times 2000\,m$ with smooth cavities or depressions all over the domain (see Figure 11.23), discretized in a coarse mesh composed by 10376 cells. It is designed to examine the capability of the model to predict the inundation extent in a slow unsteady flow. The details of the configuration of the test case can be found in [121].

From a dry initial state, a flood hydrograph with a peak flow of $20m^3/s$ during 1h 25min is introduced as inlet boundary condition (see Figure 11.24, left) in a 100 m line on the North-Western corner of the domain (Figure 11.24, right). Different probes located at the deepest point of each depression will be considered to compare the numerical results achieved by the FOU and by the LTS scheme.

The simulation is carried out during 48 h until the flow has filled the mentioned

Figure 11.23: Test case 7: Topography

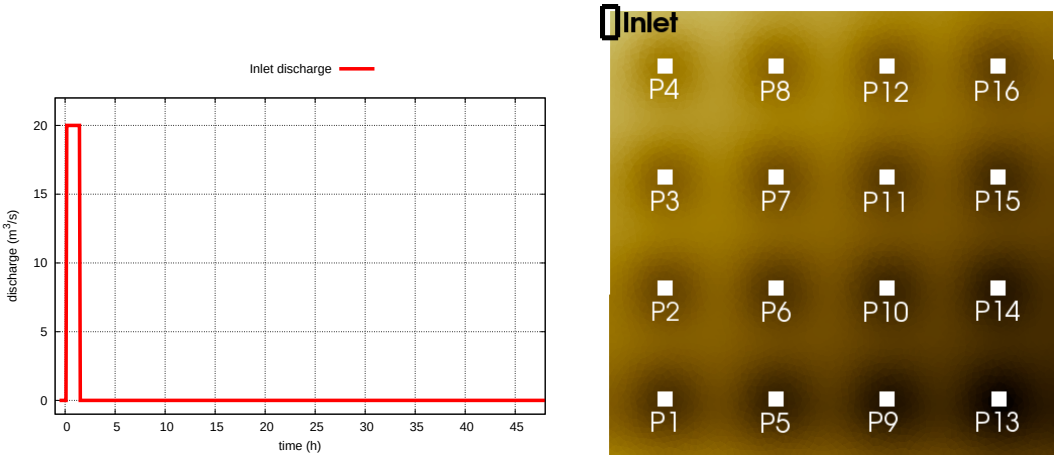

Figure 11.24: Test case 7: Inflow hydrograph (left) and location of the inlet boundary conditions and the probes (right)

depressions. As an example, four snapshots simulated by the LTS scheme with CFL 2.9 corresponding to times t=1h, t=4h, t=8h and t=48h (end) are shown in Figure 11.25. Moreover, the evolution in time at each probe defined in Figure 11.24 of the water depth predicted by both the FOU scheme with CFL 0.5 and the LTS scheme with a value of CFL=2.9 is represented in Figure 11.26.

The comparison at each probe reveals that the LTS scheme achieves the same results in terms of water depth than the FOU scheme. All probes are well reproduced even those which are dry (probes 9, 13, 14, 15 and 16). The wet/dry fronts under slow flow and subcritical conditions are also well captured by the LTS scheme, achieving promising results in terms of accuracy.

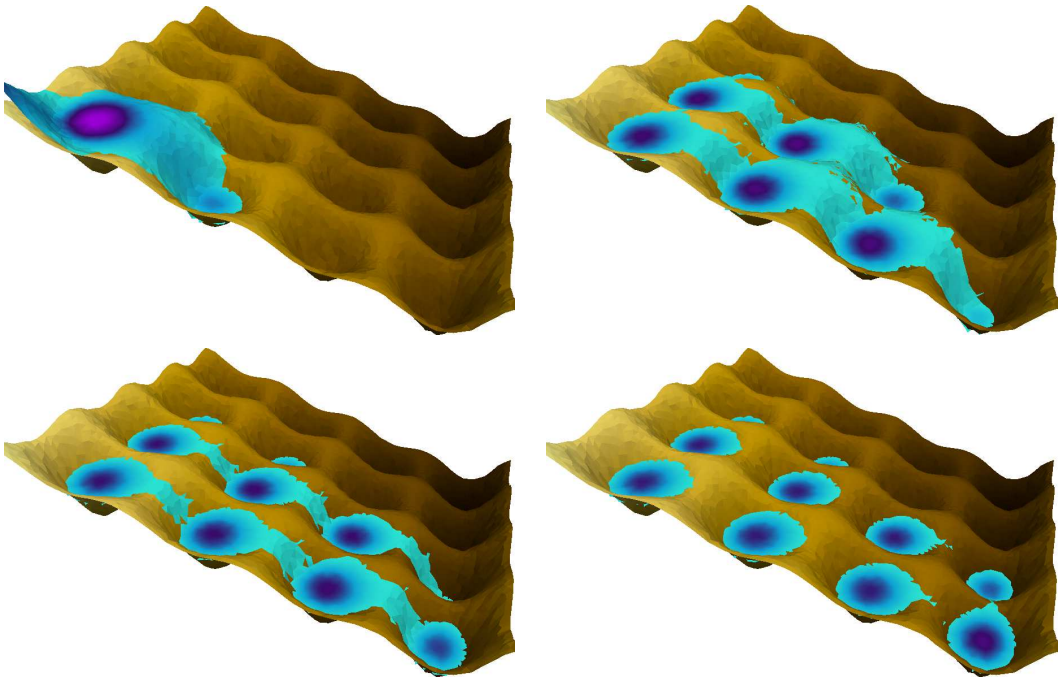

Figure 11.25: Test case 7. 3D view of the filling process with the LTS scheme with CFL 2.9 at t=1h (upper left), t=4h (upper right), t=8h (lower left) and at t=48h (end of the simulation, lower right)

11.6.3 Computational time

The use of a LTS scheme with larger CFL values than the conventional schemes should imply a reduction in the computational burden. Table 11.1 summarizes the CPU time consumed by each scheme (FOU and LTS) in each test case of relevance (test case 1 has been omitted due to the short computational time). Note that the CFL value of 0.5 (the maximum allowable in squared meshes) is used for the computation with the FOU scheme for test cases 2-4 and for test case 6-7 with the triangular unstructured grid. In test case 5, the FOU scheme is simulated with a CFL=0.9. The number of cells in both models (FOU and LTS) is obviously the same for each test case.

As can be seen, the results show a computational gain associated to the LTS scheme. However, the correspondence between the speed-up and the choice of the CFL value does not scale linearly. Two main factors affect considerably this response. First, it is important to highlight the complexity of the algorithms to send appropriately the information: shocks and rarefactions in the square grid, solid and not-solid wet/dry

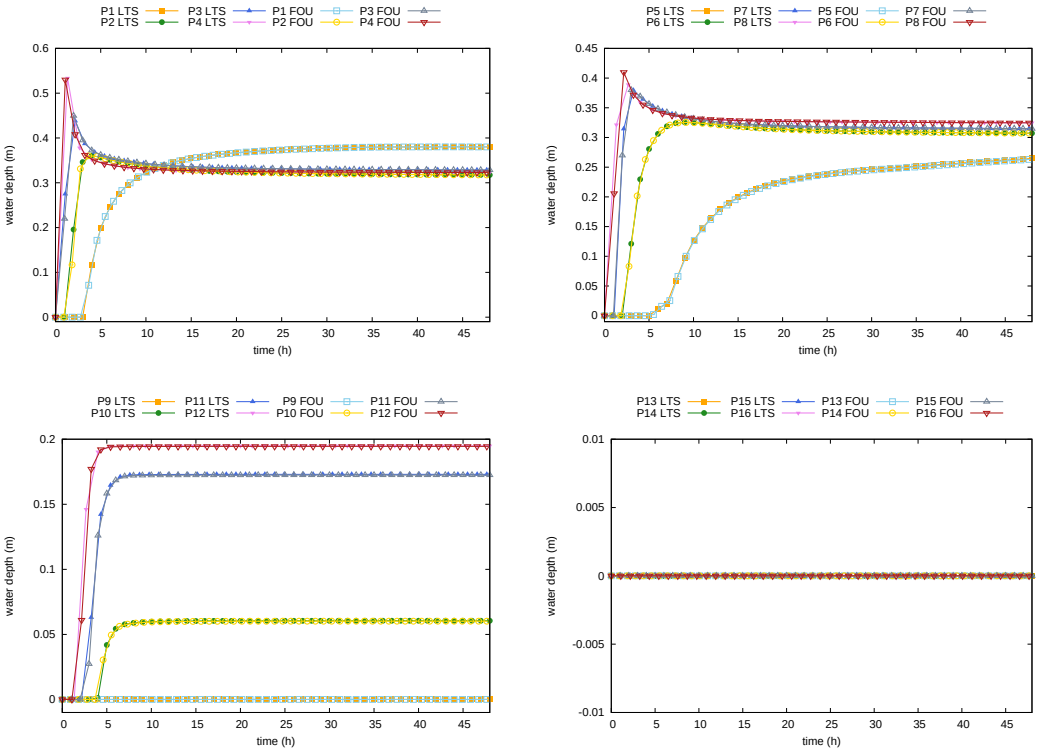

Figure 11.26: Test case 7: Time evolution of water depth at probes 1-4 (upper left), probes 5-8 (upper right), probes 9-12 (lower left) and probes 13-16 (lower right) achieved by the LTS scheme with CFL 2.9 and the FOU with CFL 0.5

Test case	FOU time (s)	LTS		Speed-up
		CFL number	time (s)	
2	11227	CFL 3.7	5105	2.199
3	72	CFL 2.4	48	1.5
		CFL 4.8	40	1.8
		CFL 7.2	46	1.565
4	22380	CFL 4.2	7405	3.022
5	357	CFL 5.0	138	2.587
6	424	CFL 4.78	128	3.31
7	233	CFL 2.9	101	2.307

Table 11.1: CPU time consumed by the each model in each test case of relevance

interfaces, closed boundaries, in addition to the reduction of the CFL value or the appearance of negative depths in the presence of large discontinuities and complex

topographies.

Secondly, in the case of square grids, the structure of the dimensional splitting procedure doubles the interface accessing and triples the cell updating, making the process slower due to the memory access. In the case of the triangular grid, the distinction between valid, not valid and partially valid paths in the triangular configurations and the adequate way to send the information far from the neighbouring cells increase considerable the computational time.

Summing up, although the number of time steps carried out is reduced, the cost of each one is increased.

Chapter 12

Conclusions

In this part, an extension of the Large Time Step (LTS) scheme developed by Leveque has been presented in order to complete and generalise this method first for scalar equations and then for the shallow water equations with source terms.

The proposed LTS scheme, when applied to 1D non-linear scalar cases, requires the discrete representation of the rarefaction wave in the form of several discontinuities travelling at different speeds if an accurate solution is sought at large CFL values. A simple rule to estimate these speeds has been proposed. When incorporating the presence of a source term in 1D non-linear scalar equations, the LTS scheme can be extended following the same procedure as in the homogeneous case provided that the original explicit scheme was already well-balanced. However, it is important to remark that the quality of the numerical solution deteriorates as the CFL grows in presence of relatively important source terms due to the fact that the scheme is based on the advection speed of the homogeneous system. The 1D inviscid Burgers equation with source term has been used to propose a second estimation of the advection speed that takes into account the presence of the source term in the form of an intermediate state. The effectiveness of this treatment has been illustrated for the 1D Burgers equation with source term achieving accurate numerical solutions in a single time step.

The extension to one dimensional non-linear systems of equations with source terms has been explored and applied to the 1D shallow water system. The splitting technique required in rarefactions has been extended to systems and shown to produce good results that preserve conservation. The bed slope and friction source terms have been incorporated in a compact formulation. From that formulation of the well-balanced explicit scheme, the extension leading to the LTS scheme has been possible. In the case of systems, the LTS shows a good performance for CFL>1 but,

as in the scalar case, the solution is worse as the CFL grows in presence of strong discontinuities and/or relatively important source terms. Looking for a compromise between accuracy and efficiency in the method, instead of devising a complex procedure to improve the estimation of the advection speeds in presence of strong discontinuities and/or relatively important source terms, a new parameter ξ is proposed in order to detect these situations and to reduce accordingly the initial target CFL number. This target CFL value should be chosen always smaller then the number of grid cells and, as a rule of thumb, one order of magnitude less than it in cases of convergence to steady flow and two orders of magnitude smaller in cases of unsteady computations.

The treatment of open and closed boundary conditions in the 1D configuration has been explored, and two possible techniques are provided for the second case. Among them, the reflection technique, that sends back the information that would cross the boundary when using large CFL values, is recommended in the case of closed boundaries. At open boundaries, no special treatment is required for the information going out of the computational domain apart from the logical control of the conservation.

With the proposed modifications, the LTS scheme has been used to reproduce all kind of flow conditions. Its performance has been illustrated using test cases with exact solution of steady and unsteady open channel flow problems. In the steady open channel flow test cases, the LTS scheme has proved efficient and accurate allowing the use of very high CFL values. The technique proposed to control the size of the CFL in presence of discontinuities has been effective in the steady flow problems with hydraulic jump. A series of frictionless dam break problem with all kind of discontinuous geometry have been used as validation test cases. Again, the LTS has been supplied with the parameter dynamically controlling the appearance of strong discontinuities and/or important source terms that has been able to adjust accordingly the maximum allowable CFL value to produce accurate and stable numerical solutions at the cost of reducing the proportional gain that the LTS offers in linear cases.

The extension to the 2D framework is performed distinguishing between square and triangular grids. The implementation on square grids is achieved by means of the dimensional splitting technique. Previous advances related to the source term discretization and boundary conditions treatment detailed for the 1D case are

preserved due to the splitting procedure, solving "by rows" or "by columns" three 1D problems per time step. The 2D LTS scheme on square grid has been presented for the scalar case, dealing with constant and variable velocity fields and with boundary conditions. An easy to follow algorithm is detailed. Some considerations have been highlighted connected to the boundary treatment and information provided by the characteristic curves has been utilised. The scheme is less diffusive than the first order upwind (FOU) scheme with a CFL of 0.5 for the 2D scalar equation.

When dealing with triangular grids, the LTS scheme has to be reformulated. The previous 1D reasoning to pack and send the information is based on assuming certain hypothesis related to the uniformity in the normal direction of the computational edges and in the cell size. When dealing with triangular grids, this assumption is not valid and the contributions have to be homogenized at each wall according not only to the length but also to the orientation of the normal direction of the edge. Once the information is packed with this technique, an algorithm to send the information is proposed, taking into account the velocity field and the orientation of the edges. It is described for the 2D scalar equation and some test cases are considered to illustrate the behaviour of the proposed LTS scheme in comparison to the FOU scheme.

The extension to systems of equations has been described generally, and is then applied to the 2D shallow water equations with source terms. The ideas advanced for the scalar case on square grids as well as on triangular grids are extended. Wet/dry fronts are of interest in any 2D shallow water model. A short procedure based on the reflection technique at closed boundaries is proposed here for dealing with them. It consists of identifying the wet/dry solid interfaces and ensuring that information is not sent through them. The proposed wet/dry treatment, combined with a careful source term discretization, ensures the well-balanced property and makes the reduction in the time step size and the appearance of negative values of the water depth less extreme.

Realistic and notably complex test cases have been suggested to evaluate the performance of the 2D LTS scheme under exacting conditions. As expected, it is demonstrated to be less diffusive than the standard FOU scheme, although several oscillations appear in the most extreme situations in square grids, as in the 1D case. In the case of triangular grids, the information is spread out in many directions and the oscillations are partially eliminated. In general, the wet/dry fronts are

well reproduced, achieving results which are as good as those of the conventional first order upwind scheme, but with the larger CFLs giving the potential for faster computation.

The computational time is assessed briefly for six test cases. An appreciable gain is achieved when dealing with the 2D LTS scheme although the improvement is less than the ratio of the respective CFL numbers. It is important to note that, in the context of the shallow water equations, moderate CFL value are recommended to be used.

Finally, this LTS scheme is an explicit method, and the advantages related with this kind of schemes are conserved. Moreover, the CFL condition is relaxed and larger time steps can be used, so that a computational gain and less diffusive results can be achieved in most cases. The obtained results point out that the LTS scheme is able to predict faithfully the overall behaviour of the solution.

Part III

1D-2D coupled models

Introduction

To combine the advantages of each model, coupled 1D-2D models have been proposed. The first simplified 1D-quasi 2D model dates to 1975 with the Mekong river delta model [35], where a 1D model of looped channel flow, solving the SWE with the Preissmann scheme, was integrated with a storage cell algorithm using the mass conservation equation to link domains. The storage cell approach was later adopted also by Blade et al. [9] on academic test cases. In a similar way Kuiry et al [68] applied a simplified 1D-quasi 2D model to a stretch of River Severn, solving 1D SWE in the river channel and using a storage cell method to compute the overbank flow. The link between 1D and 2D models is represented by deriving the flow rate exchange from the diffusive wave approximated equation. Villanueva and Wright integrated a 1D model with two 2D models [124], the first based on a storage cell approach and the second on a Riemann solver. These models were linked via spills between the main channel and the floodplain with mass transfer. In [83] two strategies were reviewed to improve urban flood forecasting. The first consists of a simplification of the mathematical formulation using an efficient 2D raster storage cell approach coupled to a 1D channel model. The second one used a sub-grid parametrization to represent the effects of buildings and micro topography on flow pathways and floodplain storage. The two strategies were evaluated through a numerical experiment designed to reconstruct a flood in the city of Linton, England. Castellarin et al. developed and tested the applicability of a quasi 2D hydraulic model [22] to aid the identification of large scale flood risk mitigation strategies. This approach considered the interaction between the channel and the floodplains only by mass transfer, completely neglecting the momentum exchange.

1D-2D models have been applied to large and complex river systems [38] where the 1D model is used only to predict flow velocity and water level in the main river. Most of the proposed models are linked by a weir equation, in which the volume exchanged between the 1D and the 2D domain is evaluated according to the water level difference [76]. The same idea was applied in [56] to solve a levee break. The

authors coupled a full 1D model based on SWE solved by Preissman method with a 2D model which solves the diffusion wave equation by a finite difference method. The overflow through the broken levee is treated as an internal boundary condition. Yin et al. coupled a 1D solution of the full form of the SWE and a 2D floodplain flow model to predict the Huangpu river flood and inundation extent [132]. In [39] the hybrid methodology was also used on a 28km reach of Reno River: flows through the lateral weir and simulated breaches were computed by a 1D approach and then adopted as the inflow boundary condition for a 2D model of the flood-prone area. Horritt and Bates [61] compared two approaches to model floodplain inundation: a raster-based approach, with channel flow being resolved separately from the floodplain using either a kinematic or diffusive wave approximation, and a finite-element hydraulic model aiming to solve the full 2D SWE. The approaches are tested on a flood event on a short reach of the upper River Thames in the UK, and are validated against the inundation extent as determined from satellite synthetic aperture radar (SAR) imagery.

Another form to couple 1D-2D hydrodynamic models consists of a transformation of 2D quantities to 1D quantities just averaging the 2D terms along the cross sections and imposing continuity at the 1D-2D interfaces. After that, an iterative procedure is carried out to solve the each coupled 1D-2D problem [44, 84]. This technique turns out to be a reliable strategy only for simple configurations (e.g. a straight channel or a river bifurcation). Yu and Lane [133] proposed a loosely coupled approach where the 1D model is used to provide boundary conditions to the 2D model at the floodplain interface prior to the initialisation of the 2D model. This study showed that, if the exchange between river and floodplain is not represented correctly, it is likely that flood inundation extent will not be modelled correctly. The importance of boundary conditions for flood inundation predictions is also emphasized.

The idea of a local zoom model superimposed over an open channel network global model is elaborated in [51, 45]. The zoom model (2D SWE) describes additional physical phenomena which are not represented by the global model (1D SWE). The application of this model is only shown for toy test cases. The same model was further developed in [80] showing results for simple test cases.

Recent research has advanced in exploring 1D-2D coupling strategies to combine the best attributes of each model. In [46], a coupled 1D-2D model was presented, in which the momentum transfer between the main channel and the floodplain is

taken into account. The model is first applied to simple test cases and then to a real world configuration.

In this work, two coupled 1D-2D models are proposed. Although the principle of conservation is the basis for both models, they are completely different in the construction. With respect to the geometric linking, both consist of 'sewing' the 1D and the 2D explicit finite volume models presented in Part I, chapter 3, by means of coupling zones composed by one 1D cell and a finite number of 2D cells.

The first approach achieves mass or mass/momentum conservation over the coupling zones depending on the flow conditions, enforcing averaged quantities that are shared in both 1D and 2D models. On the other hand, in the second approach the Riemann Problem is solved at the 1D-2D interfaces that separates the models. This novel technique must define appropriately the average values at the coupled edges. With this procedure, the Riemann Solver becomes easier given that it consists of solving the Riemann Problem at the 1D-1D walls, at the 2D-2D walls and at the coupled 1D-2D walls and sending the information accordingly. The philosophy of the 1D-2D coupled hydrodynamic model will be also extended to the solute transport equation, in which each coupled model will be linked in a conservative way according to its own coupling philosophy.

Chapter 13

Numerical schemes and geometric coupling

13.1 Review of numerical schemes for the 1D and 2D model

The governing equations as well as the numerical scheme applied in this work for the 1D model and for the 2D model must be reminded to better understand the coupling techniques proposed. In particular, the 1D shallow water equations were expressed in a conservative form as follows:

$$\frac{\partial \mathbf{U}(x,t)}{\partial t} + \frac{d\mathbf{F}(x,\mathbf{U})}{dx} = \mathbf{H}(x,\mathbf{U}) \tag{13.1}$$

$$\mathbf{U} = \begin{pmatrix} A \\ Q \end{pmatrix}, \quad \mathbf{F} = \begin{pmatrix} Q \\ \frac{Q^2}{A} + gI_1 \end{pmatrix} \quad \mathbf{H} = \begin{pmatrix} 0 \\ g\left[I_2 + A\left(S_0 - S_f\right)\right] \end{pmatrix} \tag{13.2}$$

On the other hand, the 2D shallow water equations are displayed again in a conservative formulation

$$\frac{\partial \mathbf{U}}{\partial t} + \frac{\partial \mathbf{F}(\mathbf{U})}{\partial x} + \frac{\partial \mathbf{G}(\mathbf{U})}{\partial y} = \mathbf{H}(\mathbf{U}) \tag{13.3}$$

where $\mathbf{U}$ are the conserved variables,

$$\mathbf{U} = (h,\ q_x,\ q_y)^T \tag{13.4}$$

$\mathbf{F}, \mathbf{G}$ are the fluxes of these variables,

$$\mathbf{F} = \left(q_x,\ \frac{q_x^2}{h} + \frac{1}{2} g h^2,\ \frac{q_x q_y}{h} \right)^T, \qquad \mathbf{G} = \left(q_y,\ \frac{q_x q_y}{h},\ \frac{q_y^2}{h} + \frac{1}{2} g h^2 \right)^T \tag{13.5}$$

and the source terms in (13.3) correspond to the bed and friction slopes

$$\mathbf{H} = \left(0,\ gh(S_{0x} - S_{fx}),\ gh(S_{0y} - S_{fy}) \right)^T \tag{13.6}$$

Both 1D and 2D shallow water models are based on an upwind first order finite volume schemes. The system can be written compactly:

$$\frac{\partial \mathbf{U}}{\partial t} + \overrightarrow{\nabla} \mathbf{E} = \mathbf{S} \tag{13.7}$$

where $\mathbf{E}$=$\mathbf{F}$ and $\mathbf{S} = \mathbf{H}'$ in the 1D model and $\mathbf{E}$=$(\mathbf{F}, \mathbf{G})$ and $\mathbf{S} = \mathbf{H}$ in the 2D case. This equation can be integrated in a grid cell Ω :

$$\frac{\partial}{\partial t} \int_\Omega \mathbf{U} d\Omega + \int_\Omega (\overrightarrow{\nabla} \mathbf{E}) d\Omega = \int_\Omega \mathbf{S} d\Omega \Rightarrow \frac{\partial}{\partial t} \int_\Omega \mathbf{U} d\Omega + \oint_T \mathbf{E}\ \mathbf{n} dT = \int_\Omega \mathbf{S} d\Omega \tag{13.8}$$

where $\mathbf{n}$ is the outward normal vector, $\mathbf{E}\ \mathbf{n}$ is the normal flux and T denotes the surface surrounding the volume Ω.

The normal flux $\mathbf{E}\ \mathbf{n}$ and its Jacobian $\mathbf{J_n}$ are a question of interest. Moreover $\mathbf{J_n}$ can be diagonalized

$$\mathbf{J_n} = \mathbf{P}\, \mathbf{\Lambda_n}\, \mathbf{P}^{-1}, \quad \mathbf{\Lambda_n} = \mathbf{P}^{-1} \mathbf{J_n} \mathbf{P}$$

where the diagonal matrix $\mathbf{\Lambda_n}$ is formed by the eigenvalues of $\mathbf{J_n}$, and $\mathbf{P}$ is constructed with its eigenvectors. More information can be found in part I, section 3.3.

Applying Roe's linearization [109] it is possible to decouple the original hyperbolic system (13.7) and to define locally an approximate matrix $\tilde{\mathbf{J}}_\mathbf{n}$ at each wall k whose eigenvalues $\tilde{\lambda}^m$ and eigenvectors $\tilde{\mathbf{e}}^m$ can be used to express the 1D numerical scheme [86, 16]:

$$\mathbf{U}_i^{n+1} = \mathbf{U}_i^n - \frac{\Delta t_{1D}}{\Delta x}\left[\left(\sum_m \tilde{\lambda}^+\tilde{\gamma}\tilde{\mathbf{e}}\right)_{i-1/2}^m + \left(\sum_m \tilde{\lambda}^-\tilde{\gamma}\tilde{\mathbf{e}}\right)_{i+1/2}^m\right]^n \tag{13.9}$$

where $i+1/2$ represents the computational edge between cells i and $i+1$ (analogous with $i-1/2$ and cells $i-1$ and i, $\tilde{\gamma}_{i+1/2}^m = \left(\tilde{\alpha} - \frac{\tilde{\beta}}{\tilde{\lambda}}\right)_{i+1/2}^m$ and $\tilde{\lambda}_{i+1/2}^{\pm m} = \frac{1}{2}(\tilde{\lambda} \pm |\tilde{\lambda}|)_{i+1/2}^m$. As stated in the previous chapters, the scheme is proved to be conservative, well-balanced and positivity preserving.

The time step Δt is dynamically chosen following

$$\Delta t_{1D} = CFL\frac{\Delta x}{\max_{m,i}|\tilde{\lambda}^m|_i} \qquad CFL \leq 1 \tag{13.10}$$

Analogously, the 2D numerical upwind explicit scheme can be formulated using the finite volume approach for the updating of a single cell whose area is S_i, dealing with the contributions that arrive to the cell from the neighbouring walls (see Part I, section 3.3):

$$\mathbf{U}_i^{n+1} = \mathbf{U}_i^n - \frac{\Delta t_{2D}}{S_i}\sum_{k=1}^{NE}\sum_m \left[(\tilde{\lambda}^-\tilde{\gamma}\tilde{\mathbf{e}})_k^m l_k\right]^n \tag{13.11}$$

In this expression, $m = 3$, NE indicates the number of involved neighbouring walls in the computation and l_k is the length of each edge. When considering unstructured meshes in the 2D scheme, χ_i is defined in each cell by using the area of the cell as well as the length of the k edges:

$$\chi_i = \frac{S_i}{max_{k=1,NE}l_k} \tag{13.12}$$

Therefore, the time step is chosen by using the following rule:

$$\Delta t_{2D} = CFL\frac{\min(\chi_i, \chi_j)}{\max_m|\tilde{\lambda}^m|} \qquad CFL \leq 1 \tag{13.13}$$

The transport of a solute with a concentration of ϕ is expressed for the 1D framework:

$$\frac{\partial(A\phi)}{\partial t} + \frac{\partial(Q\phi)}{\partial x} = -KA\phi \tag{13.14}$$

and the numerical scheme is formulated in a decoupled way as in part I, section 3.4.2:

$$(A\phi)_i^{n+1} = (A\phi)_i^n - \frac{\Delta t}{\Delta x}\left[(q\phi)^{\downarrow}_{i+1/2} - (q\phi)^{\downarrow}_{i-1/2}\right] \tag{13.15}$$

where

$$q^{\downarrow}_{i+1/2} = Q_i + \sum_{m=1}^{2}\left(\widetilde{\lambda}^{-}\ \widetilde{\gamma}\ \widetilde{\mathbf{e}}_1\right)^m_{i+1/2} \qquad \phi^{\downarrow}_{i+1/2} = \begin{cases} \phi_i & if \quad q^{\downarrow}_{i+1/2} > 0 \\ \phi_{i+1} & if \quad q^{\downarrow}_{i+1/2} < 0 \end{cases} \tag{13.16}$$

In the same manner, the 2D transport equation is written as follows:

$$\frac{\partial(h\phi)}{\partial t} + \frac{\partial(hu\phi)}{\partial x} + \frac{\partial(hv\phi)}{\partial y} = -Kh\phi \tag{13.17}$$

The numerical scheme is analogously decoupled from the hydrodynamic equations using a conservative formulation (see part I, section 3.4.2):

$$(h\phi)_i^{n+1} = (h\phi)_i^n - \frac{\Delta t}{A_i}\sum_{k=1}^{N_E}(q\phi)^{\downarrow}_k l_k \tag{13.18}$$

where

$$q^{\downarrow}_k = q_i + \sum_{m=1}^{3}\left(\widetilde{\lambda}^{-}\ \widetilde{\gamma}\ \widetilde{\mathbf{e}}_1\right)^m_k \qquad \phi^{\downarrow}_k = \begin{cases} \phi_i & if \quad q^{\downarrow}_k > 0 \\ \phi_j & if \quad q^{\downarrow}_k < 0 \end{cases} \tag{13.19}$$

13.2 Coupling strategy and meshing: coupling zones

A new element of discretization for the 1D-2D coupled model is defined from the discretizations of each model. This new element called *coupling zone* will always contain one 1D cell and a number NC of 2D cells. The reason behind assuming this standpoint is easy: as the advantage of the 1D model resides in the power of obtaining very good results without using a large number of cells, it is not necessary

to do a one-by-one assignment between 1D and 2D cells. Figure 13.1 shows two examples of coupling zones composed by only one 1D cell and some unstructured triangular 2D cells. As can be seen, two possible configurations may be defined with respect to the 1D model: frontal and lateral coupling. Moreover, the lateral configuration will contain left and right coupled cells.

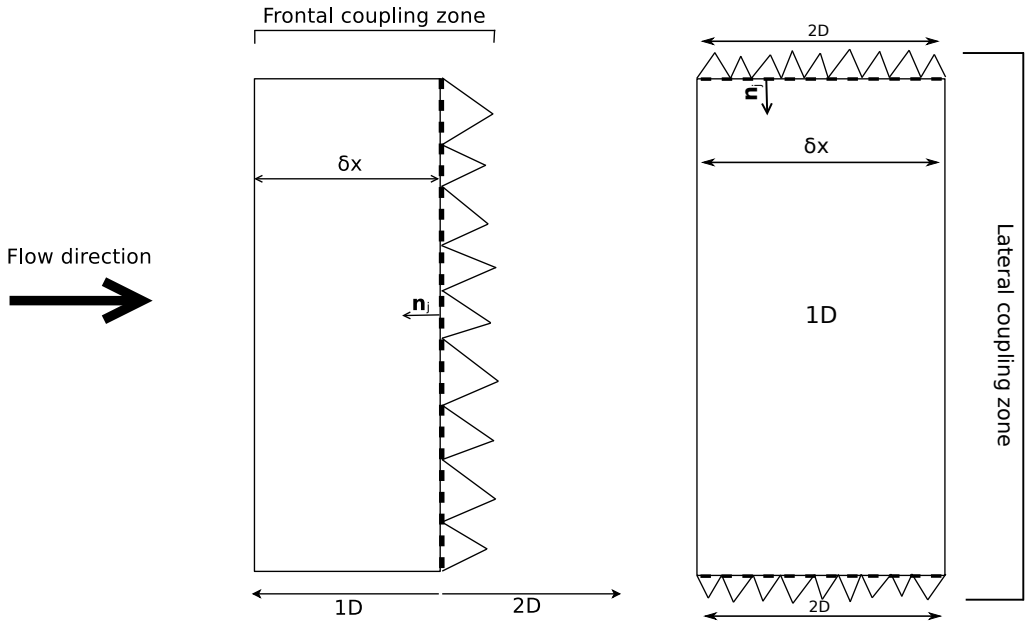

Figure 13.1: Frontal and lateral coupling zones

The most direct implication of having an exact number of 2D cells at each coupling zone is the mesh discretization for the 2D model. The proposed strategy to achieve an adequate mesh for the 2D model is schematized in Figure 13.2 for the lateral configuration: once the full domain is characterized as a part of the 1D or of the 2D model (a), the 1D domain is discretized into a number of cells (b). This fact will provide a left bank and a right bank polylines (c) that will be used as input information for the 2D model. As each node defining the mentioned polylines belongs to the 2D model, an exact number of triangles will be defined for each 1D cell (d). Finally, the 1D cell and the 2D cells that belong to the same coupling zone are labelled with the same marker in order to simplify the linkage (e).

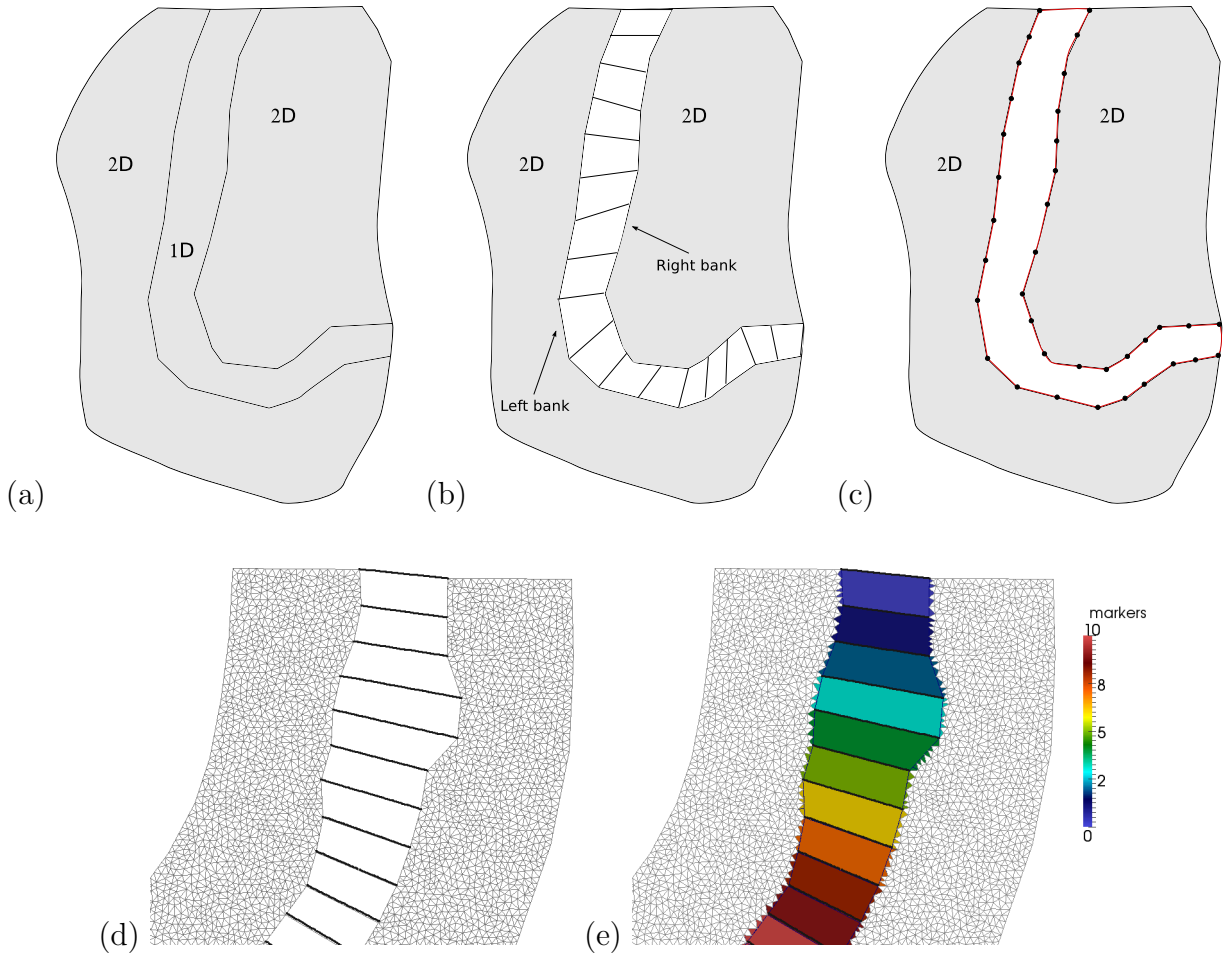

Figure 13.2: Sketch of an adequate meshing procedure for the 2D domain in the coupled model

Chapter 14

The Forced Conservative (FC) 1D-2D coupled model

14.1 Model interaction and time step choice

The main goal is not to build a new coupled model starting from scratch but to link two pre-existent 1D and 2D models hence the information provided by each model must be used in the best way. The procedure is simple: once the data reading is carried out separately by the models, we are able to build the coupling zones and to connect the 1D cells with its own 2D adjacent cells. Initial conditions are read and assigned to the corresponding cells to start the simulation. A common element in both 1D and 2D models is the evaluation of the time step. When dynamically computed from the CFL condition, Δt can be different in both models. The global Δt taken is the minimum value of the two models, that is:

$$\Delta t \;=\; \min(\Delta t_{1D}, \Delta t_{2D}) \tag{14.1}$$

Once Δt is calculated, each model computes separately their own conserved variables according to (13.9) and (13.11). The resulting values, not including yet the interaction between the two models will be called from now on *star variables*. So, in each coupling zone, $(A, Q)^*$ and $(h, hu, hv)^*$ are provided by the 1D and the 2D model respectively. Then, mass and/or momentum conservation is enforced so that the variables can be updated and finally Δt is increased. The flowchart of the coupled model is summarized in Figure 14.1.

In the frontal configuration, the 1D and the 2D models will always exchange information provided they are wet. On the opposite, in the lateral configuration, both

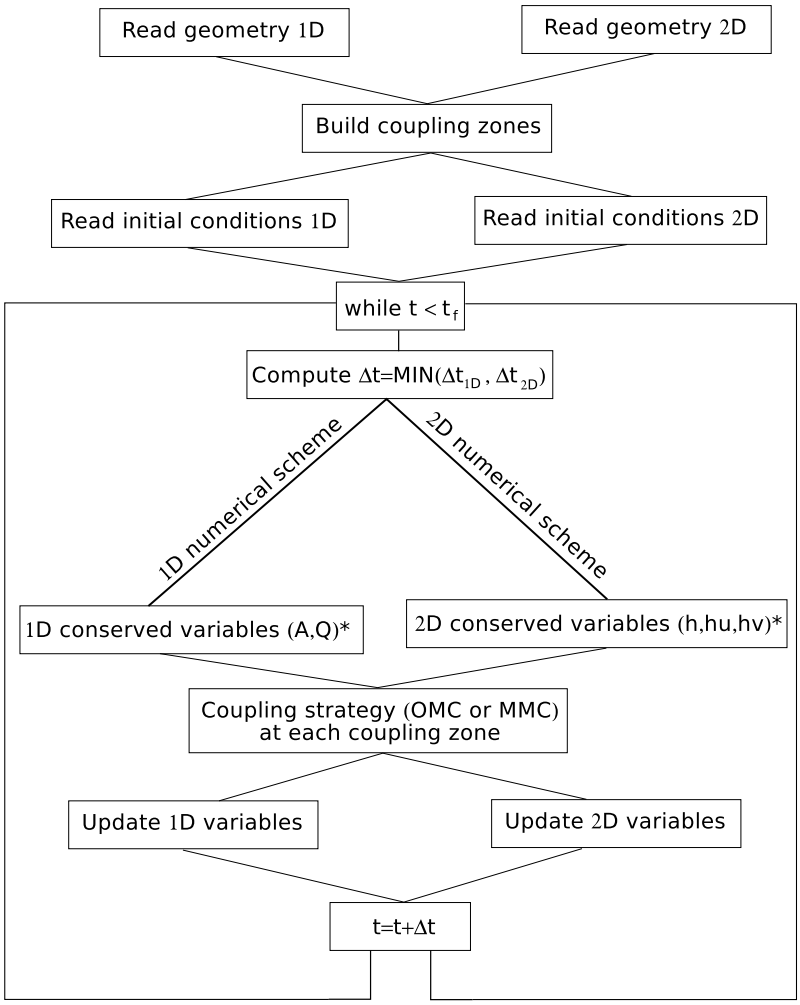

Figure 14.1: Flowchart of the FC 1D-2D scheme

models will obviously interact only when a flooding at the coupling zone is registered, whether by the 1D model or by the 2D model. Consequently, it is necessary to establish an 'overflow level' for each lateral coupling zone, which will be split into two levels (left overflow and right overflow). In this work, a simple linear interpolation between the extreme left and right points of the each 1D cross section is established as the left and right overflow levels respectively. Four possibilities arise:

- **No overflow**. There is not interaction between the models (Figure 14.2, (a)).
- **Left overflow**. The models exchange information between the 1D cell and the 2D adjacent cells which are on the left side of the coupling zone (Figure 14.2, (b)).

- **Right overflow**. The models exchange information between the 1D cell and the 2D adjacent cells which are on the right side of the coupling zone (Figure 14.2, (c)).

- **Left and right overflow**. The models exchange information between the 1D cell and all the 2D adjacent cells involved at the coupling zone (Figure 14.2, (d)).

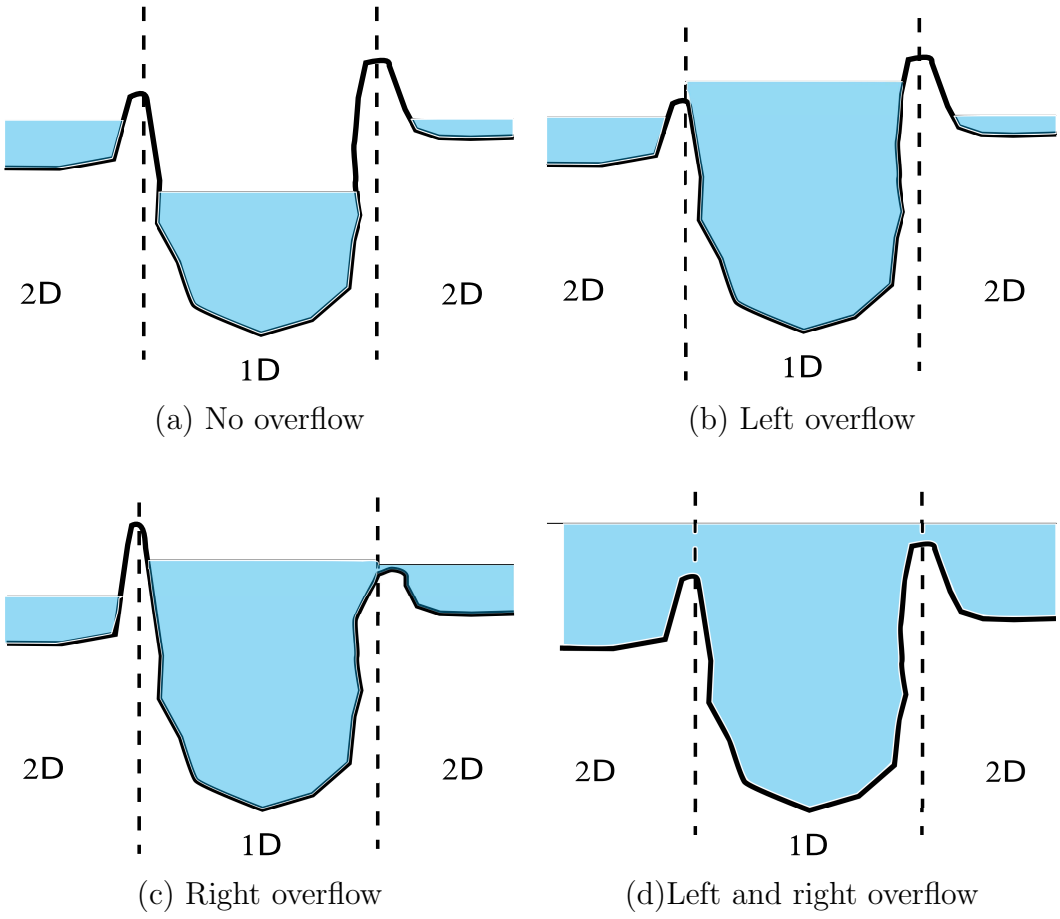

(a) No overflow (b) Left overflow

(c) Right overflow (d)Left and right overflow

Figure 14.2: Possibilities for the interaction between the 1D and the 2D models in a lateral configuration

Two different coupling strategies are presented on the basis that the computational domains connect at each coupling zone and the boundary conditions and their treatment must be continuously revisited. This is a strong point that justifies the novelty of this work in terms of mass and momentum conservation and that will be also im-

portant when choosing the adequate coupling strategy providing the flow regime at the boundary.

14.2 Only Mass Conservation (OMC)

This technique consists of imposing an average water level in the coupling zone considering the involved cells (1D and 2D computational cells) as a single domain where the water volume conservation is enforced. The common water level is based on a strict mass conservation. Both models are coupled by considering the information that crosses the internal boundaries of the coupling zone as relevant in terms of mass conservation [20]. Figure 14.3 illustrates the contributions to be considered in a frontal coupling and in a pure lateral coupling.

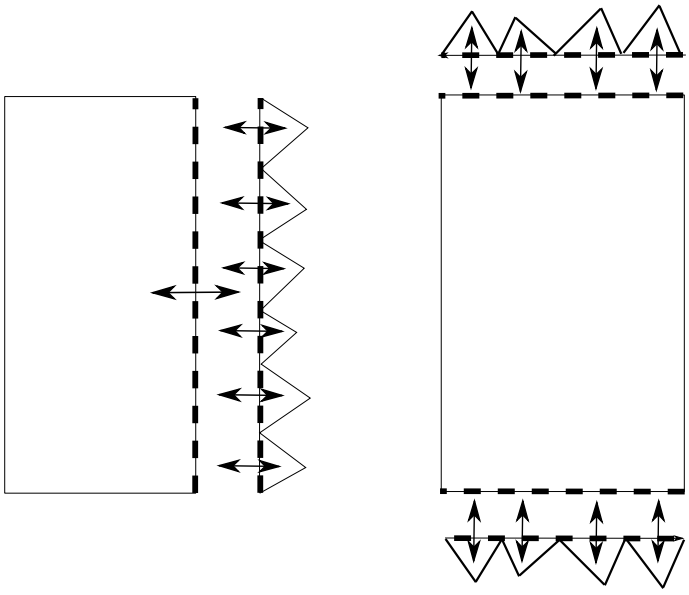

Figure 14.3: Contributions to be considered in mass conservation: frontal coupling (left) and lateral coupling (right)

The total water volume of a coupling zone, V_{CZ} can be written as follows:

$$V_{CZ} = \underbrace{A^*_{1D}\ \Delta x}_{1D\ volume} + \underbrace{\sum_{i}^{N_C} h^*_i\ S_i}_{2D\ volume} + \underbrace{Q^n_{1D}\ n_{1D}}_{1D\ flow}\ \Delta t + \underbrace{\sum_{i}^{N_C}(\mathbf{F}^n_{1i}\ \cdot \mathbf{n}_i\ l_i)}_{2D\ flow}\ \Delta t \qquad (14.2)$$

where $A^*_{1D}\ \Delta x$ is the volume of water in the 1D cell, $\sum_i^{N_C} h_i^*\ S_i$ accounts for the water volume in the N_C 2D cells (S_i is the 2D cell size), $Q^n_{1D}\ n_{1D}\ \Delta t$ represents the volume due to the 1D-flow that crosses the 'discontinuous line' separating the two models and $\sum_i^{N_C}(\mathbf{F}^n_{1i}\ \cdot \mathbf{n}_i\ l_i)\ \Delta t$ gives information about the water volume provided by the 2D-flow going across the boundaries, where $\mathbf{F}^n_{1i} = (q_x, q_y)$, $\mathbf{n}_i$ the outward normal direction and l_i the length of each wall taking part in the coupling zone. It is easy to see that $n_{1D} = \pm 1$ in the frontal coupling and $n_{1D} = 0$ in pure lateral coupling.

Once V_{CZ} is computed, a new common water level surface z_s^{n+1} is imposed in the coupling zone by distributing correctly the water volume in the 1D and the 2D system:

$$V_{CZ} = A^{n+1}_{1D}\ \Delta x + \sum_i^{N_C} h_i^{n+1}\ S_i \tag{14.3}$$

where

$$A^{n+1}_{1D} = A^{n+1}_{1D}(z_s^{n+1}) \qquad h_i^{n+1} = z_s^{n+1} - z_{b_i} \tag{14.4}$$

The computation of the new water surface level z_s^{n+1} is not a trivial task when dealing with complex topography. As a matter of fact, the meticulous technique proposed before should also be combined with a careful computation of the common level once the total water volume of the coupling zone, V_{CZ}, has been calculated. The aim is building a level-volume table for each coupling zone in the pre-process and, during the computation, to assign the corresponding level of such water volume. The procedure will be similar to those used for the computation of the pressure integrals and the hydraulic tables in part I, section 5.2.2.1. Note that the 2D cells are involved in this case.

Let consider a coupling zone as in Figure 14.4 (a), composed by one 1D irregular cell, two coupled 2D cells called 1 and 2 on the left side and three coupled 2D cells called 3, 4 and 5 respectively on the right side. Figure 14.4 (b) shows a sliced sketch of the mentioned coupling zone, where the straight lines represent the bottom or elevation of the corresponding 2D coupled cells.

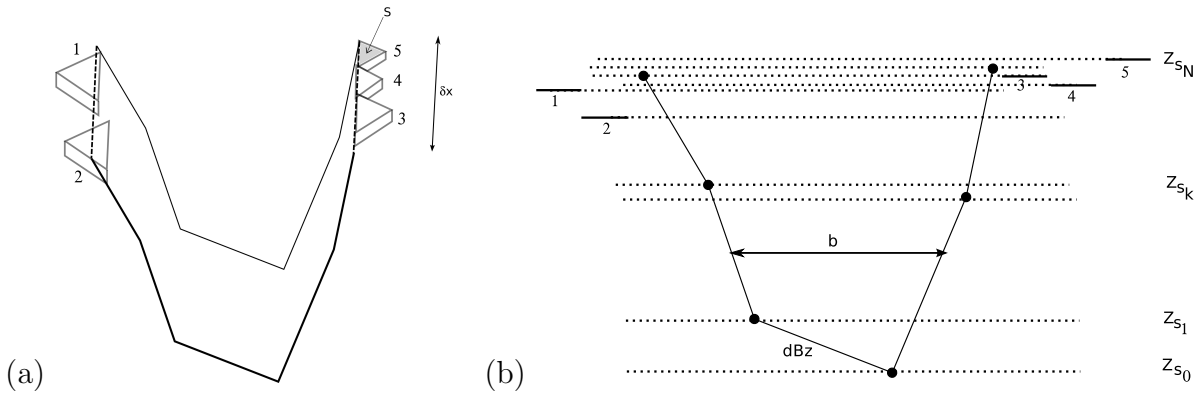

Figure 14.4: Coupling zone (a) and sliced sketch (b)

First of all, it is necessary to construct a vector of N levels z_{s_k}, where N represents the sum of the 1D points defining the irregular cross sections for the 1D model as well as the elevation of the 2D coupled cells. Then, this vector of levels is sorted from lower to higher and a table with the information included in (14.5)

$$z_{s_k} \quad b_k \quad S_k \quad dBz_k \quad V_k \tag{14.5}$$

must be filled. As displayed in Figure 14.4, k indicates the vector index, z_s is the surface level, b is the corresponding width in the 1D model, S includes the accumulated 2D cell sizes, dBz is the corresponding side slopes and V is the water volume. While the construction of z_{s_k}, b_k, S_k and dBz_k is a straightforward geometric procedure, the volume is achieved following the rule (14.6):

$$V_{k+1} = V_k + C_k(z_{s_{k+1}} - z_{s_k}) + \frac{1}{2} dBz_k \Delta x \, (z_{s_{k+1}} - z_{s_k})^2 \tag{14.6}$$

being Δx the 1D cell size and $C = b\Delta x + S$. This table (14.5) is built in the pre-process of the information.

A water volume V_{CZ} is computed from (14.2) at the coupling zone, whose corresponding correct level z_s^{n+1} will be imposed there. In order to do this assignment, the second order (in z_s^{n+1}) equation (14.7) should be solved:

$$V_{CZ} = V_j + C_j(z_s^{n+1} - z_{s_j}) + \frac{1}{2} dBz_j \Delta x \, (z_s^{n+1} - z_{s_j})^2 \tag{14.7}$$

where j is the immediately lower index from that V_{CZ} is located in the table (14.5).

Finally, the unique solution for z_s^{n+1} which stays between z_{s_j} and $z_{s_{j+1}}$ is imposed as the common water surface level.

It is important to remark that this technique provides good accuracy in the presence of irregular geometries, allowing to discern which are the 2D cells that must be wet or dry when imposing a common level surface.

14.3 Mass and Momentum Conservation (MMC)

The OMC strategy can be extended in order to achieve, apart from the mass conservation, also the exact global momentum conservation. For this purpose, not only a common water level surface is imposed at the coupling zone but also average velocities in x and y-direction. This will be called from now on MMC.

In the MMC strategy, the information about the flow direction is of interest, hence an angle θ is introduced in the 1D model in order to express the discharge Q as a vector:

$$Q \rightsquigarrow (Q_x, Q_y) = (Q\cos\theta, Q\sin\theta) \tag{14.8}$$

Using the same procedure as in OMC and also involving the same information, it is possible to define the amount of momentum in x-direction, M_x, as

$$M_x = \underbrace{Q_x^*\ \Delta x}_{1D} + \underbrace{\sum_i^{N_C}(q_x)_i^*\ S_i}_{2D} + \underbrace{E_x^n\ n_{1D}}_{1D\ flux}\ \Delta t + \underbrace{\sum_i^{N_C}(\mathbf{F}_{2i}^n\ \cdot \mathbf{n}_i\ l_i)}_{2D flux}\ \Delta t \tag{14.9}$$

where $Q_{x1D}^*\ \Delta x$ is the momentum in the 1D-system, $\sum_i^{N_C}(q_x)_i^*\ S_i$ in the 2D-system and E_x^n and $\mathbf{F}_{2i}^n$ account for the corresponding fluxes that cross the boundary shared by 1D and 2D models respectively.

$$E_x^n = \left(\frac{(Q_x)^2}{A} + gI_1\right)^n \qquad \mathbf{F}_{2i}^n = \left(\frac{q_x^2}{h} + \frac{1}{2}gh^2, \frac{q_x q_y}{h}\right)_i^n \tag{14.10}$$

The momentum considering the y-direction:

$$M_y = \underbrace{Q_y{}^* \ \Delta x}_{1D} \ + \ \underbrace{\sum_{i}^{N_C} (q_x)_i^* \ S_i}_{2D} \ + \ \underbrace{E_y^n \ n_{1D}}_{1D \ flux} \ \Delta t \ + \ \underbrace{\sum_{i}^{N_C} (\mathbf{F}_{3i}^n \ \cdot \mathbf{n}_i \ l_i)}_{2D \ flux} \ \Delta t \qquad (14.11)$$

where

$$E_y^n = \left(\frac{(Q_y)^2}{A} + gI_1 \right)^n \qquad \mathbf{F}_{3i}^n = \left(\frac{q_x q_y}{h}, \frac{q_y^2}{h} + \frac{1}{2} g h^2 \right)_i^n \qquad (14.12)$$

It is clear again that $n_{1D} = \pm 1$ in the frontal coupling and n_{1D} becomes nil in pure lateral coupling.

Once M_x and M_y are computed, average velocity components in x-direction, $\overline{u}$, and in y-direction, $\overline{v}$, can be derived from the total water volume in the coupling zone V_{CZ} using

$$V_{CZ} \ \overline{u} = M_x \qquad V_{CZ} \ \overline{v} = M_y \qquad (14.13)$$

Finally, the conserved variables are updated for both the 1D and the 2D models as:

$$(q_x)_i^{n+1} = h_i^{n+1} \ \overline{u} \qquad (q_y)_i^{n+1} = h_i^{n+1} \ \overline{v}$$

$$Q_{1D}^{n+1} = A_{1D}^{n+1} \ (\overline{u} \cos\theta + \overline{v} \sin\theta)$$

14.4 Boundary conditions and the choice of the adequate coupling strategy

When detailing the coupling strategies presented before (OMC, MMC), the information that crosses the internal line that links both models has been included in order to contemplate a fully conservative method. However, it is not the only point to be considered. For example, in a frontal coupling configuration, where the end of the 1D domain connects with the beginning of the 2D system, the boundary conditions are entirely present and it is relevant whether a supercritical or subcritical

flow is present at the coupling zone. On the same manner, the 2D domain always ends up at each coupling zone either frontal or lateral.

This information must be carefully handled for building the coupled model. In this work, the choice of the adequate strategy (*OMC* or *MMC*) will depend on the flow regime that is taking place at the coupling zone. In order to decide, average Froude numbers are evaluated separately in both models, at each coupling zone:

$$Fr_{1D} = \frac{Q}{A\sqrt{g\frac{A}{B}}} \qquad \overline{Fr_{2D}} = \frac{1}{N_C}\sum_{i}^{N_C} Fr_i \tag{14.14}$$

where i runs the 2D cells at the coupling zone. When either the 1D or the 2D model is supercritical in the coupling zone, the MMC strategy, which accounts for mass and momentum conservation must be imposed. Otherwise, the OMC strategy, where only one of the variables (a common water surface level) is enforced, must be used. It can be summarized in Algorithm 4. According to it, the adequate coupling strategy is dynamically chosen at each coupling zone in each time step.

Algorithm 4 Choosing the adequate strategy

for each CZ **do**
  Evaluate Fr_{1D} at the 1D cell
  Evaluate the average Froude number of all the involved 2D cells
$\overline{Fr_{2D}} = \frac{1}{N_C}\sum_{i}^{N_C} Fr_i$
  if $((Fr_{1D} > 1.0)$ or $(\overline{Fr_{2D}} > 1.0))$ **then**
    Use *MMC*
  else
    Use *OMC*
  end if
end for

The *MMC* strategy is designed so that it reduces automatically to the *OMC* when less boundary conditions have to be imposed at the coupling zone. Indeed, the *MMC* strategy seems a priori to be more sophisticated than *OMC* due to the fact that it is being exchanging information not only related to the mass in both 1D and 2D

models but also related to the momentum. However, when dealing with subcritical flow at the coupling zone, only one variable (the common water level surface, *OMC* strategy) has to be imposed. Otherwise, if enforcing the *MMC* technique, more information than necessary is provided so that the system is "overdetermined" in a certain way and may produce non-physical results.

14.5 Solute transport

The coupling strategy can be easily applied to the solute transport equation. Let consider the transport of a substance with a concentration of ϕ. Analogously of computing the existent water volume at the coupling zone, the solute volume V^{ϕ} can be evaluated as follows:

$$V_{CZ}^{\phi} = (A\phi)_{1D}^{*}\,\Delta x + \sum_{i}^{N_C} (h\phi)_i^{*}\,S_i + (Q\phi)_{1D}^{n}\,n_{1D}\,\Delta t + \sum_{i}^{N_C} (\mathbf{F}_{\mathbf{s}1i}^{n}\cdot\mathbf{n}_i\,l_i)\,\Delta t \quad (14.15)$$

where $\mathbf{F}_{1i}^{n} = (q_x\phi, q_y\phi)$, the n-superscript represents the previous time step and the $*$-superscript indicates the current time step, understood as the result of computing each numerical method separately, i.e., without any interaction between the models. As the total volume of water inside the coupling zone V_{CZ} is known, it is feasible to define an average concentration $\overline{\phi}$

$$\overline{\phi} = \frac{V_{CZ}^{\phi}}{V_{CZ}} \quad (14.16)$$

that will be imposed at both the 1D and the 2D cells as follows:

$$(A\phi)_{1D}^{n+1} = A_{1D}^{n+1}\,\overline{\phi} \qquad (h\phi)_i^{n+1} = h_i^{n+1}\,\overline{\phi} \quad (14.17)$$

It is worth remarking that A_{1D}^{n+1} and h_i^{n+1} are previously computed according to (14.4).

Chapter 15

The Riemann Coupled Edges (RCE) 1D-2D model

15.1 Model interaction: Riemann Problem across the coupled edges

The FC approach is able to ensure mass or mass/momentum conservation when necessary but the technique of imposing the same level along the coupling zone and, in the case of momentum conservation, also the same average velocities, may distort the phenomena that occur at the 1D-2D frontier. This chapter deals with the construction of a new 1D-2D coupled model by approximating the interaction between the models using a different point of view: the definition of local Riemann Problem across the edges that separate the 1D and the 2D models and their numerical resolution.

As in the FC 1D-2D coupled model, the geometric link between the models is performed by using coupling zones. Figure 15.1 shows an example of a lateral coupling zone, representing the irregular bathymetry that can be found in a river channel in a 3D view (left) and in plant view (right).

The identification of each coupling zone is done in the pre-process. Afterwards, the set of initial conditions for each model is applied and the computation starts. This approach is based on computing the fluxes at each interface, whether 1D-1D edge, 2D-2D edge or 1D-2D edge. As the computation of the numerical fluxes for the 1D-1D and the 2D-2D edges is performed by using the conventional first order upwind scheme explained in (13.9) and (13.11) respectively, the focus will be put on the 1D-2D edges.

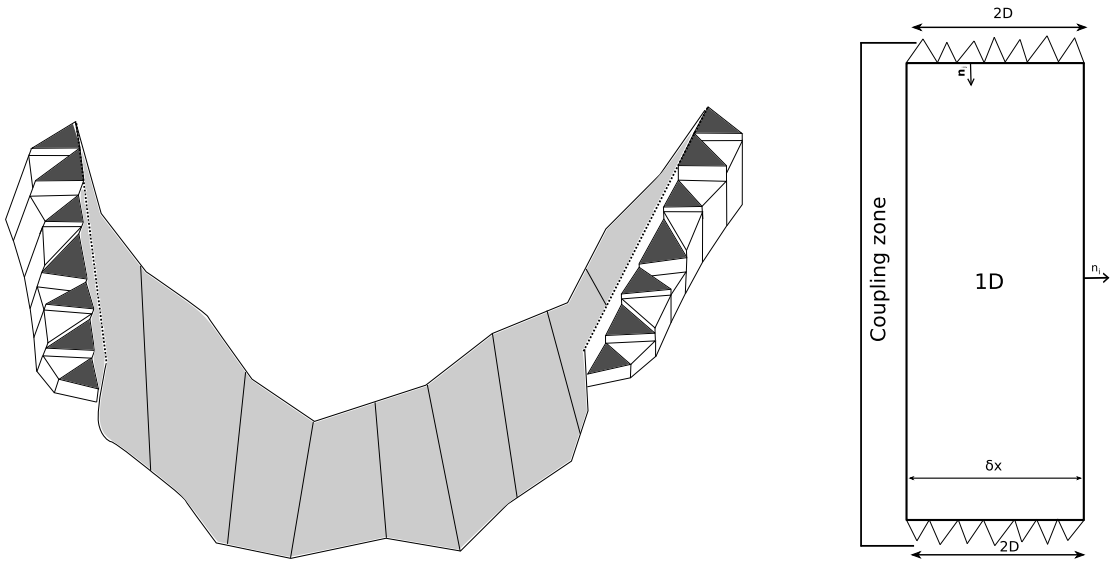

Figure 15.1: Lateral coupling zone: 3D view (left) and plant view (right)

The strategy is based on the resolution of the local Riemann Problems at each 1D-2D interfaces, which requires the definition of discrete averaged values at each coupling edge. The idea developed in this work consists of transforming the 1D quantities into 2D quantities to solve the corresponding Riemann Problem as if it was a 2D-2D interface. Although the problem is undetermined in a certain way, estimations of the velocity field, the water depth and the bottom are required to define the local Riemann Problem and to be able to define the averaged quantities.

First, the bed level is set to the lowest point in the 1D cell and the water depth is chosen as the water depth of the 1D cell. Furthermore, the discharge in the 1D model, Q_{1D}, can be converted into a vector according to the coupling zone angle θ as in (14.8) and consequently, the velocity vector $\mathbf{u}_{1D}$ and the unit discharge vector $\mathbf{q}_{1D}$ are easily estimated as:

$$\begin{aligned} \mathbf{u}_{1D} &= (u_{1D}, v_{1D}) = (\left(\frac{Q}{A}\right)_{1D} \cos\theta, \left(\frac{Q}{A}\right)_{1D} \sin\theta) \\ \mathbf{q}_{1D} &= (q_{x1D}, q_{y1D}) = (\left(\frac{Q}{B}\right)_{1D} \cos\theta, \left(\frac{Q}{B}\right)_{1D} \sin\theta) \end{aligned} \tag{15.1}$$

where A_{1D} and B_{1D} are the wetted area and the top width surface respectively. It is worth noting that, in the case of the lateral configuration, this angle is characterized

for each coupling zone side θ_L or θ_R (left or right). Therefore, each Riemann Problem can be projected over the direction x' given by the normal vector $\mathbf{n}_\kappa$ at each 1D-2D wall or edge κ (see Figure 15.2)

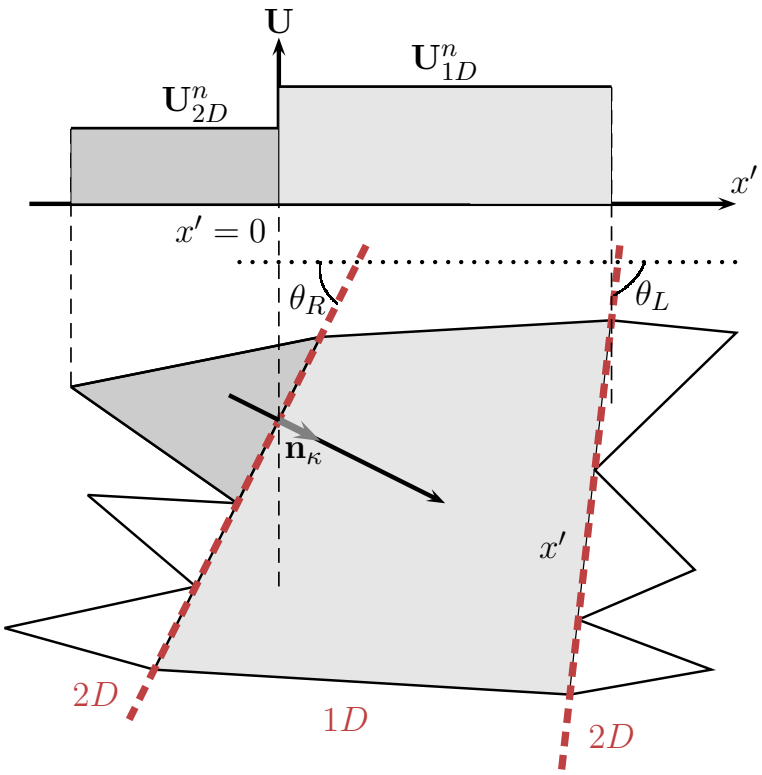

Figure 15.2: Riemann problem in the 1D-2D edge

The average quantities that allow to define the local Riemann Problem are consequently written as follows:

$$\tilde{u} = \frac{\sqrt{h_{2D}}\,u_{2D} + \sqrt{h_{1D}}\,u_{1D}}{\sqrt{h_{2D}} + \sqrt{h_{1D}}}, \quad \tilde{v} = \frac{\sqrt{h_{2D}}\,v_{2D} + \sqrt{h_{1D}}\,v_{1D}}{\sqrt{h_{2D}} + \sqrt{h_{1D}}}, \quad \tilde{c} = \sqrt{g\,\frac{h_{2D} + h_{1D}}{2}} \tag{15.2}$$

where $\delta h = h_{1D} - h_{2D}$, $\delta z = z_{1D} - z_{2D}$, $\delta q_x = q_{x_{1D}} - q_{x_{2D}}$, $\delta q_y = q_{y_{1D}} - q_{y_{2D}}$, $\tilde{\mathbf{u}} \cdot \mathbf{n} = \tilde{u}\,n_x + \tilde{v}\,n_y$, $\delta \mathbf{q} \cdot \mathbf{n} = \delta q_x\,n_x + \delta q_y\,n_y$ and the average states at each coupled 1D-2D wall κ are represented with the tilde variables. The local eigenvalues $\widetilde{\lambda}^m$ and eigenvectors $\widetilde{\mathbf{e}}^m$, as well as the contributions due to the fluxes and the source terms are defined as in the 2D case (part I, (3.31) and (3.34)). Note that $S_{f,\mathbf{n}}$ in

Part I, (3.32) requires the definition of an average Manning roughness coefficient between cells 1D and 2D and also the computation of the normal distance between the centroid of the involved cells.

Once the averaged quantities for the 1D-2D edges are defined, the time step size is question of interest. It should be chosen as the minimum of the time step sizes of the three mentioned interfaces:

$$\Delta t \;=\; \min(\Delta t_{1D}, \Delta t_{2D}, \Delta t_{1D2D}) \tag{15.3}$$

where Δt_{1D} and Δt_{2D} are the time step sizes for the 1D-1D edges and for the 2D-2D edges, as defined in (13.10) and (13.13) respectively. Given a 1D-2D edge κ with length l_κ, separating a 1D cell and a 2D adjacent cell with area S_{2D}, Δt_{1D2D} is defined as:

$$\Delta t_{1D2D} = \mathrm{CFL}\frac{\chi_\kappa}{\max_{m,\kappa} |\tilde{\lambda}^m|_\kappa} \qquad \chi_\kappa = min(\Delta x_{1D}, S_{2D}/l_\kappa) \tag{15.4}$$

with κ runs over the coupling edges and the CFL number is chosen as the more restrictive between the CFL's selected for the 1D and the 2D models:

$$\mathrm{CFL} = \min(\mathrm{CFL}_{1D}, \mathrm{CFL}_{2D}) \tag{15.5}$$

Once the contributions due to the fluxes and sources terms are sent, the conserved variables are updated and the time is increased as usual, according to the time step size. The procedure can be summarized in Figure 15.3, where a flowchart of the RCE 1D-2D model is included.

15.2 Extended numerical scheme

The numerical resolution of the RCE coupled model is indeed composed by three sub-solvers, each one in charge of a different type of edges. As mentioned above, the 1D-1D edges as well as the 2D-2D edges are solved as usual, i.e., sending the information as if there were not any connection between the models. The third one involves the 1D-2D interfaces and is fairly similar to the resolution of the 2D-2D

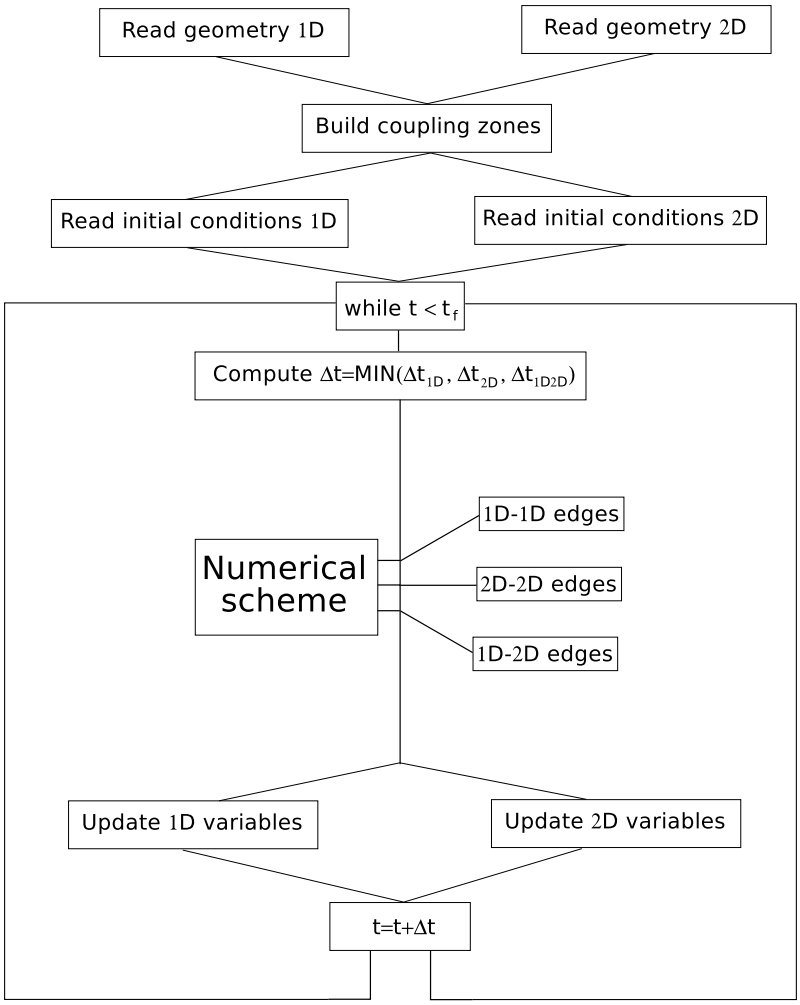

Figure 15.3: Flowchart of the RCE 1D-2D scheme

edges. Figure 15.4 shows a sketch of the contributions from each type of edge in the RCE 1D-2D coupled model.

The expression of the numerical scheme for the updating of a 2D triangular cell, including the contributions from the 2D-2D edges k as well as those coming from the 1D-2D edges κ is

$$\mathbf{U}_i^{n+1} = \mathbf{U}_i^n - \underbrace{\frac{\Delta t}{S_i}\sum_{k=1}^{N_E}\sum_m \left[(\tilde{\lambda}^-\tilde{\gamma}\tilde{\mathbf{e}})_k^m l_k\right]^n}_{2D-2D \text{ edges}} - \underbrace{\frac{\Delta t}{S_i}\sum_m \left[(\tilde{\lambda}^-\tilde{\gamma}\tilde{\mathbf{e}})_\kappa^m l_\kappa\right]^n}_{1D-2D \text{ edges}} \tag{15.6}$$

where $m = 1..3$ and N_E represents the number of neighbouring 2D cells. In the case of inner cells, $N_E = 3$; otherwise $N_E = 2$ if the cell is a non-corner boundary cell

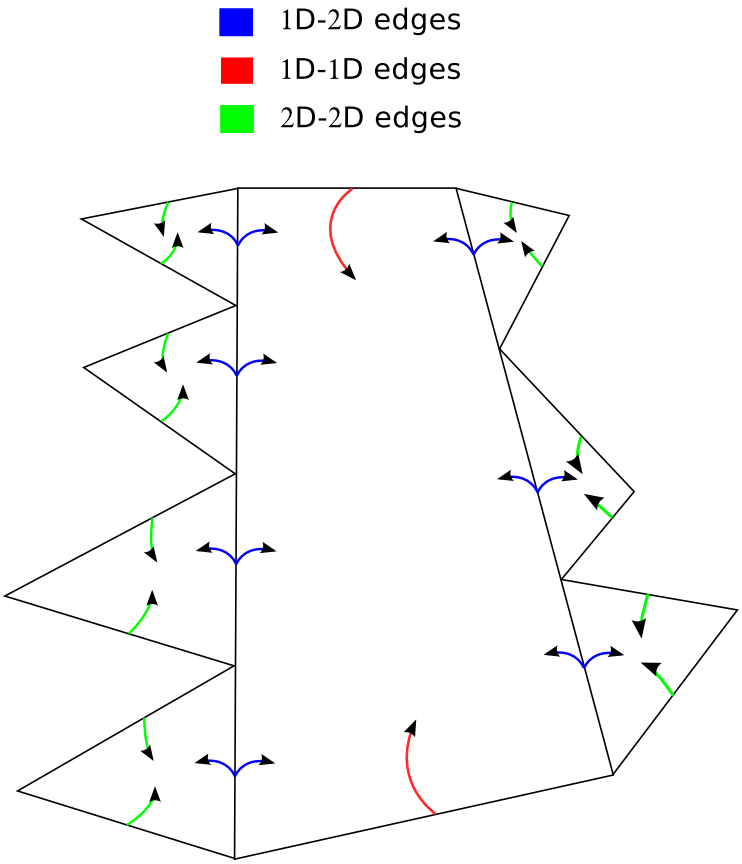

Figure 15.4: Sketch of the contributions in the RCE 1D-2D model

and $N_E = 1$ if it is a corner boundary cell.

On the contrary, the 1D numerical scheme including both the contributions of the 1D-1D and the 1D-2D edges must be split into two expressions, representing the updating of the wetted area:

$$A_i^{n+1} = A_i^n - \underbrace{\frac{\Delta t}{\Delta x}\left[\left(\sum_{m_1}\tilde{\lambda}^+\tilde{\gamma}\tilde{e}_1\right)_{i-1/2}^{m_1} + \left(\sum_{m_1}\tilde{\lambda}^-\tilde{\gamma}\tilde{e}_1\right)_{i+1/2}^{m_1}\right]^n}_{1D-1D \text{ edges}} \\ \underbrace{- \frac{\Delta t}{\Delta x}\sum_{i=0}^{N_C}\sum_{m_2=1}^{3}\left[(\tilde{\lambda}^-\tilde{\gamma}\tilde{e}_1)_\kappa^{m_2} l_\kappa\right]^n}_{1D-2D \text{ edges}} \tag{15.7}$$

and of the discharge:

$$Q_i^{n+1} = Q_i^n - \underbrace{\frac{\Delta t}{\Delta x}\left[\left(\sum_{m_1}\tilde{\lambda}^{+}\tilde{\gamma}\tilde{e}_2\right)_{i-1/2}^{m_1} + \left(\sum_{m_1}\tilde{\lambda}^{-}\tilde{\gamma}\tilde{e}_2\right)_{i+1/2}^{m_1}\right]^n}_{1D-1D \text{ edges}}$$
$$- \underbrace{\frac{\Delta t}{\Delta x}\sum_{i=0}^{N_C}\sum_{m_2=1}^{3}\left[(\tilde{\lambda}^{-}\tilde{\gamma}\tilde{e}_2)_\kappa^{m_2} l_\kappa\right]^n cos\theta - \frac{\Delta t}{\Delta x}\sum_{i=0}^{N_C}\sum_{m_2=1}^{3}\left[(\tilde{\lambda}^{-}\tilde{\gamma}\tilde{e}_3)_\kappa^{m_2} l_\kappa\right]^n sin\theta}_{1D-2D \text{ edges}} \tag{15.8}$$

where $m_1 = 1..2$ and N_C is the number of adjacent 2D cells associated to the 1D cell in the coupling zone.

All techniques explained in part I for the correction of the source amount in the case of wet/wet problems, friction issues and the algorithm to handle wet/dry fronts must be applied to the 1D-2D edges. Furthermore, it should be noted that, in the lateral configuration, the contribution from the 1D-2D edges are non-zero when an overflow occurs. Otherwise, solid wall or zero flow has to be imposed over the 2D cells that could have water depth greater than zero.

15.2.1 Solute transport

The RCE strategy to couple the 1D and the 2D models can be conveniently extended to the solute transport equations using the separate conservative approach explained in part I, section 3.4. Let consider a solute with a concentration ϕ. The numerical flux for the solute equation can be written for the 1D-2D edges κ

$$q_\kappa^{\downarrow} = q_{2D} + \sum_{m=1}^{3}\left(\widetilde{\lambda}^{-}\ \widetilde{\gamma}\ \widetilde{\mathbf{e}}_1\right)_\kappa^m \qquad \phi_\kappa^{\downarrow} = \begin{cases} \phi_{2D} & if \quad q_\kappa^{\downarrow} > 0 \\ \phi_{1D} & if \quad q_\kappa^{\downarrow} < 0 \end{cases} \tag{15.9}$$

where $q_{2D} = (q_x n_x + q_y n_y)_{2D}$ is the normal unit discharge of the 2D cell. The complete 2D numerical scheme, combining the contributions coming from the 2D-2D edges and those arriving from the 1D-2D edges, is formulated in a conservative way

$$(h\phi)_i^{n+1} = (h\phi)_i^n - \underbrace{\frac{\Delta t}{A_i}\sum_{k=1}^{N_E}(q\phi)_k^{\downarrow} l_k}_{2D-2D \text{ edges}} - \underbrace{\frac{\Delta t}{A_i}(q\phi)_\kappa^{\downarrow} l_\kappa}_{1D-2D \text{ edges}} \tag{15.10}$$

The 1D scheme can be expressed compactly again, adding to (13.15) the contributions from the N_C adjacent 2D cells associated to the 1D cell through the corresponding coupling zone:

$$(A\phi)_i^{n+1} = (A\phi)_i^n - \underbrace{\frac{\Delta t}{\Delta x}\left[(q\phi)_{i+1/2}^{\downarrow} - (q\phi)_{i-1/2}^{\downarrow}\right]}_{1D-1D \text{ edges}} - \underbrace{\frac{\Delta t}{\Delta x}\sum_{\kappa=1}^{N_C}(q\phi)_\kappa^{\downarrow} l_\kappa}_{1D-2D \text{ edges}} \tag{15.11}$$

Chapter 16

Numerical results

The main objective of this chapter is to test the two 1D-2D coupled models presented in the previous chapters by means of different test cases. One test has been chosen for calibration corresponding to a extreme dam break in a channel propagating into a flood plain [125]. Being a test case without almost influence of source terms, the hydrodynamic of the system can be deeply analysed when coupling both models. Then, a trapezoidal channel connected laterally with a floodplain area is used as validation test case including steady and unsteady flow scenarios and comparing the numerical results with a fully 2D model in terms of time evolution at several probes over the domain. The behaviour of the coupled models is also tested in a Y-shape junction problem, with two geometry configurations that have an impact on the flow regime. The implementation of the solute transport coupling is also tested by means of the same trapezoidal channel described above, with a simplified nitrogen Water Quality Model. After, it is applied to the Ebro river, a real meandering river with complex topography where the numerical results of the coupled model in terms of flooding extension and longitudinal profiles are compared with those obtained with a fully 2D modelization. Finally a realistic simulation of a five day flooding event in the Tiber river (Italy) combined with the transport of a passive solute is performed. The numerical results are compared with field measurements as well as with a refined fully 2D model.

The computational gain achieved by the proposed 1D-2D coupled models is also estimated in all the test cases presented, analysing the results in terms of speed-up in comparison with a complete 2D model.

16.1 Test case 1: Experimental dam-break in a channel with a floodplain

In this section, the simulation of a dam break in a channel that ends into a flood plain [125] is presented. The test case was designed and measured in the National Laboratory of Civil Engineering in the IST in Portugal. Initial conditions are h=0.504 m at the reservoir and h=0.003 m in the rest of the channel and flood plain [125]. Solid walls are all around except at the outlet that is free (see Figure 16.1). A flat bed level is assumed all over the domain and the friction was previously calibrated with a Manning coefficient of n=0.009 $s/m^{\frac{1}{3}}$. The time evolution of the water depth was measured at probes P1, P2, P3, P4, P5 and P6 displayed in Figure 16.1.

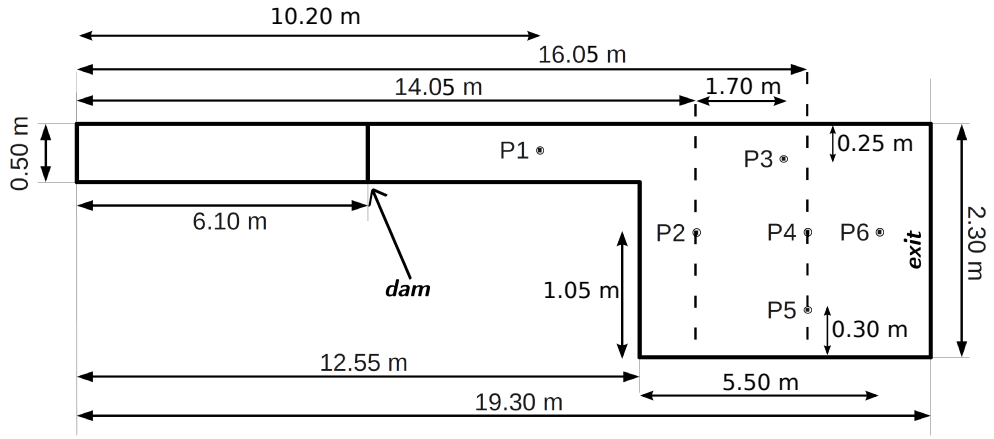

Figure 16.1: Description of the test case 1. Geometrical data. Gauge points location

Figure 16.2 illustrates the discretization used for both frontal and lateral configurations. The mesh used in the 2D domain of the coupled model is unstructured triangular grid. Apart from experimental data, the fully 2D model, used as reference solution whose discretization is composed by 8760 unstructured triangular cells and the fully 1D model, discretized with Δx=0.1 m are also included in order to evaluate the relative behaviour of the proposed coupled model. It is worth emphasizing here that the main objective of this work is to evaluate whether a coupled model is able to produce numerical results at least of the same accuracy of those from the 2D numerical model but at a reduced computational cost.

Despite the apparent simplicity, this test case involves large Froude numbers (near to 4) at the location of the wave front. The measurements of the water depth

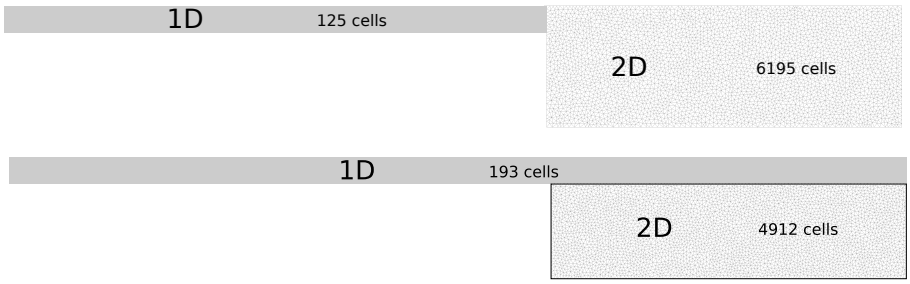

Figure 16.2: Test case 1: Upper: discretization of the frontal coupling domain. Lower: discretization of the lateral coupling domain

contain an experimental uncertainty. As the water depth values are relatively small in this test case (around centimetres) the experimental error is rather noticeable in some probes showing oscillatory experimental data. As already noticed in [125], the numerical models are sometimes unable to reproduce exactly these experimental measurements.

Figure 16.3 shows the comparison of the numerical results obtained with the FC 1D-2D frontal and lateral coupling, the fully 1D model, the fully 2D model and the experimental measurements in time evolution of the depth of water at the gauge points. The same evaluation is carried out for the RCE 1D-2D model in Figure 16.4. As the results between both coupled models (FC and RCE) are very similar, the following discussion of the results will be referred to the 1D-2D coupled model in general.

Attending to probes P2 and P6, both the 1D-2D frontal and lateral coupling models are able to reproduce faithfully the experimental measurements being very similar to the fully 2D approach. However, at probe P6, the RCE 1D-2D model approximate slightly better the rebound. At probe P1, located within the narrow region, the predictions of all models almost coalesce but they are all unable to approximate well the experimental data. This was already noticed in the original work [125]. The same happens at probe P4, where unexpected oscillatory measurements are not reproduced by any model. The behaviour at probe P3 is slightly different. The 1D-2D lateral coupling model does not approximate accurately the experimental data at this probe due to the 1D cross section averaging and the 1D-2D frontal coupling strategy propagates the flood wave slower than the fully 2D model or the experimental data. Probe 5 is located near the lateral wall were the shock wave reflects so that it shows first the arrival of the front and then the arrival of the

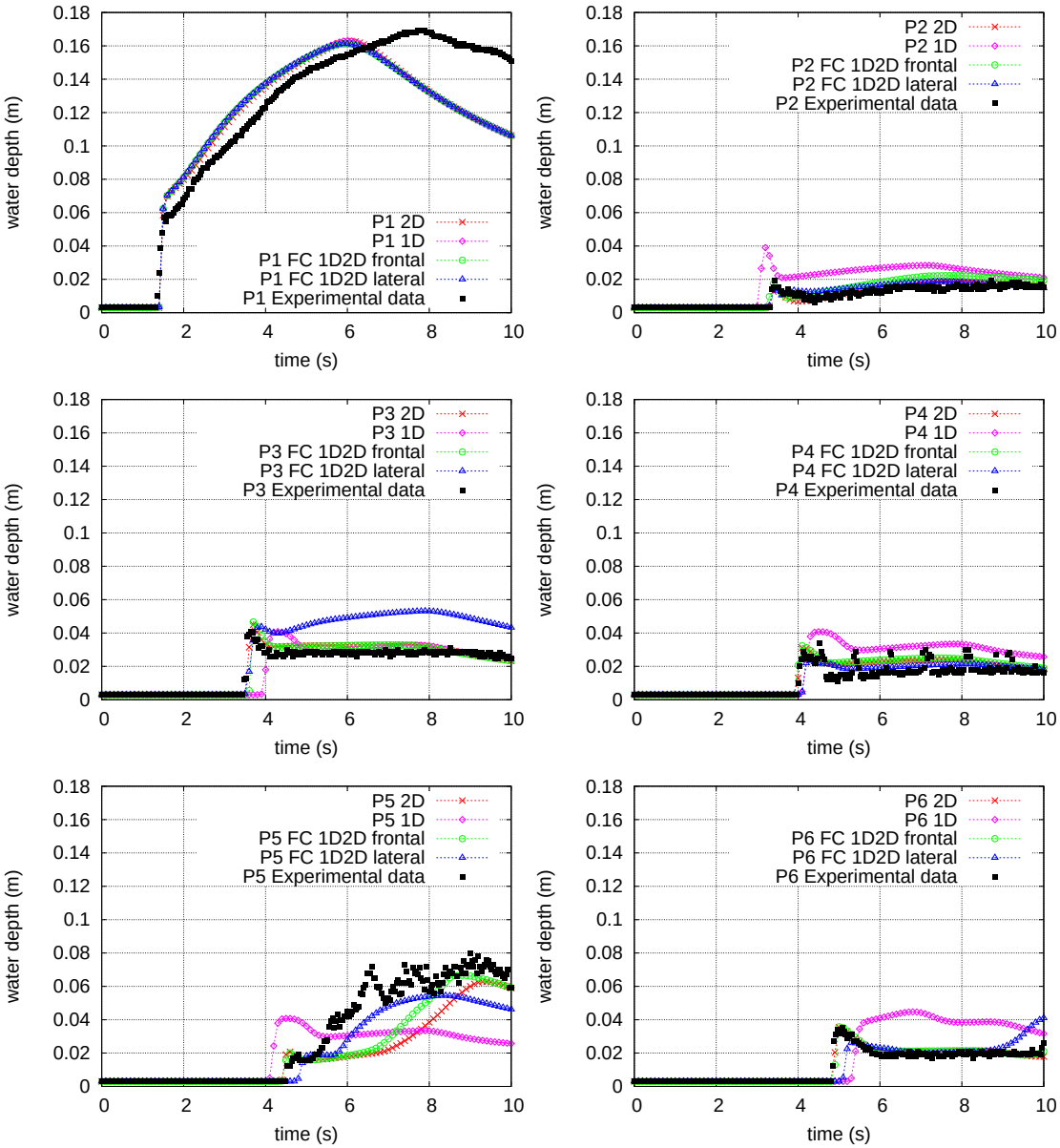

Figure 16.3: Test case 1: Comparison of numerical results (FC 1D-2D model) and experimental measurements for the water depth at the gauge point P1 to P6, from upper left to lower down respectively

reflected wave. The fully 2D model and the 1D-2D frontal coupled model, with all the floodplain considered as a 2D domain, show the best results. They compare to those reported in [125]. The 1D-2D lateral coupled model performs worse due to the forced average values introduced along the 1D domain.

On the other hand, as expected, the fully 1D model, which represents the floodplain

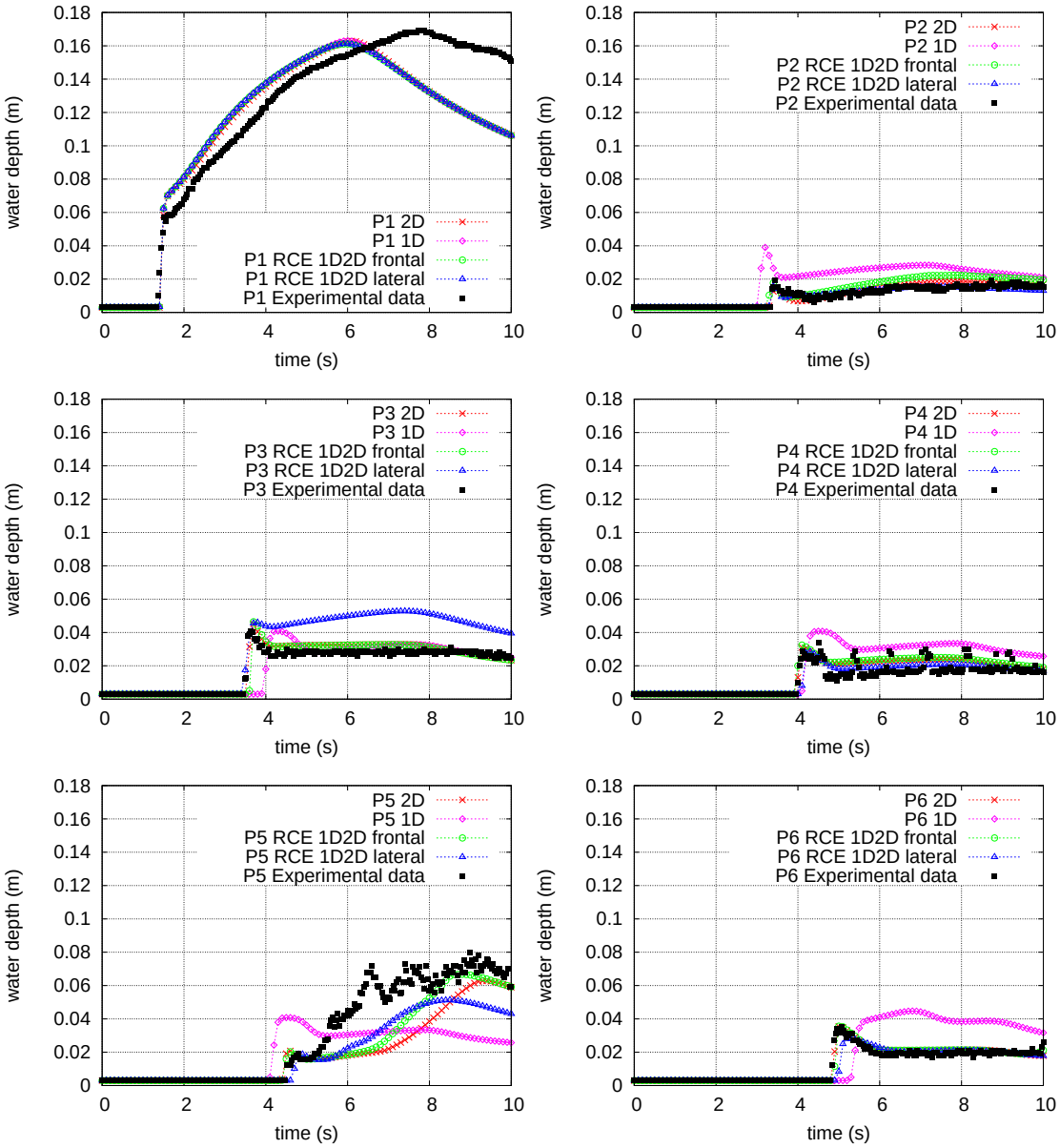

Figure 16.4: Test case 1: Comparison of numerical results (RCE 1D-2D model) and experimental measurements for the water depth at the gauge point P1 to P6, from upper left to lower down respectively

as a sudden enlargement, propagates a flood wave faster than the 2D model, giving unrealistic results and providing the worst numerical approximation.

Therefore, both 1D-2D models are able to estimate reasonably the results obtained by the 2D model. In particular, the FC 1D-2D model is able to detect dynamically the Froude numbers at each side of the coupling zone and determine the adequate

technique at each moment. For example, the nature of this test case indicates that, during the simulation time, the coupling technique internally adopted by the model is always the *MMC* strategy due to the supercritical flow regime.

It is worth emphasizing that boundary conditions play an important role in the FC 1D-2D coupled model proposed in this work. Therefore, a remarkable statement derived from the information needed at the boundaries is that not all strategies are valid for computing certain scenarios. For this purpose, the same dambreak test case is simulated enforcing a *OMC* strategy everywhere all the time. Results are shown in Figure 16.5, plotting the experimental measurements at the known gauge points against the *OMC* approach results. The *OMC* strategy is unable to approximate the experimental data at almost any of the gauge points, providing also non-physical results as a consequence of a wrong boundary treatment at the coupling zone where less information than the necessary is provided.

16.2 Test case 2: Channel with a lateral floodplain area

This academic test case deals with a 2000 m long and 60 m base wide trapezoidal channel connected laterally with a floodplain area (Figure 16.6). A longitudinal slope of 1/1000 is assumed and the friction is modelled by using different Manning coefficients: n=0.015 $s/m^{\frac{1}{3}}$ in the river bed and n=0.035 $s/m^{\frac{1}{3}}$ in the lateral floodplain.

Being a synthetic test case, the numerical results obtained by both coupled models will be compared with a fully 2D model through 10 probes situated in the floodplain area. A sketch of the test case containing the location of the probes can be observed in Figure 16.7.

The comparison with a fully 2D model is only a good measure of the behaviour of a new coupled model when the mesh is fine enough. Contrary to the previous test case, the channel and floodplain are not flat. The 2D grid refinement should represent faithfully the topography. In this case, the topography is represented by the 2D model through computational cells covering all the domain and the representation of the terrain is as accurate as the mesh resolution.

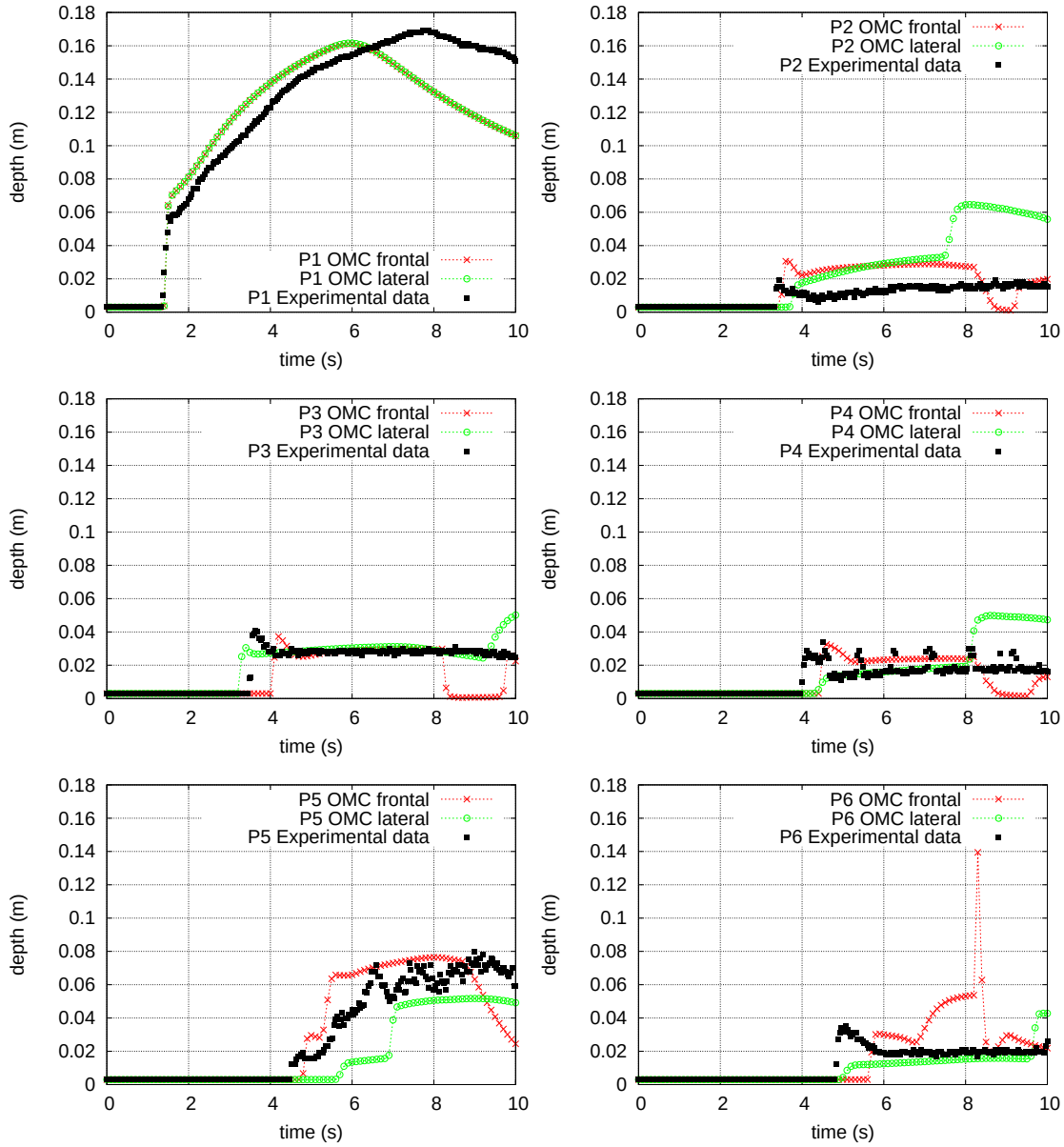

Figure 16.5: Test case 1: Comparison of numerical results with an OMC strategy and experimental measurements for the water depth at the gauge point P1 to P6, from upper left to lower down respectively

The trapezoidal cross section is represented by unstructured triangular cells (Figure 16.8) so that, if a fine discretization is not applied, some errors can be derived from this aspect.

Two scenarios involving lateral coupling are simulated in order to evaluate again the performance of the scheme: steady and unsteady flow.

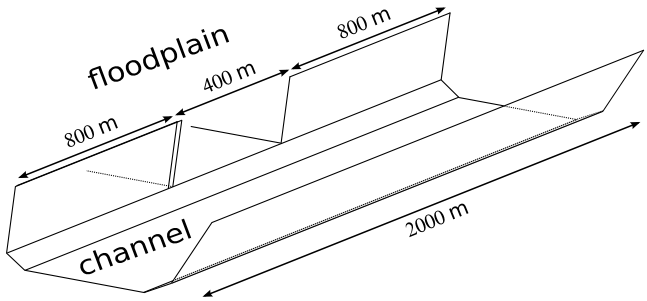

Figure 16.6: Description of the test case 2: a channel connected laterally with a floodplain area

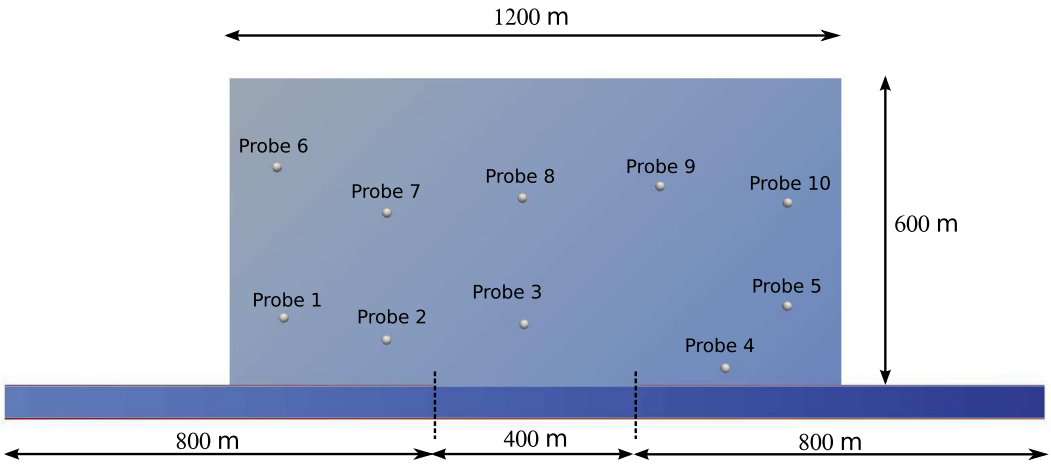

Figure 16.7: Test case 2: Position of the probes

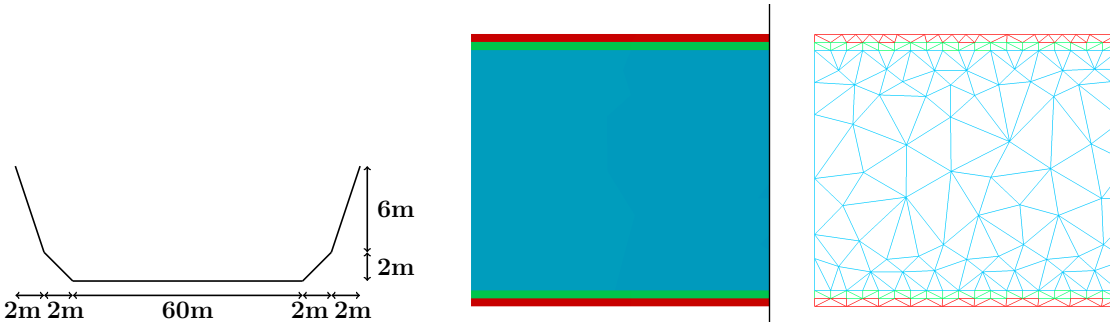

Figure 16.8: Test case 2: channel cross section geometry and 2D discretization into triangular cells

16.2.1 Steady flow

A constant discharge of 600 m^3/s is introduced as the upstream inlet boundary condition and the model is run until convergence to steady state. A gauging curve

is used as outlet boundary condition at the end of the channel. The numerical results obtained by the FC and RCE 1D-2D models are compared with a fully 2D model in terms of longitudinal profile along the channel center line once the steady state is reached (Figure 16.9) and also registering the time evolution of the water depth at each probe (Figures 16.10 and 16.11).

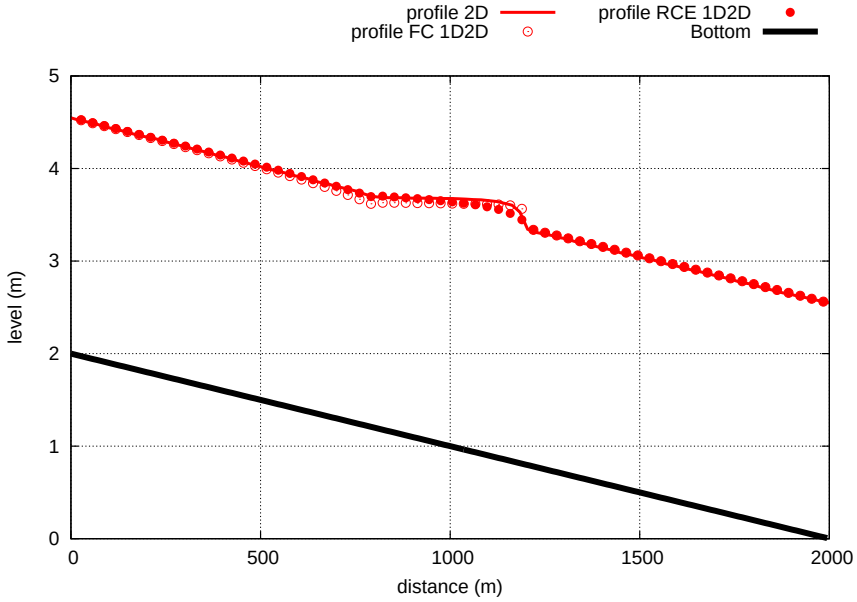

Figure 16.9: Test case 2 steady flow: longitudinal profile along the channel

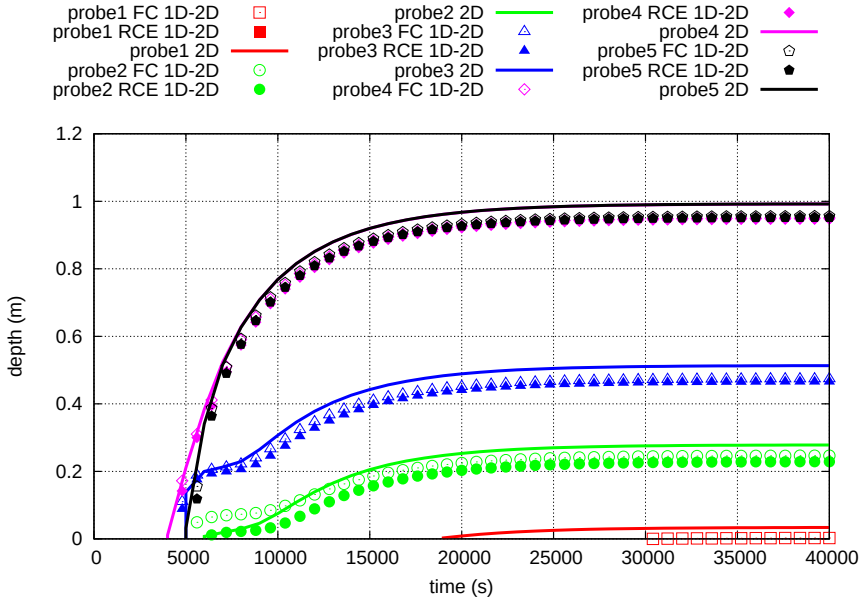

Figure 16.10: Test case 2 steady flow: probes 1-5. 1D-2D (points) , fully 2D (lines)

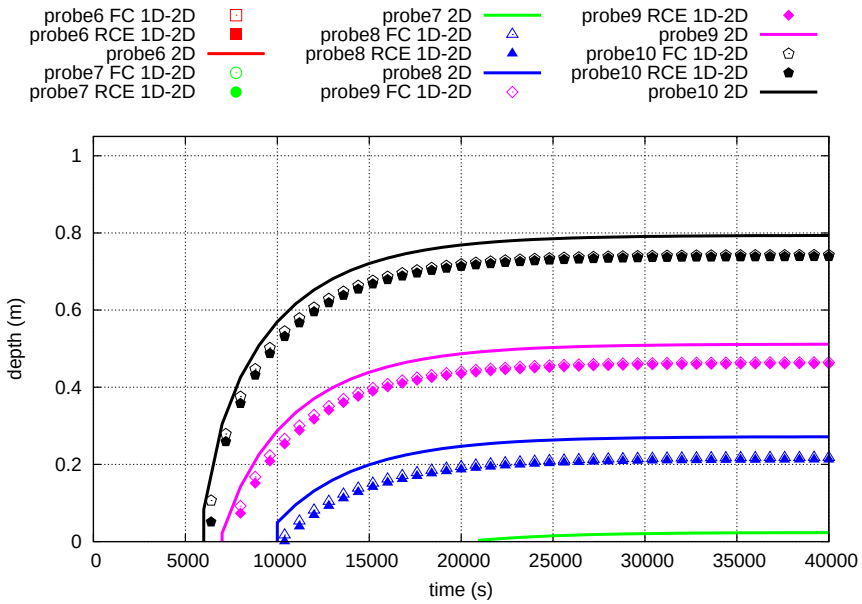

Figure 16.11: Test case 2 steady flow: probes 6-10. 1D-2D (points) , fully 2D (lines)

Observing the results, an almost constant difference is appreciated between the fully 2D numerical model and the proposed 1D-2D coupling models. As the difference is almost constant in all the probes it may indicate that the deviation is due to the Manning roughness coefficient in the river bed and its adjustment for each model. In both simulations, the choice of this coefficient has the same value but, however, it is underestimated by the 1D approach (included in the coupled model) achieving a lower water depth in the time evolution of each probe.

In order to corroborate this hypothesis, a new simulation has been carried out by tuning manually the Manning coefficient to n=0.0155 $s/m^{\frac{1}{3}}$ in the river bed for the coupled model. The results can be observed in Figure 16.12 plotting the longitudinal profile all along the channel and in Figures 16.13 and 16.14, where the water depth time evolution is registered for the three models.

As shown, the results obtained by both coupled models coalesce almost exactly with the same obtained with the fully 2D model. In particular, the behaviour at probe 6 that is always 'dry' is emulated in both models.

The Froude number is less than one in all the domain, so the test case is always developed in a subcritical regime. Therefore, the FC 1D-2D coupled model is automatically using the *OMC* strategy during all the simulation in order to compute the water surface level at each coupling zone. In order to check again the importance of

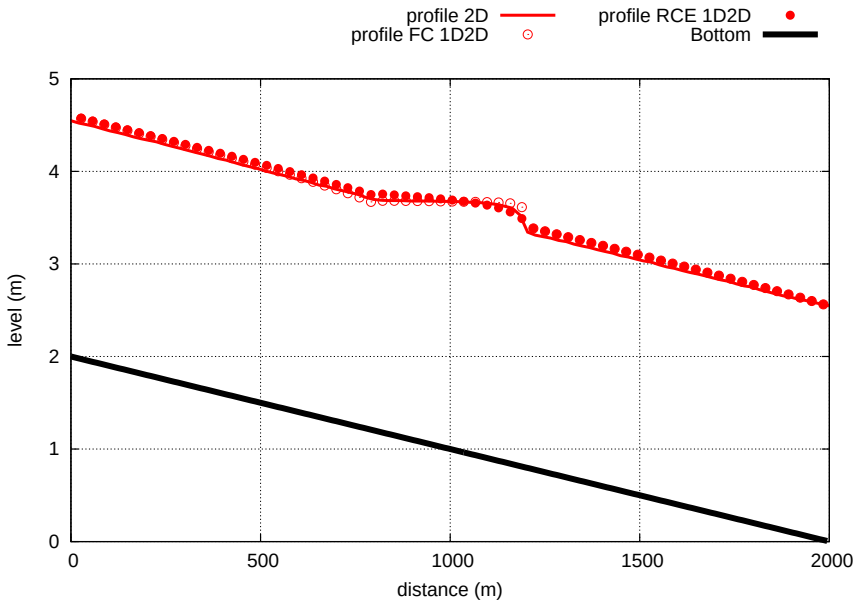

Figure 16.12: Test case 2 steady flow: longitudinal profile along the channel

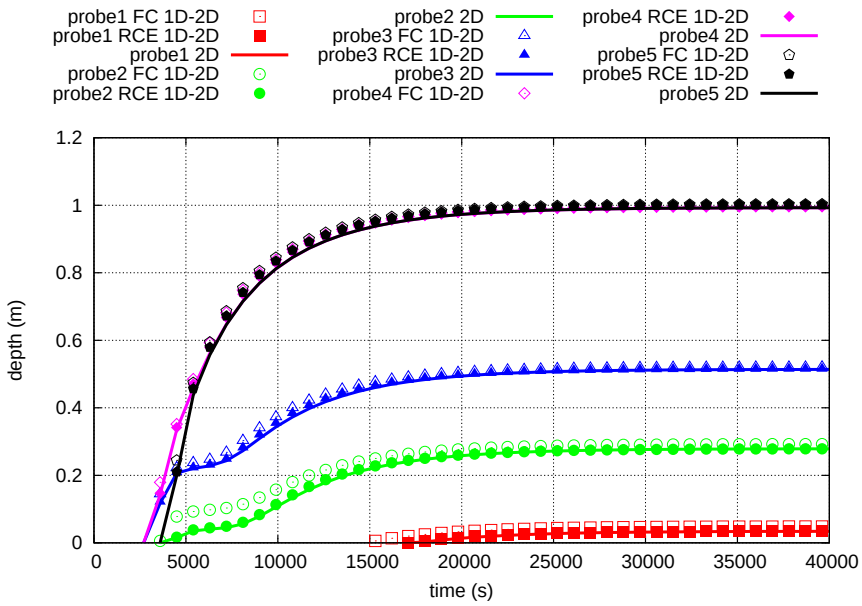

Figure 16.13: Test case 2 steady flow: probes 1-5. n=0.0155 $s/m^{\frac{1}{3}}$ in the river bed. 1D-2D (points) , fully 2D (lines)

the boundary treatment, the same case is simulated enforcing the *MMC* strategy. Results are shown in terms also of longitudinal profile and time evolution of water depth at each measurement point in Figures 16.15, 16.16 and 16.17. When using the *MMC* strategy in presence of a subcritical regime, more information than necessary

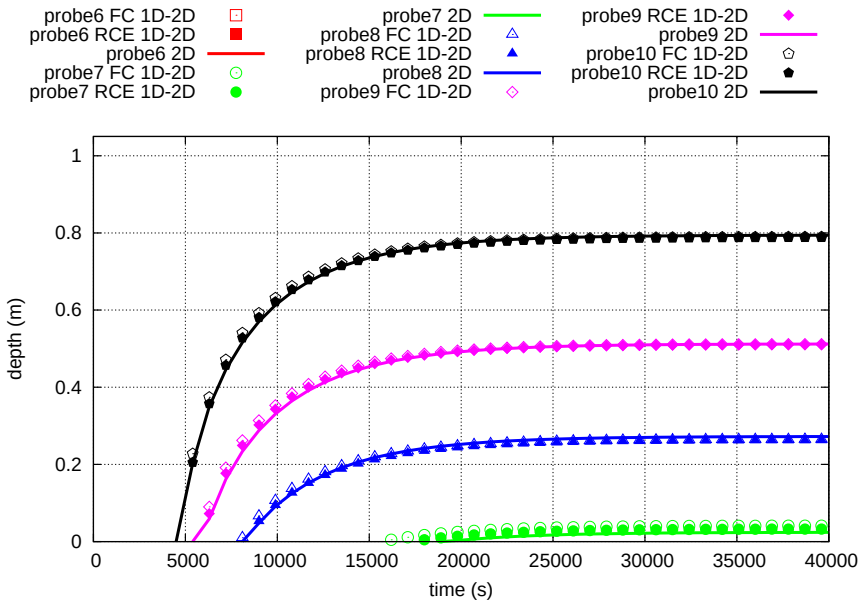

Figure 16.14: Test case 2 steady flow: probes 6-10. n=0.0155 $s/m^{\frac{1}{3}}$ in the river bed. 1D-2D (points) , fully 2D (lines)

is provided, and the numerical solution achieved by the FC 1D-2D coupled model is far from that obtained by the fully 2D model arriving to non-physical results.

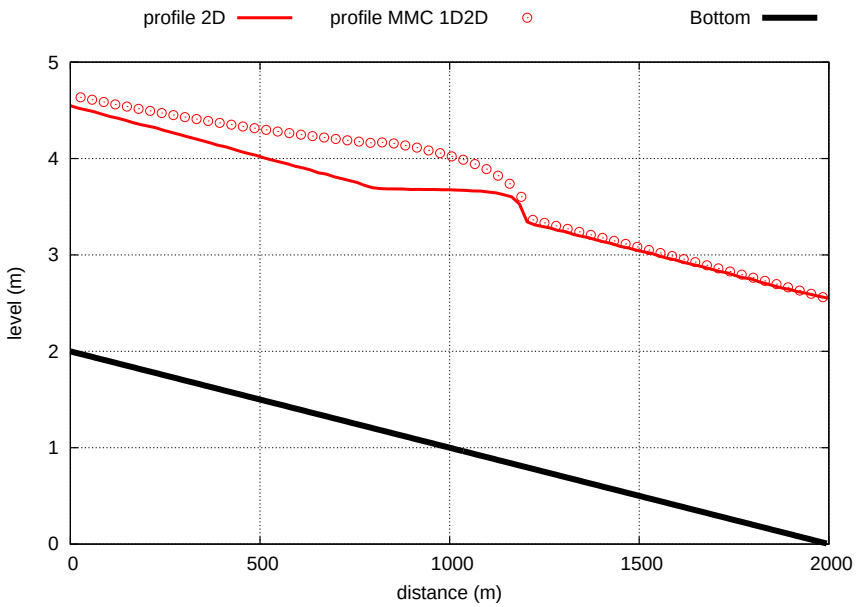

Figure 16.15: Test case 2 steady flow: longitudinal profile along the channel. *MMC* strategy

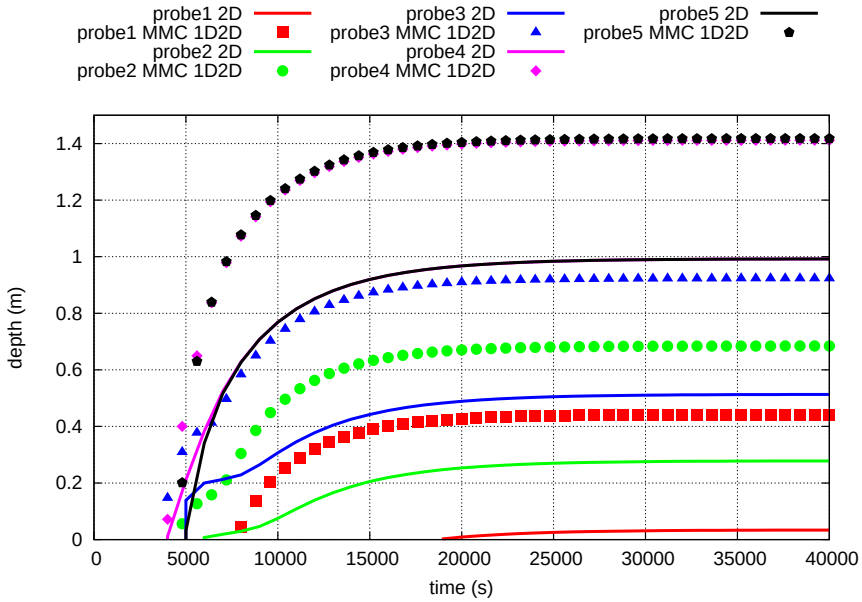

Figure 16.16: Test case 2 steady flow: probes 1-5. n=0.0155 $s/m^{\frac{1}{3}}$ in the river bed. *MMC* strategy. 1D-2D (points) , fully 2D (line)

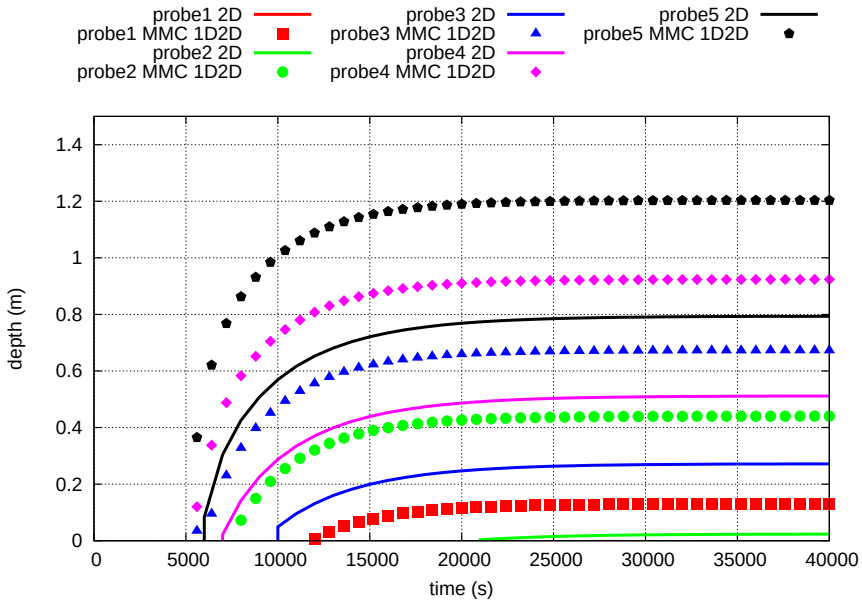

Figure 16.17: Test case 2 steady flow: probes 6-10. n=0.0155 $s/m^{\frac{1}{3}}$ in the river bed. *MMC* strategy. 1D-2D (points) , fully 2D (lines)

16.2.2 Unsteady flow

Adopting the modified Manning roughness coefficient n=0.0155 $s/m^{\frac{1}{3}}$ in the river bed for the coupled model, a new comparison is proposed by using the same test

case now considering unsteady flow. A triangular inlet discharge hydrograph (Figure 16.18) with a peak discharge of 600 m^3/s is introduced to the system. The water depth time evolution at the gauge points (Figure 16.7) resulting from the coupled models is compared again with a fully 2D model in Figures 16.19 and 16.20.

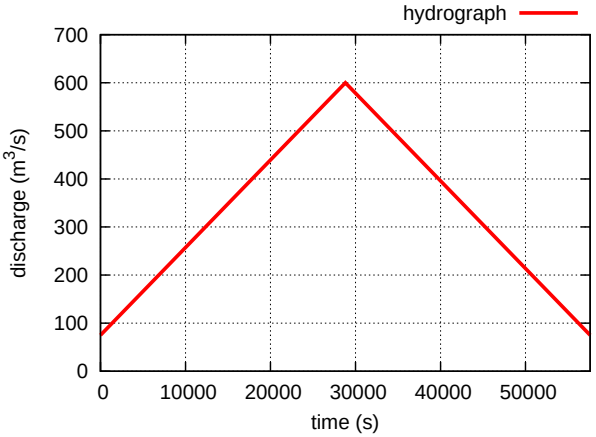

Figure 16.18: Test case 2: Triangular inlet hydrograph

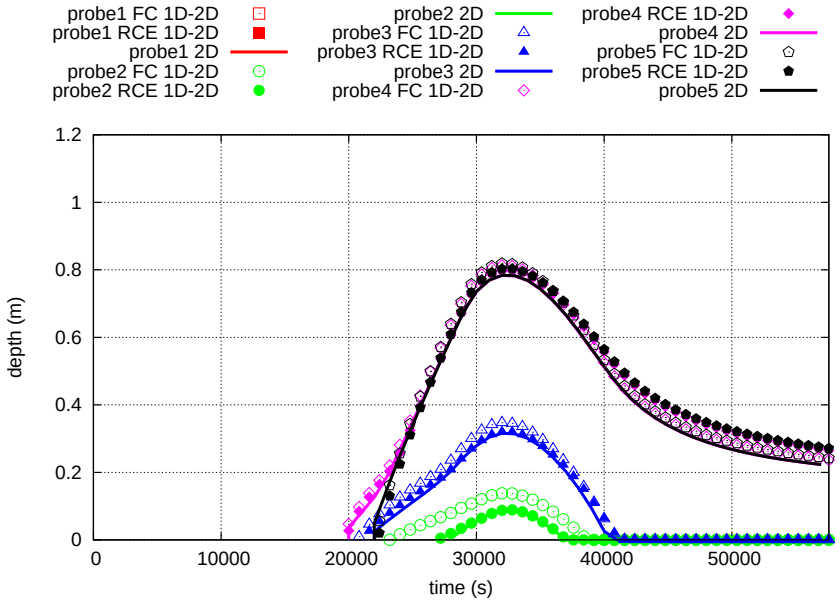

Figure 16.19: Test case 2 unsteady flow: probes 1-5. 1D-2D (points) , fully 2D (lines)

A good agreement is achieved between both sets of numerical results. Not only the shape of the probes registering some water is respected but also the absence of water at probes 1, 6 and 7 is well reproduced by the coupled model.

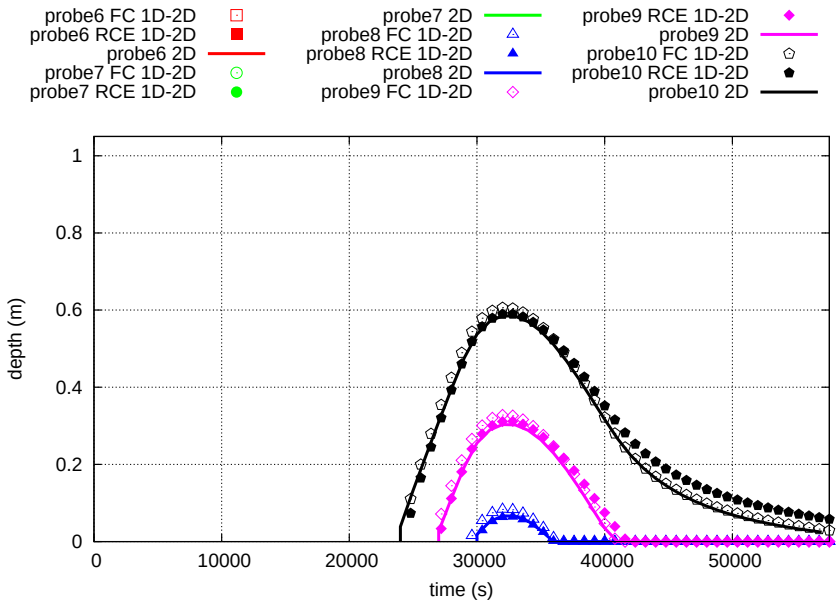

Figure 16.20: Test case 2 unsteady flow: probes 6-10. 1D-2D (points) , fully 2D (lines)

16.3 Test case 3: Convergence to steady state in a Y junction

Two cases of numerical simulation of the evolution of flow towards steady state at a junction of three channels of large slope are next presented. The interest of this test case lies in the changing flow regime due to the configuration of the system. The dynamical choice of the adequate strategy (OMC or MMC) for the FC 1D-2D coupled model will be evaluated as well as the ability of RCE 1D-2D model to solve the Riemann Problem under these conditions.

A rectangular cross section channel 1m wide (channel 1) branching into two channels of the same geometry (channels 2 and 3) are considered. A constant discharge of 3 m^3/s is assumed at the inlet point to channel 1 and a fixed Froude number of 0.14 is enforced at the outlet of channels 2 and 3, starting from the initial conditions of uniform water depth of 2 m.

As experimental data are not available for this test case, a fully 2D model is used to compare with the results achieved by the proposed 1D-2D coupled models. The comparison will be made through the longitudinal profiles achieved by each model as well as through several probes or gauge points placed all along the domain, including the three channels and the junction location. The exact position of the probes is

shown in Figure 16.21.

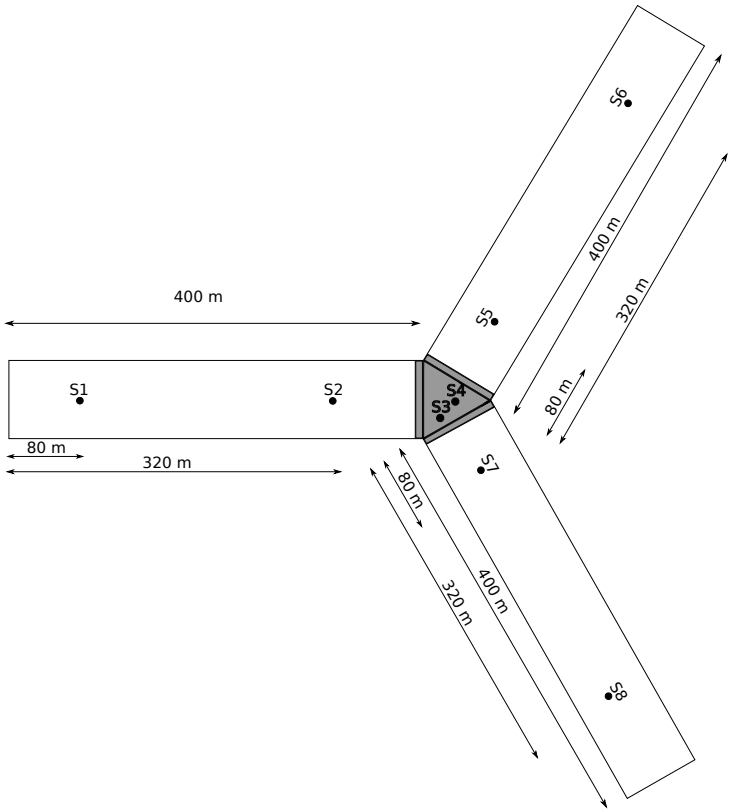

Figure 16.21: Description of the test case 3. Location of the gauge points. Plain background: 1D zone in the coupled model. Gray background: 2D zone in the coupled model made of 1033 triangular cells

Two configurations are proposed by changing the bed slope of each channel, leading to different flow regimes. The Manning roughness coefficient is uniformly chosen as n=0.009 $s/m^{\frac{1}{3}}$.

16.3.1 Supercritical junction

In this example, the values of bed slope are

$$S_{0_1} = S_{0_2} = S_{0_3} = 0.01 \tag{16.1}$$

The steady state is reached starting from a fully subcritical flow due to the initial condition. When convergence to steady state is achieved, the flow is supercritical

all over the domain except for the downstream part of channels 2 and 3, in which identical hydraulic jumps develop to connect with the outlet boundary condition at these locations (Figure 16.22). The results in terms of water level surface at each probe are plotted in Figure 16.23 where the both the FC and RCE 1D-2D models are represented with points and the fully 2D model in lines as before.

As can be observed, there is a good agreement between both numerical 1D-2D approaches and the complete 2D model, not only in all the probes but also regarding the longitudinal profile.

16.3.2 Subcritical junction

With another choice of the bed slope,

$$S_{0_1} = 0.01 \qquad S_{0_2} = S_{0_3} = 0.001 \tag{16.2}$$

the equilibrium flow reached is subcritical at the junction but discontinuous in channel 1, where a hydraulic jump connects the two regimes. Therefore, channels 2 and 3 remain always in a subcritical regime. The longitudinal profile for this configuration, when the steady state is reached, is plotted in Figure 16.24. Also numerical results concerning the evolution in time of the water level surface from the FC and the RCE coupled models and the fully 2D model are shown in Figure 16.25.

The results are almost the same in the fully 2D model and in both the coupled models. In particular some oscillations appear in probes 3 to 8 due to the proximity of the hydraulic jump which are well reproduced by the proposed FC and RCE 1D-2D coupled models.

16.4 Test case 4: Transport of two solutes

This case is designed to compare the proposed FC and RCE 1D-2D schemes with the transport of two substances: nitrate (NO_3) and ammonium (NH_4). These substances represents a simplified Water Quality Model for the nitrogen cycle, are interdependent and usually, the NO_3 concentration increases in the detriment of NH_4. In fact, the solute equations can be written for the 1D configuration:

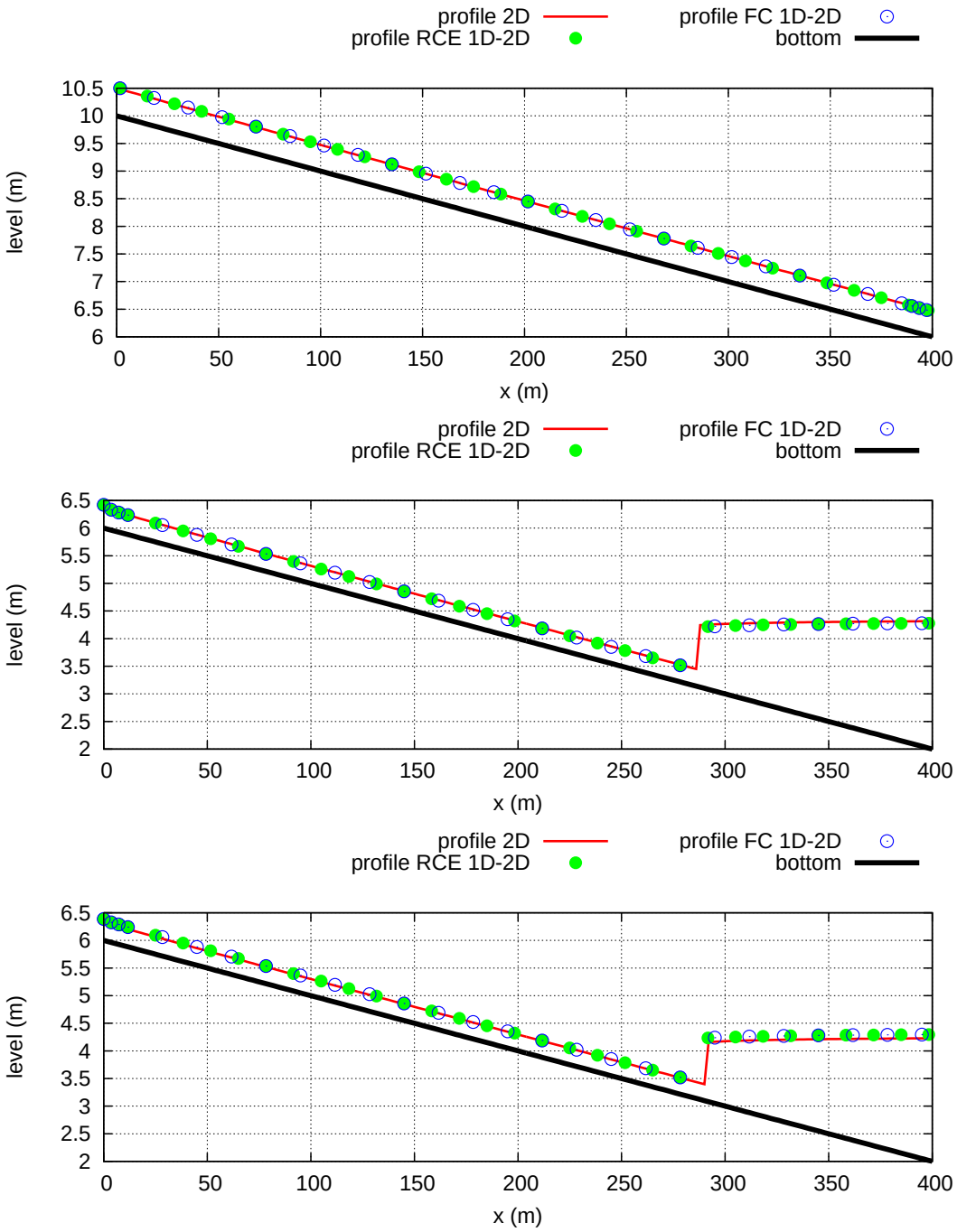

Figure 16.22: Test case 3: Longitudinal profiles of channel 1 (upper), channel 2 (intermediate) and channel 3 (lower). Supercritical junction. 1D-2D (points), fully 2D (lines)

$$\frac{\partial(A\phi_1)}{\partial t} + \frac{\partial(Q\phi_1)}{\partial x} = -K_1 A\phi_1$$
$$\frac{\partial(A\phi_2)}{\partial t} + \frac{\partial(Q\phi_2)}{\partial x} = K_1 A\phi_1 - K_2 A\phi_2 \tag{16.3}$$

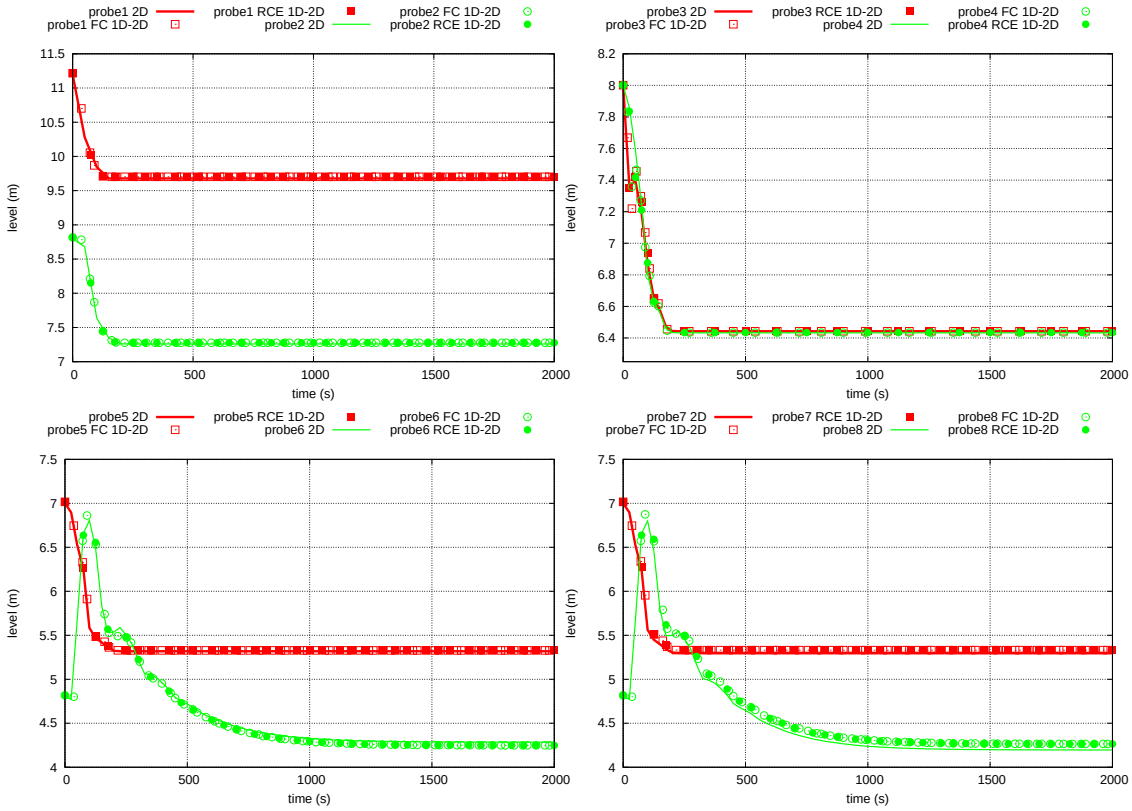

Figure 16.23: Test case 3: Comparison in terms of water level surface between the coupled models and the fully 2D model at each probe. Supercritical junction. 1D-2D (points), fully 2D (lines)

and for the 2D framework:

$$\begin{aligned} \frac{\partial(h\phi_1)}{\partial t} + \frac{\partial(hu\phi_1)}{\partial x} + \frac{\partial(hv\phi_1)}{\partial y} &= -K_1 A \phi_1 \\ \frac{\partial(h\phi_2)}{\partial t} + \frac{\partial(hu\phi_2)}{\partial x} + \frac{\partial(hv\phi_2)}{\partial y} &= K_1 A \phi_1 - K_2 A \phi_2 \end{aligned} \tag{16.4}$$

where ϕ_1, ϕ_2 are the ammonium and nitrate concentration respectively and K_1, K_2 are the uptake constants expressed as follows:

$$K_1 = K_{NH_4} 10^{0.0293T} \qquad K_2 = K_{NO_3} 1.0698\ 10^{0.0293T} \tag{16.5}$$

being T the water temperature (^oC) and K_{NH_4}, K_{NO_3} the nitrification and denitrification rate coefficients at $T = 20\ ^oC$.

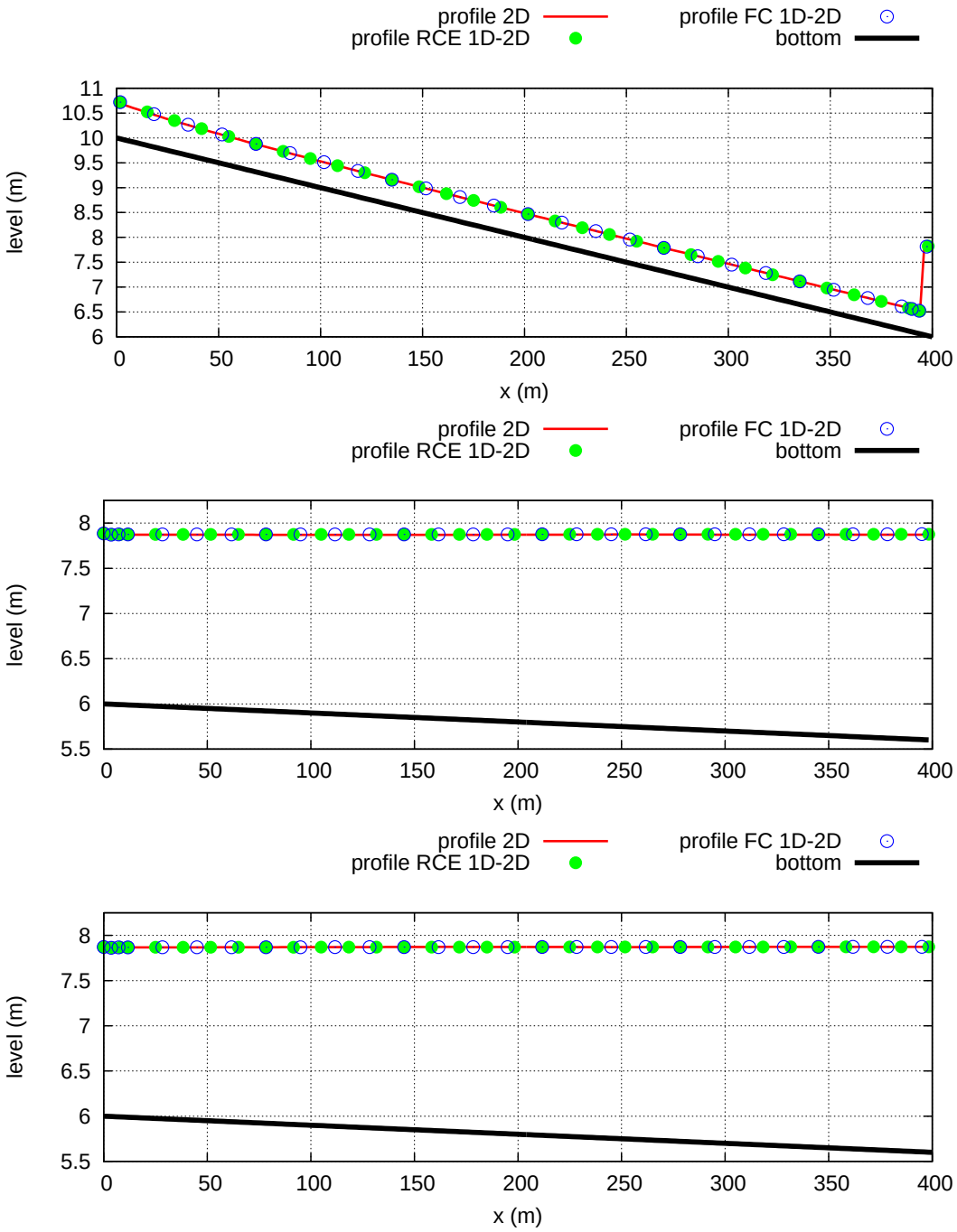

Figure 16.24: Test case 3: Longitudinal profiles of channel 1 (upper), channel 2 (intermediate) and channel 3 (lower). Subcritical junction. 1D-2D (points), fully 2D (lines)

Following the same geometric configuration of test case 2, a constant discharge of 600 m^3/s with constant ammonium ($\phi_1 = 0.2$) and nitrate concentration ($\phi_2 =$

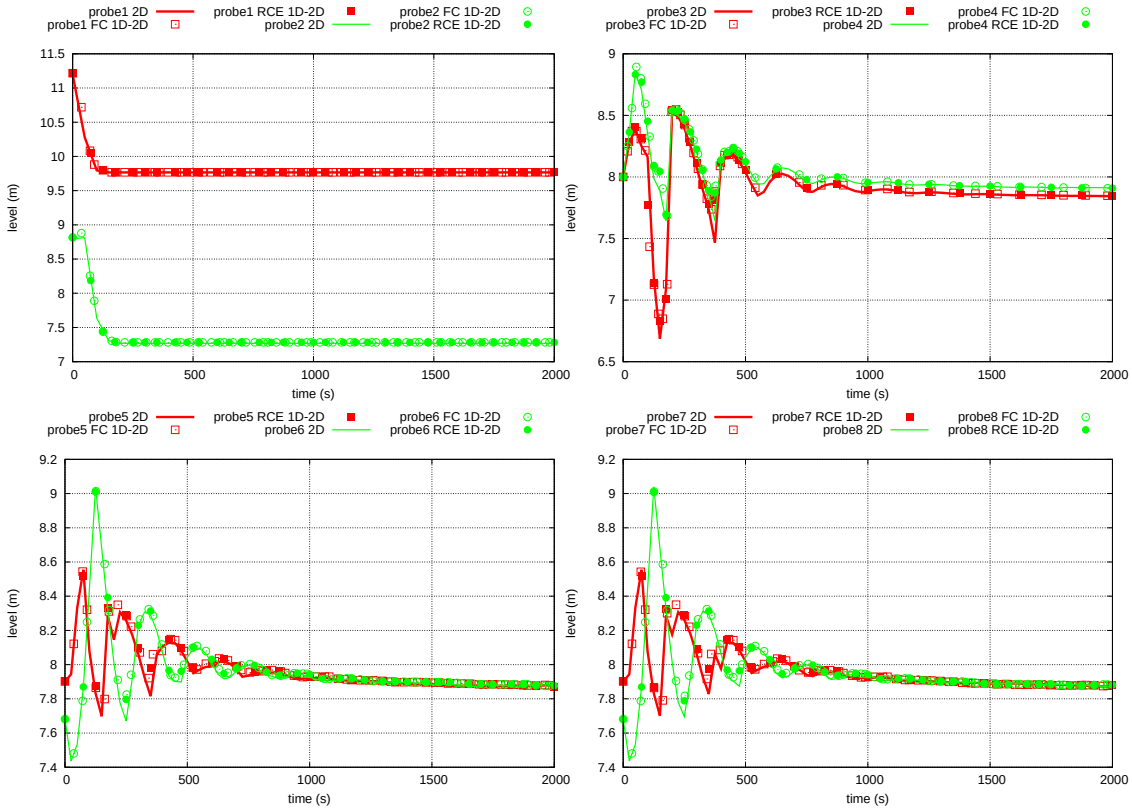

Figure 16.25: Test case 3: Comparison in terms of water level surface between the coupled models and the fully 2D model at each probe. Subcritical junction. 1D-2D (points), fully 2D (lines)

3.0) is introduced as inlet boundary condition. Once the steady state is reached, a rapid change in both concentrations ($\phi_1 = 2.0$, $\phi_2 = 5.5$) is injected to the system emulating a dump upstream the river reach considered. After one hour, the concentrations turn back to their initial configuration. Figure 16.26 shows the evolution in time of the inlet ammonium and nitrate concentration.

The simulation is carried out during 12h. Figure 16.27 shows two snapshots at t=7.5h for the ammonium concentration (left) and at t=12h for the nitrate concentration (right). The numerical schemes used are the fully 2D model (upper), the FC 1D-2D model (middle) and the RCE 1D-2D model (lower). As displayed in these figures, the RCE 1D-2D coupled model is qualitative able to approximate the results achieved by the 2D model. However, the FC 1D-2D model does not represent correctly the advances of the solute front.

In order to corroborate this conjecture, the evolution in time of each probe defined

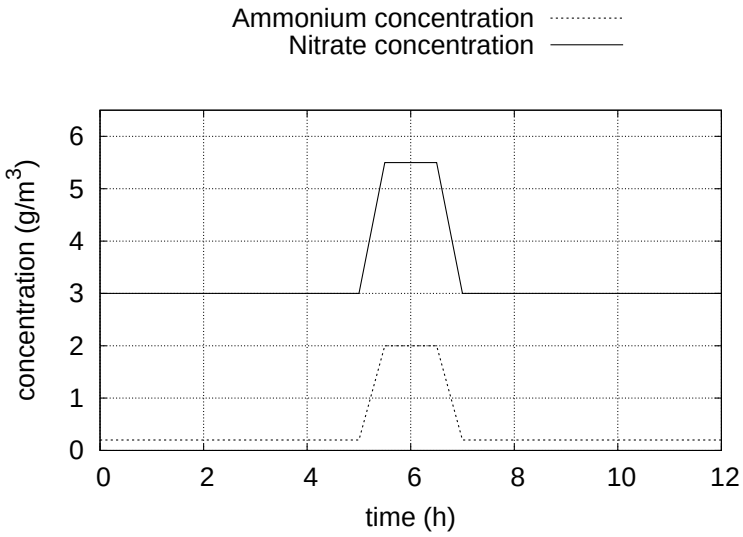

Figure 16.26: Test case 4: Evolution in time of the inlet nitrate and ammonium concentration

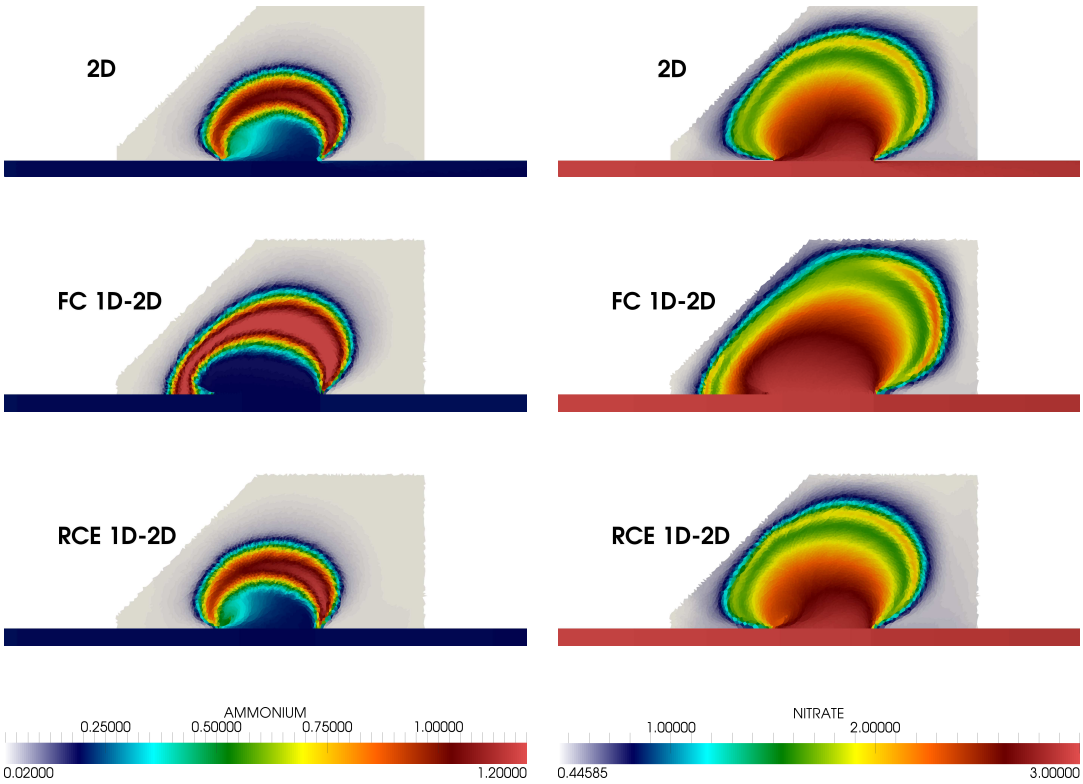

Figure 16.27: Test case 4: Snapshots at t=7.5h for the ammonium concentration (left) and at t=12h for the nitrate concentration (right). Fully 2D model (upper), FC 1D-2D model (middle) and RCE 1D-2D model (lower)

for the system in 16.6 is again registered for the ammonium and for the nitrate concentration in Figures 16.28 and 16.29 respectively.

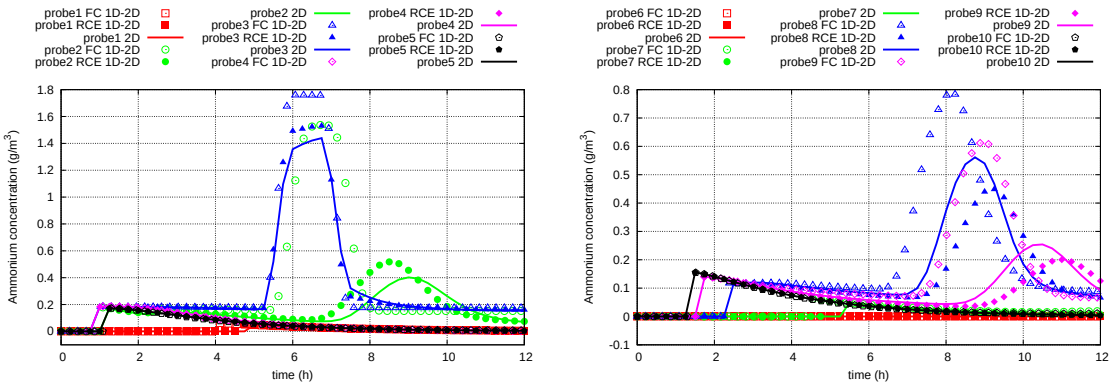

Figure 16.28: Test case 4: Numerical solution of the time evolution of the ammonium concentration at probes 1-5 (left) and at probes 6-10 (right)

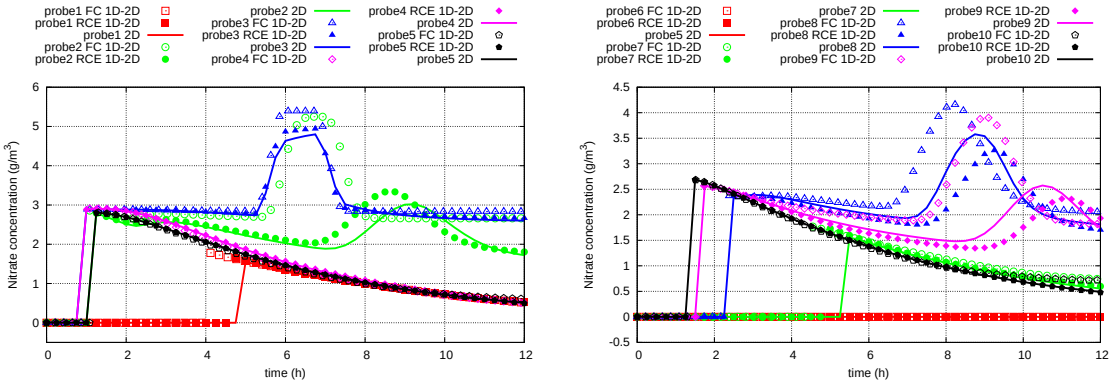

Figure 16.29: Test case 4: Numerical solution of the time evolution of the nitrate concentration at probes 1-5 (left) and at probes 6-10 (right)

The FC 1D-2D model behaves worse than the RCE 1D-2D model when observing the spatial distribution of the solute concentrations. Although some probes are well characterized, the peaks for the nitrate and for the ammonium arrive beforehand at probe 2, probe 8 and probe 9. The solute transport equation is indeed very sensitive to the velocity field hence little changes in these variable may produce large changes in the spatial and temporal distribution of the solute. Moreover, contrary to the water surface level, the averaging process between the 1D cell and the 2D adjacent cells to compute a common solute concentration for both models does not seem to

be adequate in this kind of scenarios.

On the other hand, the RCE 1D-2D model registers some delays at probes 8 and 9 and arrives earlier than the 2D model at probe 3. These wrong estimations can be attributed to the velocity field for the RCE 1D-2D model, that is slightly different from the 2D complete model and does not capture the partial bidimensionality of the main channel an the end of the floodplain. However, the overall behaviour is very similar to the 2D model, achieving very good results in terms of accuracy.

16.5 Test case 5: A meandering river reach. The Ebro river

A case study based on a reach of the Ebro river near urban area (see Figure 16.30) has been selected to evaluate the uncertainty in the flooding predictions introduced by the choice of the proposed coupled models. The Digital Terrain Model (DTM) used in this work was provided by the Ebro River Basin Administration (www.chebro.es). It had been obtained using the Laser Induced Direction And Ranging (LIDAR) data, by means of a test programme using a single pulse scanning sensor, with 0.10 m vertical accuracy and 1 m horizontal resolution. The DTM provides data of great accuracy, but does not furnish any information of the region covered by the water. However, the uncertainty on the particular shape of the river bed under the water surface has been eliminated by reconstructing the river able to convey the water discharge that was flowing in the moment of the LIDAR measurements and so that it reproduces the water surface extension and slope as measured. The DTM plus the river bed reconstruction were used as a full bed topography to provide information to both 2D and coupled models.

Two scenarios have been carried out in order to see the performance of the coupled schemes: steady and unsteady flow. Not having an exact solution or measured data in this river reach, the numerical solution from a fully tested 2D simulation model with a fine grid of 200000 unstructured triangular cells (Figure 16.31 (left)) has been used as a reference solution. In both the FC and the RCE coupled models, the floodplain inundation is clearly complex hence requiring a 2D model when numerical simulation is sought as more than one flow direction are relevant. Therefore, the river bed will be simulated with a 1D model laterally connected with the 2D model.

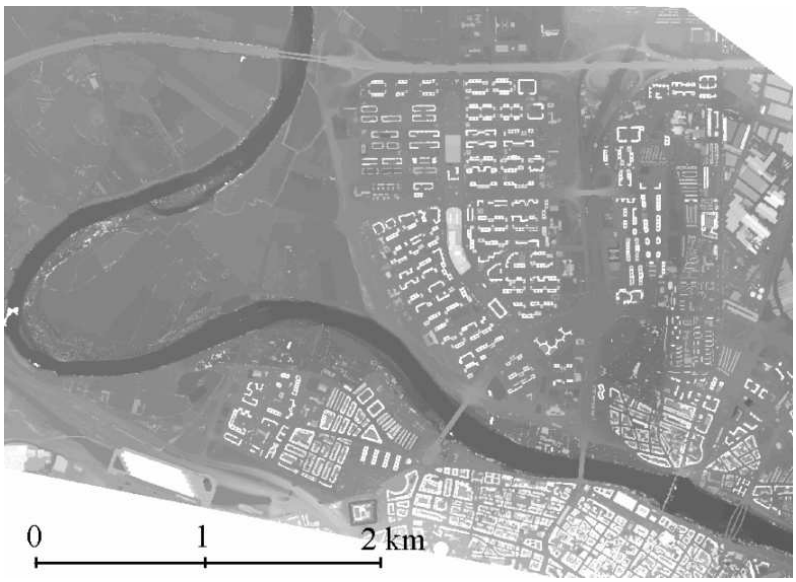

Figure 16.30: Description of the test case 4

A detail of the coupling model domains is shown in Figure 16.31 (right). The discretization in the 1D model is made of 113 cross sections and 112 computational cells, and the 2D domain is covered by almost 46000 triangular cells. It is worth noting that the discretization of the pressure integrals in the 1D model has been done using the integral formulation and the developments described in part I, section 5.

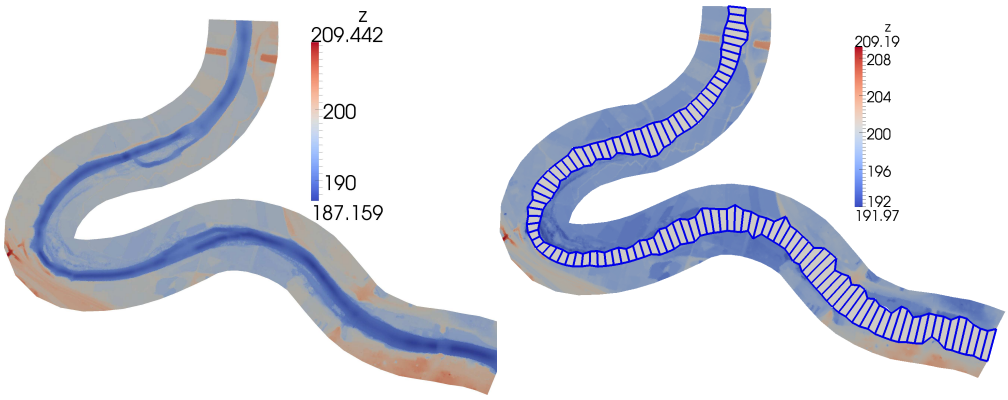

Figure 16.31: Test case 5: 2D model (left) and 1D-2D coupled model (right) for the Ebro river reach

The 2D computations use a single Manning coefficient n = 0.035 $s/m^{\frac{1}{3}}$ all over the domain. However, the 1D scheme 'inside' the coupled models needs a greater coefficient in order to diminish the differences with a 2D model. For this purpose,

n = 0.035 $s/m^{\frac{1}{3}}$ has been chosen all along the 2D sub-domain and n=0.038 $s/m^{\frac{1}{3}}$ in the 1D sub-domain of the coupled models.

16.5.1 Steady flow

The generation of steady state conditions in the river reach has been achieved by convergence to the steady state starting from an empty or dry river. It consists of applying a constant upstream discharge of 600 m^3/s until the river reach fills up and the outlet discharge is equal to the inlet discharge. Figure 16.33 illustrates the flooding map predicted by the 2D model (upper), by the FC 1D-2D model (middle) and by the RCE 1D-2D model (lower). In the 1D-2D representation, the 1D sub-domain shows the cross sectional basis whereas the 2D sub-domain is meshed in triangles. A zoom view of the flooding area has been highlighted.

Both coupled models approach very finely the results predicted by the fully 2D model respecting the wet and the dry regions. Moreover, having a coarse representation of the information in the 1D domain (only 112 sections), the color scale for the river bed elevation is almost exactly reproduced. In order to corroborate this hypothesis, the longitudinal profiles along the river centerline, achieved by each numerical model is plotted in Figure 16.32. As can be appreciated, there is a good agreement between the 2D numerical model and the both the FC and the RCE coupled schemes.

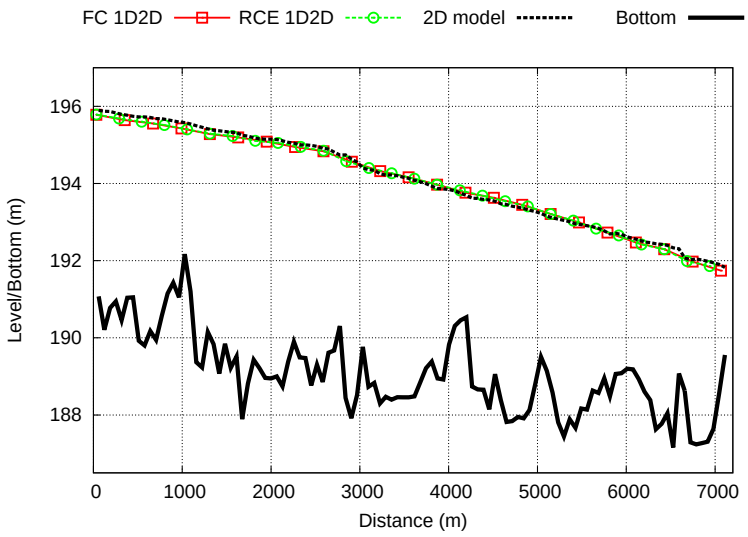

Figure 16.32: Test case 5: longitudinal profile along the river bed for the steady case

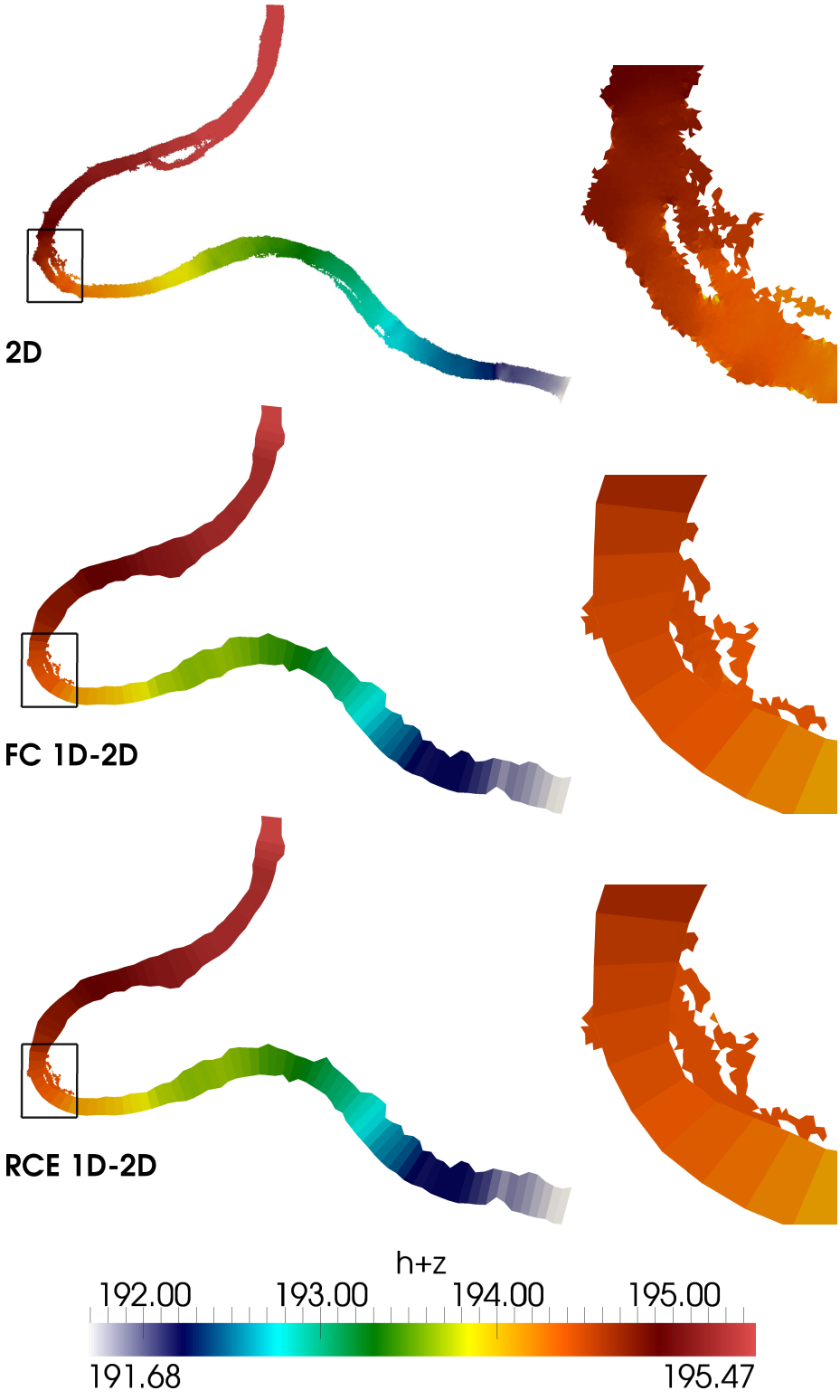

Figure 16.33: Test case 5: Numerical simulation of a steady flow of 600 m^3/s in the Ebro river. Flooded area in the fully 2D model (upper), in the FC 1D-2D model (middle) and in the RCE 1D-2D model (lower)

The flooded area predicted by each model represents another measurement of the quality of the results. Table 16.1 contains the information about the flooded area computed by the 1D-2D coupled models proposed as well as by the 2D model. The relative error (less than 3%) shows that the coupled schemes are able to approximate well the results achieved by the 2D model.

16.5.2 Unsteady flow

From a 75 m^3/s steady state, unsteady calculations were performed by assuming a triangular shape inlet discharge hydrograph rising to 1300 m^3/s in 12 hours. The predicted flood inundations at t=50000 s are shown in Figure 16.35, computed with a fully 2D model (upper), by the FC 1D-2D model (middle) and also calculated with the proposed RCE 1D-2D model (lower).

The numerical results indicate that there is a good adjustment between the fully 2D model and both the coupled model, respecting mainly the wet and dry zones. Small differences are observed in the first part of the river reach, upstream the island, where the flooded zone predicted by the fully 2D model is larger than that provided by the FC and the RCE 1D-2D coupled models. The overall color scale used shows a good agreement not only along the river bed but also over the floodplain.

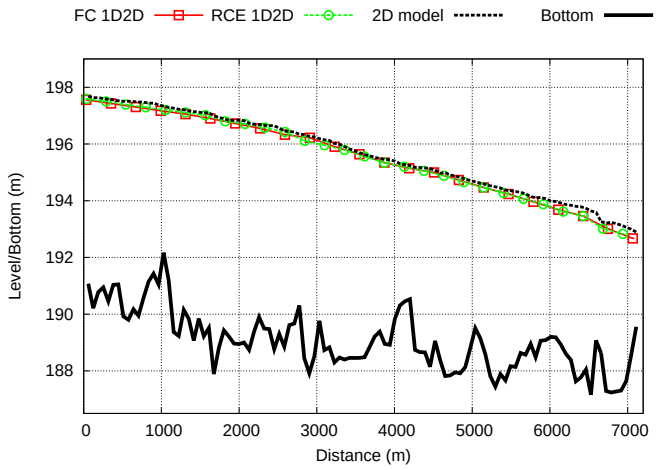

Figure 16.34: Test case 5: longitudinal profile along the river bed for the unsteady case at t=50000 s

The longitudinal profile (see Figure 16.34) as well as the flooded area predicted by each model (Table 16.1) display the quality of the results obtained by the coupled

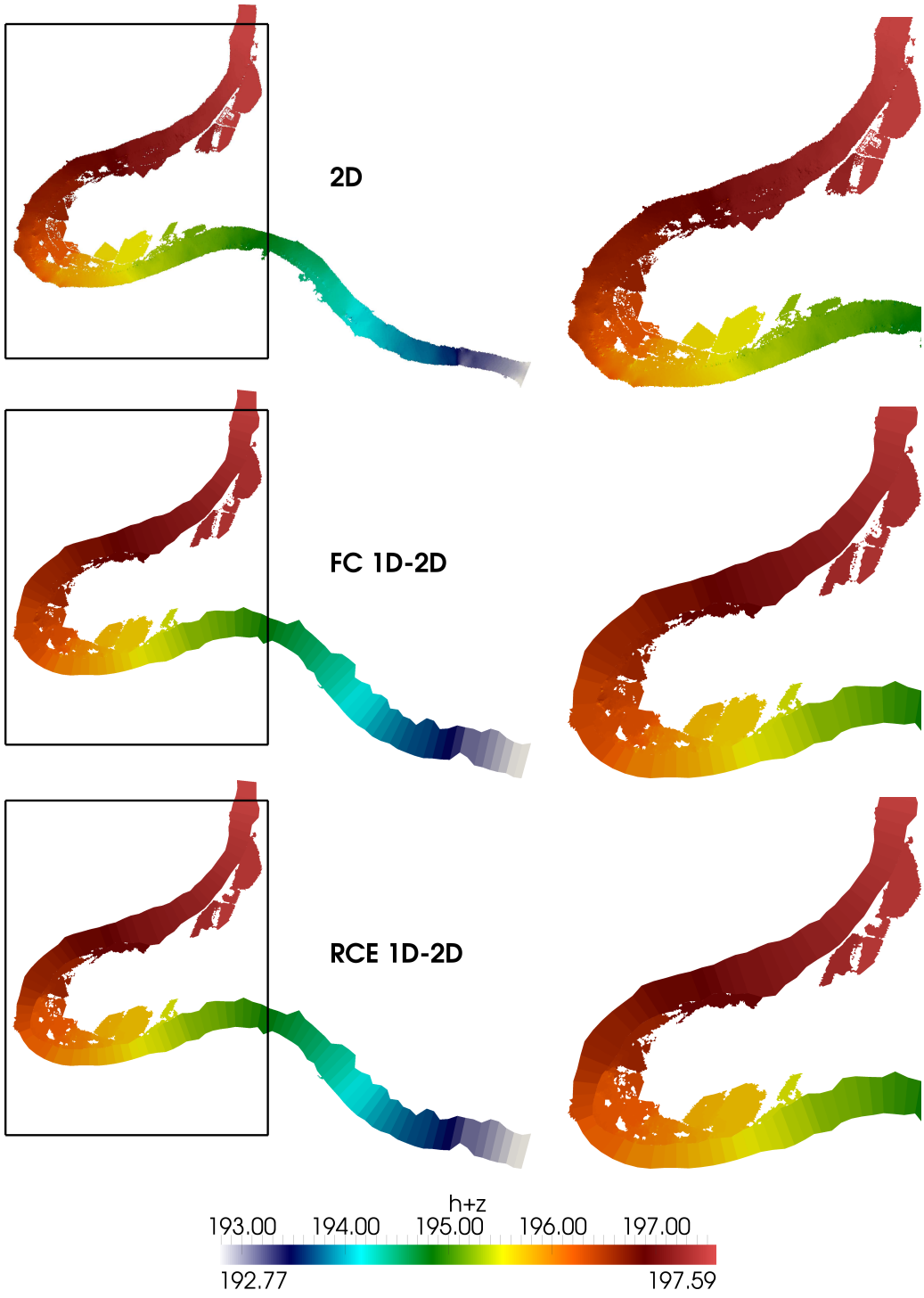

Figure 16.35: Test case 5: Numerical simulation of a unsteady flow in the Ebro river. Flooded area in the fully 2D model (upper), in the FC 1D-2D model (middle) and in the RCE 1D-2D model (lower) at t=50000 s

model in comparison with the complete 2D model. Both coupled models are able to reproduce all kind of flow situations and predict faithfully the water level surface as presented before hence it may be a 2D model overestimation of the flooding due to the spatial discretization of the river bed bathymetry.

	Flooded area (m^2) 2D	Flooded area (m^2) / Relative error (%) FC 1D-2D	Flooded area (m^2) / Relative error (%) RCE 1D-2D
Steady	9.60089e+05	9.81052e+05 / 2.18%	9.81622e+05 / 2.24%
Unsteady	1.47066e+06	1.48577e+06 / 1.02%	1.49124e+06 / 1.39%

Table 16.1: Test case 5: Flooded area computed by the FC and RCE 1D-2D coupled models and the 2D model and relative error

16.6 Test case 6: Flooding event in the Tiber river with solute transport

Developments in GIS software and in computer processing allow the use of high-resolution DEMs in hydraulic simulations. Hydraulic variables like flow depth and velocity components can be highly variable over small spatial scales and, as such, are extremely sensitive to terrain discretization in topography-based simulation models. Small errors in specifying bed elevation may have a large impact on the prediction of the flooding area.

The data available for this study were a cartography (scale 1:10000) covering the bottom of the valley together with aerial photographs. Moreover a 2 m x 2 m resolution digital elevation model (DEM) was also available together with 600 cross sections coming from land surveys. The topography used by the authors was obtained integrating the DEM with the land surveyed cross sections (10 for the considered reach displaced in orange in Figure 16.36) in order to describe correctly the floodplain and the main channel.

The geometric description of the river channel and surrounding topography was

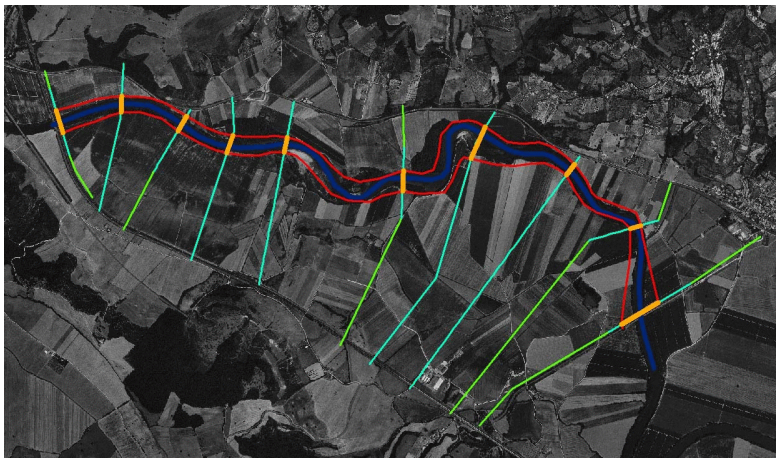

Figure 16.36: Aerial photograph of Ponzano area with original and interpolated 1D cross sections

essential for creating a computational mesh consistent with the surface of the study area. It can significantly affect the numerical results. In this case, first, the banklines were delineated to separate the river from the flooding area. Then, the 2D domain was built in order to guarantee the best match between land surveyed cross section in the river and DEM extracted cross sections. As an example, Figure 16.37 shows a particular 1D cross section coming from the land survey and the corresponding one extracted by the modified DEM. Since the comparison is reasonable, the modified DEM was used in this work.

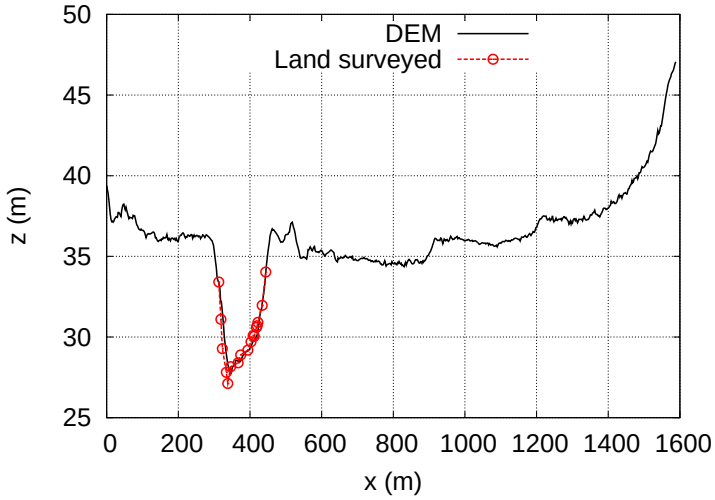

Figure 16.37: Comparison between the land surveyed and the DEM reconstructed extraction for section 5 in Ponzano reach

16.6.1 Tiber river flood

Tiber river is one of the most important Italian rivers: the catchment area at Rome is about 17000 km^2. It is 406 km long, flowing from the Apennine Mountains to the Tyrrhenian Sea. Its mean discharge is 267 m^3/s while the discharge for a return period of 200 years is 3200 m^3/s. For this study, a 6×2 km reach is considered, which will be referred to in what follows as the Ponzano reach. The flood here simulated occurred between the 27th of November and the 1st of December 2005. Its estimated return period is 50 years. The maximum discharge in the Ponzano reach was about 1440 m^3/s and the surrounding area was almost completely flooded. As a result, several measurements were registered at different sections. Figure 16.38 shows the inflow hydrograph (left) imposed as upstream boundary condition. The recorded evolution in time of the water level surface as well as the discharge at the outlet section were used to build the downstream boundary condition in the form of a gauging curve (see Figure 16.38, right).

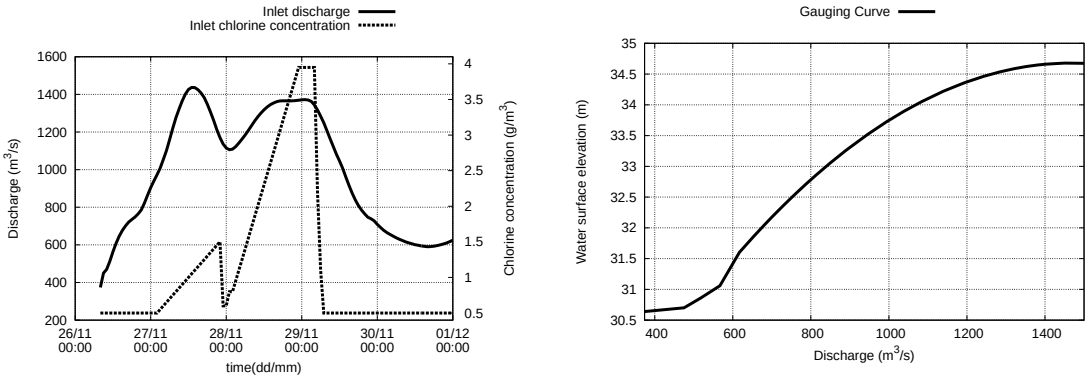

Figure 16.38: Ponzano reach: upstream (left) and downstream (right) boundary conditions

In order to simulate a passive solute transport (chlorine) associated to this particular flooding event, the solute concentration is also introduced as boundary condition, mimicking the dump of a substance upstream the river reach of study. The evolution in time of this solute concentration is also plotted in Figure 16.38 (left).

The water surface elevation was measured in two sections in the Ponzano reach (S1 and S2), located inside the main channel. Besides the observed data, five probes were selected in order to compare all the proposed numerical models. The location

of sections and probes as well as the topography of the Ponzano reach are shown in Figure 16.39 (left).

Two different Manning coefficients are used: 0.035 $m/s^{1/3}$ for the main channel and 0.0446 $m/s^{1/3}$ for the floodplain (Figure 16.39, right).

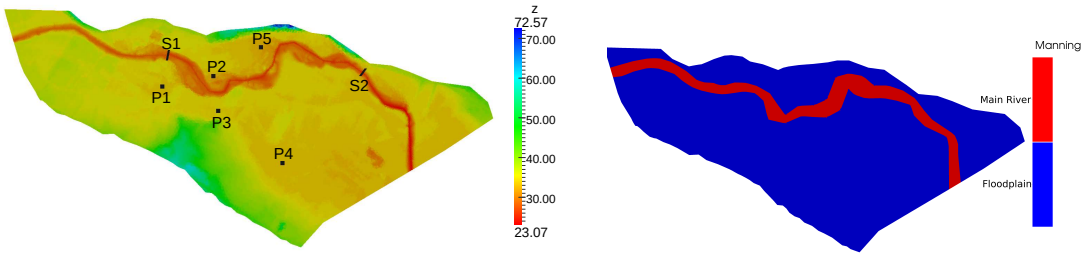

Figure 16.39: Test case 6. Ponzano reach: Topography and location of section and probes (left) and Manning roughness map (right)

For the simulation of this event, two numerical models are used: a fully 2D numerical model and the suggested coupled FC and RCE 1D-2D models. A refined mesh only in the main channel is used as reference, made of 26895 elements while a coarse mesh covers the floodplain in the fully 2D model as well as the 2D sub-domain in the 1D-2D coupled models. The detail of the two meshes used for the computation is displayed in Figure 16.40. Note that the pressure integrals in the 1D model are approximated by means of the integral formulation and the developments explained in part I, section 5.

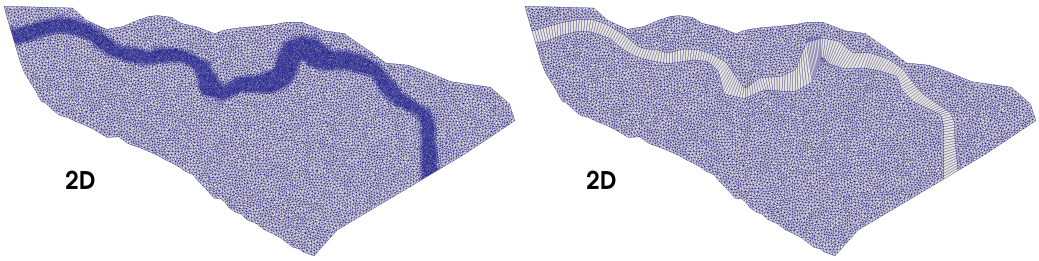

Figure 16.40: Test case 6. Fully 2D mesh (left) and 1D-2D coupled mesh (right)

The recorded water elevations in sections S1 and S2 are compared, in Figure 16.41, with the numerical results on the fully 2D model and with the FC and RCE 1D-2D models.

The numerical models can be also compared by using the information of the evolution in time registered at the probes P1-P5 by each numerical scheme for the water depth

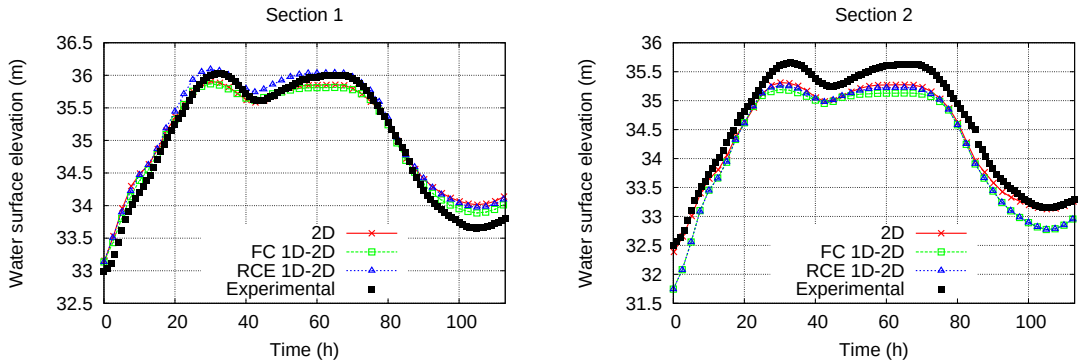

Figure 16.41: Test case 6: Comparison between measured and computed data for sections S1 and S2

(Figure 16.42, left) and for the chlorine concentration (Figure 16.42, right).

As displayed in the previous figures, both the FC and the RCE 1D-2D models and the fully 2D model generate almost the same results. Not only the maximum peaks in water surface elevation are fairly captured in comparison to the measured information but also the peak times are well reproduced and the flooding wave comes almost at the same time in all the models. This behaviour is also observed at probes P1-P5 if compared to the 2D complete model for the water depth and for the solute evolution in time. All the numerical results underestimate the water peaks in section 2 hence it could be an effect of the downstream boundary condition, the Manning roughness coefficient (assumed constant along the main river) or even a bad representation of the bathymetry near this zone.

In general, both the FC and the RCE 1D-2D coupled models achieve reasonable results, compared to those obtained by the fully 2D simulation. In terms of timing they predict similar results at sections S1 and at all the observations points P1-P5. However, the water depth is sometimes underestimated (mainly probe P4). With respect to the chlorine concentration, results are very similar in all the probes excluding P1, in which the solute is accumulated when using the FC and the RCE 1D-2D models.

This analysis is based on local measurements (sections and probes) along the domain. However, the differences can be estimated in terms of inundation maps generated by each numerical model. As an example, two snapshots during the flood at times t=72h and t=113h (final state) are plotted at Figures 16.43 and 16.44.

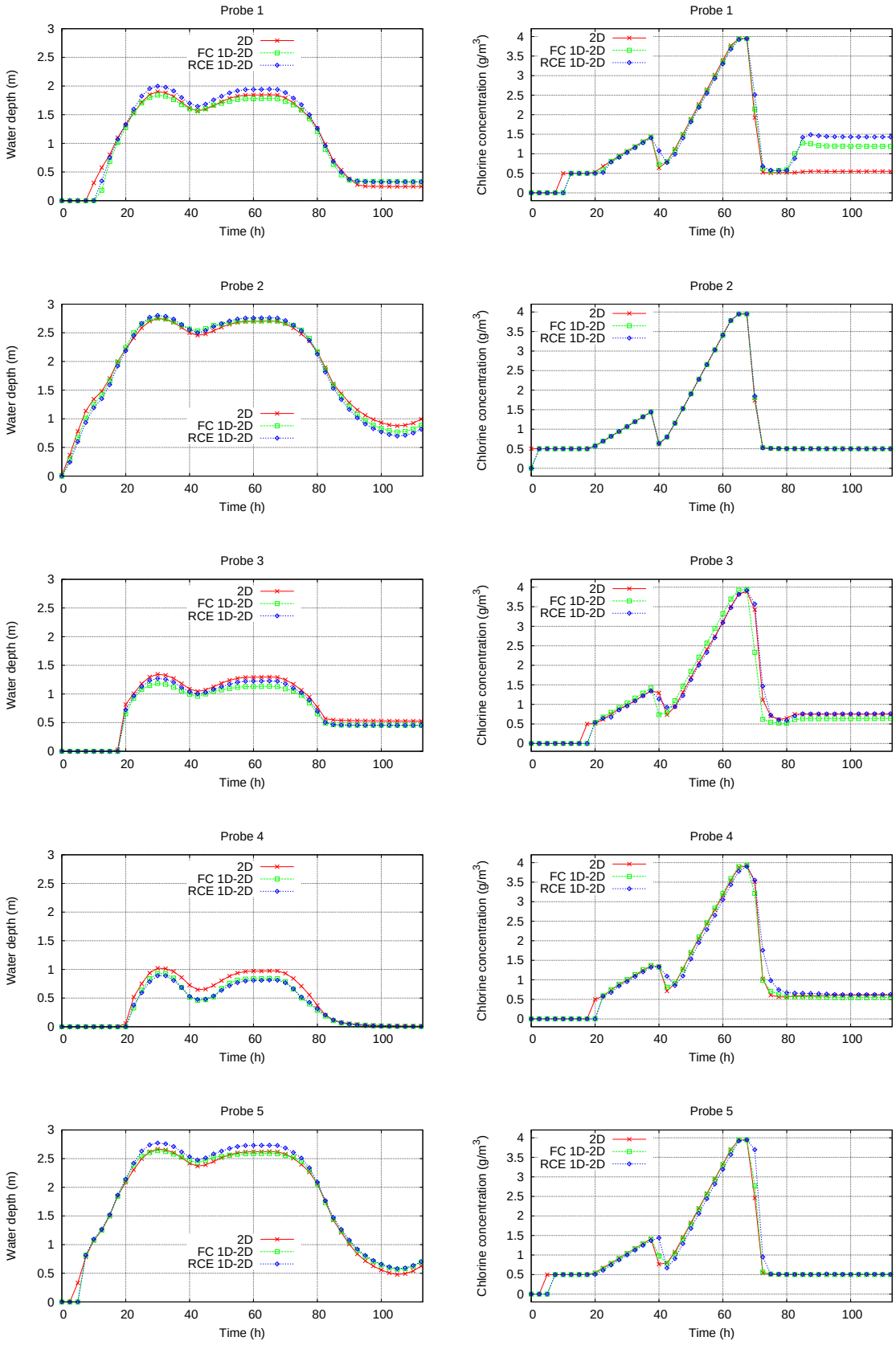

Figure 16.42: Test case 6: Comparison of water depth (left) and chlorine concentration (right) among the different numerical models at probes P1-P5

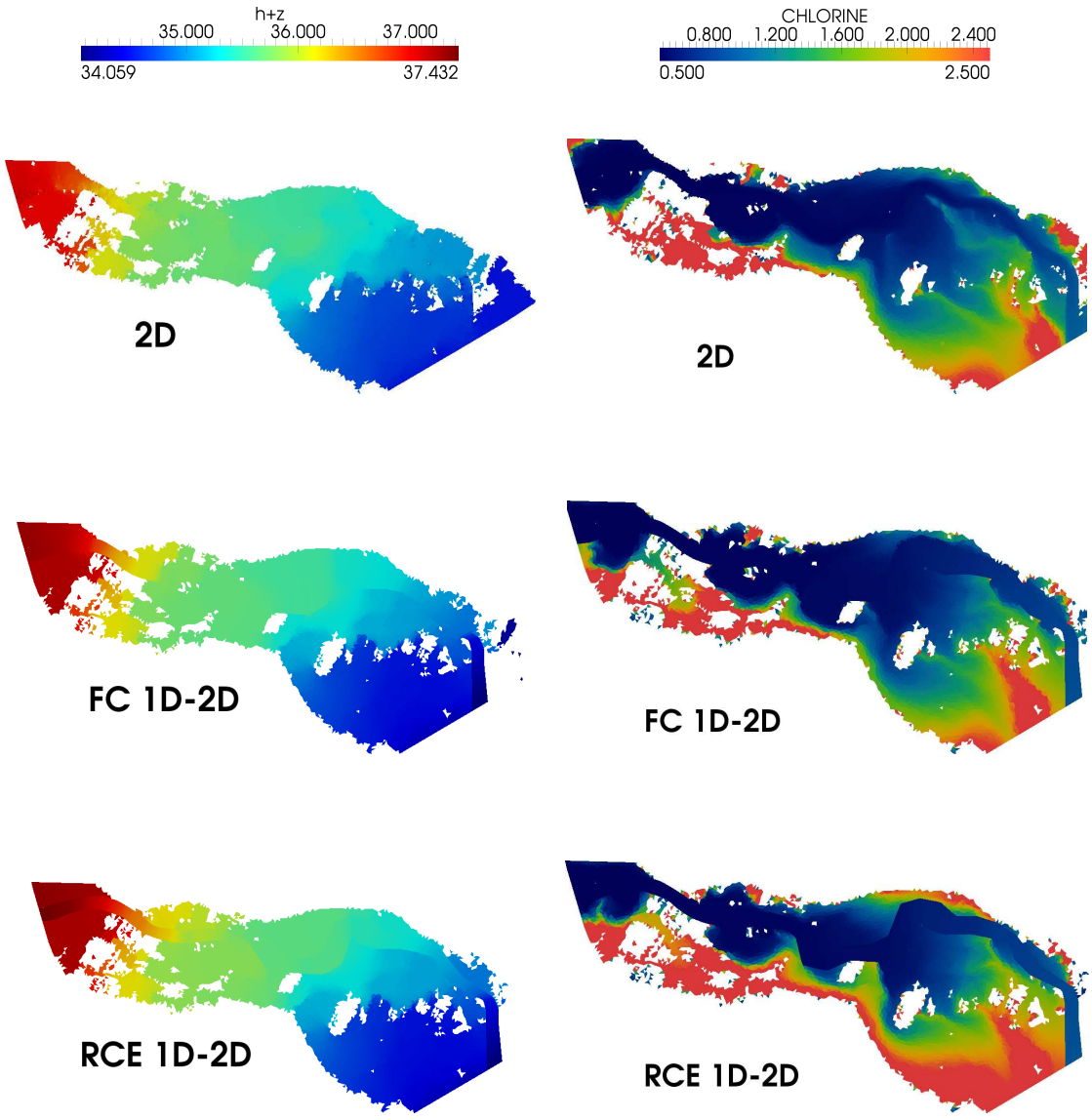

Figure 16.43: Test case 6: Flooded area (left) and solute distribution (right) at time t=72 h, computed by the fully 2D model(upper), FC 1D-2D codel (middle) and RCE 1D-2D model (lower)

As can be observed, the flooding extension is almost well captured by all the schemes presented. Indeed, both coupled schemes are able to reproduce appropriately the overall behaviour of the water surface elevation achieved by the 2D reference solution. However, at the right side of the end of the river reach, there is an area which is flooded by the 2D model and dried by both the coupled models.

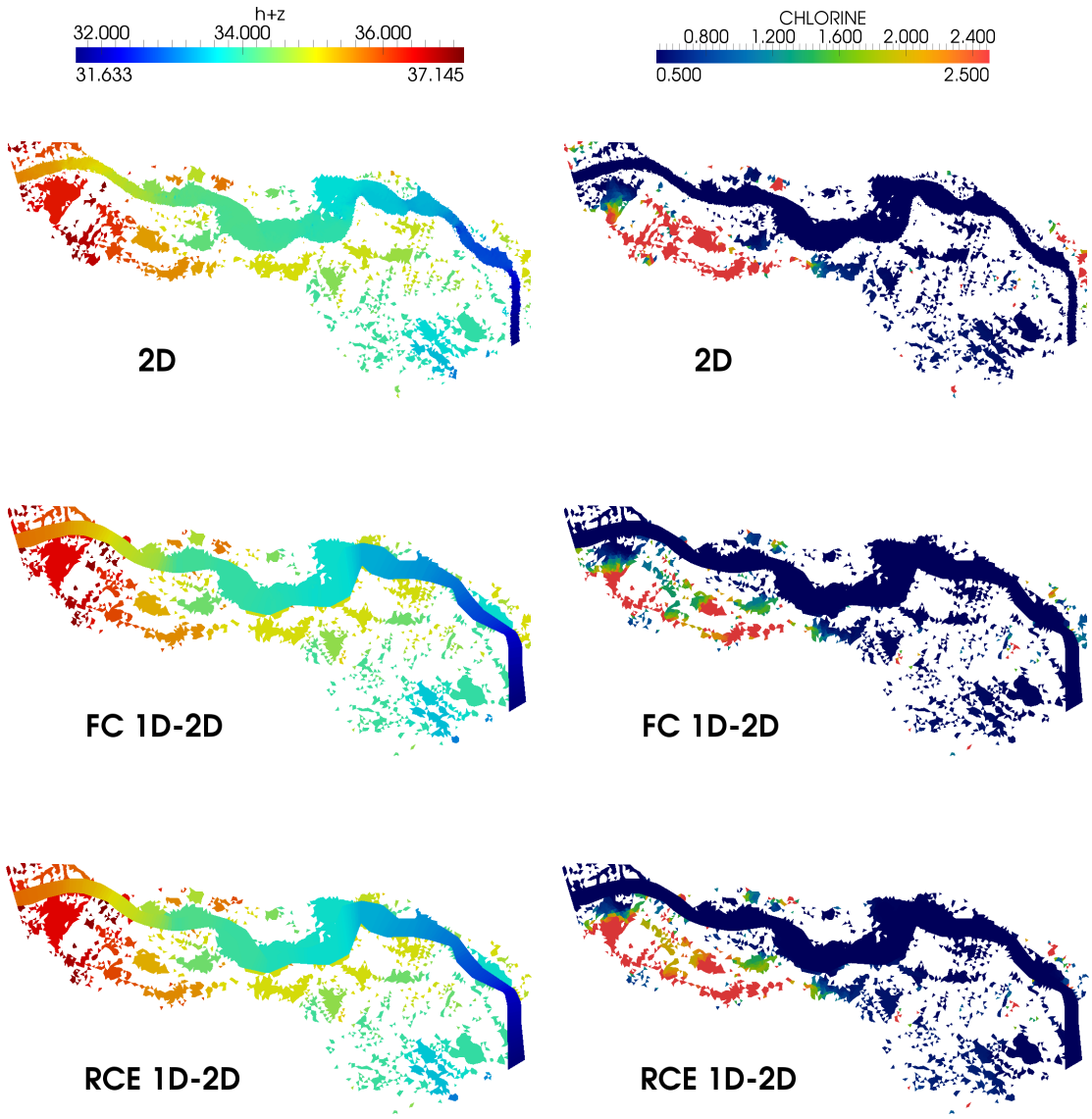

Figure 16.44: Test case 6: Flooded area (left) and solute distribution (right) at time t=113 h, computed by the fully 2D model(upper), FC 1D-2D codel (middle) and RCE 1D-2D model (lower)

Two main factors can be responsible for this: the outlet boundary condition, which is slightly different between the fully 2D model and the coupled 1D-2D models, and the discretization of the river bathymetry in the 2D configuration, which may increase the water level surface in the main river and, as a consequence, may overflow the right bank. Regarding the spatial distribution of the solute concentration, it can be concluded that is also well propagated by using the 1D-2D coupled models, although several regions are partially overestimated, closed to the boundaries.

16.7 Computational time

The previous test cases are useful to test the accuracy of the numerical results achieved by the proposed FC and RCE coupled model. As seen, they are able to approach satisfactorily the results offered by the pure 2D model. However, the 2D model has a clear disadvantage associated to the topography discretization due to the fact that the computational time is governed by the cell sizes. Therefore, a compromise between the CPU time and the topography representation must be achieved. In particular, when dealing with a flood scenario, a wrong representation of the bottom bathymetry in the river bed entails wrong results concerning the extension of the flooding. Therefore, a fine discretization should be considered in order to ensure reasonable results with the extra cost in terms of CPU time.

The 1D-2D coupled models eliminates this fine discretization associate to the river bed topography since the 1D model is able to reproduce it very accurately, requiring less information and saving computational time. Not only a lot of cells which discretized the river bed are discarded for the 2D domain, but also they are possibly the cells which limited the time step size. Therefore, the computational time should be reduced 'a priori' when dealing with a 1D-2D coupled model.

In order to compare the CPU time consumed, the Table 16.2 is attached where each test case enclosed its computational time is analysed for the simulations computed by the fully 2D model, by the FC 1D2D model and also by the RCE 1D-2D model presented before. The maximum triangle cell area constraint in the fully 2D model has been chosen equal from that of the 2D domain of the coupled model for each test case hence the uncertainty related with the choice of different computational cell sizes is eliminated. All the simulations were carried out in a Intel Core 2 Duo Quad Core Q9550 2.83 GHz.

The results highlight a computational gain achieved by using the proposed coupled model. Test case 1 is the less representative in terms of speed-up due to the simulation time (only 10 seconds) as well as the number of cells in the fully 2D model in comparison with the coupled models. However, when dealing with test cases 2, 3 and 4, the speed-up reached by the both coupled models is not inconsiderable at all. In test case 4, involving the transport of two substances, the performance of both coupled models decreases in terms of speed-up with respect to the complete 2D model. On the other hand, in a real configuration (test case 5) where the 1D

Test case		Fully 2D Time (s)	FC 1D-2D Time (s)	FC 1D-2D Speed-up	RCE 1D-2D Time (s)	RCE 1D-2D Speed-up
1		31	17	1.82	**15**	2.06
2	Steady	66341	**2032**	32.65	2120	31.29
	Unsteady	11155	376	29.66	**369**	30.23
3	Supercritical	38416	966	39.77	**950**	40.43
	Subcritical	32521	**1013**	32.1	1021	32.49
4		39180	1832	21.38	**1496**	26.19
5	Steady	31952	117	273.09	**108**	295.85
	Unsteady	50368	439	114.73	**438**	114.95
6		120223	5231	22.98	**5006**	24.01

Table 16.2: CPU time consumed by the 2D model, the FC 1D-2D model and the RCE 1D-2D model in each test case

model represents only the river bed and the adjacent low-laying areas are covered by a 2D discretization, the gain observed is particularly noticeable, always achieved without essentially loss of accuracy. Test case 6, which involves solute transport achieves a lower gain than the previous test cases due to the discretization in the fully 2D model.

It is worth noting the similarity in terms of computational time between the two strategies proposed to couple the 1D and the 2D models. When the solute transport participates, the FC 1D-2D model increases its computational time with respect to the RCE 1D-2D model.

Chapter 17

Conclusions

Two 1D-2D numerical coupled models built from existing both 1D and 2D models are presented in this work. The implementation of these kind of 1D-2D model seems a good solution to eliminate not only the limitations of the 1D model related with the underlying mathematical hypothesis which introduce some errors when modelling flooding waves over 2D domains, but also the uncertainty in the 2D model associated to the discrete representation of the topography in the river bed. The advantages of representing the main river with a 1D model are conserved, avoiding the required fine discretization when using a fully 2D model. The correct propagation along the floodplain is also guaranteed due to the use of the 2D domain out of the river channel.

Both 1D and 2D models are based on a conservative upwind cell-centered finite volume approach, using the Roe's linearization. A new element of discretization called coupling zone is defined, composed of one 1D cell and a finite number of adjacent 2D triangular cells. This requirement implies a suitable meshing procedure, able to achieve a perfect match between the 1D and the 2D domains that are geometrically coupled.

Two possible strategies to couple both models are presented. The Forced Conservative (FC) 1D-2D model is constructed over the complete conservation property, taking into account the information that leaves each domain. In this approach, two possible coupling techniques are considered. The Only Mass Conservation (OMC) technique is derived from a total mass conservation in the coupling zone. A new common level surface is established from the total water volume existing at the coupling zone. The Mass and Momentum Conservation (MMC) strategy, considered as an extension of the OMC enforces not only a new common level at the coupling zone, but also the velocities u and v in x and y direction coming from a strictly

mass and momentum control. It is important to remark the importance of computing the exact mass and/or momentum conservation, considering the information that crosses the limits of the 1D or 2D domains. Thus, the use of each strategy is not transparent to the boundary conditions of the 1D and the 2D models. The boundary treatment must be revisited and, according to the flow regime, the OMC or MMC strategy must be used to avoid non-physical results. A similar procedure can be done for the solute transport equation: a total solute mass is computed over the coupling zone, which is converted into a common concentration for the 1D and the 2D coupled cells.

On the other hand, another strategy based on the resolution of the Riemann Problem across the coupled edges (RCE) is considered. The solver computes the average values not only at the 1D-1D and the 2D-2D edges as usual, but also at the well-defined 1D-2D edges. Consequently, it is necessary to determine adequate average values at these edges, able to maintain the conservation property in the sense of Roe. For this purpose, the 1D quantities are 'bidimenionalized', that is, converted into 2D quantities that allow to characterize the Riemann Problem at the 1D-2D coupled edge. When dealing with the solute transport equation, the separated strategy used to compute a numerical flux through both the 1D-1D edges and 2D-2D edges explained in part I is also applied to the 1D-2D edges, defining the appropriate variables.

The effectiveness of both FC and RCE 1D-2D models is tested through diverse test cases where the performed numerical results of the coupling models are compared with a fully 2D model as well as with experimental and measured data if existing. It has also been evaluated in two real world configurations, simulating a reach of the Ebro river (Spain) by means of a 1D model connected with the riverside floodplain areas which are covered by a 2D domain, and reproducing the flooding event occurred in the Tiber river (Italy) in 2005, adding the transport of a passive solute. The results achieved by both FC and RCE 1D-2D models are proved to be accurate with respect to those obtained by the fully 2D model.

Finally, the computational gain achieved by the proposed coupled models is analysed in comparison with the CPU time consumed by a complete 2D model. An appreciable speed-up is highlighted.

Conclusiones generales

En este trabajo se han desarrollado métodos numéricos eficientes para la resolución de las ecuaciones de aguas poco profundas unidimensionales (1D) y bidimensionales (2D) con transporte de soluto. Este desarrollo se basa en métodos numéricos existentes de la familia de los esquemas *upwind* explícitos *Godunov* de primer orden, los cuales se han modificado o reinterpretado con el objetivo de conseguir métodos más eficientes, entendida la eficiencia no solo en términos de tiempo de cálculo como en precisión. Destacan tres contribuciones principales: la discretización adecuada de los términos fuente presentes en las ecuaciones de aguas poco profundas (Parte I), el desarrollo y la implementación de modelos *Large Time Step* tanto para las ecuaciones 1D como 2D de aguas poco profundas (Parte II) y el acoplamiento numérico de los modelos 1D y 2D en un modelo acoplado 1D-2D de aguas poco profundas con transporte de soluto (Parte III).

La parte I se concibe como una introducción a las leyes de conservación y a los esquemas sobre los que se basan los desarrollos que se realizan en todo el trabajo. En primer lugar se presentan las formulaciones diferencial e integral para las leyes de conservación mencionadas, haciendo énfasis en el concepto de *Problema de Riemann* y en sus resolución para ecuaciones y sistemas de ecuaciones tanto lineales como no lineales. Igualmente se detalla el esquema numérico de Roe en su versión aumentada, que permite linealizar los sistemas hiperbólicos de ecuaciones con términos fuente y dar una receta para su resolución numérica.

Las ecuaciones de aguas poco profundas, tanto en su versión 1D como 2D, se expresan en forma de sistema hiperbólico de leyes de conservación, con lo que es posible aplicar las técnicas mencionadas anteriormente para su resolución numérica. Asimismo, en este trabajo se adopta una técnica reciente y novedosa para la resolución de la ecuación el transporte de soluto, que permite desacoplarla del sistema hidrodinámico de manera conservativa.

El tratamiento de los términos fuente y de las fronteras seco-mojado en las ecuaciones de aguas poco profundas se aborda en los siguientes capítulos. En primera instancia, los modelos numéricos deben evitar algunas situaciones no físicas como la aparición de calados negativos. Con este propósito y basándonos en las soluciones aproximadas del problema de Riemann en cada pared de cálculo, se propone expresar

matemáticamente estas restricciones físicas con el fin de limitar de alguna manera la "cantidad de termino fuente" cuando las ecuaciones se discretizan. Esto permite distribuir de manera inteligente las contribuciones tanto en fronteras mojado-mojado como en seco-mojado.

En segundo lugar, se presenta una nueva técnica de discretización del término fuente de fondo basada en la formulación integral de las ecuaciones. Esta nueva técnica permite aproximar mejor el flujo en soluciones discontinuas, en donde la formulación diferencial no siempre es válida. Esta aproximación se desarrolla primero para las ecuaciones 1D con sección rectangular constante y se extiende después para geometrías irregulares.

Los avances relacionados con la discretización de los términos fuente se validan mediante diferentes casos test, con y sin solución analítica, en los cuales se evalúan las formulaciones diferencial e integral en caso de fuertes contracciones y expansiones de flujo.

En la parte II se presenta el desarrollo y la implementación para las ecuaciones de aguas poco profundas del esquema *Large Time Step* (LTS). Este esquema permite relajar la condición de estabilidad asociada a los esquemas explícitos (*CFL condition*), consiguiendo pasos de tiempo más grandes y, como consecuencia, una reducción considerable del tiempo de cálculo.

En primer lugar se plantea el esquema propuesto por Leveque para ecuaciones escalares. Las rarefacciones requieren de un tratamiento especial en forma de varias discontinuidades que se propagan a diferentes velocidades para poder representar correctamente su comportamiento. La presencia de los términos fuente se analiza para el caso escalar y se propone una discretización adecuada para el envío correcto de la información en este tipo de esquemas.

De la misma manera se propone la extensión a sistemas de leyes de conservación 1D, aplicando las técnicas descritas para el caso escalar a las ecuaciones 1D de aguas poco profundas y haciendo uso de la linealización de Roe para poder desacoplar el sistema original de ecuaciones. Los términos fuente juegan un papel importante en las ecuaciones mencionadas, por lo que se explora la posibilidad de incluir un limitador dinámico para la elección del número de CFL, permitiendo readaptar esta condición ante la presencia de importantes términos fuente y grandes discontinuidades. Además, se proponen nuevas técnicas para las condiciones de contorno

en estos esquemas LTS.

Posteriormente, se aborda la extensión a ecuaciones o sistemas de ecuaciones bidimensionales y se distinguen dos posibles procedimientos: para mallas cuadradas estructuradas y para mallas triangulares, tanto estructuradas como no estructuradas.

La primera aproximación consiste en resolver las ecuaciones o sistemas de ecuaciones 2D en mallas cuadradas estructuradas aproximándolos por sucesivos problemas 1D (*dimensional splitting*) que se resuelven en las dos direcciones del espacio. Por lo tanto es posible aplicar las técnicas desarrolladas en 1D, tanto para ecuaciones escalares como para sistemas de ecuaciones y conservar los avances relacionados con la discretización de los términos fuente, las condiciones de contorno y la limitación del paso de tiempo en presencia de fuertes discontinuidades.

Después, el esquema LTS se formula para mallas triangulares estructuradas y no estructuradas. El razonamiento anterior para empaquetar y enviar las contribuciones desde cada pared de cálculo tiene que ser redefinido, teniendo en cuenta la información que proporcionan las orientaciones de las direcciones normales de los lados de las celdas así como las longitudes de dichos lados. Además, en mallas no estructuradas, se considerará igualmente la distribución de la información según criterios de áreas.

En los modelos 2D de aguas poco profundas los frentes seco-mojado son extremadamente importantes. Por este motivo se propone una estrategia basada en definir paredes sólidas, a través de las cuales la información no puede pasar y tiene que ser reflejada. Además se formula conceptualmente de la misma manera para los casos de mallas cuadradas y triangulares.

El rendimiento y la precisión de este esquema LTS tanto en configuraciones 1D como 2D se evalúa mediante escenarios diseñados para tal efecto: casos test que cubren diferentes rangos de dificultad y de interacción con condiciones de contorno, términos fuente, frentes seco-mojado y campos de velocidad complejos y variables en espacio y tiempo. El esquema LTS no sólo mantiene el carácter conservativo sino que además demuestra tener la misma robustez e igual o mayor precisión en los resultados considerando no obstante una reducción muy importante en el número de operaciones efectuadas. Esto da como resultado una solución mucho más económica en términos computacionales y más precisa en términos numéricos.

Por último, se presenta en la parte III el acoplamiento de los modelos 1D y 2D de

las aguas poco profundas. La implementación de este tipo de modelos acoplados 1D-2D se demuestra como una buena solución ya que elimina no solo las limitaciones relacionadas con los modelos 1D y sus errores cuando se modelan llanuras de inundación, sino también la incertidumbre asociada a la representación discreta de la batimetría del río del modelo 2D. Por ello conserva las ventajas de ambos modelos, permitiendo además acelerar considerablemente el tiempo de cálculo.

En este apartado se construyen dos modelos acoplados 1D-2D, ambos basados en la propiedad conservativa. Los dos procedimientos requieren de un proceso de mallado adecuado para permitir que cada celda de cálculo 1D se acople con un número exacto de celdas 2D.

El modelo *Forced-Conservative (FC)* se construye teniendo en cuenta la información que sale de ambos modelos e imponiendo cantidades constantes en las zonas de acoplamiento. Para ello, se proponen dos posibles ténicas: *Only Mass Conservation (OMC)*, basada en la conservación de la masa y en la que se impone un nivel común en la zona de acoplamiento y *Mass and Momentum Conservation (MMC)*, considerada como una extensión de la primera, en la cual se impone, además de un nivel común, unas velocidades promedio comunes en la zona de acoplamiento. Se propone un procedimiento similar para la ecuación del transporte de soluto, definiendo una concentración promedio en la zona de acoplamiento. Las condiciones de contorno están muy presentes en este modelo acoplado y la decisión de imponer una u otra estrategia vendrá condicionada por el régimen de flujo (subcrítico o supercrítico) y su relación con las condiciones de contorno en ambos modelos.

Por otra parte, se presenta el modelo *Riemann Coupled Edges (RCE)*, basado en la definición del problema de Riemann en las paredes 1D-2D y en la posterior resolución de éste con las técnicas numéricas explicadas anteriormente. Para ello, las cantidades provenientes del modelo 1D se bidimensionalizan, es decir, se convierten en cantidades promediadas del modelo 2D para poder caracterizar el problema de Riemann en la pared de cálculo. La ecuación de transporte de soluto puede ser discretizada de la misma manera, definiendo apropiadamente un flujo numérico en las paredes de cálculo acopladas 1D-2D.

La precisión y el rendimiento de los modelos acoplados propuestos en este trabajo se compara mediante diferentes casos test con datos experimentales y con modelos complemente bidimensionales, que se toman como solución de referencia en ausencia

de datos medidos. Los modelos acoplados 1D-2D se demuestran precisos, proporcionando resultados muy similares a los conseguidos por los modelos bidimensionales y obteniendo además, una ganancia computacional notable. Esto permite pensar en la utilización de estos modelos acoplados 1D-2D como herramienta potente y fiable para la simulación de flujo de inundaciones.

Bibliography

[1] Aggett, G. and Wilson, J. 2009. Creating and coupling a high-resolution DTM with a 1-d hydraulic model in a GIS for scenario-based assessment of avulsion hazard in a gravel-bed river. *Geomorphology 113,* 1-2, 21 – 34. Understanding earth surface processes from remotely sensed digital terrain models.

[2] Aizinger, V. and Dawson, C. 2002. A discontinuous galerkin method for two-dimensional flow and transport in shallow water. *Advances in Water Resources 25,* 1, 67–84.

[3] Alcrudo, F. and Benkhaldoun, F. 2001. Exact solutions to the riemann problem of the shallow water equations with a bottom step. *Computers & Fluids 30,* 6, 643 – 671.

[4] Alcrudo, F. and Garcia-Navarro, P. 1993. High-resolution godunov-type scheme in finite volumes for the 2d shallow-water equations. *International Journal for Numerical Methods in Fluids 16,* 6, 489–505.

[5] Anastasiou, K. and Chan, C. 1997. Solution of the 2d shallow water equations using the finite volume method on unstructured triangular meshes. *International Journal for Numerical Methods in Fluids 24,* 11, 1225–1245.

[6] Audusse, E., Bouchut, F., Bristeau, M.-O., Klein, R., and Perthame, B. 2004. A fast and stable well-balanced scheme with hydrostatic reconstruction for shallow water flows. *SIAM J. Sci. Comput. 25,* 6 (June), 2050–2065.

[7] Begnudelli, L. and Sanders, B. 2006. Unstructured grid finite-volume algorithm for shallow-water flow and scalar transport with wetting and drying. *Journal of Hydraulic Engineering 132,* 4, 371–384.

[8] Bernetti, R., Titarev, V., and Toro, E. 2008. Exact solution of the riemann problem for the shallow water equations with discontinuous bottom geometry. *Journal of Computational Physics 227,* 6, 3212 – 3243.

[9] Bladé, E., Gómez-Valentín, M., Dolz, J., Aragón-Hernández, J., Corestein, G., and Sánchez-Juny, M. 2012. Integration of 1d and 2d finite volume schemes for computations of water flow in natural channels. *Advances in Water Resources 42,* 0, 17 – 29.

[10] Bohorquez, P. and Darby, S. 2008. The use of one- and two-dimensional hydraulic modelling to reconstruct a glacial outburst flood in a steep alpine valley. *Journal of Hydrology 361,* 3-4, 240 – 261.

[11] Bohorquez, P., García-García, F., Pérez-Valera, F., and Martínez-Sánchez, C. 2013. Unsteady two-dimensional paleohydraulic reconstruction of extreme floods over the last 4000 yr in segura river, southeast spain. *Journal of Hydrology 477,* 0, 229 – 239.

[12] Bradford, S. and Sanders, B. 2002. Finite-volume model for shallow-water flooding of arbitrary topography. *Journal of Hydraulic Engineering 128,* 3, 289–298.

[13] Brufau, P., García-Navarro, P., and Vázquez-Cendón, M. E. 2004. Zero mass error using unsteady wetting/drying conditions in shallow flows over dry irregular topography. *International Journal for Numerical Methods in Fluids 45,* 10, 1047–1082.

[14] Brufau, P., Vázquez-Cendón, M. E., and García-Navarro, P. 2002. A numerical model for the flooding and drying of irregular domains. *International Journal for Numerical Methods in Fluids 39,* 3, 247–275.

[15] Bukreev, V., Gusev, A., and Ostapenko, V. 2003. Breakdown of a discontinuity of the free fluid surface over a bottom step in a channel. *Fluid Dynamics 38,* 6, 889–899.

[16] Burguete, J. and García-Navarro, P. 2001. Efficient construction of high-resolution tvd conservative schemes for equations with source terms: application to shallow water flows. *International Journal for Numerical Methods in Fluids 37,* 2, 209–248.

[17] Burguete, J., García-Navarro, P., and Murillo, J. 2008. Friction term discretization and limitation to preserve stability and conservation in the 1d

shallow-water model: Application to unsteady irrigation and river flow. *International Journal for Numerical Methods in Fluids 58,* 4, 403–425.

[18] Burguete, J. and García-Navarro, P. 2004a. Implicit schemes with large time step for non-linear equations: application to river flow hydraulics. *International Journal for Numerical Methods in Fluids 46,* 6, 607–636.

[19] Burguete, J. and García-Navarro, P. 2004b. Improving simple explicit methods for unsteady open channel and river flow. *International Journal for Numerical Methods in Fluids 45,* 2, 125–156.

[20] Burguete, J., García-Navarro, P., and Murillo, J. 2006. Numerical boundary conditions for globally mass conservative methods to solve the shallow-water equations and applied to river flow. *International Journal for Numerical Methods in Fluids 51,* 6, 585–615.

[21] Canestrelli, A., Dumbser, M., Siviglia, A., and Toro, E. F. 2010. Well-balanced high-order centered schemes on unstructured meshes for shallow water equations with fixed and mobile bed. *Advances in Water Resources 33,* 3, 291 – 303.

[22] Castellarin, A., Domeneghetti, A., and Brath, A. 2011. Identifying robust large-scale flood risk mitigation strategies: A quasi-2d hydraulic model as a tool for the po river. *Physics and Chemistry of the Earth, Parts A/B/C 36,* 7-8, 299 – 308. Recent Advances in Mapping and Modelling Flood Processes in Lowland Areas.

[23] Castro, M., Ferreiro, A. F., García-Rodríguez, J., González-Vida, J., Macías, J., Parés, C., and Vázquez-Cendón, M. E. 2005. The numerical treatment of wet/dry fronts in shallow flows: application to one-layer and two-layer systems. *Mathematical and Computer Modelling 42,* 3-4, 419 – 439.

[24] Castro, M., Gallardo, J. M., and Parés, C. 2006. High order finite volume schemes based on reconstruction of states for solving hyperbolic systems with nonconservative products. applications to shallow-water systems. *Mathematics of computation 75*, 1103–1134.

[25] Casulli, V. 1990. Semi-implicit finite difference methods for the two-dimensional shallow water equations. *Journal of Computational Physics 86,* 1, 56 – 74.

[26] Casulli, V. 2009. A high-resolution wetting and drying algorithm for free-surface hydrodynamics. *International Journal for Numerical Methods in Fluids 60,* 4, 391–408.

[27] Casulli, V. and Cattani, E. 1994. Stability, accuracy and efficiency of a semi-implicit method for three-dimensional shallow water flow. *Computers & Mathematics with Applications 27,* 4, 99 – 112.

[28] Casulli, V. and Cheng, R. T. 1992. Semi-implicit finite difference methods for three-dimensional shallow water flow. *International Journal for Numerical Methods in Fluids 15,* 6, 629–648.

[29] Casulli, V. and Zanolli, P. 2005. High resolution methods for multidimensional advection-diffusion problems in free-surface hydrodynamics. *Ocean Modelling 10,* 1-2 SPEC. ISS., 137–151.

[30] Cea, L., Puertas, J., and Vázquez-Cendón, M.-E. 2007. Depth averaged modelling of turbulent shallow water flow with wet-dry fronts. *Archives of Computational Methods in Engineering 14,* 3, 303–341.

[31] Cobby, D. M., Mason, D. C., Horritt, M. S., and Bates, P. D. 2003. Two-dimensional hydraulic flood modelling using a finite-element mesh decomposed according to vegetation and topographic features derived from airborne scanning laser altimetry. *Hydrological Processes 17,* 10, 1979–2000.

[32] Courant, R., Friedrichs, K., and Lewy, H. 1967. On the partial difference equations of mathematical physics. *IBM J. Res. Dev. 11,* 2 (March), 215–234.

[33] Cozzolino, L., Morte, R. D., Covelli, C., Giudice, G. D., and Pianese, D. 2011. Numerical solution of the discontinuous-bottom shallow-water equations with hydrostatic pressure distribution at the step. *Advances in Water Resources 34,* 11, 1413 – 1426.

[34] Crnković, B., Crnjarić-Zic, N., and Kranjcević, L. 2009. Improvements of semi-implicit schemes for hyperbolic balance laws applied on open channel flow equations. *Computers & Mathematics with Applications 58,* 2, 292 – 309.

[35] Cunge, J., Holly, F., and Verwey, A. 1980. *Practical aspects of computational river hydraulics.* Monographs and surveys in water resources engineering. Pitman Advanced Publishing Program.

[36] Dawson, C., Westerink, J., Feyen, J., and Pothina, D. 2006. Continuous, discontinuous and coupled discontinuous-continuous galerkin finite element methods for the shallow water equations. *International Journal for Numerical Methods in Fluids 52,* 1, 63–88.

[37] Delis, A., Nikolos, I., and Kazolea, M. 2011. Performance and comparison of cell-centered and node-centered unstructured finite volume discretizations for shallow water free surface flows. *Archives of Computational Methods in Engineering 18,* 1, 57–118.

[38] Dhondia, J. and Stelling, G. 2002. Application of one-dimensional-two-dimensional integrated hydraulic model for flood simulation and damage assessment. *Hydroinformatics 2002: Proceedings of the Fifth International Conference on Hydroinformatics Model Development and Data Management 1*, 265–276.

[39] Di Baldassarre, G., Castellarin, A., Montanari, A., and Brath, A. 2009. Probability-weighted hazard maps for comparing different flood risk management strategies: a case study. *Natural Hazards 50,* 3, 479–496.

[40] Doswell, C. A. 1984. A kinematic analysis of frontogenesis associated with a nondivergent vortex. *Journal of the atmospheric sciences 41,* 7, 1242–1248.

[41] Dumbser, M., Castro, M., Parés, C., and Toro, E. F. 2009. ADER schemes on unstructured meshes for nonconservative hyperbolic systems: Applications to geophysical flows. *Computers & Fluids 38,* 9, 1731 – 1748.

[42] Dumbser, M. and Casulli, V. 2013. A staggered semi-implicit spectral discontinuous galerkin scheme for the shallow water equations. *Applied Mathematics and Computation 219,* 15, 8057 – 8077.

[43] Dumbser, M. and Toro, E. F. 2011. A simple extension of the osher riemann solver to non-conservative hyperbolic systems. *J. Sci. Comput. 48,* 1-3 (July), 70–88.

[44] E. Miglio, S. P. and Saleri, F. 2005. Model coupling techniques for free-surface flow problems: Part i. *Nonlinear Analysis: Theory, Methods & Applications 63,* 5-7, e1885 – e1896. Invited Talks from the Fourth World Congress of Nonlinear Analysis (WCNA 2004).

[45] Fernández-Nieto, E., Marin, J., and Monnier, J. 2010. Coupling superposed 1d and 2d shallow-water models: Source terms in finite volume schemes. *Computers & Fluids 39,* 6, 1070 – 1082.

[46] Finaud-Guyot, P., Delenne, C., Guinot, V., and Llovel, C. 2011. 1d-2d coupling for river flow modeling. *Comptes Rendus Mécanique 339,* 4, 226 – 234.

[47] Gallardo, J. M., Parés, C., and Castro, M. 2007. On a well-balanced high-order finite volume scheme for shallow water equations with topography and dry areas. *Journal of Computational Physics 227,* 1, 574 – 601.

[48] Gallouët, T., Hérard, J.-M., and Seguin, N. 2003. Some approximate godunov schemes to compute shallow-water equations with topography. *Computers & Fluids 32,* 4, 479 – 513.

[49] García-Navarro, P. and Playán, E. 2008. *Numerical Modelling of Hydrodynamics for Water Resources: Proceedings of the International Workshop on Numerical Modelling of Hydrodynamics for Water Resources (Zaragoza, Spain, 18-21 June 2007).* Balkema-proceedings and monographs in engineering, water, and earth sciences. Taylor & Francis.

[50] García-Navarro, P. and Vázquez-Cendón, M. E. 2000. On numerical treatment of the source terms in the shallow water equations. *Computers & Fluids 29,* 8, 951–979.

[51] Gejadze, I. and Monnier, J. 2007. On a 2d 'zoom' for the 1d shallow water model: Coupling and data assimilation. *Computer Methods in Applied Mechanics and Engineering 196,* 45-48, 4628 – 4643.

[52] George, D. L. 2008. Augmented riemann solvers for the shallow water equations over variable topography with steady states and inundation. *Journal of Computational Physics 227,* 6, 3089 – 3113.

[53] Godlewski, E. and Raviart, P. 1996. *Numerical Approximation of Hyperbolic Systems of Conservation Laws.* Applied mathematical sciences. Springer-Verlag.

[54] Godunov, S. K. 1959. A difference method for numerical calculation of discontinuous solutions of the equations of hydrodynamics. *Mat. Sb. (N.S.) 47,* 271–306.

[55] Gregory, M., Walker, B., Yi, S., Cunningham, B., and Kjelds, J. *Case Studies in Automated Floodplain Mapping*, Chapter 34, pp. 367–375.

[56] Han, K.-Y., Lee, J.-T., and Park, J.-H. 1998. Flood inundation analysis resulting from levee-break. *Journal of Hydraulic Research 36,* 5, 747–759.

[57] Harten, A. 1986. On a large time-step high resolution scheme. *Math. Comput. 46,* 174 (April), 379–399.

[58] Heniche, M., Secretan, Y., Boudreau, P., and Leclerc, M. 2000. A two-dimensional finite element drying-wetting shallow water model for rivers and estuaries. *Advances in Water Resources 23,* 4, 359–372.

[59] Hervouet, J.-M. 2007. *Hydrodynamics of Free Surface Flows: Modelling with the finite element method.*

[60] Hólm, E. 1993. *A Fully Two-dimensional, Non-oscillatory Advection Scheme for Momentum and Scalar Transport Equations.* Report (Stockholms universitet. Meteorologiska institutionen). University of Stockholm, Department of Meteorology.

[61] Horritt, M. S. and Bates, P. D. 2001. Predicting floodplain inundation: raster-based modelling versus the finite-element approach. *Hydrological Processes 15,* 5, 825–842.

[62] Hou, J., Liang, Q., Simons, F., and Hinkelmann, R. 2013. A 2d well-balanced shallow flow model for unstructured grids with novel slope source term treatment. *Advances in Water Resources 52,* 0, 107 – 131.

[63] Hou, J., Simons, F., and Hinkelmann, R. 2013. A new tvd method for advection simulation on 2d unstructured grids. *International Journal for Numerical Methods in Fluids 71,* 10, 1260–1281.

[64] Hou, J., Simons, F., Mahgoub, M., and Hinkelmann, R. 2013. A robust well-balanced model on unstructured grids for shallow water flows with wetting and drying over complex topography. *Computer Methods in Applied Mechanics and Engineering 257,* 0, 126 – 149.

[65] Hubbard, M. and Garcia-Navarro, P. 2000. Flux difference splitting and the balancing of source terms and flux gradients. *Journal of Computational Physics 165,* 1, 89 – 125.

[66] Johnson, L., Richards, C., Host, G., and Arthur, J. 1997. Landscape influences on water chemistry in midwestern stream ecosystems. *Freshwater Biology 37,* 1, 193–208.

[67] Kreiss, H.-O. 1970. Initial boundary value problems for hyperbolic systems. *Communications on Pure and Applied Mathematics 23,* 3, 277–298.

[68] Kuiry, S., Sen, D., and Bates, P. 2010. Coupled 1d-quasi-2d flood inundation model with unstructured grids. *Journal of Hydraulic Engineering 136,* 8, 493–506.

[69] LeFloch, P. G. and Thanh, M. D. 2007. The riemann problem for the shallow water equations with discontinuous topography. *Communications in Mathematical Sciences 5,* 4 (12), 865–885.

[70] Leveque, R. 1982. Large time step shock-capturing techniques for scalar conservation laws. *SIAM Journal on Numerical Analysis 19,* 6, 1091–1109.

[71] LeVeque, R. 1985. A large time step generalization of godunov's method for systems of conservation laws. *SIAM Journal on Numerical Analysis 22,* 6, 1051–1073.

[72] LeVeque, R. 2002. *Finite Volume Methods for Hyperbolic Problems.* Cambridge Texts in Applied Mathematics. Cambridge University Press.

[73] Liang, Q. 2010. Flood simulation using a well-balanced shallow flow model. *Journal of Hydraulic Engineering 136,* 9, 669–675.

[74] Liang, Q. and Borthwick, A. G. 2009. Adaptive quadtree simulation of shallow flows with wet-dry fronts over complex topography. *Computers & Fluids 38,* 2, 221 – 234.

[75] Liang, Q. and Marche, F. 2009. Numerical resolution of well-balanced shallow water equations with complex source terms. *Advances in Water Resources 32,* 6, 873 – 884.

[76] Lin, B., Wicks, J., Falconer, R., and Adams, K. 2006. Integrating 1d and 2d hydrodynamic models for flood simulation. *Proceedings of the ICE - Water Management 159*, 19–25(6).

[77] Liu, P., Yeh, H., and Synolakis, C. 2008. *Advanced Numerical Models for Simulating Tsunami Waves and Runup.* Advances in coastal and ocean engineering. World Scientific.

[78] MacDonald, I. 1996. *Analysis and Computation of Steady Open Channel Flow.* University of Reading.

[79] MacDonald, I., Baines, M., Nichols, N., and Samuels, P. 1997. Analytic benchmark solutions for open-channel flows. *Journal of Hydraulic Engineering 123,* 11, 1041–1045.

[80] Marin, J. and Monnier, J. 2009. Superposition of local zoom models and simultaneous calibration for 1d-2d shallow water flows. *Mathematics and Computers in Simulation 80,* 3, 547 – 560.

[81] Matsuyama, M. and Tanaka, H. 2001. An experimental study of the highest run-up height in the 1993 hokkaido nansei-oki earthquake tsunami. *U.S. National Tsunami Hazard Mitigation Program Review and International Tsunami Symposium (ITS)Chinese Science Bulletin*, 879–889.

[82] Mattiussi, C. 2000. The finite volume, finite element, and finite difference methods as numerical methods for physical field problems. *Journal of Computational Physics 133*, 289–309.

[83] McMillan, H. K. and Brasington, J. 2007. Reduced complexity strategies for modelling urban floodplain inundation. *Geomorphology 90,* 3-4, 226 –

243. Reduced-Complexity Geomorphological Modelling for River and Catchment Management.

[84] Miglio, E., Perotto, S., and Saleri, F. 2005. Model coupling techniques for free-surface flow problems: Part i. *Nonlinear Analysis: Theory, Methods & Applications 63,* 5-7, e1885 – e1896. Invited Talks from the Fourth World Congress of Nonlinear Analysts (WCNA 2004).

[85] Mignosa, P., Aureli, F., and Tomirotti, M. 1999. Dam-break flows in presence of abrupt bottom variations. *Biennial congress 28th, International Association for Hydraulic Research.*

[86] Morales-Hernández, M., García-Navarro, P., Burguete, J., and Brufau, P. 2013. A conservative strategy to couple 1d and 2d models for shallow water flow simulation. *Computers & Fluids 81,* 0, 26 – 44.

[87] Morales-Hernandez, M., García-Navarro, P., and Murillo, J. 2012. A large time step 1d upwind explicit scheme (CFL > 1): Application to shallow water equations. *Journal of Computational Physics 231,* 19, 6532 – 6557.

[88] Morales-Hernández, M., Hubbard, M. E., and García-Navarro, P. 2014. A 2d extension of a large time step explicit scheme (CFL > 1) for unsteady problems with wet/dry boundaries. *J. Comput. Phys. 263*, 303–327.

[89] Morales-Hernández, M., Murillo, J., and García-Navarro, P. 2013. The formulation of internal boundary conditions in unsteady 2-d shallow water flows: Application to flood regulation. *Water Resources Research 49,* 1, 471–487.

[90] Murillo, J. 2006. *Two-dimensional finite volume numerical models for unsteady free surface flows, solute transport and erosion/deposition processes.* PhD Thesis. University of Zaragoza.

[91] Murillo, J., Burguete, J., Brufau, P., and García-Navarro, P. 2005. Coupling between shallow water and solute flow equations: analysis and management of source terms in 2d. *International Journal for Numerical Methods in Fluids 49,* 3, 267–299.

[92] Murillo, J. and García-Navarro, P. 2010. Weak solutions for partial differential equations with source terms: Application to the shallow water equations. *Journal of Computational Physics 229,* 11, 4327–4368.

[93] Murillo, J. and García-Navarro, P. 2012. Wave riemann description of friction terms in unsteady shallow flows: Application to water and mud/debris floods. *Journal of Computational Physics 231,* 4, 1963 – 2001.

[94] Murillo, J., García-Navarro, P., Brufau, P., and Burguete, J. 2006. Extension of an explicit finite volume method to large time steps (CFL $>$ 1): application to shallow water flows. *International Journal for Numerical Methods in Fluids 50,* 1, 63–102.

[95] Murillo, J., García-Navarro, P., and Burguete, J. 2008. Analysis of a second-order upwind method for the simulation of solute transport in 2d shallow water flow. *International Journal for Numerical Methods in Fluids 56,* 6, 661–686.

[96] Murillo, J. and García-Navarro, P. 2013. Energy balance numerical schemes for shallow water equations with discontinuous topography. *Journal of Computational Physics 236,* 0, 119 – 142.

[97] Murillo, J., García-Navarro, P., Burguete, J., and Brufau, P. 2007. The influence of source terms on stability, accuracy and conservation in two-dimensional shallow flow simulation using triangular finite volumes. *International Journal for Numerical Methods in Fluids 54,* 5, 543–590.

[98] Murillo, J., Latorre, B., and García-Navarro, P. 2012. A riemann solver for unsteady computation of 2d shallow flows with variable density. *Journal of Computational Physics 231,* 14, 4775 – 4807.

[99] Nikolos, I. and Delis, A. 2009. An unstructured node-centered finite volume scheme for shallow water flows with wet/dry fronts over complex topography. *Computer Methods in Applied Mechanics and Engineering 198,* 47-48, 3723 – 3750.

[100] Noelle, S., Pankratz, N., Puppo, G., and Natvig, J. 2006. Well-balanced finite volume schemes of arbitrary order of accuracy for shallow water flows. *Journal of Computational Physics 213,* 2, 474–499.

[101] Noelle, S., Xing, Y., and Shu, C.-W. 2007. High-order well-balanced finite volume weno schemes for shallow water equation with moving water. *Journal of Computational Physics 226,* 1, 29–58.

[102] Norman, M. R., Nair, R. D., and Semazzi, F. H. 2011. A low communication and large time step explicit finite-volume solver for non-hydrostatic atmospheric dynamics. *Journal of Computational Physics 230,* 4, 1567 – 1584.

[103] Parés, C. 2006. Numerical methods for nonconservative hyperbolic systems: a theoretical framework. *SIAM Journal on Numerical Analysis 44,* 1, 300–321.

[104] Parker, J. T. C., Fossum, K. D., and Ingersoll, T. L. 2000. Chemical characteristics of urban stormwater sediments and implications for environmental management, maricopa county, arizona. *Environmental Management 26,* 1, 99–115.

[105] Petaccia, G., Natale, L., Savi, F., Velickovic, M., Zech, Y., and Soares-Frazão, S. 2013. Flood wave propagation in steep mountain rivers. *Journal of Hydroinformatics 15,* 1.

[106] Qian, Z. and Lee, C.-H. 2011. A class of large time step godunov schemes for hyperbolic conservation laws and applications. *Journal of Computational Physics 230,* 19, 7418 – 7440.

[107] Qian, Z. and Lee, C.-H. 2012. On large time step TVD scheme for hyperbolic conservation laws and its efficiency evaluation. *Journal of Computational Physics 231,* 21, 7415 – 7430.

[108] Remo, J. W., Pinter, N., and Heine, R. 2009. The use of retro- and scenario-modeling to assess effects of 100+ years river of engineering and land-cover change on middle and lower mississippi river flood stages. *Journal of Hydrology 376,* 3-4, 403 – 416.

[109] Roe, P. 1981. Approximate riemann solvers, parameter vectors, and difference schemes. *Journal of Computational Physics 43,* 2, 357 – 372.

[110] Roe, P. 1986. A basis for upwind differencing of the two-dimensional unsteady euler equations. *Numerical Methods in Fluid Dynamics II*, 55–80.

[111] Rosatti, G. and Begnudelli, L. 2010. The riemann problem for the one-dimensional, free-surface shallow water equations with a bed step: Theoretical analysis and numerical simulations. *Journal of Computational Physics 229,* 3, 760 – 787.

[112] Sleigh, P., Gaskell, P., Berzins, M., and Wright, N. 1998. An unstructured finite-volume algorithm for predicting flow in rivers and estuaries. *Computers and Fluids 27,* 4, 479–508.

[113] Stelling, G. S. and Duinmeijer, S. P. A. 2003. A staggered conservative scheme for every froude number in rapidly varied shallow water flows. *International Journal for Numerical Methods in Fluids 43,* 12, 1329–1354.

[114] Stoker, J. 1958. *Water Waves : The Mathematical Theory with Applications*, Volume 4. New York: Interscience Publishers, 1957.

[115] Strang, G. 1968. On the construction and comparison of difference schemes. *SIAM J. Numer. Anal. 5*, 506–517.

[116] Tavelli, M. and Dumbser, M. 2014. A high order semi-implicit discontinuous galerkin method for the two dimensional shallow water equations on staggered unstructured meshes. *Applied Mathematics and Computation 234,* 0, 623 – 644.

[117] Toro, E. 2001. *Shock-capturing methods for free-surface shallow flows.* John Wiley.

[118] Toro, E. 2009. *Riemann Solvers and Numerical Methods for Fluid Dynamics: A Practical Introduction.* Springer.

[119] Toro, E. and Garcia-Navarro, P. 2007. Godunov-type methods for free-surface shallow flows: A review. *Journal of Hydraulic Research 45,* 6, 736–751.

[120] Toumi, I. 1992. A weak formulation of roe's approximate riemann solver. *Journal of Computational Physics 102,* 2, 360 – 373.

[121] UK Environment Agency 2010. *Benchmarking of 2D Hydraulic Modelling Packages.* Environment Agency Report. UK Environment Agency.

[122] Vázquez-Cendón, E. 1999. Improved treatment of source terms in upwind schemes for the shallow water equations in channels with irregular geometry. *Journal of Computational Physics 148,* 2, 497 – 526.

[123] Vázquez-Cendón, E. 2011. *Lecture Notes on Numerical Methods for Hyperbolic Equations: Short Course Book*. Balkema book. Taylor & Francis Group.

[124] Villanueva, I. and Wright, N. G. 2006. Linking riemann and storage cell models for flood prediction. *Proceedings of the ICE - Water Management 159*, 27–33(6).

[125] Viseu, T., Franco, A., and Almeida, A. Numerical and computational results of the 2-d biplan model. *4th Meeting of the Working Group on Dam-Break Modelling (1st CADAM Meeting)* 3.

[126] Vreugdenhil, C. 1994. *Numerical Methods for Shallow-Water Flow*. NATO Asi Series. Series C, Mathematical and Physical Science. Springer.

[127] Warzyński, A. 2013. *Runge-Kutta Residual Distribution Schemes*. PhD. Thesis. University of Leeds.

[128] Wissmar, R. C. and Beschta, R. L. 1998. Restoration and management of riparian ecosystems: a catchment perspective. *Freshwater Biology 40,* 3, 571–585.

[129] Xing, Y. and Shu, C.-W. 2005. High order finite difference weno schemes with the exact conservation property for the shallow water equations. *Journal of Computational Physics 208,* 1, 206–227.

[130] Xing, Y. and Shu, C.-W. 2006. High order well-balanced finite volume weno schemes and discontinuous galerkin methods for a class of hyperbolic systems with source terms. *Journal of Computational Physics 214,* 2, 567–598.

[131] Xing, Y., Zhang, X., and Shu, C.-W. 2010. Positivity-preserving high order well-balanced discontinuous galerkin methods for the shallow water equations. *Advances in Water Resources 33,* 12, 1476 – 1493.

[132] Yin, J., Yu, D., Yin, Z., Wang, J., and Xu, S. 2013. Multiple scenario analyses of huangpu river flooding using a 1D/2D coupled flood inundation model. *Natural Hazards 66,* 2, 577–589.

[133] Yu, D. and Lane, S. 2007. Coupling of a 2d diffusion-based flood inundation model to a 1d river flow for urban flood inundation modelling. *Proceedings of the Congress-International Association for Hydraulic Research 32,* 1, 30.